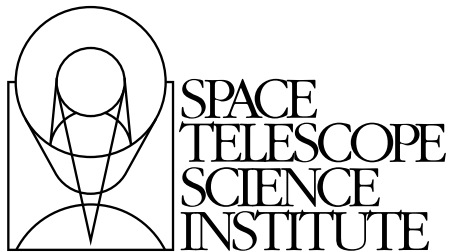

Version 8.0
December 2007

Advanced Camera for Surveys Instrument Handbook for Cycle 17



Space Telescope Science Institute
3700 San Martin Drive
Baltimore, Maryland 21218
help@stsci.edu

User Support

For prompt answers to any question, please contact the STScI Help Desk.

- **E-mail:** help@stsci.edu
- **Phone:** (410) 338-1082
(800) 544-8125 (U.S., toll free)

World Wide Web

Information and other resources are available on the ACS Web site:

- **URL:** <http://www.stsci.edu/hst/acs>

Revision History

| Version | Date | Editors |
|---------|---------------|--------------------------|
| 8.0 | December 2007 | Boffi, F.R., et al |
| 7.0 | October 2006 | Pavlovsky, C., et al. |
| 6.0 | October 2005 | Gonzaga, S., et al. |
| 5.0 | October 2004 | Pavlovsky, C., et al. |
| 4.0 | October 2003 | Pavlovsky, C., et al. |
| 3.0 | October 2002 | Pavlovsky, C., et al. |
| 2.1 | July 2001 | Pavlovsky, C., et al. |
| 2.0 | June 2001 | Suchkov, A., et al. |
| 1.0 | June 2000 | Jedrzejewski, R., et al. |

Citation

In publications, refer to this document as:

Boffi, F.R., et al. 2007, "ACS Instrument Handbook", Version 8.0, (Baltimore: STScI).

Send comments or corrections to:
Space Telescope Science Institute
3700 San Martin Drive
Baltimore, Maryland 21218
E-mail: help@stsci.edu

Acknowledgments

The technical and operational information contained in this Handbook is the summary of the experience gained by members of the STScI ACS-WFPC2 Team (AWT), the ACS group at ST-ECF, and by the ACS IDT.

Members of the STScI AWT are Marco Sirianni (lead), John Biretta, Francesca Boffi, Ralph Bohlin, Marco Chiaberge (ESA), Colin Cox, Andrew Fruchter, Ron Gilliland, Shireen Gonzaga, Anton Koekemoer, Ray Lucas, Jennifer Mack, Max Mutchler, Cheryl Pavlovsky, Vera Platais, Charles Proffitt, Kailash Sahu, and Nolan Walborn.

The ST-ECF ACS group is Richard Hook, Martin Kuemmel, Harald Kuntschner, and Jeremy Walsh.

The ACS IDT is Holland Ford (PI), Garth Illingworth (Deputy PI), George Hartig, Mark Rafal, Frank Bartko, Tom Broadhurst, Bob Brown, Chris Burrows, Ed Cheng, Mark Clampin, Jim Crocker, Paul Feldman, Marijn Franx, David Golimowski, Randy Kimble, John Krist, Tom La Jeunesse, Mike Lesser, Doug Leviton, George Miley, Marc Postman, Piero Rosati, Bill Sparks, Pam Sullivan, Zlatan Tsvetanov, Paul Volmer, Rick White, Bob Woodruff, David Ardila, Narciso Benitez, John Blakeslee, Rychard Bouwens, Larry Bradley, Nicholas J.G. Cross, Ricardo Demarco, Tomotsugu Goto, Caryl Gronwall, Brad Holden, Nicole Homeier, André Martel, Simona Mei, Felipe Menanteau, Gerhardt Meurer, Veronica Motta, Marco Sirianni, and Hien Tran.

The contributions of Ilana Dashevski, Warren Hack, Alan Welty, Tom Wheeler, and Susan Rose are greatly appreciated.

Table of Contents

| | |
|---|-----|
| Acknowledgments | iii |
| Chapter 1: Introduction | 1 |
| Chapter 2: Special Considerations for Cycle 16 | 5 |
| 2.1 Operation of the Side-2 electronics | 5 |
| 2.2 Dithering in Cycle 16 | 6 |
| Chapter 3: Introduction to ACS | 7 |
| 3.1 ACS Location in the HST Focal Plane | 7 |
| 3.2 Instrument Capabilities | 9 |
| 3.3 Instrument Design | 10 |
| 3.3.1 Detectors | 10 |
| 3.3.2 ACS Optical Design | 11 |
| 3.4 Basic Instrument Operations | 13 |
| 3.4.1 Target Acquisitions | 13 |
| 3.4.2 Typical ACS Observing Sequence | 14 |
| 3.4.3 Data Storage and Transfer | 14 |
| 3.5 ACS Quick Reference Guide | 15 |
| Chapter 4: Detector Performance | 21 |
| 4.1 Overview | 21 |
| 4.2 The CCDs | 21 |
| 4.2.1 Detector Properties..... | 21 |
| 4.2.2 CCD Spectral Response | 22 |
| 4.2.3 Quantum Efficiency Hysteresis..... | 23 |
| 4.2.4 CCD Long-Wavelength Fringing..... | 23 |
| 4.2.5 Readout Format..... | 23 |
| 4.2.6 Analog-To-Digital Conversion..... | 24 |
| 4.2.7 Flat Fields | 25 |

| | |
|--|-----------|
| 4.3 CCD Operations and Limitations..... | 27 |
| 4.3.1 CCD Saturation: the CCD Full Well | 27 |
| 4.3.2 CCD Shutter Effects on Exposure Times | 28 |
| 4.3.3 Readnoise | 28 |
| 4.3.4 Dark Current | 29 |
| 4.3.5 Warm and hot pixels..... | 33 |
| 4.3.6 Cosmic Rays..... | 39 |
| 4.3.7 Charge Transfer Efficiency | 41 |
| 4.3.8 UV Light and the HRC CCD | 44 |
| 4.4 The SBC MAMA | 44 |
| 4.4.1 MAMA Properties..... | 44 |
| 4.4.2 SBC Spectral Response | 46 |
| 4.4.3 Optical Performance | 48 |
| 4.5 SBC Operations and Limitations | 48 |
| 4.5.1 SBC Scheduling Policies | 48 |
| 4.5.2 MAMA Overflow of the 16 Bit Buffer | 49 |
| 4.5.3 MAMA Darks..... | 49 |
| 4.5.4 SBC signal-to-noise Ratio Limitations | 50 |
| 4.5.5 SBC Flatfield..... | 51 |
| 4.5.6 SBC Nonlinearity | 52 |
| 4.6 SBC Bright-Object Limits..... | 53 |
| 4.6.1 Overview..... | 53 |
| 4.6.2 Observational Limits | 54 |
| Chapter 5: Imaging..... | 55 |
| 5.1 Imaging Overview | 55 |
| 5.2 Important Considerations for ACS Imaging | 60 |
| 5.2.1 Optical Performance | 62 |
| 5.2.2 CCD Throughput Comparison | 62 |
| 5.2.3 Limiting Magnitudes..... | 62 |
| 5.2.4 Signal-To-Noise Ratios..... | 63 |
| 5.2.5 Saturation | 64 |
| 5.3 Wide Field Optical CCD Imaging | 64 |
| 5.3.1 Filter Set | 64 |
| 5.4 High-Resolution Optical and UV Imaging..... | 66 |
| 5.4.1 Filter Set | 66 |
| 5.4.2 Multiple Electron Events | 67 |
| 5.4.3 Red Leaks..... | 67 |

| | |
|--|----|
| 5.5 Ultraviolet Imaging with the SBC..... | 68 |
| 5.5.1 Filter Set | 68 |
| 5.5.2 Red Leaks..... | 68 |
| 5.5.3 SBC Imaging Filter Shifts..... | 69 |
| 5.6 ACS Point Spread Functions | 70 |
| 5.6.1 CCD Pixel Response Function | 70 |
| 5.6.2 Model PSFs | 71 |
| 5.6.3 Encircled Energy..... | 72 |
| 5.6.4 Geometric Distortions | 72 |
| 5.6.5 PSFs at Red Wavelengths and the UV | 75 |
| 5.6.6 Residual Aberrations | 76 |

Chapter 6: Polarimetry, Coronagraphy and Prism/Grism Spectroscopy.....

| | |
|---|-----|
| 6.1 Polarimetry..... | 79 |
| 6.2 Coronagraphy | 85 |
| 6.2.1 Coronagraph Design | 86 |
| 6.2.2 Acquisition Procedure and Pointing Accuracy..... | 89 |
| 6.2.3 Vignetting and Flat Fields | 90 |
| 6.2.4 Coronagraphic Performance | 91 |
| 6.2.5 Subtraction of the coronagraphic PSF..... | 94 |
| 6.2.6 The Off-Spot PSF | 99 |
| 6.2.7 Occulting Spot Motions..... | 100 |
| 6.2.8 Planning ACS Coronagraphic Observations | 101 |
| 6.2.9 Choice of Filters for Coronagraphic Observations | 104 |
| 6.3 Grism/Prism Spectroscopy | 104 |
| 6.3.1 WFC G800L..... | 105 |
| 6.3.2 HRC G800L | 107 |
| 6.3.3 HRC PR200L..... | 109 |
| 6.3.4 SBC PR110L | 110 |
| 6.3.5 SBC PR130L | 112 |
| 6.3.6 Observation Strategy | 113 |
| 6.3.7 Extraction and Calibration of Spectra | 115 |

| | |
|---|-----|
| Chapter 7: Observing Techniques | 117 |
| 7.1 Designing an ACS Observing Proposal..... | 117 |
| 7.1.1 Identify Science Requirements and Define ACS Configuration..... | 119 |
| 7.1.2 Use of Available-but-Unsupported Capabilities | 120 |
| 7.1.3 Determine Exposure Time and Check Feasibility | 121 |
| 7.1.4 Identify Need for Additional Exposures | 122 |
| 7.1.5 Data Volume Constraints..... | 122 |
| 7.1.6 Determine Total Orbit Request..... | 123 |
| 7.1.7 Charge Transfer Efficiency | 123 |
| 7.1.8 Image Anomalies..... | 124 |
| 7.2 SBC Bright Object Protection..... | 125 |
| 7.2.1 How Do You Determine if You Violate a Bright Object Limit for SBC Exposures? | 125 |
| 7.2.2 Policy and Observers' Responsibility in Phase I and Phase II | 126 |
| 7.2.3 Bright-Object Protection for Solar System Observations | 130 |
| 7.2.4 Prime and Parallel Observing with the SBC | 131 |
| 7.3 Operating Modes..... | 132 |
| 7.3.1 WFC ACCUM Mode | 132 |
| 7.3.2 HRC ACCUM Mode..... | 135 |
| 7.3.3 SBC ACCUM Mode | 136 |
| 7.3.4 HRC ACQ Mode | 136 |
| 7.4 Patterns and Dithering | 137 |
| 7.5 A Road Map for Optimizing Observations..... | 138 |
| 7.6 CCD Gain Selection | 140 |
| 7.6.1 WFC Gain..... | 140 |
| 7.6.2 HRC Gain | 141 |
| 7.7 ACS Apertures | 142 |
| 7.7.1 WFC Apertures | 142 |
| 7.7.2 Ramp Filter Apertures..... | 143 |
| 7.7.3 The Small Filter Apertures..... | 146 |
| 7.7.4 Polarizer Apertures | 148 |
| 7.7.5 HRC Apertures | 148 |
| 7.7.6 SBC Apertures..... | 151 |

| | |
|--|-----|
| 7.8 Specifying Orientation on the Sky | 152 |
| 7.8.1 Determining Orientation for Phase II | 156 |
| 7.9 Parallel Observations | 156 |
| 7.9.1 Parallel Observing | 156 |
| 7.10 Pointing Stability for Moving Targets | 162 |

Chapter 8: Overheads and Orbit-Time Determination

| | |
|--|-----|
| 8.1 Overview | 165 |
| 8.2 ACS Exposure Overheads..... | 166 |
| 8.2.1 Subarrays | 169 |
| 8.3 Orbit Use Determination Examples | 170 |
| 8.3.1 Sample Orbit Calculation 1:..... | 170 |
| 8.3.2 Sample Orbit Calculation 2:..... | 171 |
| 8.3.3 Sample Orbit Calculation 3:..... | 172 |
| 8.3.4 Sample Orbit Calculation 4:..... | 173 |
| 8.3.5 Sample Orbit Calculation 5:..... | 174 |

Chapter 9: Exposure-Time Calculations

| | |
|---|-----|
| 9.1 Overview | 175 |
| 9.1.1 The ACS Exposure Time Calculator..... | 175 |
| 9.2 Determining Count Rates from Sensitivities | 176 |
| 9.2.1 Imaging | 179 |
| 9.2.2 Spectroscopy | 181 |
| 9.3 Computing Exposure Times | 182 |
| 9.3.1 Calculating Exposure Times for a Given signal-to-noise | 182 |
| 9.3.2 Exposure Time Estimates for Red Targets in F850LP | 183 |
| 9.4 Detector and Sky Backgrounds | 185 |
| 9.4.1 Detector Backgrounds | 185 |
| 9.4.2 Sky Background | 185 |
| 9.5 Extinction Correction | 190 |

| | |
|--|-----|
| 9.6 Exposure-Time Examples..... | 191 |
| 9.6.1 Example 1: WFC Imaging a Faint Point Source | 191 |
| 9.6.2 Example 2: SBC Objective Prism Spectrum of a UV Spectrophotometric Standard Star..... | 193 |
| 9.6.3 Example 3: WFC VIS Polarimetry of the Jet of M87 | 193 |
| 9.6.4 Example 4: SBC imaging of Jupiter’s Aurora at Lyman-alpha..... | 194 |
| 9.6.5 Example 5: Coronagraphic imaging of the Beta-Pictoris Disk..... | 194 |
| 9.7 Tabular Sky Backgrounds..... | 195 |

Chapter 10: Imaging Reference

| | |
|--|-----|
| Material | 197 |
| 10.1 Introduction..... | 198 |
| 10.2 Using the Information in this Chapter | 198 |
| 10.2.1 Sensitivity Units and Conversions | 198 |
| 10.2.2 Signal-to-Noise | 199 |
| 10.2.3 Point Spread Functions | 200 |
| 10.3 Distortion in the ACS..... | 246 |
| 10.3.1 WFC..... | 247 |
| 10.3.2 HRC..... | 248 |
| 10.3.3 SBC | 250 |

| | |
|-----------------------|-----|
| Glossary | 253 |
|-----------------------|-----|

| | |
|--------------------|-----|
| Index | 257 |
|--------------------|-----|

Introduction

The Advanced Camera for Surveys (ACS), a third-generation instrument, was installed in the Hubble Space Telescope during Servicing Mission 3B (http://www.stsci.edu/hst/HST_overview/servicing_missions) on March 7, 2002. Its primary purpose is to increase HST imaging discovery efficiency by about a factor of 10, with a combination of detector area and quantum efficiency that surpasses previous instruments.

ACS has three independent cameras that provide wide-field, high resolution, and ultraviolet imaging capabilities respectively, using a broad assortment of filters designed to address a large range of scientific goals. In addition, coronagraphic, polarimetric, and grism capabilities make this a versatile and powerful instrument.

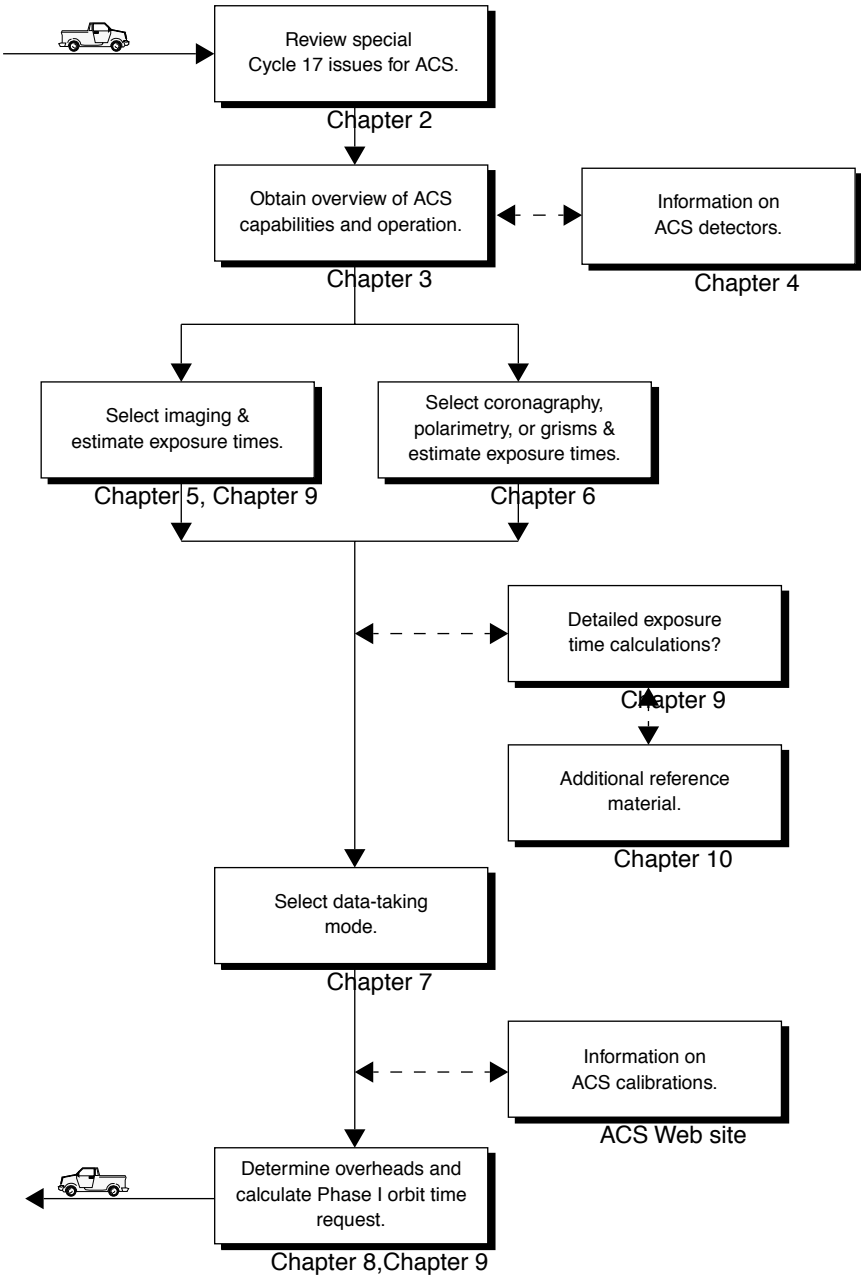
The *ACS Instrument Handbook*, which is maintained by the AWT at STScI, describes the instrument properties, performance, operations, and calibration. It is the basic technical reference manual for the instrument, and should be used with other documents (listed in Table 1.1) for writing Phase I proposals, detailed Phase II programs, and for data analysis. (See Figure 1.1).

The documents in Table 1.1 can be downloaded from the ACS STScI Web site, <http://www.stsci.edu/hst/acs>. Paper copies can be requested by sending a message to help@stsci.edu or by calling 410-338-1082. European users may also contact the Space Telescope European Coordinating Facility (ST ECF) at Garching, Germany (+49-89-320 06-291, stdesk@eso.org).

Table 1.1: Useful documents

| Purpose | Document or resource |
|---------------------------------|--|
| General observatory information | HST Primer http://www.stsci.edu/hst/proposing/docs/proposing/documents/cp/primer.pdf |
| Phase I proposals | Proposing Overview http://www.stsci.edu/hst/proposing/docs/proposingOverview Call for Proposals http://www.stsci.edu/hst/hst/proposing/documents/cp/cp_cover.html |
| Phase II programs | Phase II Proposal Instructions http://www.stsci.edu/hst/programs/hst/proposing/docs/p2pi.html Astronomer's Proposal Tool (APT) for Phase II preparations http://apt.stsci.edu/ Two-Gyro Web site http://www.stsci.edu/hst/HST_overview/TwoGyroMode Two-Gyro Handbook http://www.stsci.edu/hst/HST_overview/TwoGyroMode/handbook/cover.html |
| Data analysis | ACS Data Handbook http://www.stsci.edu/hst/acs/documents/handbooks/DataHandbookv4/ACS_longdnhbcover.html Dither Handbook http://www.stsci.edu/instruments/wfpc2/Wfpc2_driz/dither_handbook.html Space Telescope Analysis Newsletter http://www.stsci.edu/hst/acs/documents/isrs/hst/acs/documents/newsletters Instrument Science Reports http://www.stsci.edu/hst/acs/documents/isrs Calibration and Pipeline Information http://www.stsci.edu/hst/Post-observation |
| Instrument specific | ACS Web page http://www.stsci.edu/hst/acs ACS Forum http://forums.stsci.edu/phpbb/viewforum.php?f=14 |

Figure 1.1: Handbook roadmap for proposal preparation.





CHAPTER 2:

Special Considerations for Cycle 16

In this chapter . . .

2.1 Operation of the Side-2 electronics / 5

2.2 Dithering in Cycle 16 / 6

2.1 Operation of the Side-2 electronics

On June 19, 2006, ACS suspended activities due to an anomaly in a circuit board component in one of the low voltage power supplies used to power the ACS CCD detectors. ACS was reactivated on a completely redundant set of electronics on July 2, 2006. With the electronics switch-over the ACS remains fully functional.

As part of the reactivation of ACS, the AWT lowered the Wide Field Channel (WFC) CCD temperature setpoint from $-77\text{ }^{\circ}\text{C}$ to $-81\text{ }^{\circ}\text{C}$. By doing so, it was possible to improve the instrument performance as well as combine the calibrations needed for both activities. Lowering the WFC CCD operating temperature has significantly reduced the number of hot pixels and dark current in the WFC images, thereby improving image quality and detectability of faint objects.

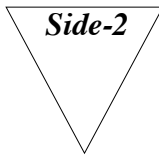
The AWT is currently implementing the calibrations necessary to fully characterize the instrument in its new condition. Some of these calibration results have already been incorporated into the standard ACS data pipeline, and others will be as the analyses are completed. The WFC CCDs are expected to have changes of 1-3% in overall sensitivity with some spatial dependence both on the large and small scale. Many ACS programs require

high photometric precision ($\sim 1\%$), and new calibration of the flat fields and quantum efficiency are needed to support these programs.

Items that may be affected by the Side-2 and WFC temperature setpoint changes include readout noise, the hot pixel population, charge transfer efficiency, quantum efficiency, sensitivity, and flat fields. Most of the changes are expected to be small, and the values currently listed in the Handbook for Side-1 are good approximations to those expected for Side-2. Observers should consult the ACS Web site:

<http://www.stsci.edu/hst/acs/>

for the most up to date information on instrument performance, including instrument science reports (ISRs) that describe the calibration results in detail.



We will use this symbol to highlight through the text all sections or parameters that could be affected by the change in electronics or operational temperature. Readers are encouraged to look for updates on the ACS Web site whenever they encounter such symbol.

2.2 Dithering in Cycle 16

The AWT has long recommended that observers dither (or offset) their observations to remove hot pixels, cosmetic defects, and cosmic rays in the combined data. Dithering allows for optimal sampling of the point spread function and provides substantive improvements over the use of CR-SPLITS, which do not remove hot pixels or other permanent cosmetic defects (e.g., bad columns or the WFC interchip gap). Dithering can be achieved in two ways: 1) By using exposure-to-exposure position offsets specified explicitly by POS-TARGs, or 2) By using flexible predefined dither patterns. Both POS-TARGs and dither patterns now result in associations, and dither patterns can also be nested to achieve various pixel sampling strategies for a wide variety of science goals. Currently available dither patterns within APT and their recommended uses are described on the ACS Dither Web page:

<http://www.stsci.edu/hst/acs/proposing/dither>

We strongly encourage observers to dither their ACS observations. Beginning in Cycle 16, observers who choose not to dither their ACS WFC and HRC imaging exposures should provide sound scientific justification for not doing so in the Phase I Proposal Description of Observations. The choice of dither pattern is left to the discretion of the observer since it may depend upon the science goals of the program. The AWT is ready to assist observers who need help in selecting the appropriate pattern for their observations.

Introduction to ACS

In this chapter . . .

| |
|---|
| 3.1 ACS Location in the HST Focal Plane / 7 |
| 3.2 Instrument Capabilities / 9 |
| 3.3 Instrument Design / 10 |
| 3.4 Basic Instrument Operations / 13 |
| 3.5 ACS Quick Reference Guide / 15 |

3.1 ACS Location in the HST Focal Plane

ACS is mounted in one of the instrument bays behind the HST primary mirror. The relative locations of the science instruments in the focal plane and their fields of view are shown schematically in Figure 3.1. When referring to the HST and its focal plane, we use a coordinate system that is fixed to the telescope and consists of three orthogonal axes: U1, U2 and U3. U1 lies along the optical axis, U2 is parallel to the solar-array rotation axis, and U3 is perpendicular to the solar-array axis. (Note: Some HST documentation uses the alternative V1, V2, V3 coordinate system for which $V1=U1$, $V2=-U2$ and $V3=-U3$.)

Figure 3.1: The HST field of view with the locations of the SI and the FGS apertures in the (U₂,U₃) focal plane. The scale in arcsec is indicated.

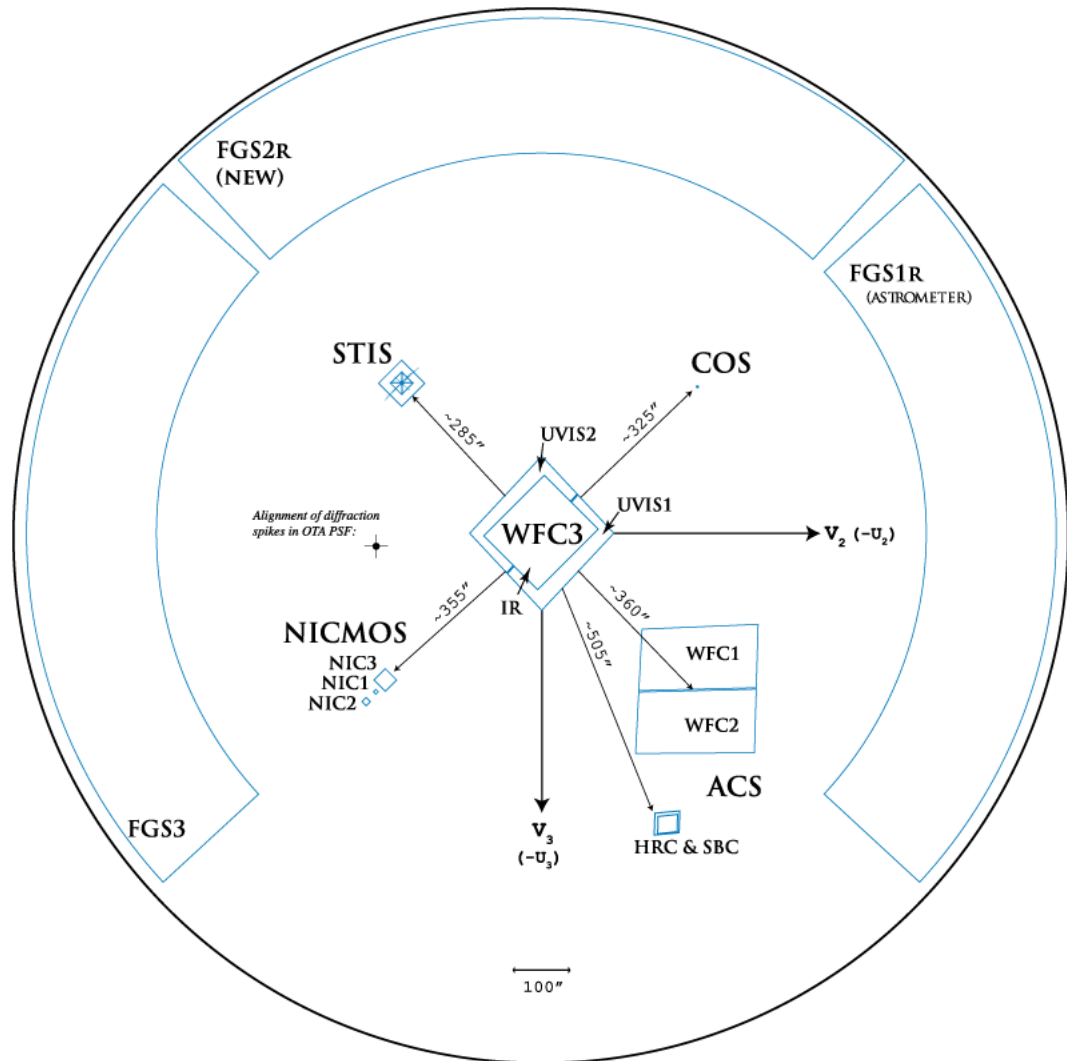


Figure 3.1 shows the layout of the instrument entrance apertures in the telescope focal plane as projected onto the sky.

3.2 Instrument Capabilities

ACS is a versatile instrument that can be applied to a broad range of scientific programs. The three prime capabilities of ACS are:

- Deep, wide-field imaging from visible to near-IR wavelengths.
- High spatial resolution imaging from near-UV to near-IR wavelengths.
- Solar blind UV imaging.

ACS has three channels, each optimized for a specific goal:

- Wide Field Channel (WFC): 202 x 202 arcsecond field of view from $\sim 3500 \text{ \AA}$ to $11,000 \text{ \AA}$, and peak efficiency of 48% (including the Optical Telescope Assembly (OTA)). The plate scale of ~ 0.05 arcseconds/pixel provides critical sampling at $11,600 \text{ \AA}$.
- High Resolution Channel (HRC): 29 x 26 arcsecond field of view from $\sim 1700 \text{ \AA}$ to $11,000 \text{ \AA}$, and peak efficiency of 29%. The plate scale of ~ 0.027 arcseconds/pixel provides critical sampling at 6300 \AA .
- Solar Blind Channel (SBC): 34.6 x 30.5 arcsecond field of view from 1150 \AA to 1700 \AA , plate scale of ~ 0.032 arcseconds/pixel, and peak efficiency of 7.5%.

In addition to these three prime capabilities, ACS also provides:

- Grism spectroscopy: Low resolution ($R \sim 100$ @ 8000 \AA) wide field spectroscopy from 5500 \AA to $10,500 \text{ \AA}$ available in both the WFC and the HRC.
- Prism spectroscopy: Low resolution ($R = 59$ @ 2500 \AA) near-UV spectroscopy from 1700 \AA to 3900 \AA available in the HRC.
- Prism spectroscopy: Low resolution ($R \sim 100$ @ 1500 \AA) far-UV spectroscopy from 1250 \AA to 1800 \AA available in the SBC.
- Coronagraphy: Aberrated beam coronagraphy in the HRC from 2000 \AA to $11,000 \text{ \AA}$ with 1.8 arcsecond and 3.0 arcsecond diameter occulting spots.
- Imaging Polarimetry: Polarimetric imaging in the HRC and WFC with relative polarization angles of 0° , 60° , and 120° .

3.3 Instrument Design

3.3.1 Detectors

ACS uses the following detectors in each channel:

- The WFC employs a mosaic of two 4096 x 2048 Scientific Imaging Technologies (SITe) CCDs. The 15 x 15 μm pixels provide ~ 0.05 arcseconds/pixel spatial resolution, with critical sampling at 11,600 \AA , resulting in a nominal 202 x 202 arcsecond field of view (FOV). The spectral sensitivity of the WFC ranges from ~ 3500 \AA to $\sim 11,000$ \AA , with a peak efficiency of 48% at ~ 7000 \AA (including OTA).
- The HRC detector is a 1024 x 1024 SITe CCD, with 21 x 21 μm pixels that provide ~ 0.028 x 0.025 arcsecond/pixel spatial resolution with critical sampling at 6300 \AA . This gives the HRC a nominal 29 x 26 arcsecond field of view. The spectral response of the HRC ranges from ~ 1700 \AA to $\sim 11,000$ \AA , and it has a peak efficiency of 29% at ~ 6500 \AA (including OTA).
- The SBC detector is a solar-blind CsI microchannel plate (MCP) with Multi-Anode Microchannel Array (MAMA) readout. It has 1024 x 1024 pixels, each 25 x 25 μm in size. This provides a spatial resolution of ~ 0.034 x 0.030 arcseconds/pixels, producing a nominal FOV of 34.6 x 30.1 arcseconds. The SBC UV spectral response ranges from ~ 1150 \AA to ~ 1700 \AA with a peak efficiency of 7.5% at 1250 \AA .

The WFC & HRC CCDs

The ACS CCDs are thinned, backside-illuminated full-frame devices cooled by thermo-electric cooler (TEC) stacks housed in sealed, evacuated dewars with fused silica windows. The spectral response of the WFC CCDs is optimized for imaging at visible to near-IR wavelengths, while the HRC CCD spectral response is optimized specifically for near-UV wavelengths. Both CCD cameras produce a time-integrated image in the ACCUM data-taking mode. As with all CCD detectors, there is noise (readout noise) and time (read time) associated with reading out the detector following an exposure.

The minimum exposure time is 0.1 seconds for the HRC and 0.5 seconds for the WFC. Between successive identical exposures, the minimum time is 45 seconds for the HRC, and 135 seconds for the WFC, for full-frame readouts. However, this can be reduced to as little as ~ 35 seconds for WFC subarray readouts. The dynamic range for a single exposure is ultimately limited by the depth of the CCD full well ($\sim 85,000$ e^- for the WFC and 155,000 e^- for the HRC), which determines

the total amount of charge that can accumulate in any one pixel during an exposure without saturation. Cosmic rays will affect all CCD exposures. CCD observations should be broken into multiple exposures whenever possible to allow removal of cosmic rays in post-observation data processing. Section 4.3.6

The SBC MAMA

The SBC MAMA is a photon-counting detector which provides a two-dimensional ultraviolet capability. It can only be operated in ACCUM mode. In order to preserve its functionality, the SBC MAMA detector is subject to both scientific and absolute brightness limits. At high local (≥ 50 counts/second/pixel) and global ($> 200,000$ counts/second) illumination rates, counting becomes nonlinear in a way that is not correctable. At only slightly higher illumination rates, the MAMA detectors are subject to damage. We have therefore defined absolute local and global count rate limits, which translate to a set of configuration-dependent bright-object screening limits. Sources which violate the screening limits in a given configuration cannot be observed in those configurations, as discussed in Section 4.6 and Section 7.2.

3.3.2 ACS Optical Design

The ACS design incorporates two main optical channels: one for the WFC, and one which is shared by the HRC and SBC. Each channel has independent corrective optics to compensate for spherical aberration in the HST primary mirror. The WFC has three silver-coated optics to optimize instrument throughput in the visible and near-IR. The silver coatings cut off at wavelengths shortward of 3500 \AA . The WFC has two filter wheels which it shares with the HRC, offering the possibility of internal WFC/HRC parallel observing for some filter combinations (Section 7.9). The optical design of the WFC is shown schematically in Figure 3.2. The HRC/SBC optical chain comprises three aluminized mirrors overcoated with MgF_2 , shown schematically in Figure 3.3. The HRC or SBC channels are selected by means of a plane fold mirror (M3 in Figure 3.3). The HRC is selected by inserting the fold mirror into the optical chain so that the beam is imaged onto the HRC detector through the WFC/HRC filter wheels. The SBC channel is selected by moving the fold mirror out of the beam to yield a two mirror optical chain that focuses light through the SBC filter wheel onto the SBC detector. The aberrated beam coronagraph is accessed by inserting a mechanism into the HRC optical chain. This mechanism positions a substrate with two occulting spots at the aberrated telescope focal plane and an apodizer at the re-imaged exit pupil.

While there is no mechanical reason why the coronagraph could not be used with the SBC, for health and safety reasons, use of the coronagraph is forbidden with the SBC.

Figure 3.2: ACS optical design: wide field channel.

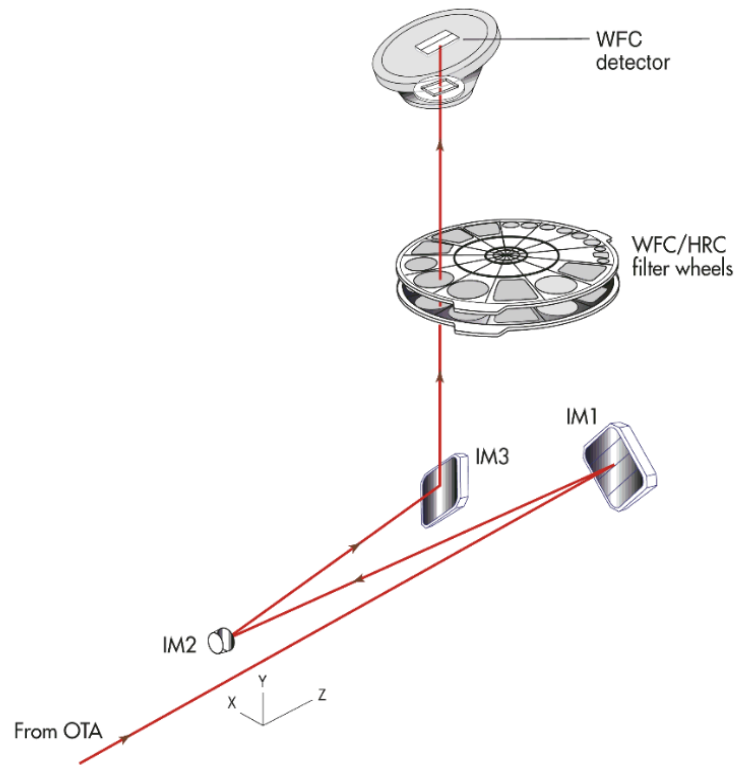
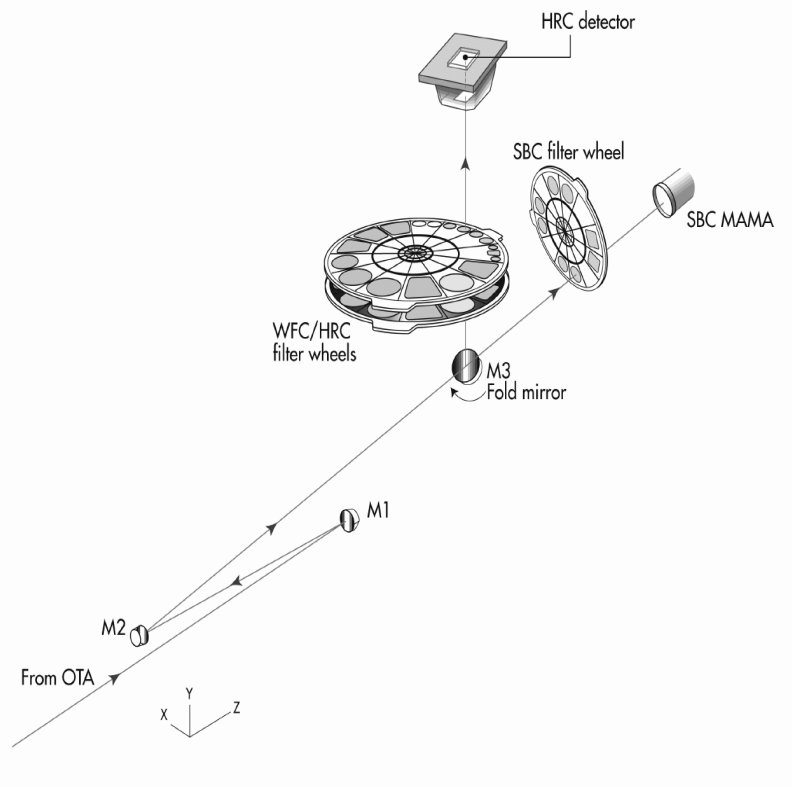


Figure 3.3: ACS optical design: high resolution/solar blind channels



Filter Wheels

ACS has three filter wheels: two shared by the WFC and HRC, and a separate wheel dedicated to the SBC. The WFC/HRC filter wheels contain the major filter sets. Each wheel also contains one clear WFC aperture and one clear HRC aperture (see Chapter 5 for more on filters). Parallel WFC and HRC observations are possible for some filter combinations (auto-parallels) and these are automatically added by the Astronomer's Proposal Tool (APT) (<http://apt.stsci.edu/>) in Phase II, unless the user disables this option via the PAREXP optional parameter, or if adding the parallel observations disallowed due to timing considerations. Because the filter wheels are shared, it is not possible to independently select the filter for WFC and HRC parallel observations.

Calibration-Lamp Systems

ACS has a calibration subsystem consisting of tungsten lamps and a deuterium lamp for internally flat fielding each of the optical chains. The calibration subsystem illuminates a diffuser on the rear surface of the ACS aperture door, which must be closed for calibration exposures. Under normal circumstances, users are not allowed to use the internal calibration lamps.

In addition, a post-flash capability was added to the instrument to provide the means of mitigating the effects of Charge Transfer Efficiency (CTE) degradation. We do not expect to use this facility at present (except for calibration and characterization) but in later years, as radiation damage of the CCDs causes the CTE to degrade, it is possible that some users will want to avail themselves of this facility. Astrometry programs may particularly benefit from the use of this capability, as is discussed briefly in Section 4.3.7. Since we are not yet at a stage where use of post-flash is expected to be useful for any science observations, we do not provide an extensive discussion related to it.

3.4 Basic Instrument Operations

3.4.1 Target Acquisitions

For the majority of ACS observations target acquisition is simply a matter of defining the appropriate aperture for the observation. Once the telescope acquires its guide stars, your target will be within ~ 1 to 2 arcseconds of the specified pointing. For observations with the ramp filters, one must specify the desired central wavelength for the observation. For the special case of coronagraphic observations, an onboard target acquisition will need to be specified. The nominal accuracy of the onboard target acquisition process is ~ 6 milliarcseconds.

3.4.2 Typical ACS Observing Sequence

ACS is expected to be used primarily for deep, wide-field survey imaging. Important issues for observers to consider will be the “packaging” of their observations, how observations are CR-SPLIT to mitigate the impact of cosmic rays, how sub-stepping or “dithering” of images for removal of hot pixels is implemented, and how, if necessary, to construct a mosaic pattern to map the target. HRC observations and narrowband observations with the WFC are more likely to be readnoise limited, requiring consideration of optimum number of readouts. Observations with the MAMA detectors are not affected by cosmic rays or readnoise, but long integration times will often be needed to obtain sufficient signal-to-noise.

A typical ACS observing sequence is expected to consist of a series of 10 to 20 minute dithered exposures for each program filter. Coronagraphic observations will require an initial target acquisition observation to permit centering of the target under the occulting mask. Observers will generally not take their own calibration exposures. See Chapter 7 for more details about observing strategies.

3.4.3 Data Storage and Transfer

At the conclusion of each exposure, the science data are read out from the detector and placed in ACS’s internal buffer memory, where it is stored until it can be transferred to the HST solid state data recorder (and thereafter to the ground). The internal buffer memory is large enough to hold one WFC image, or sixteen HRC or SBC images, and so the buffer will typically need to be dumped before or during the following WFC exposure. If the following exposure is longer than ~339 seconds, then the buffer dump from the preceding exposure will be performed during integration (see Section 8.2 for a more complete discussion).

ACS’s internal buffer stores the data in a 16 bit-per-pixel format. This structure imposes a maximum of 65,535 counts per pixel. For the MAMA detectors this maximum is equivalent to a limit on the total number of detected photons per pixel which can be accumulated in a single exposure. For the WFC and HRC, the 16 bit buffer format (and not the full well) limits the photons per pixel which can be accumulated without saturating in a single exposure when GAIN=1 for WFC, and GAIN=2 for the HRC is selected. See Chapter 4 and Chapter 7 for a detailed description of ACS instrument operations.

3.5 ACS Quick Reference Guide

Table 3.1: Instrument characteristics.

| | WFC | HRC | SBC |
|------------------------------------|--|---|--|
| Field of View | 202" × 202" | 29" × 26" | 34.6" × 30.8" |
| Plate Scale | ~0.05"/pixel | ~0.028 × 0.025"/pixel | ~0.034 × 0.030"/pixel |
| Pixel Size | 15 × 15 μm | 21 × 21 μm | 25 × 25 μm |
| Image Format | 2 × 2048 × 4096 pixels | 1024 × 1024 pixel | 1024 × 1024 pixel |
| Spectral Response | ~3500 Å to 11,000 Å | ~1700 Å to 11,000 Å | ~1150 Å to 1700 Å |
| Detector | SITe CCDs thinned backside illuminated, anti-reflection coated, multiphased pinned | SITe CCD thinned backside illuminated, anti-reflection coated, multiphased pinned | CsI MCP with MAMA readout |
| Detector Efficiency | ~77% at 4000 Å ~83% at 6000 Å ~67% at 8000 Å | ~33% at 2500 Å ~69% at 6000 Å ~53% at 8000 Å | ~19.2% @ 1216 Å |
| Peak Efficiency ² | 48% at ~7000 Å | 29% at ~6500 Å | 7.5% at ~1250 Å |
| Readnoise | 5.0 e ⁻ | 4.7 e ⁻ | 0 counts |
| Dark Current ² | 0.0029 e ⁻ /s/pixel | 0.0058 e ⁻ /s/pixel | 1.241 × 10 ⁻⁵ e ⁻ /s/pixel |
| Full Well ² | 84,700 e ⁻ | 155,000 e ⁻ | ¹ Detector count rate linearity limit: 200,000 counts/second Pixel count-rate linearity limit: ~22 counts/second/pixel |
| Gain | 1,2,4 and 8 e ⁻ /DN (Max 65,535 DN) | 1,2,4 and 8 e ⁻ /DN (Max 65,535 DN) | n/a |
| Operating Temperature ² | -80°C | -81°C | n/a |

1. Loss of linearity occurs at count rates larger than these values. For more information, please see Section 4.5.6.

2. Average value for WFC1 and WFC2

Table 3.2: Calibration accuracies.

| Attribute | WFC | HRC | SBC | Limiting factor |
|--|---|---|----------------|--|
| Distortion Solution Accuracy | 0.1 pixel | 0.1 pixel | 0.25 pixel | Calibration & stability of geometric distortion ¹ |
| Absolute Astrometry | 0.5" to 1" | 1" | 1" | Guide Star Catalog uncertainties ² |
| Absolute Photometry | 3% | 2% | 5% | Absolute calibration, standards |
| Relative Photometry within an Image | 1% | 1% | 2% | Flat-field characterization or characterization of geometric distortion. |
| Repeated Photometry of Same Star | 0.3% | 0.3% | 1% | Stability of flat field |
| Transformation to Standard Magnitude Systems | 0.02 mag SDSS 0.025 mag WFPC2 0.03 mag BVRI | 0.02 mag SDSS 0.025 mag WFPC2 0.03 mag BVRI | n/a | DQE curve determination Color terms |
| Polarimetry | 1% | 1% | n/a | |
| Wavelength Calibration | 20 Å grism | 12 Å grism | 1 pixel prisms | Accuracy of dispersion solution |
| Spectrophotometry | 6% (Grism) | 10% (Grism) | 20% (Prism) | |

1. Anderson & King, ISR 04-15 (<http://www.stsci.edu/hst/acs/documents/isrs/isr0415.pdf>)2. Koekemoe, et. al., ISR 05-06 (<http://www.stsci.edu/hst/acs/documents/isrs/isr0506.pdf>)

Table 3.3: ACS filters.

| Filter type | Filter description | Camera |
|---------------|--|-------------------------|
| Broadband | Sloan Digital Sky Survey (SDSS): F475W, F625W, F775W, F850LP | WFC/HRC |
| | B, V, Medium V, Wide V, I: F435W, F555W, F550M, F606W, F814W | WFC/HRC |
| | Near-UV: F220W, F250W, F330W | HRC |
| | No Filter: CLEAR | WFC/HRC |
| Narrowband | H α (2%), [OIII] (1%), [NII] (1%): F658N, F502N, F660N | WFC/HRC |
| | NeV (3440 Å): F344N | HRC |
| | Methane (8920 Å): F892N | HRC/[WFC ¹] |
| Ramp filters | 2% bandpass (3700-10,700 Å): FR388N, FR505N, FR656N | WFC/HRC |
| | 2% bandpass (3700-10,700 Å): FR423N, FR462N, FR716N, FR782N, FR853N, FR931N, FR1016N, FR551N, FR601N | WFC |
| | 9% bandpass (3700-10,700 Å): FR459M, FR914M | WFC/HRC |
| | 9% bandpass (3700-10,700 Å): FR647M | WFC |
| Spectroscopic | Grism: G800L | WFC/HRC |
| | Prism: PR200L | HRC |
| Polarizers | Visible (0°, 60°, 120°): POL0V, POL60V, POL120V | HRC/[WFC ¹] |
| | Near-UV (0°, 60°, 120°): POL0UV, POL60UV, POL120UV | HRC/[WFC ¹] |
| Medium Band | Lyman-Alpha: F122M | SBC |
| Long Pass | MgF2, CaF2, BaF2, Quartz, Fused Silica: F115LP, F125LP, F140LP, F150LP, F165LP | SBC |
| Prisms | LiF, CaF2: PR110L, PR130L | SBC |

1. Limited field of view (72" x 72") for these filters using WFC

Table 3.4: ACS polarizers.

| Polarizer set | Filters | Filter comments |
|---------------------------|---------|-----------------|
| POL0UV, POL60UV, POL120UV | F220W | HRC NUV short |
| | F250W | HRC NUV long |
| | F330W | HRC U |
| | F435W | Johnson B |
| | F814W | Broad I |
| POL0V, POL60V, POL120V | F475W | SDSS g |
| | F606W | Johnson V |
| | F625W | SDSS r |
| | F658N | H α |
| | F775W | SDSS i |

Table 3.5: ACS dispersers.

| Disperser | Channel | Wavelength range (Å) | Resolving power |
|-----------|---------|---------------------------|-----------------|
| G800L | WFC | 1st order: 5500 to 10,500 | 100 @8000 Å |
| G800L | WFC | 2nd order: 5000 to 8500 | 200 @8000 Å |
| G800L | HRC | 1st order: 5500 to 10,500 | 140 @8000 Å |
| G800L | HRC | 2nd order: 5500 to 8500 | 280 @8000 Å |
| PR200L | HRC | 1700 to 3900 | 59 @2500 Å |
| PR110L | SBC | 1150 to 1800 | 79 @1500 Å |
| PR130L | SBC | 1250 to 1800 | 96 @1500 Å |

Table 3.6: Useful tables and figures list.

| Topics | Tables |
|--|---|
| Proposal Preparation Tips | <p>Table 6.1: Examples of polarizer and non-polarizer exposures in a Phase II proposal.</p> <p>Table 7.1: Science decision guide.</p> <p>Table 7.2: Science feasibility guide.</p> <p>Table 9.1: Useful quantities for the ACS WFC.</p> <p>Table 9.2: Useful quantities for the ACS HRC.</p> <p>Table 9.3: Useful quantities for the ACS SBC.</p> |
| Overheads | <p>Table 8.1: Science exposure overheads: general.</p> <p>Table 8.2: ACS science exposure overhead times (minutes).</p> |
| Auto-parallels | <p>Table 7.12: Filter combinations for auto-parallels in the two cases of (i) HRC camera prime and (ii) WFC camera prime.</p> <p>Table 7.13: Minimum primary exposure time (seconds) to attach an auto-parallel for CR-SPLIT=n.</p> |
| Aperture Parameters | <p>Table 7.7: WFC aperture parameters.</p> <p>Table 7.8: Ramp filter apertures.</p> <p>Table 7.9: HRC aperture parameters.</p> <p>Table 7.10: SBC aperture parameters</p> <p>Table 7.11: Plate scales and axis angles for the 3 ACS channels.</p> <p>Figure 3.1: The HST field of view with the locations of the SI and the FGS apertures in the (U2,U3) focal plane. The scale in arcsec is indicated.</p> <p>Figure 7.8: Aperture and image feature orientation.</p> <p>Figure 7.9: ACS apertures in the V2/V3 reference frame.</p> |
| Detector Characteristics | <p>Table 3.1: Instrument characteristics.</p> <p>Table 4.1: CCD gain and readout noise (e- rms) under SIDE-1 operation (03/2002->06/2006).</p> <p>Table 4.8: SBC detector performance characteristics.</p> |
| SBC Bright Object Protection Limits | <p>Table 7.3: Absolute SBC count rate screening limits for nonvariable and variable objects.</p> <p>Table 7.4: Bright limit V-band magnitudes for observations with the SBC filters and prisms (no reddening).</p> <p>Table 7.6: Bright object protection policy for SBC observations.</p> |

| Topics | Tables |
|-----------------------------------|---|
| Hot and Warm Pixels | <p>Table 4.3: Creation rate of new hot pixels (pixel/day).</p> <p>Table 4.5: Permanent warm and hot pixel growth (%/yr).</p> <p>Figure 4.12: Growth of permanent warm and hot pixel population as a function of time (WFC top, HRC bottom).</p> |
| Charge Transfer Efficiency | <p>Table 4.6: Charge transfer efficiency measurements for the ACS CCDs at installation time (Fe55 test at 1620 e⁻).</p> <p>Table 4.7: Example of science applications and their assumed parameters.</p> <p>Figure 4.15: Projected CTE losses in WFC (and equivalently, the size of corrections).</p> |
| Geometric Distortion | <p>Figure 10.127: The geometric distortion map for the ACS/WFC, which shows only the non-linear component to the solution. Note that this figure is rotated 180° with respect to the pipeline calibration products, where WFC2 is the lower half of the detector.</p> <p>Figure 10.128: The map of the effective pixel areas of the ACS/WFC chips.</p> <p>Figure 10.129: The geometric distortion map for the HRC.</p> <p>Figure 10.130: The map of the effective pixel areas of the HRC.</p> |
| Encircled Energy | <p>Table 5.4: Encircled energy measurements for the ACS channels.</p> <p>Table 9.4: Encircled energy comparison for WFC/F850LP.</p> <p>Figure 4.18: MAMA point spread function.</p> <p>Figure 5.9: Encircled energy for the CCD channels.</p> <p>Figure 5.10: Encircled energy for the SBC.</p> |
| PSF | <p>Figure 5.8: Kernels representing CCD pixel functions for HRC and WFC.</p> <p>Table 5.10: Model ACS SBC PSFs.</p> <p>Figure 5.9: Encircled energy for the CCD channels.</p> |
| Plate Scale | <p>Table 7.11: Plate scales and axis angles for the 3 ACS channels.</p> |
| Filters | <p>Table 3.3: ACS filters.</p> <p>Table 3.5: ACS dispersers.</p> <p>Table 5.1: ACS WFC/HRC filters in Filter Wheel #1.</p> <p>Table 5.2: ACS WFC/HRC filters in Filter Wheel #2.</p> <p>Table 5.3: ACS SBC filter complement.</p> <p>Table 5.6: In-band flux as a percentage of the total flux.</p> <p>Table 5.7: Visible-light rejection of the SBC F115LP imaging mode.</p> |
| Polarizers: | <p>Table 3.4: ACS polarizers.</p> <p>Table 6.1: Examples of polarizer and non-polarizer exposures in a Phase II proposal.</p> <p>Table 6.2: Filters that can be used in conjunction with the ACS polarizers.</p> |
| Photometry | <p>Table 5.5: V detection limits for ACS, HRC, and SBC direct imaging.</p> <p>Table 9.1: Useful quantities for the ACS WFC.</p> <p>Table 9.2: Useful quantities for the ACS HRC.</p> <p>Table 9.3: Useful quantities for the ACS SBC.</p> <p>Table 10.1: Color corrections AB_n to go from Johnson V magnitude to AB magnitude for the WFC.</p> <p>Table 10.2: Color corrections AB_n to go from Johnson V magnitude to AB magnitude for the HRC.</p> <p>Table 10.3: Color corrections AB_n to go from Johnson V magnitude to AB magnitude for the SBC.</p> |

| Topics | Tables |
|---|---|
| Limiting Magnitudes for Direct Imaging | Table 5.5: V detection limits for ACS, HRC, and SBC direct imaging. |
| Spectroscopy | <p>Table 6.3: Optical parameters of ACS dispersers.</p> <p>Table 6.4: V detection limits for the ACS grism/prism modes.</p> <p>Figure 6.15: Sensitivity versus wavelength for WFC G800L.</p> <p>Figure 6.16: Sensitivity versus pixel position for WFC G800L.</p> <p>Figure 6.18: Sensitivity versus wavelength for HRC G800L.</p> <p>Figure 6.19: Sensitivity versus pixel position for HRC G800L.</p> <p>Figure 6.21: Sensitivity versus wavelength for HRC/PR200L.</p> <p>Figure 6.22: Sensitivity versus wavelength for SBC PR110L.</p> <p>Figure 6.24: Sensitivity versus wavelength for SBC/PR130L.</p> |
| Sky Backgrounds | <p>Table 9.5: Approximate zodiacal sky background as a function of ecliptic latitude and ecliptic longitude (in V magnitudes per square arcseconds).</p> <p>Table 9.6: Geocoronal emission lines.</p> <p>Table 9.7: High sky backgrounds.</p> <p>Figure 9.1: High sky background intensity as a function of wavelength.</p> <p>Figure 9.2: Background contributions in V magnitude per arcseconds² due to the zodiacal light, Moon, and the sunlit Earth, as a function of angle between the target and the limb of the Earth or Moon.</p> <p>Figure 9.3: Extinction versus wavelength.</p> |
| Calibration Accuracies | <p>Table 3.2: Calibration accuracies.</p> <p>Figure 4.5: Dark rate trend with time for the WFC CCDs.</p> |

Detector Performance

In this chapter. . .

| |
|---|
| 4.1 Overview / 21 |
| 4.2 The CCDs / 21 |
| 4.3 CCD Operations and Limitations / 27 |
| 4.4 The SBC MAMA / 44 |
| 4.5 SBC Operations and Limitations / 48 |
| 4.6 SBC Bright-Object Limits / 53 |

4.1 Overview

ACS employs two fundamentally different types of detectors: CCDs for use from the near-UV to the near-IR, and a Multi-Anode Microchannel Array detector known as a MAMA for use in the ultraviolet. The CCD and the MAMA detectors are used in different ways and impose their own unique limitations on the feasibility of observations performed with them. This chapter covers the properties of the ACS detectors, descriptions of how to use them to optimize scientific programs, and steps needed to ensure the feasibility of observations.

4.2 The CCDs

4.2.1 Detector Properties

WFC Properties

The WFC/CCD consists of two 4096 x 2048 charge-coupled devices that are sensitive from the near-UV to the near-IR. These CCDs are

thinned, backside-illuminated devices manufactured by Scientific Imaging Technologies (SITe) and are butted together along their long dimension to create an effective 4096×4096 array with a gap corresponding to approximately 50 pixels between the chips. The CCD camera design incorporates a warm dewar window, designed to prevent buildup of contaminants on the window that cause a loss of UV throughput.

A summary of the ACS CCD performance is given in Table 3.1.

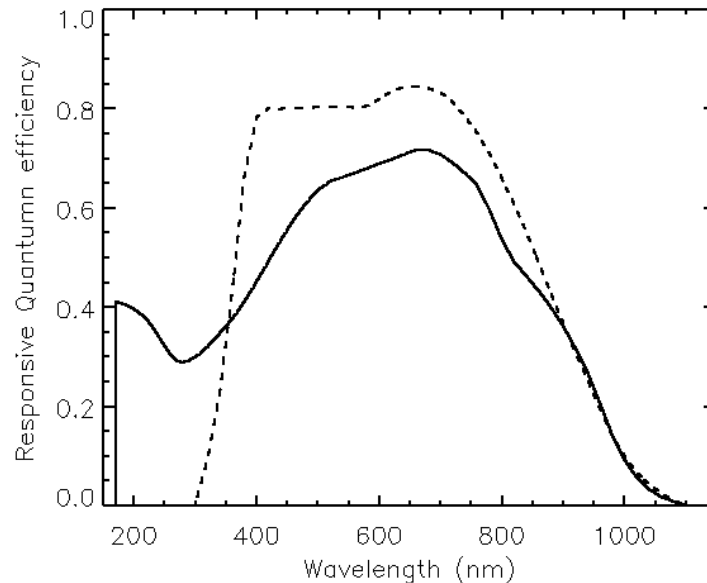
HRC

The HRC CCD is a flight-spare STIS 1024×1024 CCD and is a thinned, backside-illuminated device, manufactured at SITe. The coating uses a process developed by SITe to provide good quantum efficiency in the near-ultraviolet. The performance characteristics and specifications are given in Table 3.1

4.2.2 CCD Spectral Response

The responsive quantum efficiency (RQE) of the WFC and HRC CCDs is shown in Figure 4.1; the RQE includes corrections needed to reproduce the instrument sensitivity measured on orbit ([ACS ISR 2007-06](#)). The total spectral response of the camera (see Figure 5.7) is given by the convolution of the RQEs shown here and the throughput of optical elements of the camera. For example, the WFC silver coated mirrors enhance the reflectivity in the near-IR but impose a violet cutoff below 370nm.

Figure 4.1: Responsive quantum efficiency of the HRC CCD (solid line) and WFC CCDs (dashed line).



4.2.3 Quantum Efficiency Hysteresis

Based on current data, the ACS CCDs do not suffer from quantum efficiency hysteresis (QEH). The CCDs respond in the same way to light levels over their whole dynamic range, irrespective of the previous illumination level.

4.2.4 CCD Long-Wavelength Fringing

Like most thinned CCDs, the ACS CCDs exhibit fringing in the red, longward of $\sim 7500 \text{ \AA}$. The amplitude of the fringes is a strong function of wavelength and spectral resolution. The fringe pattern can be corrected by rectification with an appropriate flat field. The fringe pattern is a convolution of the contours of constant distance between the front and back surfaces of the CCD, and the wavelength of light on a particular part of the CCD. The fringe pattern has been shown to be very stable in similar devices, as long as the wavelength of light on a particular part of the CCD stays constant. In practice, this means that the fringe pattern is dependent on the spectrum of the light incident on the detector, with the sensitivity to the source spectrum a function of the bandwidth of the filter.

4.2.5 Readout Format

WFC

Each CCD chip is read out as a 4144×2068 array, including physical and virtual overscans. Two different amplifiers are used to read out each half of the chip. The final images consist of 24 columns of physical overscan, 4096 columns of pixel data, and another 24 columns of physical overscan. Each column consists of 2048 rows of pixel data followed by 20 rows of virtual overscan. The orientation of the chip is such that for the grism spectra, the dispersed images have wavelength increasing from left to right in the positive x-direction.

HRC

The HRC CCD is read out as a 1062×1044 array, including physical and virtual overscans. There are 19 columns of physical overscan, followed by 1024 columns of pixel data, and then 19 more columns of physical overscan. Each column consists of 1024 rows of pixel data followed by 20 rows of virtual overscan. As with the WFC, the orientation of the chip was chosen so that grism images have wavelength increasing from left to right.

4.2.6 Analog-To-Digital Conversion

Electrons which accumulate in the CCD wells are read out and converted to data numbers (DN) by the analog-to-digital converter (ADC). The ADC output is a 16 bit number, producing a maximum of 65,535 DN in one pixel.

Up to Cycle 15 the CCDs were capable of operating at gains of 1, 2, 4 or 8 electrons/DN. While for the HRC operation no changes are expected for Cycle 17, the possible gain settings for the WFC are still to be defined. In principle, use of a lower gain value can increase the dynamic range of faint source observations by reducing the quantization noise; however, in practice this improvement is not significant. Table 4.1 and Table 4.2 show the actual gain levels and readout noise in electrons for the four WFC amps, and the default C amp used for the HRC for SIDE 1 and SIDE 2 respectively.

Table 4.1: CCD gain and readout noise (e^- rms) under SIDE-1 operation (03/2002->06/2006).

| Chip | Amp | Gain=1 | | Gain=2 (default) | | Gain=4 | |
|------|-----|--------|-------|------------------|-------|--------|-------|
| | | Gain | Noise | Gain | Noise | Gain | Noise |
| WFC1 | A | 1.000 | 5.57 | 2.002 | 5.84 | 4.01 | --- |
| WFC1 | B | 0.972 | 4.70 | 1.945 | 4.98 | 3.90 | --- |
| WFC2 | C | 1.011 | 5.18 | 2.028 | 5.35 | 4.07 | --- |
| WFC2 | D | 1.018 | 4.80 | 1.994 | 5.27 | 4.00 | --- |
| HRC | C | 1.163 | 4.46 | 2.216 | 4.80 | 4.235 | 5.86 |

Table 4.2: CCD gain and readout noise (e^- rms) under SIDE-2 operation (07/2006-01/2008)

| Chip | Amp | Gain=1 | | Gain=2 (default) | | Gain=4 | |
|------|-----|--------|-------|------------------|-------|--------|-------|
| | | Gain | Noise | Gain | Noise | Gain | Noise |
| WFC1 | A | 1.000 | 5.29 | 2.002 | 5.62 | 4.01 | --- |
| WFC1 | B | 0.972 | 4.45 | 1.945 | 4.74 | 3.90 | --- |
| WFC2 | C | 1.011 | 5.03 | 2.028 | 5.34 | 4.07 | --- |
| WFC2 | D | 1.018 | 4.55 | 1.994 | 4.89 | 4.00 | --- |
| HRC | C | 1.163 | 4.36 | 2.216 | 4.82 | 4.235 | 5.44 |

As in previous cycles the number of fully supported gain factors will be likely limited to two per each camera. The remaining gain factors will be available but unsupported so users of those modes will need to plan their

own calibration. The supported gain factors will provide the lowest readnoise and/or the better sampling of the detector full well. Further information about gain values for cycle 17 will be made available in the ACS Web page as soon as is available.

4.2.7 Flat Fields

WFC

The flat fields for the WFC combine information from two sources. Ground-based flats were obtained for all filters at a signal-to-noise of ~ 300 per pixel. To refine the low-frequency domain of the ground flats, in-flight observations of a rich stellar field with large scale dithers have been analyzed (see [ACS ISR 2002-08](#) and [2003-10](#)). The required L-flat correction is a corner-to-corner gradient of 10 to 18%, dependent on wavelength. The resulting flat field supports photometry to $\sim 1\%$ over the full WFC field of view.

Figure 4.2 shows the corrected WFC ground flats for several broadband filters. **Note: the 50 pixel gap seen in external images, between the top and bottom chips, is not shown here.** Since the two CCDs were cut from the same Si wafer, and have undergone similar treatments, there is a significant continuity in the response across the gap. The central donut-like structure is wavelength dependent, where pixels in the central region are less sensitive than surrounding pixels in the blue F435W filter, for example, and more sensitive in the red F850LP filter. For further discussion of WFC flat fields, see ACS ISRs [2001-11](#), [2002-04](#), [2003-10](#), [2003-11](#), [2005-02](#), and [2005-09](#).

HRC

As for the WFC, the HRC ground flats were refined using in-flight observations of a rich stellar field with large scale dithers to determine the low-frequency domain of the flat fields. The correction required for the visible filters is a corner-to-corner gradient of 6% to 12%, dependent on wavelength. For the NUV filters, flats were taken in-flight using observations of the bright earth (see [ACS ISR 2003-02](#)) and include both the pixel-to-pixel and low-frequency structure of the detector response.

Currently, HRC flat fields have a signal-to-noise of ~ 300 per pixel and support photometry to $\sim 1\%$ over the full HRC field of view. Figure 4.3 shows the corrected HRC ground flats, derived for 6 broadband optical filters. The donut-like structure seen in the WFC response is not found in the HRC flats. For further discussion of HRC flat fields, see ACS ISRs [2001-11](#) and [2002-04](#).

Figure 4.2: WFC flat field.

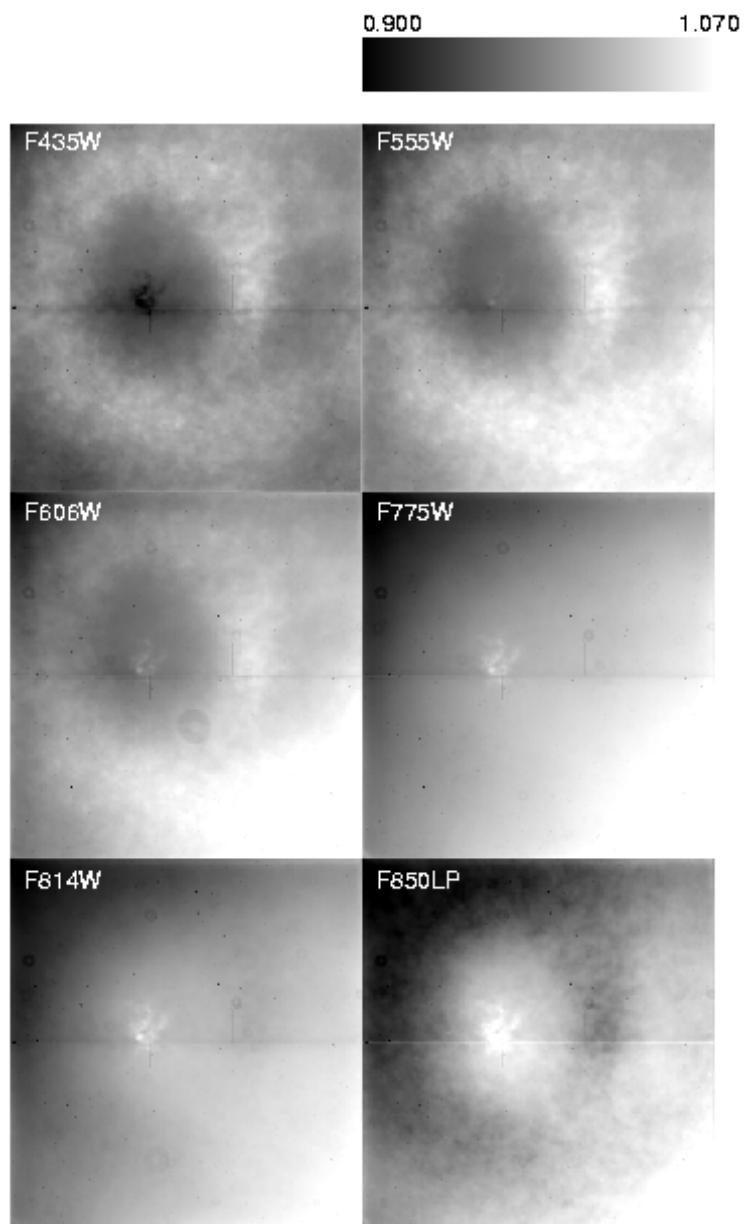
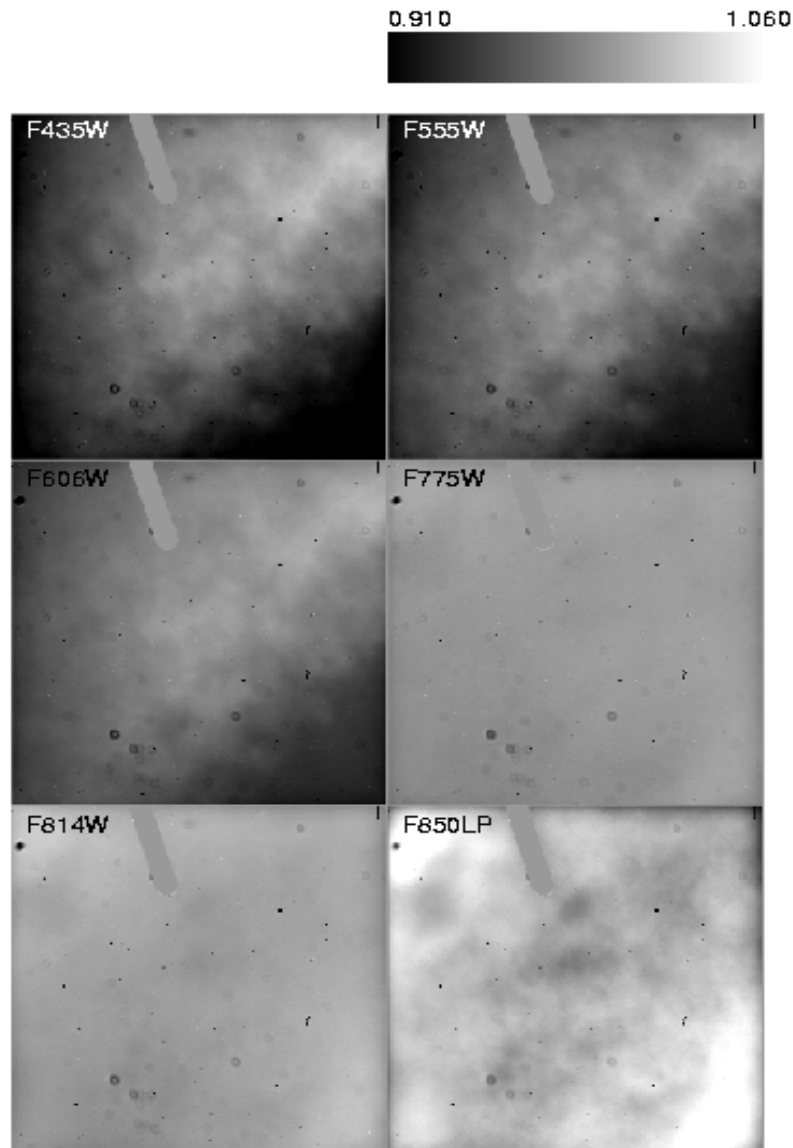


Figure 4.3: HRC flat field.



4.3 CCD Operations and Limitations

4.3.1 CCD Saturation: the CCD Full Well

The full well capacity for the ACS CCDs is given in Table 3.1 as $84,700 e^-$ for the WFC and $155,000 e^-$ for the HRC. This is somewhat dependent on the position on the chip, with variations of the order 10% and 18% across the field of view for the WFC and the HRC, respectively. If the CCD is over-exposed, blooming will occur. This happens when a pixel

becomes full, so excess charge flows into the next pixels along the column. However, extreme overexposure is not believed to cause any long-term damage to the CCDs, so there are no bright object limits for the ACS CCDs. When using GAIN=2 on the WFC and GAIN=4 on the HRC, it has been shown that the detector response remains linear to well under 1% up to the point when the central pixel reaches the full well depth. On-orbit tests have demonstrated that when using aperture photometry and summing over the surrounding pixels affected by bleeding, linearity to $\leq 1\%$ holds even for cases in which the central pixel has received up to 10 times the full well depth (see [ACS ISR 2004-01](#) for details). After the ACS repair, on-orbit tests will be devoted to characterize the linearity of both CCDs.

4.3.2 CCD Shutter Effects on Exposure Times

The ACS camera has a very high-speed shutter; even the shortest exposure times are not significantly affected by the finite traversal time of the shutter blades. On-orbit testing reported in [ACS ISR 2003-03](#) has verified that shutter shading corrections are not necessary to support 1% photometry for either the HRC or WFC.

A total of 4 exposure times are known to be in error by up to 4.1%; the nominal 0.1 seconds HRC exposure is really 0.1041 seconds (updates for reference files have been made to use the correct values in pipeline processing). No significant differences exist between exposure times controlled by the two shutters (A and B), with the possible exception of non-repeatability up to $\sim 1\%$ on the WFC for exposures in the 0.7 to 2.0 second range. The HRC provides excellent shutter time repeatability.

4.3.3 Readnoise

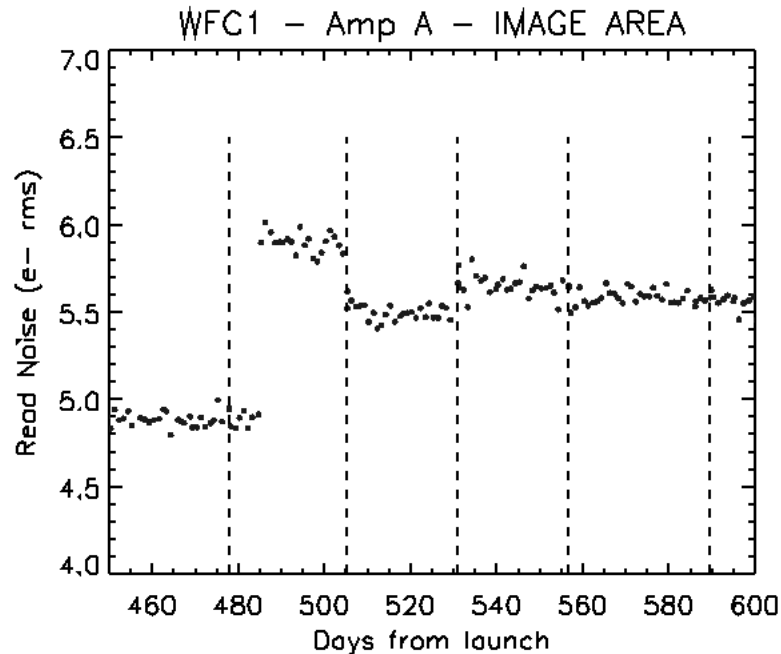
WFC

We measured the readnoise level in the active area and overscan regions for all the amplifiers at the default gain settings. In general the readnoise has been constant with time. On June 29, 2003, just after a transit through the South Atlantic Anomaly (SAA) the readnoise in Amp A changed from ~ 4.9 to ~ 5.9 electrons rms. Although the telemetry did not show any anomaly in any component of the camera, it is likely that the readnoise jump was due to some sort of radiation damage. Amp A is the only amplifier that showed this anomaly. The amplitude of the variation ($\sim 1 e^-$) was the same for GAIN 1 and 2. After the following anneal date the readnoise dropped to $\sim 5.5 e^-$ and it remained constant for 27 days. After the following two anneal cycles the readnoise reached stability at $\sim 5.6 e^-$ rms, approximately $0.7 e^-$ higher than before the change, and has remained constant since then. Figure 4.4 shows the readnoise in the image area for amplifier A during the “instability” period. The readnoise of all the other

amplifiers have been very stable since launch with post-launch figures almost unchanged from the pre-launch measurements made during ground testing.

Even with a slightly higher readnoise in Amp A most of the WFC broadband science observations are sky limited, while narrowband observations are primarily readnoise limited. Table 4.1 and Table 4.2 list the CCD gain measured under side-1 and side-2 operations. The ACS repair is expected to produce read noise levels comparable or better than listed for Side-1.

Figure 4.4: Readnoise jump in WFC Amp A (occurred on June 29, 2003).



The vertical dashed lines indicate the annealing dates. See Table 4.1 for CCD gain and readout noise values.

HRC

The readnoise is monitored only for the default readout amplifier C at the default gain setting ($2 e^-/DN$). No variations have been observed with time. The readnoise measured in the image area (Tables 4.1 and 4.2) is in agreement with the readnoise measured in the two overscan regions, and it is comparable to the pre-flight value of $4.74 e^-$.

4.3.4 Dark Current

All ACS CCDs are buried channel devices which have a shallow n-type layer implanted below the surface to store and transfer the collected signal charge away from the traps associated with the Si-SiO₂ interface.

Moreover, ACS CCDs are operated in Multi Pinned Phases (MPP) mode so that the silicon surface is inverted and the surface dark current is suppressed. ACS CCDs therefore have very low dark current. The WFC CCDs are operated in MPP mode only during integration, so the total dark current figure for WFC includes a small component of surface dark current accumulated during the readout time.

Like all CCDs operated in a low earth orbit radiation environment, the ACS CCDs are subject to radiation damage by energetic particles trapped in the radiation belts. Ionization damage and displacement damage are two types of damage caused by protons in silicon. The MPP mode is very effective in mitigating the damage due to ionization such as the generation of surface dark current due to the creation of trapping states in the Si-SiO₂ interface. Although only a minor fraction of the total energy is lost by a proton via nonionizing energy loss, the displacement damage can cause significant performance degradation in CCDs by decreasing the charge transfer efficiency (CTE), increasing the average dark current, and introducing pixels with very high dark current (hot pixels). Displacement damage to the silicon lattice occurs mostly due to the interaction between low energy protons and silicon atoms. The generation of phosphorous-vacancy centers introduces an extra level of energy between the conduction band and the valence band of the silicon. New energetic levels in the silicon bandgap have the direct effect of increasing the dark current as a result of carrier generation in the bulk depletion region of the pixel. As a consequence, the dark current of CCDs operated in a radiative environment is predicted to increase with time.

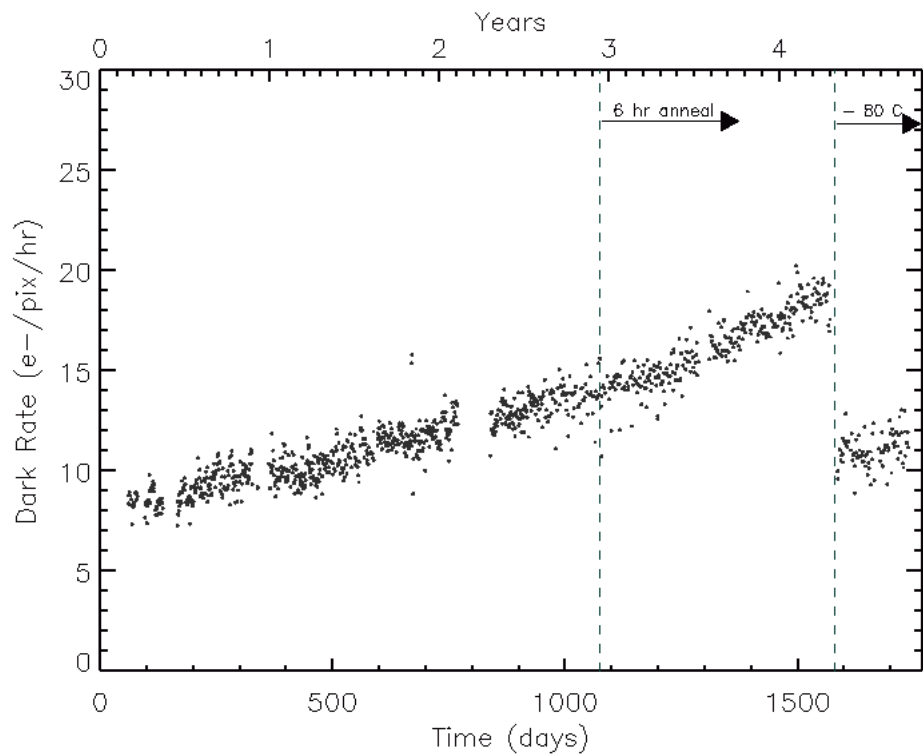
Ground testing of the WFC CCDs, radiated with a cumulative fluence equivalent to 2.5 and 5 years of on-orbit exposure, predicted a linear growth of $\sim 1.5 \text{ e}^-/\text{pixel}/\text{hour}/\text{year}$.

The dark current in ACS CCDs is monitored four days per week with the acquisition of four 1000 seconds dark frames (totaling 16 images per week). Dark frames are used to create reference files for the calibration of scientific images, and to track and catalog hot pixels as they evolve. The four daily frames are combined together to remove cosmic rays and to extract hot pixel information for any specific day. The dark reference files are generated by combining two weeks of daily darks in order to reduce the statistical noise. The hot pixel information for a specific day is then added to the combined bi-weekly dark. In order to study the evolution of the dark current with time, the modal dark current value in the cosmic-ray free daily darks is calculated. As expected, the dark current increases with time (Figure 4.5). The observed linear growth rates of dark current are 2.1 and 1.6 $\text{e}^-/\text{pixel}/\text{hour}/\text{year}$ for WFC1 and WFC2 respectively, and 2.1 $\text{e}^-/\text{pixel}/\text{hour}/\text{year}$ for the HRC CCD. These rates are in general agreement with the ground test predictions.

Simultaneously to the beginning of the side-2 operation in July 2006 the temperature set point of the WFC has been lowered from -77 C to -80 C (see ACS TIR 2006-02).

Dark current and hot pixels depended strongly on the operating temperature. The reduction of the operating temperature of the WFC CCDs reduced them by almost 50%. The dark rate shows a clear drop on July 4, 2006, when the temperature was changed, and Figures 4.7 and 4.8 illustrate the before-and-after effect directly. The new operating temperature brought the dark current of the WFC CCDs back to the level eighteen months after the launch.

Figure 4.5: Dark rate trend with time for the WFC CCDs.



Dark current as a function of time for one of the WFC CCDs. The first dashed line indicates the change in the anneal procedure from twelve to six hours for the duration of the warm-up period. The shorter anneal slightly increased the rate of growth of the dark current. The second dashed line indicates the change in temperature set point for the CCDs. As expected the dark current dropped drastically at the new temperature.

Figure 4.6: Dark current as a function of time for the HRC

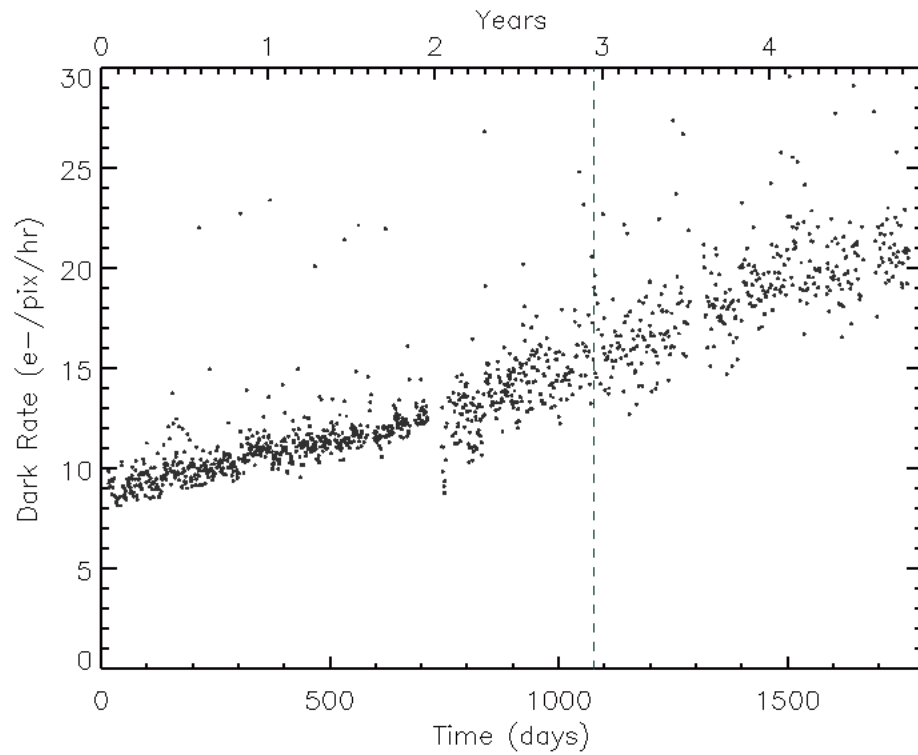


Figure 4.7: Histogram of WFC dark frames taken before and after the change in temperature.

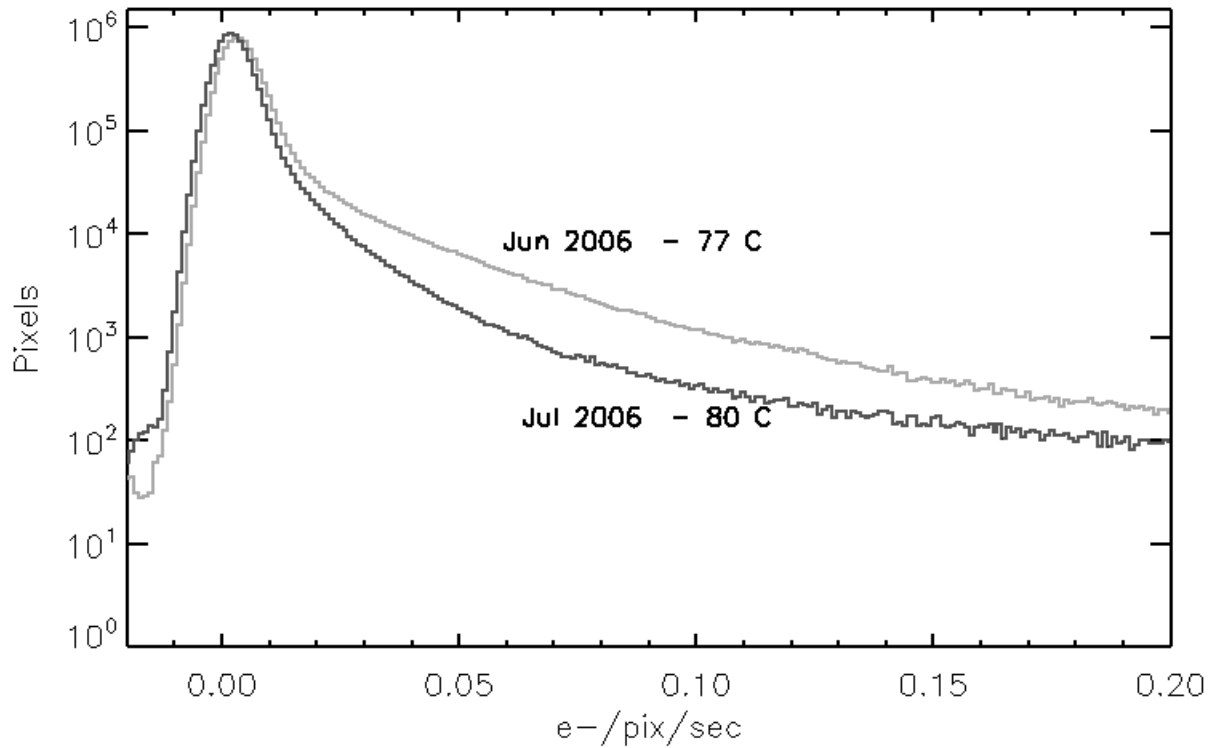
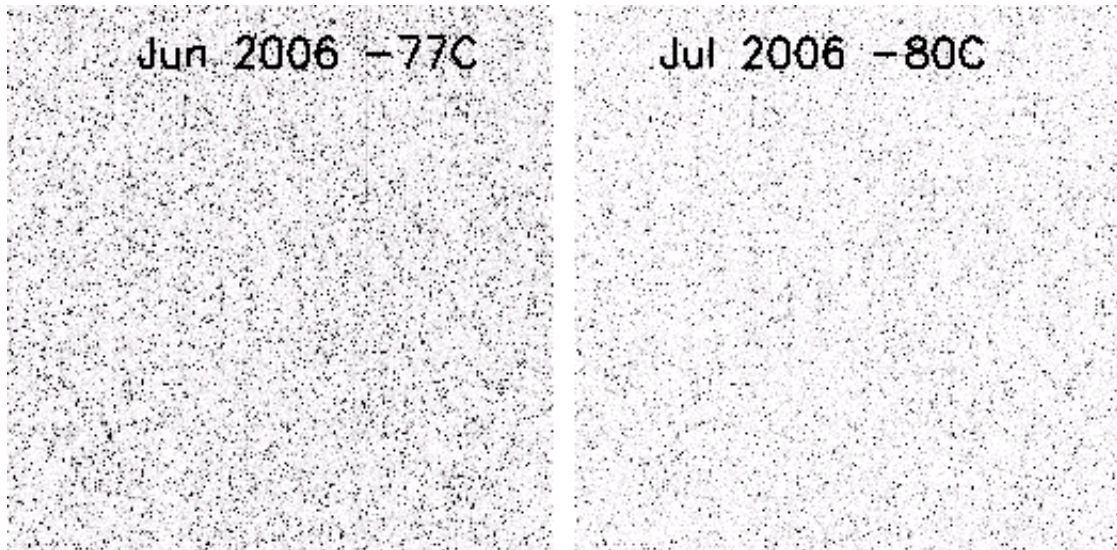


Figure 4.8: Sub-section of WFC dark frames showing hot pixel contamination before and after the change in temperature on July 4, 2006



4.3.5 Warm and hot pixels

In the presence of a high electric field, the dark current of a single pixel can be greatly enhanced. Such pixels are called dark spikes or hot pixels. Although the increase in the mean dark current with proton irradiation is important, of greater consequence is the large increase in dark current nonuniformity.

We have chosen to classify the field-enhanced dark spikes into two categories: warm and hot pixels. The definition of “warm” and “hot” pixel is somewhat arbitrary. We have chosen a limit of $0.08 \text{ e}^-/\text{pixel}/\text{seconds}$ as a threshold above which we consider a pixel to be “hot”. We identify “warm” pixels as those which exceed by about 5σ ($\sim 0.02 \text{ e}^-/\text{pixel}/\text{second}$) the normal distribution of the pixels in a dark frame up to the threshold of the hot pixels (See Figure 4.11) for a typical dark rate pixel distribution)

Warm and hot pixels accumulate as a function of time on orbit. Defects responsible for elevated dark rate are created continuously as a result of the ongoing displacement damage on orbit. The number of new pixels with a dark current higher than the mean dark date increases every day by few to several hundreds depending on the threshold. The reduction of the operating temperature of the WFC CCDs has dramatically reduced the dark current of the hot pixels and therefore many pixels previously classified as hot are now warm or normal pixels.

Table 4.3: Creation rate of new hot pixels (pixel/day).

| Threshold ($e^-/\text{pixel}/\text{second}$) | WFC(-77 C) | WFC (-80 C) | HRC(-81 C) |
|---|--------------|--------------|--------------|
| 0.02 | 815 ± 56 | N.A. | 125 ± 12 |
| 0.04 | 616 ± 22 | 427 ± 34 | 96 ± 2 |
| 0.06 | 480 ± 13 | 292 ± 8 | 66 ± 1 |
| 0.08 | 390 ± 9 | 188 ± 5 | 48 ± 1 |
| 0.10 | 328 ± 8 | 143 ± 12 | 35 ± 1 |
| 1.00 | 16 ± 1 | 10 ± 1 | 1 ± 0.5 |

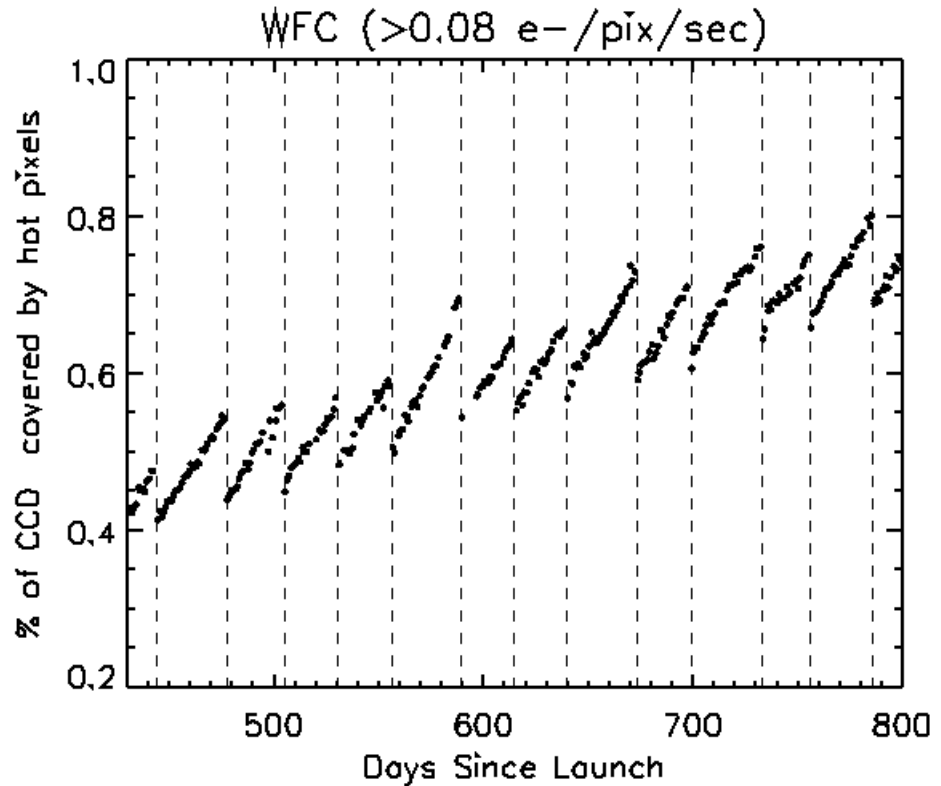
Table 4.4: Annual permanent hot pixel contamination (%).

| Threshold ($e^-/\text{pixel}/\text{second}$) | WFC(-77 C) | WFC (-80 C) | HRC(-81 C) |
|---|------------|-------------|------------|
| >0.02 | 1.60 | N.A. | 1.54 |
| >0.04 | 0.78 | 0.32 | 0.52 |
| >0.06 | 0.46 | 0.18 | 0.29 |
| >0.08 | 0.30 | 0.16 | 0.21 |
| >0.10 | 0.23 | 0.13 | 0.17 |
| >1.0 | 0.03 | 0.02 | 0.02 |

Most of these new hot pixels are transient. Like others CCDs on HST, the ACS devices undergo a monthly annealing process. The CCDs and the thermal electric coolers (TECs) are turned off and the heaters are turned on to warm the chips to $\sim 19^\circ\text{C}$. Although the annealing mechanism at such low temperatures is not yet understood, after this “thermal cycle” the population of hot pixels is greatly reduced (see Figure 4.9). The anneal rate depends on the dark current rate with very hot pixels being annealed easier than warmer pixels. For pixels classified as “hot” (those with dark rate $> 0.08 e^-/\text{pix}/\text{sec}$) the anneal rate is $\sim 82\%$ for WFC and $\sim 86\%$ for HRC.

Annealing has no effect on the normal pixels that are responsible for the increase in the mean dark current rate. Such behavior is similar to what is seen with STIS SITe CCD and WFC3 CCDs during ground radiation testing.

Figure 4.9: Hot pixel growth in the WFC CCDs.



The vertical dashed lines indicate the annealing dates.

During early annealing episodes the ACS CCDs were warmed up for 24 hours. But the annealing time was reduced to 6 hours in spring of 2004 to allow better scheduling of HST time. Even with a shorter cycle the effectiveness of the anneal in ACS CCDs has remained the same. It is interesting to note that since ACS launch, four HST safing events have occurred; after each event the population of hot pixels was reduced as if a normal anneal cycle has occurred. During the safing events the CCDs and the TECs were turned off. Since the heaters were not turned on, the CCDs warmed-up to only about $-10 \text{ }^\circ\text{C}$. After a period of time ranging from 24 to 48 hours, HST resumed normal operation. The dark frames taken after the safing events showed a reduction in hot pixel population similar to those observed during normal annealing cycles.

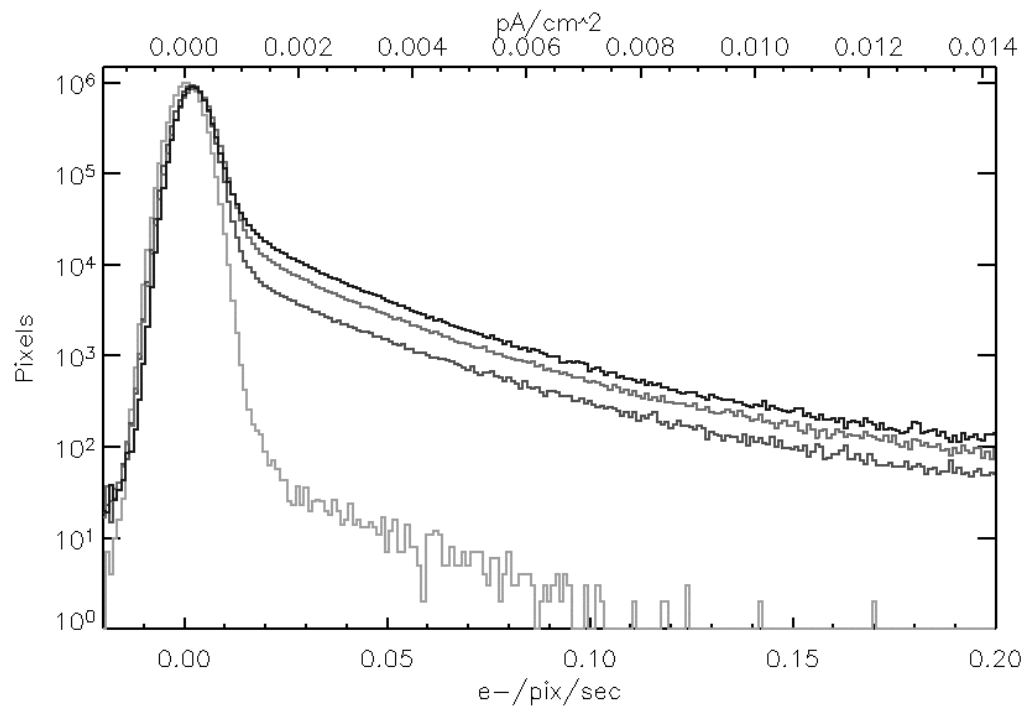
Since the anneals cycle do not repair 100% of the hot pixels, there is a growing population of permanent hot pixels (see Figure 4.10 and Figure 4.11).

Figure 4.10: A subsection of WFC1 dark frames taken at different epochs showing the increasing population of hot pixels.



From left to right: before launch, and after 1, 2 and 3 years on orbit.

Figure 4.11: Histogram of WFC dark frames taken at different epochs.



Epochs pre-launch, and after 1, 2, and 3 years on orbit. Both the mean dark rate increase and the growing population of permanent hot pixels are visible.

According to the current trend, about 0.3% of WFC (0.22% of HRC) pixels became permanently hot every year (see Table 4.5). In a typical 1000 second exposure the percentage of pixels contaminated by cosmic rays ranges between 1.5% and 3% of the total. By spring of 2007 the contamination from hot pixels will impact about 2% of the pixels (See Figure 4.12.).

Table 4.5: Permanent warm and hot pixel growth (%/yr).

| Threshold ($e^-/\text{pix}/\text{sec}$) | WFC | HRC |
|--|------|------|
| 0.02 | 174 | 1.52 |
| 0.04 | 0.86 | 0.50 |
| 0.06 | 0.50 | 0.31 |
| 0.08 | 0.30 | 0.22 |
| 0.10 | 0.25 | 0.18 |
| 1.00 | 0.04 | 0.03 |

In principle, warm and hot pixels could be eliminated by the superdark subtraction. However, some pixels show a dark current that is not stable with time but switches between well defined levels. These fluctuations may have timescales of a few minutes and have the characteristics of random telegraph signal (RTS) noise. The dark current in field-enhanced hot pixels can be dependent on the signal level, so the noise is much higher than the normal shot noise. As a consequence, since the locations of warm and hot pixels are known from dark frames, they are flagged in the data quality. The hot pixels can be discarded during image combination if multiple exposures have been dithered.

While the standard CR-SPLIT approach allows for cosmic ray subtraction, without additional dithering, it will not eliminate hot pixels in post-observation processing.



We recommend that observers who would have otherwise used a simple CR-SPLIT now use some form of dithering instead. Any form of dithering providing a displacement of at least a few pixels can be used to simultaneously remove the effects of cosmic ray hits and hot pixels in post-observation processing.

For example, a simple ACS-WFC-DITHER-LINE pattern has been developed, based on integer pixel offsets, which shifts the image by 2 pixels in X and 2 pixels in Y along the direction that minimizes the effects of scale variation across the detector. The specific parameter values for this pattern are given on the ACS dithering Web page at:

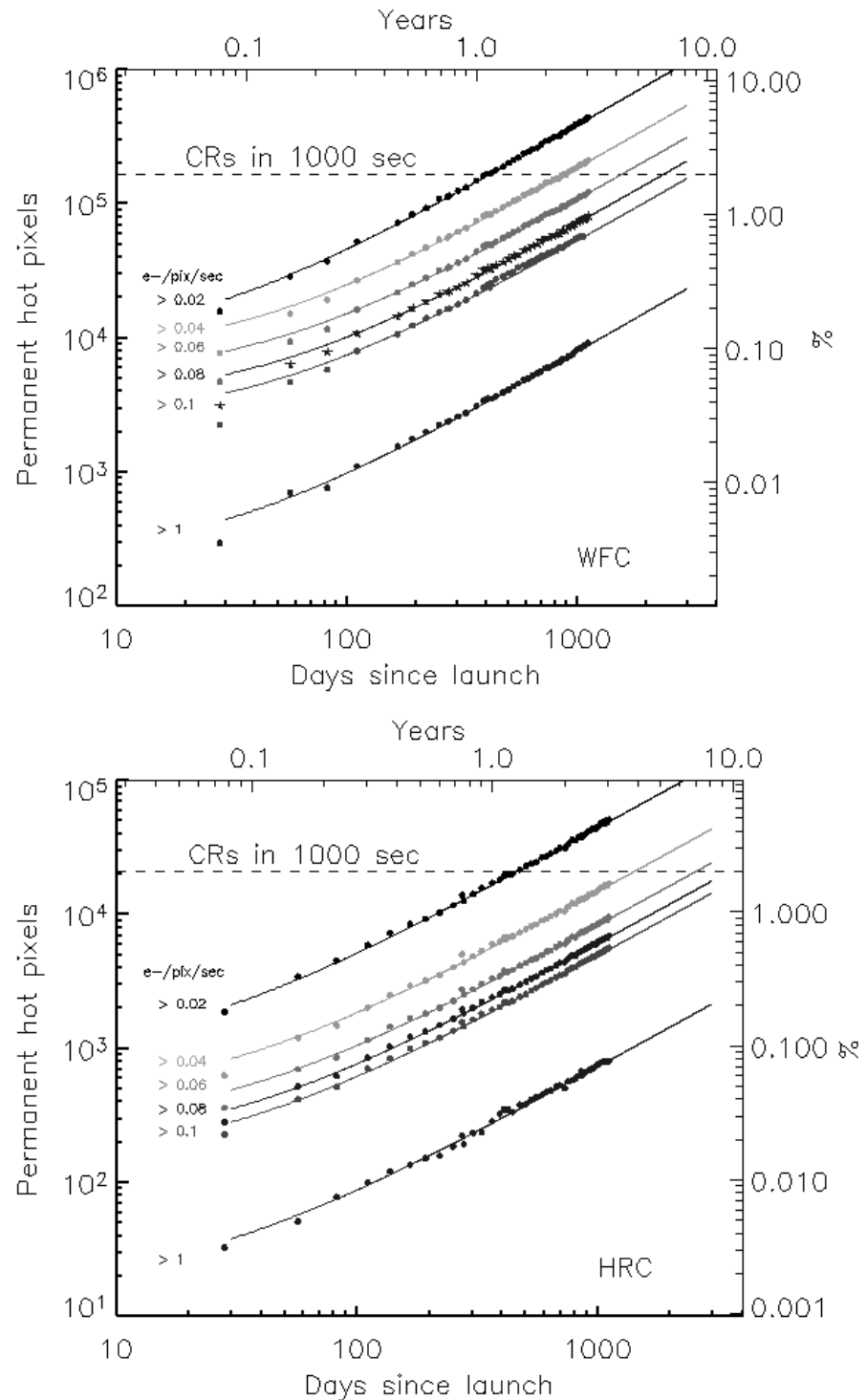
<http://www.stsci.edu/hst/acs/proposing/dither>.

Additional information can be found in the *Phase II Proposal Instructions*.

Given the transient nature of hot pixels, users are reminded that a few hot pixels may not be properly flagged in the data quality array (because

they spontaneously “healed” or because their status changed in the period spanning the reference file and science frame acquisition), and therefore could create false positive detections in some science programs.

Figure 4.12: Growth of permanent warm and hot pixel population as a function of time (WFC top, HRC bottom).



The contamination level due to cosmic rays accumulated in a 1000 second exposure is shown with a dashed line.

4.3.6 Cosmic Rays

Initial studies have been made of the characteristics of cosmic ray impacts on the HRC and WFC. The fraction of pixels affected by cosmic rays varies from 1.5% to 3% during a 1000 second exposure for both cameras, similar to what was seen on WFPC2 and STIS. This number provides the basis for assessing the risk that the target(s) in any set of exposures will be compromised. The affected fraction is the same for the WFC and HRC despite their factor of two difference in pixel areas because the census of affected pixels is dominated by charge diffusion, not direct impacts. Observers seeking rare or serendipitous objects, as well as transients, may require that every single WFC pixel in at least one exposure among a set of exposures is free from cosmic ray impacts. For the cosmic ray fractions of 1.5% to 3% in 1000 seconds, a single ~ 2400 second orbit must be broken into 4 exposures of 500 to 600 seconds each to reduce the number of uncleanable pixels to 1 or less. Users seeking higher S/N (lower readnoise) may prefer the trade-off of doing 3 exposures of ~ 800 seconds, where CR-rejection should still be very good for most purposes. But we do NOT recommend 2 long exposures (i.e. 1200 seconds), where residual CR contamination would be unacceptably high in most cases. We recommend that users dither these exposures to remove hot pixels as well as cosmic rays (see Section 7.4).

The flux deposited on the CCD from an individual cosmic ray does not depend on the energy of the cosmic ray but rather the length it travels in the silicon substrate. The electron deposition due to individual cosmic rays has a well defined cut-off with negligible events of less than $500 e^-$ and a median of $\sim 1000 e^-$ (see Figure 4.13 and Figure 4.14).

Figure 4.13: Electron deposition by cosmic rays on WFC.

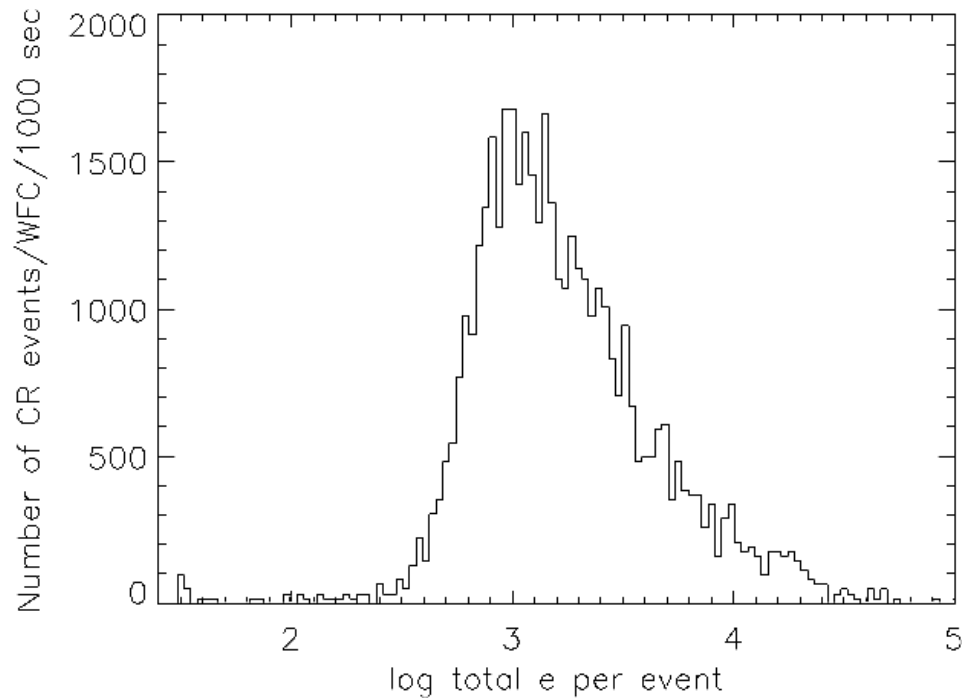
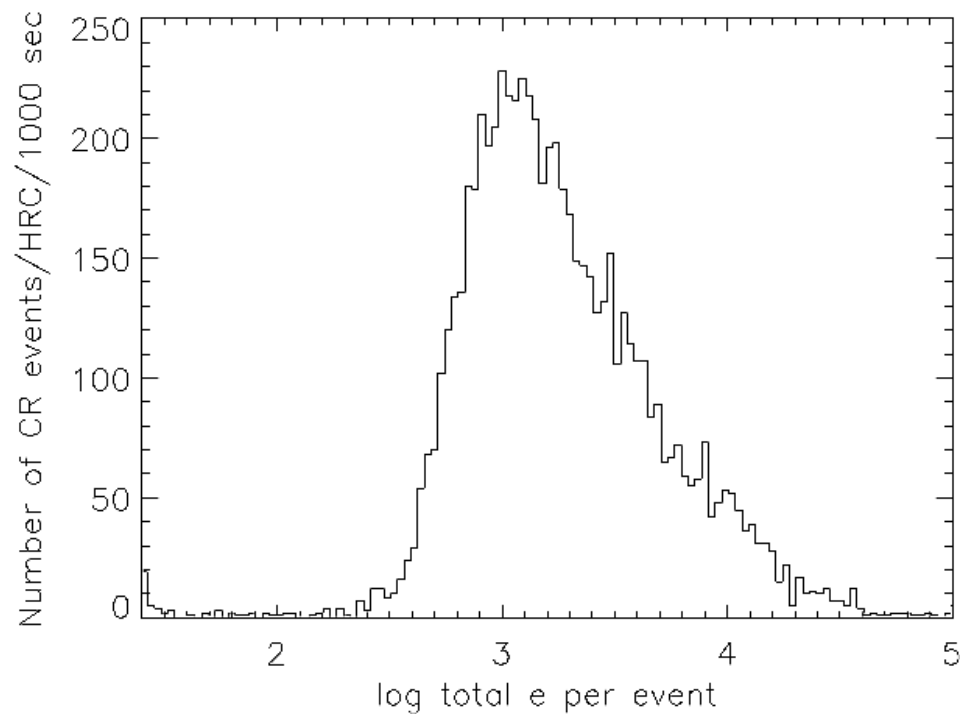


Figure 4.14: Electron deposition of cosmic rays on HRC.



The distribution of the number of pixels affected by a single cosmic ray is strongly peaked at 4 to 5 pixels. Although a few events are seen which encompass only one pixel, examination of these events indicate that at least

some, and maybe all of these sources are actually transient hot pixels or unstable pixels which can appear hot in one exposure (with no charge diffusion) and normal in the next. Such pixels are very rare but do exist. There is a long tail in the direction towards increasing numbers of attached pixels.

Distributions of sizes and anisotropies can be useful for distinguishing cosmic rays from astrophysical sources in a single image. The size distribution for both chips peaks near 0.4 pixels as a standard deviation (or 0.9 pixels as a FWHM). This is much narrower than for a PSF and is thus a useful discriminant between unresolved sources and cosmic rays.

4.3.7 Charge Transfer Efficiency

Charge transfer efficiency (CTE) is a measure of how effective the CCD is at moving charge from one pixel location to the next when reading out the chip. A perfect CCD would be able to transfer 100% of the charge as the charge is shunted across the chip and out through the serial register. In practice, small traps in the silicon lattice compromise this process by holding on to electrons, releasing them at a later time. (Depending on the trap type, the release time ranges from a few microseconds to several seconds). For large charge packets (several thousands of electrons), losing a few electrons along the way is not a serious problem, but for smaller ($\sim 100 e^-$ or less) signals, it can have a substantial effect.

CTE is typically measured as a pixel transfer efficiency, and would be unity for a perfect CCD. The CTE numbers for the ACS CCDs at the time of installation are given in Table 4.6. While the numbers look impressive, remember that reading out the WFC CCD requires 2048 parallel and 2048 serial transfers, so that almost 2% of the charge from a pixel in the corner opposite the readout amplifier is lost.

Table 4.6: Charge transfer efficiency measurements for the ACS CCDs at installation time (Fe55 test at 1620 e^-).

| Chip | Parallel | Serial |
|------|----------|----------|
| WFC1 | 0.999995 | 0.999999 |
| WFC2 | 0.999995 | 0.999999 |
| HRC | 0.999983 | 0.999994 |

Also, the CTE numbers are significantly different for images where the pixels have a low intensity compared to those where the intensity is high.

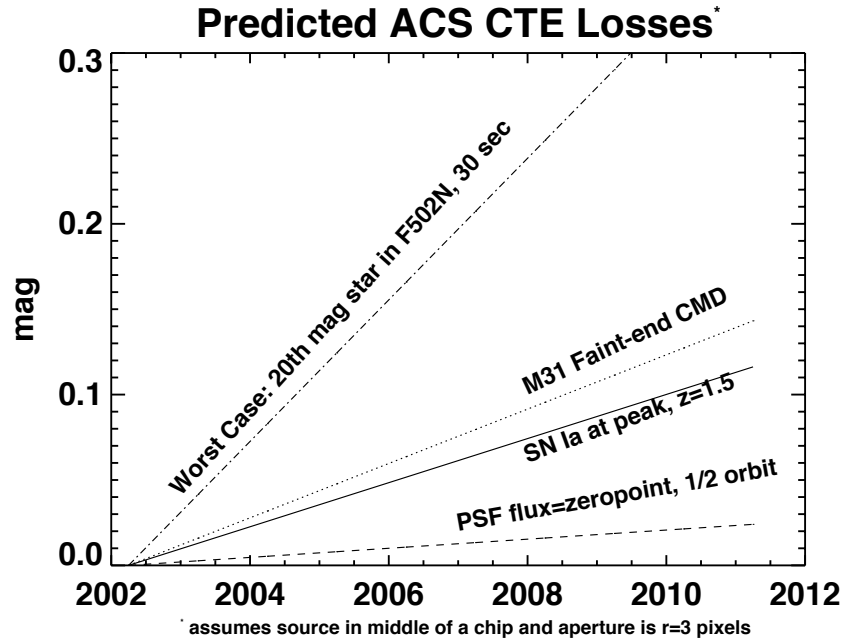
Both the WFPC2 and STIS CCDs have been found to suffer from a significant degradation in CTE since their installation in 1993 and 1997, respectively. At the end of Cycle 11 we performed the first on-orbit calibration of the photometric losses due to imperfect CTE on ACS HRC

and WFC and monitored CTE effects on photometry during the following cycles (11-14). We used images of 47 Tucanae to measure the dependence of stellar photometry on the number of parallel and serial transfers. The results are described by Riess et al. ([ACS ISR 2003-09](#)) and are summarized here. For WFC, significant photometric losses are apparent for stars undergoing numerous parallel transfers (y-direction). Extrapolated to 2008, the losses should be 3% for typical observing parameters, rising to ~15% in worst cases (faint stars, low background). The size of the photometric loss appears to have a strong power-law dependence on the stellar flux, as seen for other CCDs flown on HST.

The dependence on background is significant but for faint targets there is little advantage to increasing the background intentionally (e.g., by post-flashing) due to the added shot noise. However, in some specific cases, it may instead be useful to choose the filter in order to obtain a higher background (e.g. F606W). CTE degradation has also an impact on astrometry (see [ACS ISR 2007-04](#)). Therefore, for astrometric programs of relatively bright objects, the use of post-flash may be considered. No losses are apparent for WFC due to serial transfers (x-direction). For HRC, significant photometric losses also arise from parallel transfer (extrapolating to 2008, ~3% for typical observations, ~20% for worst case) but are not seen for serial transfer. Correction formulae are presented in [ACS ISR 2004-06](#) to correct photometric losses as a function of a source's position, flux, background, time, and aperture size. Updated formulae are in course of development and will substitute the previous ones. Users are encouraged to check the ACS Web page for updates.

Figure 4.15 shows the predicted photometric losses for the WFC due to imperfect parallel CTE as a function of time. These curves are based on the formulae published in [ACS ISR 2004-06](#) and require extreme extrapolation, therefore they should be used for planning purposes only. Four specific science applications are shown as examples: the measurement of the faint end of M31's CMD (GO 9453), the measurement of high-redshift supernovae (GO 9528), the measurement of any PSF whose brightness is the zeropoint (i.e., $1 e^-/\text{second}$), and photometry of a 20th magnitude star in a narrow band.

Figure 4.15: Projected CTE losses in WFC (and equivalently, the size of corrections).



Projected CTE losses in WFC for sample science applications described in Table 4.7. The precision of measurements is not limited by the size of the loss but rather its uncertainty. As a rule of thumb we suggest that the ultimate limit of precision will be ~25% of the loss after correction.

Table 4.7: Example of science applications and their assumed parameters.

| Science application | Source flux (e ⁻) | Sky (e ⁻) |
|--|-------------------------------|-----------------------|
| SN Ia at peak z = 1.5 | 100 | 30 |
| M31 faint-end of CMD | 40 | 100 |
| PSF e ⁻ /sec, 1/2 orbit | 1000 | 40 |
| F502N, 30 sec, 20 th mag star | 258 | 0.1 |

When observing a single target significantly smaller than a single detector, it is possible to place it near an amplifier to reduce the impact of imperfect CTE. This is easy to accomplish by judicious choice of aperture and target position, or by utilizing POS TARG commands. However, be aware that large POS TARGs are not advisable because they change the fractional pixel shifts of dither patterns due to the geometric distortion of ACS. An alternative means to achieve the placement of a target near the amplifier is by using some of the subarray apertures. For example, WFC1-512 (target will have 256 transfers in X and Y), WFC1-1K, and WFC1-2K place the target near the B amplifier (or WFC2-2K for the C amplifier).

4.3.8 UV Light and the HRC CCD

In the optical, each photon generates a single electron. However, in the near-UV, shortward of $\sim 3200 \text{ \AA}$ there is a finite probability of creating more than one electron per UV photon (see Christensen, O., *J. App. Phys.* **47**,689, 1976). At room temperature the theoretical quantum yield (i.e., the number of electrons generated for a photon of energy $E > 3.5\text{eV}$ ($\lambda \sim 3500 \text{ \AA}$)), is $N_e = E(\text{eV})/3.65$. The HRC CCDs quantum efficiency curve has not been corrected for this effect. The interested reader may wish to see the *STIS Instrument Handbook* for details on the signal-to-noise treatment for the STIS CCDs.

4.4 The SBC MAMA

4.4.1 MAMA Properties

The ACS MAMA detector is the STIS flight spare STF7. It provides coverage from 1150 \AA to 1700 \AA . The MAMA detector is a photon-counting device which processes events serially. The ACS MAMA only operates in the accumulate (ACCUM) mode, in which a time-integrated image is produced. Unlike the STIS MAMAs, the ACS does not offer the high-resolution (2048×2048) mode or time-tagged data acquisition. The primary benefits afforded by the STIS and ACS MAMAs, in comparison with previous HST UV spectroscopic detectors such as those in the GHRS and FOS, are high spatial resolution, two-dimensional imaging over a relatively large field of view, and low background for point sources.

Figure 4.16: Design of the SBC MAMA.

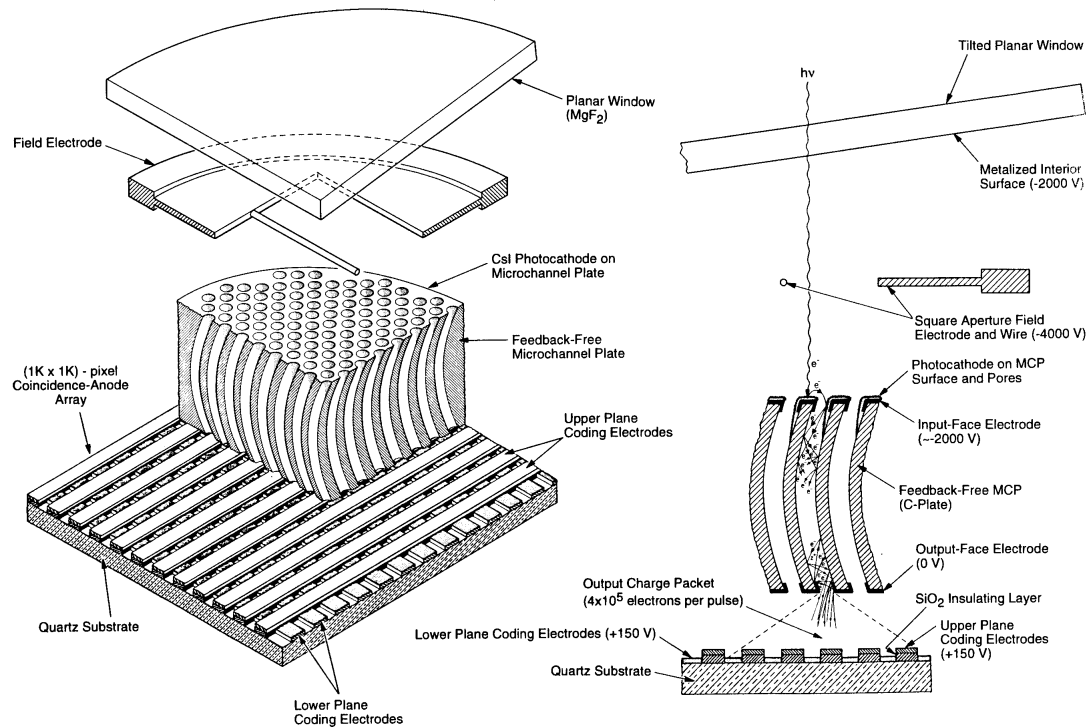


Figure 4.16 illustrates the design of the MAMA, which has an opaque CsI photocathode deposited directly on the face of the curved microchannel plate (MCP). Target photons strike the photocathode, liberating single photoelectrons which pass into the MCP. There they are multiplied to a pulse of $\sim 4 \times 10^5 e^-$. The pulse is recorded by an anode array behind the photocathode, and detected by the MAMA electronics which rejects false pulses and determines the origin of the photon event on the detector.

The field electrode, or *repeller wire*, repels electrons emitted away from the microchannel plate back into the channels. This provides an increase in quantum efficiency of the detector at the price of an increase in the detector point spread function halo. The repeller wire voltage is always on for SBC observations.

Table 4.8: SBC detector performance characteristics.

| Characteristic | SBC MAMA performance |
|--|--|
| Photocathode | CsI |
| Wavelength range | ~1150 to 1700 Å |
| Pixel format | 1024 × 1024 pixel |
| Pixel size | 25 × 25 μm |
| Plate scale | ~0.034 × 0.030 "/pixel |
| Field of view | 34.6" × 30.8" |
| Quantum efficiency | 19.2% @ 1216 Å |
| Dark count ¹ | ~5 × 10 ⁻⁵ e ⁻ /second/pixel |
| Global count-rate linearity limit ² | 360,000 counts/second |
| Local count-rate linearity limit | ~350 counts/second/pixel |
| Visible light DQE | < 1.2 × 10 ⁻⁹ above 400 nm |

1. The dark count increases with the length of time the SBC is turned on, beginning at about 10⁻⁵ electrons/pixel/second and increasing by about a factor of five over two hours.
2. Rate at which counting shows 10% deviation from linearity. These count rates are well above the bright-object screening limits.

4.4.2 SBC Spectral Response

The total transmission curve for the SBC with the PR110L prism is shown in Figure 4.17. The peak photocathode response occurs at Lyman- α . Its spectral response is defined by the cutoff of the MgF₂ window at 1150 Å at short wavelengths, and by the relatively steep decline of the CsI photocathode at long wavelengths.

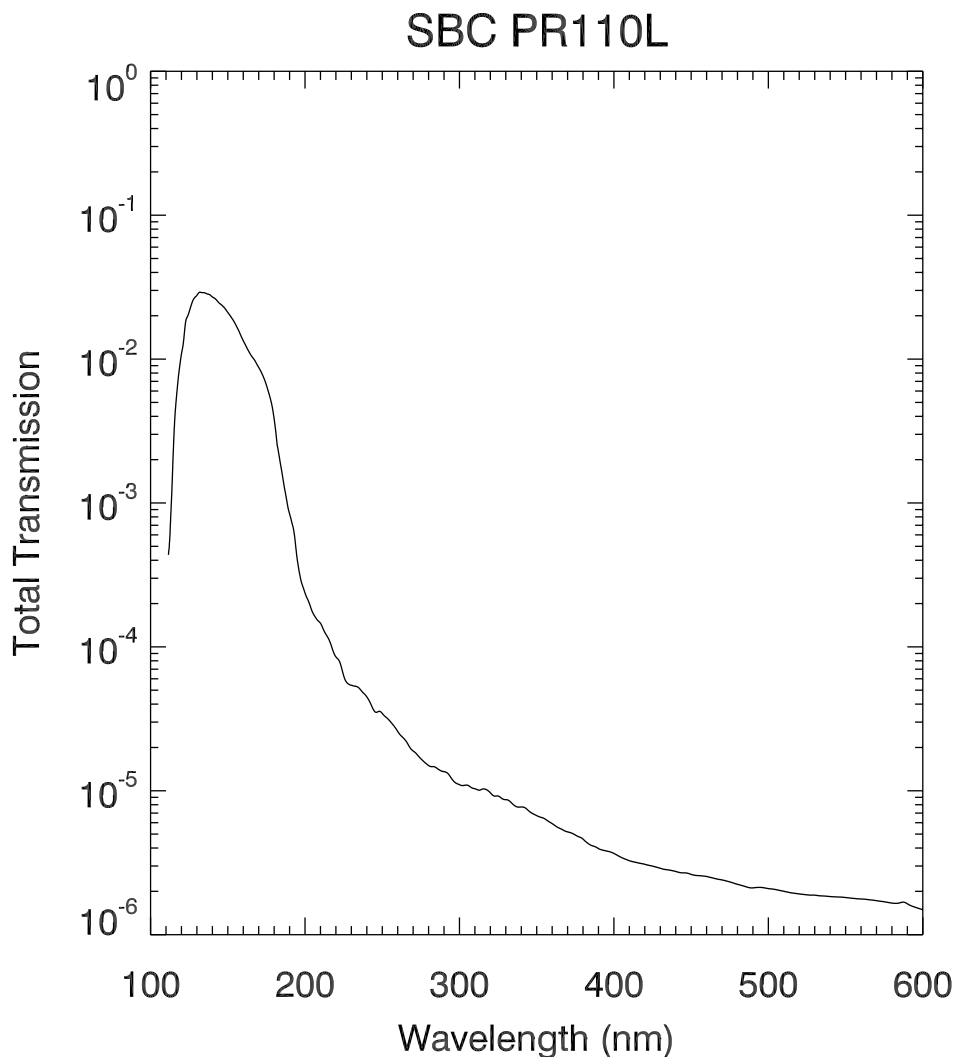
Recent observations of flux calibration stars and a G-type star using the SBC PR110L prism have revealed that the sensitivity of the MAMA detector to optical and near-UV light is apparently much larger than previously thought.

Preliminary estimates of the real SBC throughput indicates that the detector efficiency is factors of approximately 50 and 1000 higher at wavelengths of 3000 and 4000 Å respectively compared to ground testing. For a solar type spectrum, this can mean that one-half or more of the counts detected are due to optical and near-UV photons, rather than from the expected FUV photons. There is also some evidence that this red leak changes as the SBC detector warms up, increasing by as much as 30% over the course of 5 orbits. It is not yet clear if this red leak has also been

increasing secularly over time. STIS FUV MAMA data seem to show a similar, although perhaps somewhat smaller effect.

For dispersed PR110L and PR130L observations, it is straightforward to identify this extra red light; however, it clearly also affects SBC imaging observations done with the long pass filters. Until this effect is better understood and calibrated, extreme caution should be used when interpreting FUV imaging observations of red targets. Observers who need to measure FUV fluxes of red targets may wish to consider interleaving observations with two different SBC long pass filters (e.g., F140LP and F165LP), so that the difference in the count rates can be used to isolate the true FUV flux.

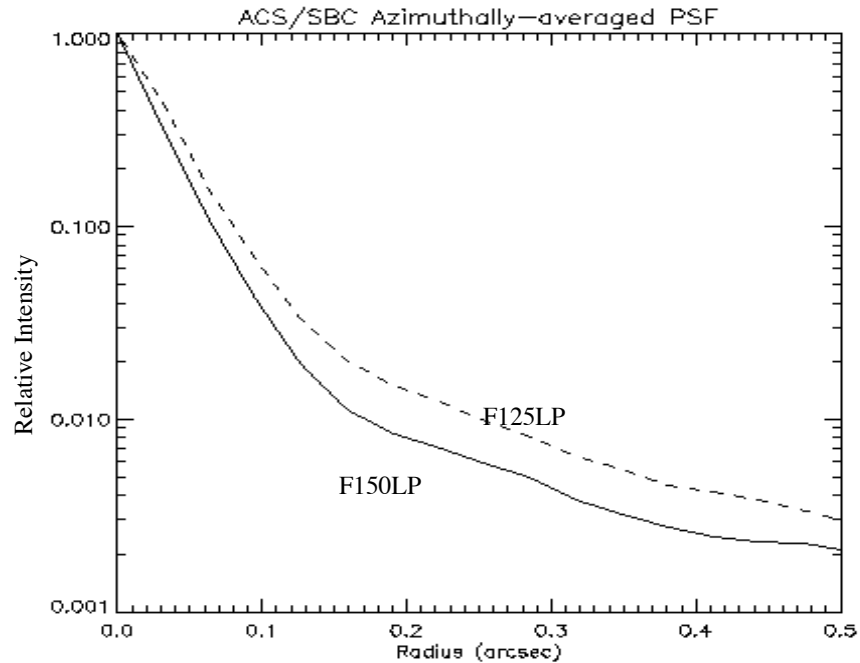
Figure 4.17: Total transmission curve for ACS SBC plus the PR110L prism



4.4.3 Optical Performance

The SBC exhibits low-level extended wings in the detector point-spread function (PSF). Sample MAMA detector PSF profiles are shown in Figure 4.18.

Figure 4.18: MAMA point spread function.



4.5 SBC Operations and Limitations

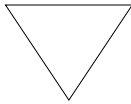
4.5.1 SBC Scheduling Policies

The STIS MAMA control electronics are subject to resets due to cosmic-ray upsets. Therefore, STIS MAMAs were operated only during the contiguous orbits of each day that are free of the South Atlantic Anomaly (SAA). Even though the design of the ACS MAMA control electronics in the SBC was modified so that they would not be susceptible to cosmic-ray hits, the background count rate still exceeds the bright object limits for the SBC during SAA passage. Consequently, the SBC will in general only be scheduled for use during SAA-free orbits.

4.5.2 MAMA Overflow of the 16 Bit Buffer

The MAMA is a photon-counting detector: as each event is recorded, the buffer memory for the corresponding pixel is incremented by one integer. The buffer memory stores values as 16 bit integers; hence the maximum number it can accommodate is 65,535 counts per pixel in a given ACCUM mode observation. The 2-Byte (16-bit) memory can hold 2^{16} values, including 0. When accumulated counts per pixel exceed this number, the values will wrap, i.e. the memory resets to 0. As an example, if you are counting at 25 counts/second/pixel, you will reach the MAMA “accumulation” limit in ~44 minutes.

One can keep accumulated counts per pixel below this value by breaking individual exposures into multiple identical exposures, each of which is short enough that fewer than 65,535 counts are accumulated per pixel. There is no readnoise for MAMA observations, so no penalty is paid in lost signal-to-noise ratio when exposures are split. There is only a small overhead for each MAMA exposure (see Section 8.2).



Keep the accumulated counts per SBC pixel below 65,535 by breaking single exposures into multiple exposures, as needed.

4.5.3 MAMA Darks

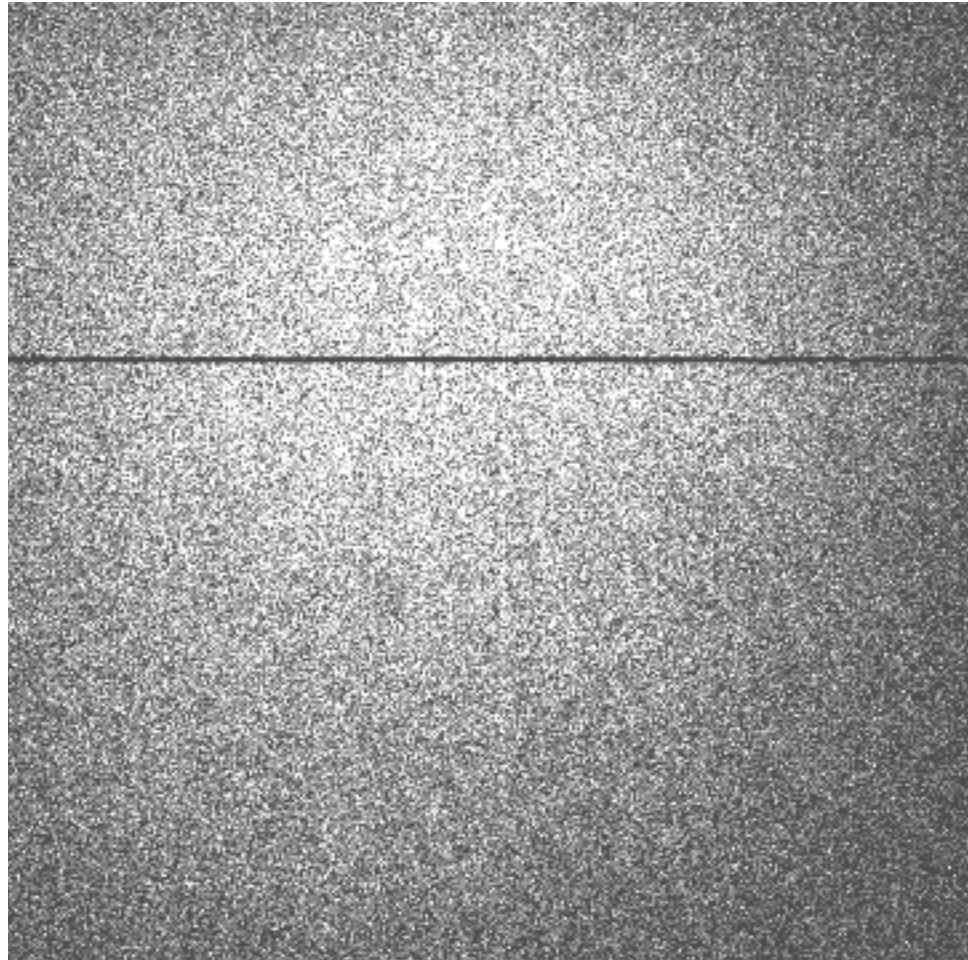
MAMA detectors have intrinsically low dark currents. Ground test measurements of the ACS MAMA showed count rates in the range of 10^{-5} to 10^{-4} counts per pixel per second as the temperature varied from 28 °C to 35 °C degrees. The count rate increased by about 30% for one degree increase in temperature. In-flight measurements, taken weekly throughout June and July 2002, show count rates between 8×10^{-6} and 10^{-5} . These measurements were taken as soon as the MAMA was turned on and were therefore at the lower end of the temperature range. A 10 hour observation in SMOV, long enough for nominal temperatures to be reached, yielded a dark current of 1.2×10^{-5} counts per second per pixel. Monthly monitoring shows the in-flight dark current to be about 9×10^{-6} counts per second per pixel. For typical SBC operations in which the detector is turned on for less than two hours, a dark image collected at lower temperatures is more suitable and replaces the current calibration image. This has a mean dark rate of 10^{-5} counts per second per pixel.

Recent measurements of SBC darks have shown a significant increase in the rate when the detector is on for several hours. The rate for the first two years remains close to 10^{-5} counts per second per pixel but after 5 hours the rate is 5×10^{-5} counts per second per pixel. When last measured in 2002 this time dependant effect was almost negligible.

The ACS MAMA has a broken anode which disables rows 599 to 605. There are three dark spots smaller than 50 microns at positions (334,977), (578,964), and (960,851), as well as two bright spots at (55,281) and (645,102) with fluctuating rates that are always less than 3 counts per second. The reference pixel has been moved to (512,400) to avoid these areas (see Table 7.10)

An example of the dark current variation across the detector can be seen in Figure 4.19 below.

Figure 4.19: MAMA dark image. Full frame MAMA dark image. The average dark rate in this image is 5×10^{-5} counts per second per pixel.



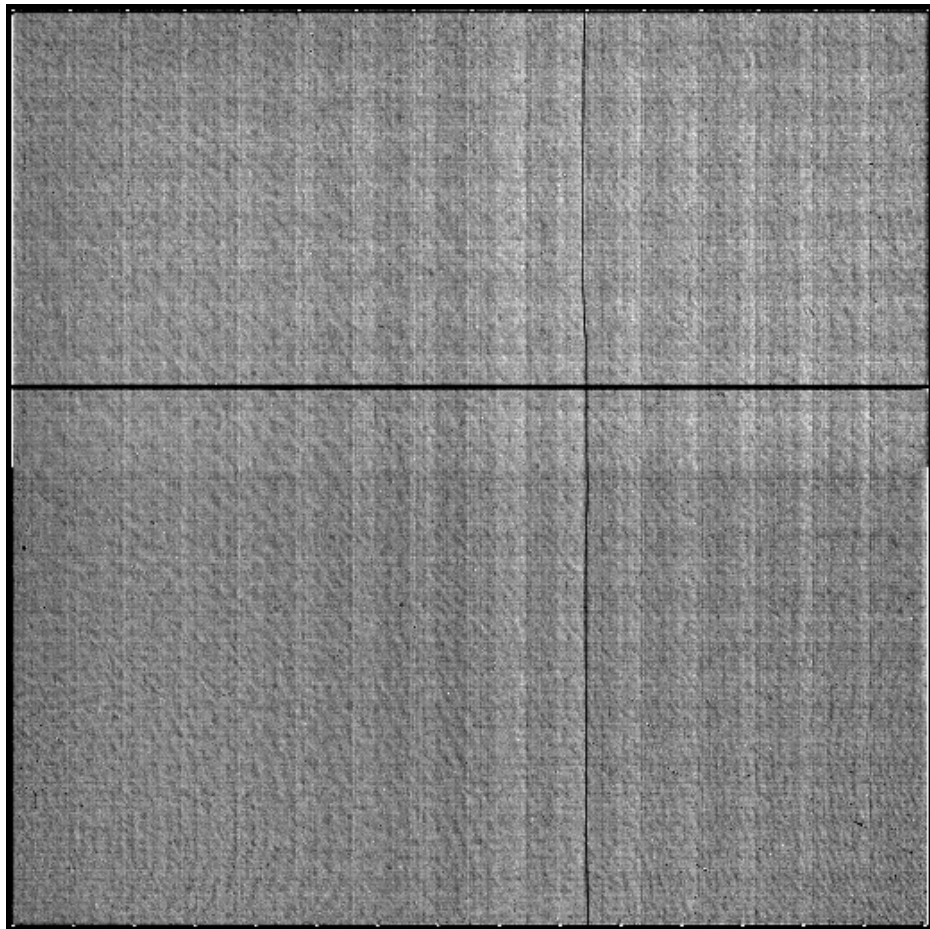
4.5.4 SBC signal-to-noise Ratio Limitations

MAMA detectors are capable of delivering signal-to-noise ratios of order 100:1 per resolution element (2×2 pixels) or even higher. Tests in orbit have demonstrated that such high S/N is possible with STIS (Kaiser et al., *PASP*, 110, 978; Gilliland, *STIS ISR 1998-16*). For targets observed at a fixed position on the detector, the signal-to-noise ratio is limited by systematic uncertainties in the small-scale spatial and spectral response of

the detector. The MAMA flats show a fixed pattern that is a combination of several effects including beating between the MCP array and the anode pixel array, variations in the charge-cloud structure at the anode, and low-level capacitive cross-coupling between the fine anode elements. Intrinsic pixel-to-pixel variations are of order 6% but are stable to < 1%. Photometric accuracy can be improved by averaging over flat field errors by dithering the observation (see Section 7.4).

4.5.5 SBC Flatfield

Figure 4.20: MAMA flat field. Wavelength independent P-Flat for the SBC MAMA (full frame shown).



The SBC requires two types of flat fields: the "pixel-to-pixel flats" (or P-flats), which take care of the high-frequency structures in the detector sensitivity, and the "low-order flats" (or L-flats), which handle the low-frequency components. Current P-flats were derived by Bohlin & Mack ([ACS ISR 2005-04](#)) using the on-board deuterium lamp and were found to be independent of wavelength. The P-flat in Figure 4.20 shows the

effect of the disabled broken anode for rows 601 to 605 and of the shadow of the repeller wire around column 577.

Low-frequency flatfield corrections for the SBC imaging modes have been derived using multiple exposures of the globular cluster NGC6681 (Mack, et. al., [ACS ISR 2005-013](#)). Variations of $\pm 6\%$ (full range) were found for the F115LP and F125LP filters, $\pm 8\%$ for the F140LP and F150LP filters, and $\pm 14\%$ for the F165LP filter. The F122M filter was not included in this analysis due to lack of sufficient data. The L-flat shows a similar general pattern in all filters, with the required correction increasing with wavelength. The L-flat analysis detected a decline in the UV sensitivity with time at a level of 2 to 4%/yr over the first 1.6 years of operation. The sensitivity appears to have leveled off after this time. A slight sensitivity loss as a function of temperature ($\sim 0.1\%/degree$) was also discovered. These effects were detected for the STIS FUV-MAMA detector (see [STIS ISRs 2003-01](#) and [2004-04](#)).

4.5.6 SBC Nonlinearity

Global

The MAMA detector begins to experience nonlinearity (photon impact rate not equal to photon count rate) at global (across the entire detector) count rates of 200,000 counts/second. The nonlinearity reaches 10% at 360,000 counts/second and can be corrected for in post-observation data processing at the price of a loss of photometric reliability. Additionally, the MAMA detector plus processing software are not able to count reliably at rates exceeding 285,000 counts/second. For this reason, and to protect the detectors, observations beyond this rate are not allowed (see Section 4.6).

Local

The MAMA detector remains linear to better than 1% up to ~ 22 counts/second/pixel. At higher rates, it experiences local (at a given pixel) nonlinearity. The nonlinearity effect is image dependent—that is, the nonlinearity observed at a given pixel depends on the photon rate affecting neighboring pixels. This property makes it impossible to correct reliably for the local nonlinearity in post-observation data processing. In addition, MAMA detectors are subject to damage at high local count rates (see Section 4.6).

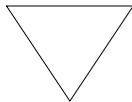
4.6 SBC Bright-Object Limits

STScI has responsibility to ensure that the MAMA detectors are not damaged through over-illumination. Consequently, we have developed procedures and rules to protect the MAMA. We ask all potential users to share in this responsibility by reading and taking note of the information in this section, and designing observing programs which operate in the safe regime for these detectors. The safety of all proposed SBC targets and fields must be discussed in the Phase I proposal, so that their feasibility can be assessed by the TAC and STScI.

4.6.1 Overview

The SBC detector is subject to catastrophic damage at high global and local count rates, and cannot be used to observe sources which exceed the defined safety limits. The potential detector damage mechanisms include over-extraction of charge from the microchannel plates causing permanent reduction of response, ion feedback from the microchannel plates causing damage to the photocathode, and release of gas which can overpressure the tube.

To safeguard the detector, checks of the global (over the whole detector) and local (per pixel) illumination rates are automatically performed in flight for all SBC exposures. The *global illumination rate* is monitored continuously; if the global rate approaches the level where the detector can be damaged, the high voltage on the detector is automatically turned off. This event can result in the loss of all observations scheduled to be taken with that detector for the remainder of the calendar (~1 week). The *peak local illumination rate* is measured over the SBC field at the start of each new exposure. If the local rate approaches the damage level, the SBC filter wheel will be used to block the light, since there is no “shutter”. Also, all subsequent SBC exposures in the obset will be lost until a new filter is requested.



Sources that would over-illuminate the SBC detector cannot be observed. It is the responsibility of the observer to avoid specifying observations that exceed the limits described below. Please refer to Section 7.2 for more information and address this issue in your Phase I proposal.

4.6.2 Observational Limits

To ensure the safety of the SBC detector and the robustness of the observing timeline, we have established observational limits on the incident count rates. Observations which exceed the allowed limits will not be scheduled. The allowed limits are given in Table 7.3, which includes separate limits for nonvariable and irregularly-variable sources. The limits for irregular variable sources are a factor 2.5 more conservative than for sources with predictable fluxes. Predictable variables are treated as nonvariable for this purpose. Examples of sources whose variability is predictable are Cepheids or eclipsing binaries. Irregularly variable sources are, for instance, cataclysmic variables or AGN.

SBC observations of targets subject to large, unpredictable outbursts must be preceded by groundbased monitoring within the previous 24 hours, or by an HRC NUV observation a couple of orbits in advance. In the latter case, the HRC observation must be included in the Phase I orbit request.

For further information about checking for SBC bright object limits while planning your observations, please refer to Section 7.2.

CHAPTER 5: Imaging

In this chapter . . .

| |
|---|
| 5.1 Imaging Overview / 55 |
| 5.2 Important Considerations for ACS Imaging / 60 |
| 5.3 Wide Field Optical CCD Imaging / 64 |
| 5.4 High-Resolution Optical and UV Imaging / 66 |
| 5.5 Ultraviolet Imaging with the SBC / 68 |
| 5.6 ACS Point Spread Functions / 70 |

5.1 Imaging Overview

ACS can be used to obtain images through a variety of optical and ultraviolet filters. When the selected ACS camera is the WFC or the HRC, the appropriate filter in one of the two filter wheels is rotated into position, and a clear aperture is automatically selected on the other filter wheel. For SBC imaging the single filter wheel is rotated to the required position. A number of apertures are defined for each ACS camera. In general, these refer to different target positions on the detector.

Table 5.1, Table 5.2, and Table 5.3 provide a complete summary of the filters available for imaging with each detector. Figures 5.1 through 5.6 show the filter transmission curves, and Figure 5.7 shows the integrated system throughputs.

The CCD filter wheels contain filters of two different sizes. Some filters (F435W, F475W, F502N, F550M, F555W, F606W, F625W, F658N, F660N, F775W, F814W, F850LP, and, G800L) are full-sized filters that can be used with both WFC and HRC. Others (F220W, F250W, F330W, F344N, F892N, POL0UV, POL60UV, POL120UV, POL0V, POL60V, POL120V, and PR200L) are smaller, giving a full unvignetted field of view when used with the HRC, but a vignetted field of view of only 72×72 arcseconds when used with the WFC. Use of the small UV filters is not supported with the WFC due to the unpredictable behavior of the silver coatings shortward of 4000 \AA .

The ramp filters are designed to allow narrow or medium band imaging centered at an arbitrary wavelength. Each ramp filter is divided into three segments, of which only the middle segment may be used with the HRC. More information is available at Section 7.7.2.

Note that although the CLEAR filters are specified in the filter wheel tables, users do not need to specify these filters in their HST proposals; they are added automatically in conjunction with the desired filter in the complementary wheel. In the SBC filter wheel, every third slot (#1, 4, 7, 10) is blocked off, so that in the case of a bright object limit violation, it is only necessary to rotate the filter wheel to an adjacent slot to block the incoming light.

With either the WFC or HRC, it is possible to select a filterless observation by specifying CLEAR (this is an “available-but-unsupported” filter) as the filter name, although the image will be of degraded quality. Rough wavelengths and widths, when used with the WFC or HRC, are listed in Table 5.1 under CLEAR entries. Use of CLEAR will provide slightly degraded PSFs with the HRC and seriously degraded PSFs for the WFC. More details on PSFs with use of CLEAR are provided in [ACS ISR 2003-03](#). Applications are expected to be rare, but a valid use could be astrometry of extremely faint targets with the HRC when color information is not required.

Table 5.1: ACS WFC/HRC filters in Filter Wheel #1.

| Filter name | Central wavelength (Å) | Width (Å) | Description | Camera |
|-------------|------------------------|-----------|-------------------|-----------|
| CLEAR | 6200 | 5200 | Clear aperture | WFC/HRC |
| F555W | 5346 | 1193 | Johnson V | WFC/HRC |
| F775W | 7764 | 1528 | SDSS i | WFC/HRC |
| F625W | 6318 | 1442 | SDSS r | WFC/HRC |
| F550M | 5580 | 547 | Narrow V | WFC/HRC |
| F850LP | 9445 | 1229 | SDSS z | WFC/HRC |
| POL0UV | 2000 to 6000 | - | 0° UV polarizer | HRC[/WFC] |
| POL60UV | 2000 to 6000 | - | 60° UV polarizer | HRC[/WFC] |
| POL120UV | 2000 to 6000 | - | 120° UV polarizer | HRC[/WFC] |
| F892N | 8917 | 154 | Methane (2%) | HRC[/WFC] |
| F606W | 5907 | 2342 | Broad V | WFC/HRC |
| F502N | 5022 | 57 | [OIII] (1%) | WFC/HRC |
| G800L | 5800 to 11,000 | - | Grism (R~100) | WFC/HRC |
| F658N | 6584 | 78 | H α (1%) | WFC/HRC |
| F475W | 4760 | 1458 | SDSS g | WFC/HRC |

[/WFC] indicates that polarizer filters, designed for the HRC field of view, induces vignetting when used with the WFC, producing a 72 by 72 arcsecond field of view.

Table 5.2: ACS WFC/HRC filters in Filter Wheel #2.

| Filter name | Central wavelength (Å) | Width (Å) | Description | Camera |
|-------------|------------------------|-----------|--------------------------------|-----------|
| CLEAR | 6000 | 5200 | Clear aperture | WFC/HRC |
| F660N | 6602 | 40 | [NII] (1%) | WFC/HRC |
| F814W | 8333 | 2511 | Broad I | WFC/HRC |
| FR388N | 3710 to 4050 | 2% | [OII] Ramp—middle segment | WFC/HRC |
| FR423N | 4050 to 4420 | 2% | [OII] Ramp—inner segment | WFC |
| FR462N | 4420 to 4820 | 2% | [OII] Ramp—outer segment | WFC |
| F435W | 4297 | 1038 | Johnson B | WFC/HRC |
| FR656N | 6270 to 6850 | 2% | H α Ramp—middle segment | WFC/HRC |
| FR716N | 6850 to 7470 | 2% | H α Ramp—inner segment | WFC |
| FR782N | 7470 to 8160 | 2% | H α Ramp—outer segment | WFC |
| POL0V | 4000 to 8000 | - | 0° Visible Polarizer | HRC[/WFC] |
| F330W | 3354 | 588 | HRC U | HRC |
| POL60V | 4000 to 8000 | - | 60° Visible Polarizer | HRC[/WFC] |
| F250W | 2696 | 549 | Near-UV broadband | HRC |
| POL120V | 4000 to 8000 | - | 120° Visible Polarizer | HRC[/WFC] |
| PR200L | 2000 to 4000 | - | NUV Prism (R~100 @ 200 nm) | HRC |
| F344N | 3434 | 60 | Ne V (2%) | HRC |
| F220W | 2228 | 485 | Near-UV broadband | HRC |
| FR914M | 7570 to 10,710 | 9% | Broad Ramp—middle segment | WFC/HRC |
| FR853N | 8160 to 8910 | 2% | IR Ramp—inner segment | WFC |
| FR931N | 8910 to 9720 | 2% | IR Ramp—outer segment | WFC |
| FR459M | 3810 to 5370 | 9% | Broad Ramp—middle segment | WFC/HRC |
| FR647M | 5370 to 7570 | 9% | Broad Ramp—inner segment | WFC |
| FR1016N | 9720 to 10,610 | 2% | IR Ramp—outer segment | WFC |
| FR505N | 4820 to 5270 | 2% | [OIII] Ramp—middle segment | WFC/HRC |
| FR551N | 5270 to 5750 | 2% | [OIII] Ramp—inner segment | WFC |
| FR601N | 5750 to 6270 | 2% | [OIII] Ramp—outer segment | WFC |

[/WFC] indicates that polarizer filters, designed for the HRC field of view, induces vignetting when used with the WFC, producing a 72 by 72 arcsecond field of view.

Table 5.3: ACS SBC filter complement.

| Filter name | Description |
|-------------|--|
| F115LP | MgF ₂ (1150 Å longpass) |
| F125LP | CaF ₂ (1250 Å longpass) |
| F140LP | BaF ₂ (1400 Å longpass) |
| F150LP | Crystal quartz (1500 Å longpass) |
| F165LP | Fused Silica (1650 Å longpass) |
| F122M | Ly- α ($\lambda = 1200$ Å, $\Delta\lambda = 60$ Å) |
| PR110L | LiF Prism (R~100) |
| PR130L | CaF ₂ Prism (R~100) |

Figure 5.1: ACS broad-band filters.

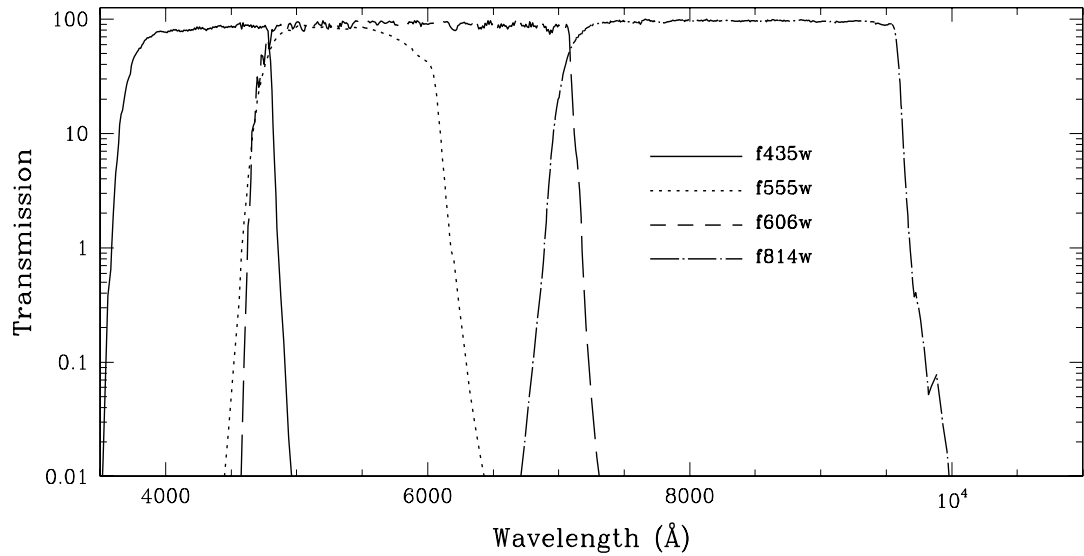


Figure 5.2: ACS SDSS filters.

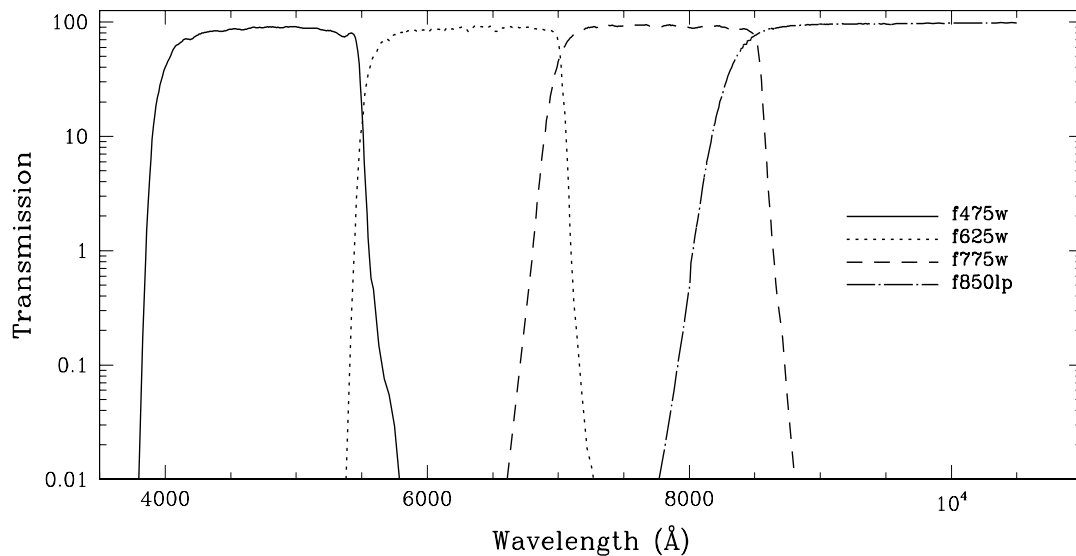


Figure 5.3: ACS UV and medium-band filters.

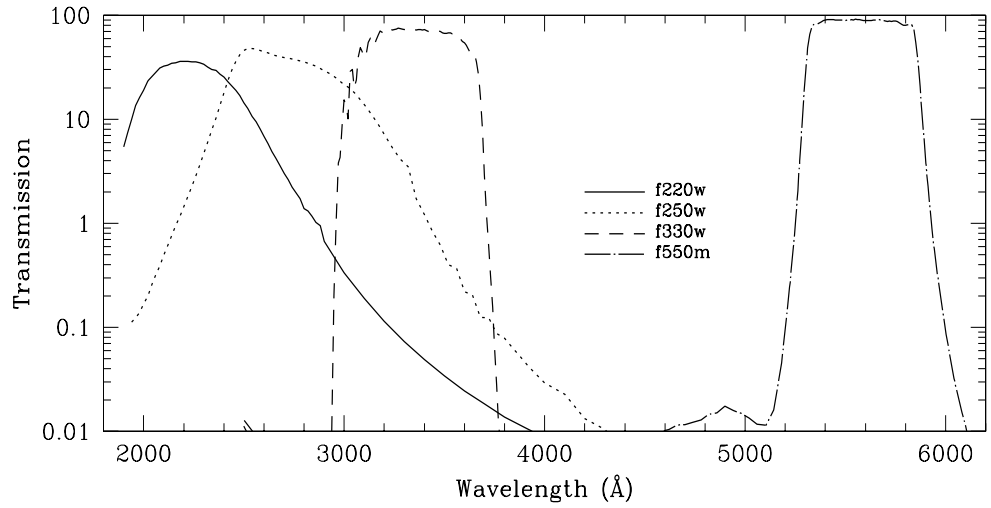


Figure 5.4: ACS narrow-band filters.

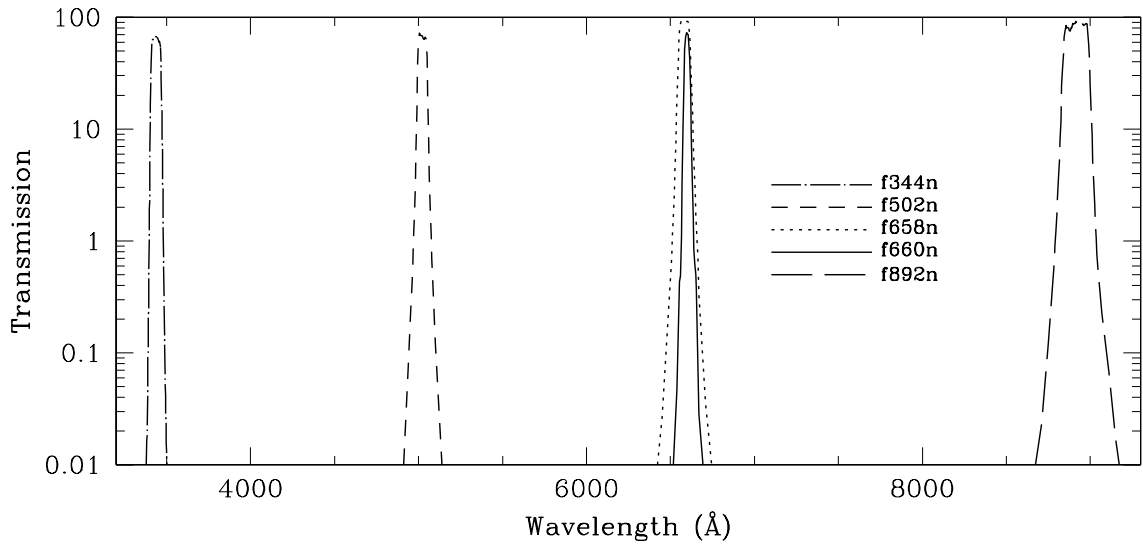


Figure 5.5: ACS SBC filters.

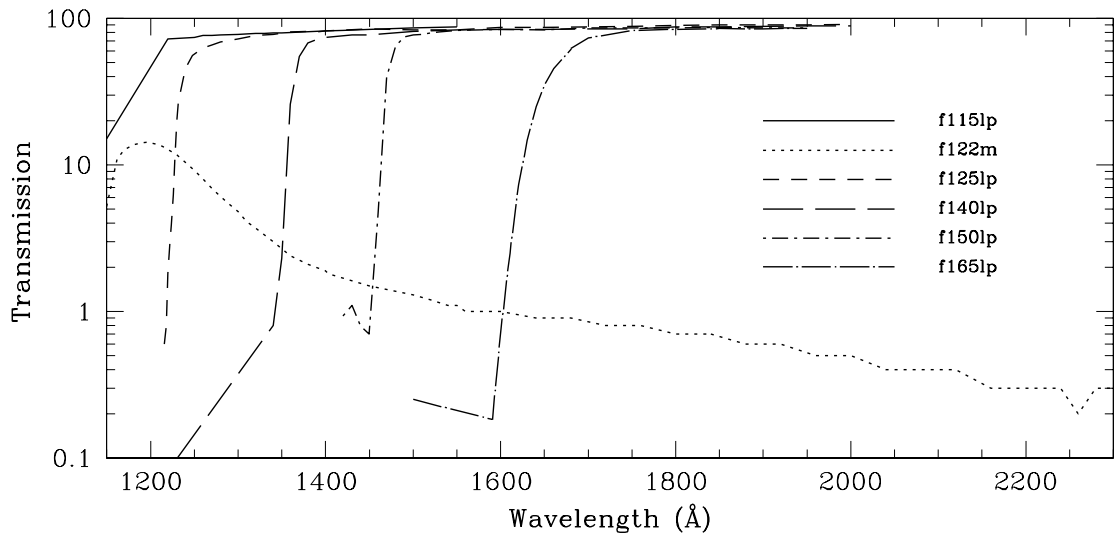
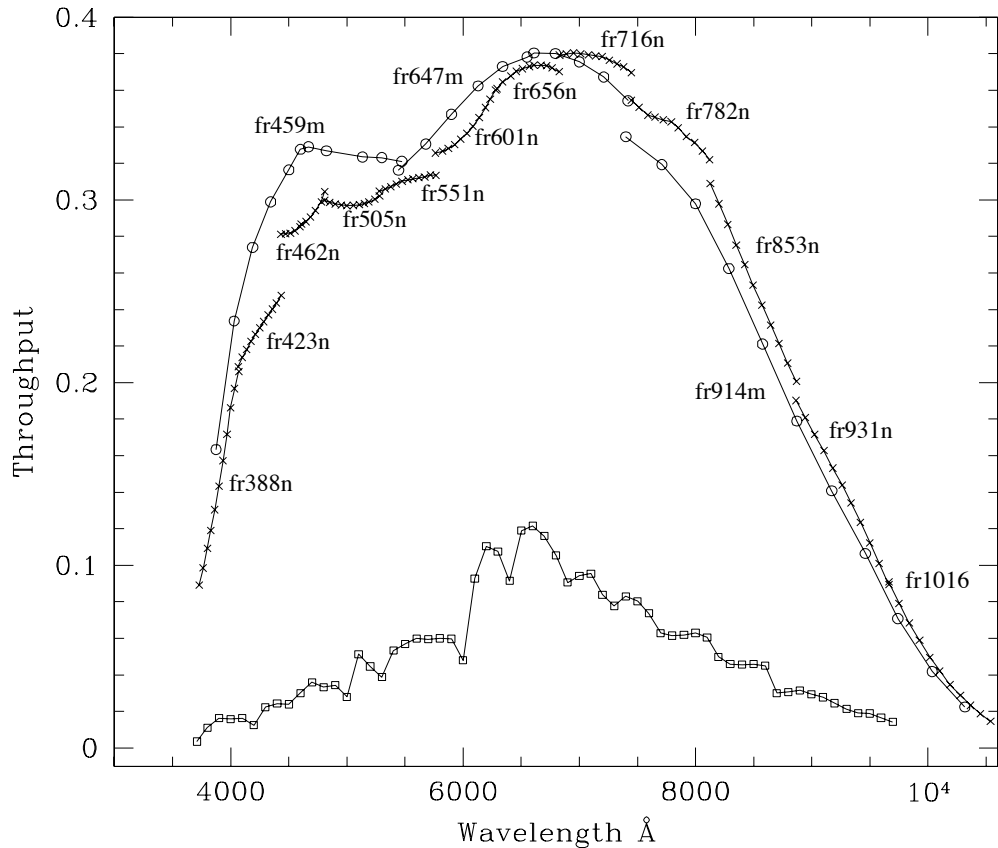


Figure 5.6: Comparison between the ACS and WFPC2 ramp filters.



The crosses and open circles are for the ACS narrow and medium band ramps. The open squares are for the 4 WFPC2 ramps. For each of the ACS ramps the peak throughput that was calculated for eleven central wavelength values is plotted. For the WFPC2 ramps, the peak throughput calculated every 100 Å within the field of view of any of the 4 chips, and a 0° filter rotation angle (as mapped in Figures 3.4 and 3.5 of the WFPC2 Instrument Handbook, version 3.0), are plotted.

5.2 Important Considerations for ACS Imaging

There are a few characteristics of ACS that should be taken into account when imaging with ACS:

- The HRC and WFC filters are housed in two filter wheels shared by both cameras. As a consequence, when a filter is chosen for the primary camera, the filter used in the parallel camera is not independently selectable.
- The ACS cameras are designed to be used with a single filter, and for this reason unfiltered imaging or imaging through two filters leads to significantly degraded imaging quality (particularly in the WFC) and is not normally used except for polarization observations, or bright

target acquisitions with the HRC. The polarizer filters were designed with a zero optical thickness so that they can and should be used with another filter.

- The geometric distortion of the WFC is significant and causes the projected pixel area to vary by $\pm 9\%$ over the field of view. This distortion affects both the photometric accuracy and the astrometric precision, and must be accounted for when the required accuracy is better than 10%.
- The ratio of in-band vs. out-of-band transmission for the ACS CCD UV filters is similar to that of WFPC2, once the two detector QE curves are taken into account (the red leak on ACS F330W is very small). This implies that the effect of filter red leaks needs to be calibrated for UV imaging of intrinsically red objects.
- The cosmic ray fluxes for HRC and WFC are comparable, respectively, to those of the STIS CCD and WFPC2. As with these instruments, typical imaging observations will need to be split or dithered for cosmic ray rejection.
- Section 4.3.5 provides further details and a recommendation that separate exposures with small dithers be used as a means of helping to remove residual hot pixels.
- The large format of the WFC requires significantly more shifts to read out data compared to STIS or WFPC2. Therefore, the impact of decreasing charge transfer efficiency will be encountered earlier. Section 4.3.7 details current expectations.
- The default GAIN setting for WFC primary observations is GAIN=2. This allows for good sampling of the readout noise and allows one to reach the full well counts of WFC. For the HRC primary observations, the default gain is GAIN=2. To sample the detector full well depth, GAIN=4 is needed, but this results in modest undersampling of the readout noise. For HRC ACQ data, the default setting is GAIN=4. Users may select the GAIN they wish to use for their ACS observations by using the GAIN optional parameter in their Phase II proposal. However, not all GAIN settings are supported (see Section 7.6).
- At wavelengths longward of $\sim 8000 \text{ \AA}$, internal scattering in the HRC CCD produces an extended PSF halo. This should affect only a small number of observations since the WFC camera is normally preferred at these wavelengths. The WFC CCDs include a front-side metallization that eliminates the large angle, long wavelength halo problem for $\lambda < 9000 \text{ \AA}$. (For observations of red targets with the F850LP refer to Section 9.3.2).

- The ACS filter complement is not as rich as that in WFPC2. In particular, the Strömgren filter set and several narrow band filters available in WFPC2 (F375N, F390N, F437N, F469N, F487N, F588N, F631N, F656N, F673N, F953N) are not available on ACS. In general, these filters were not heavily used by the GO community. For most applications they can be replaced with the ACS medium and narrow ramps.

5.2.1 Optical Performance

Testing of the WFC and HRC cameras, following fine alignment activities on-orbit, has shown that the optical quality objectives of the cameras are met. The encircled energy values obtained from observations made in SMOV are given in Table 5.4.

Table 5.4: Encircled energy measurements for the ACS channels.

| Channel | Encircled energy | |
|---|------------------|---------------|
| | Center of field | Edge of field |
| WFC at 632.8 nm in 0.25 arcseconds diameter | 80.0% | 79.4% |
| HRC at 632.8 nm in 0.25 arcseconds diameter | 81.8% | 81.6% |
| SBC at 121.6 nm in 0.10 arcseconds diameter | 28% | --- |

5.2.2 CCD Throughput Comparison

Figure 5.7 shows the throughput of the two unfiltered ACS CCD cameras: WFC and HRC. Superposed on this plot are unfiltered WFPC2 (WF4) and the clear STIS throughputs.

5.2.3 Limiting Magnitudes

Table 5.5 contains Johnson-Cousins V magnitudes for unreddened O5 V, A0 V, and G2 V stars, generated using the Exposure Time Calculator. WFC and HRC values used the parameters CR-SPLIT=2, GAIN=2, and a 0.2 arcsecond circular aperture. For the SBC, a 0.5 arcsecond circular aperture was used. An average sky background was used in these examples. However, limiting magnitudes are sensitive to the background levels; for instance, the magnitude of an A0 V in the WFC using the F606W filter changes by ± 0.4 magnitudes at the background extremes.

Figure 5.7: ACS CCD system throughputs + OTA versus those of STIS and WFPC2.

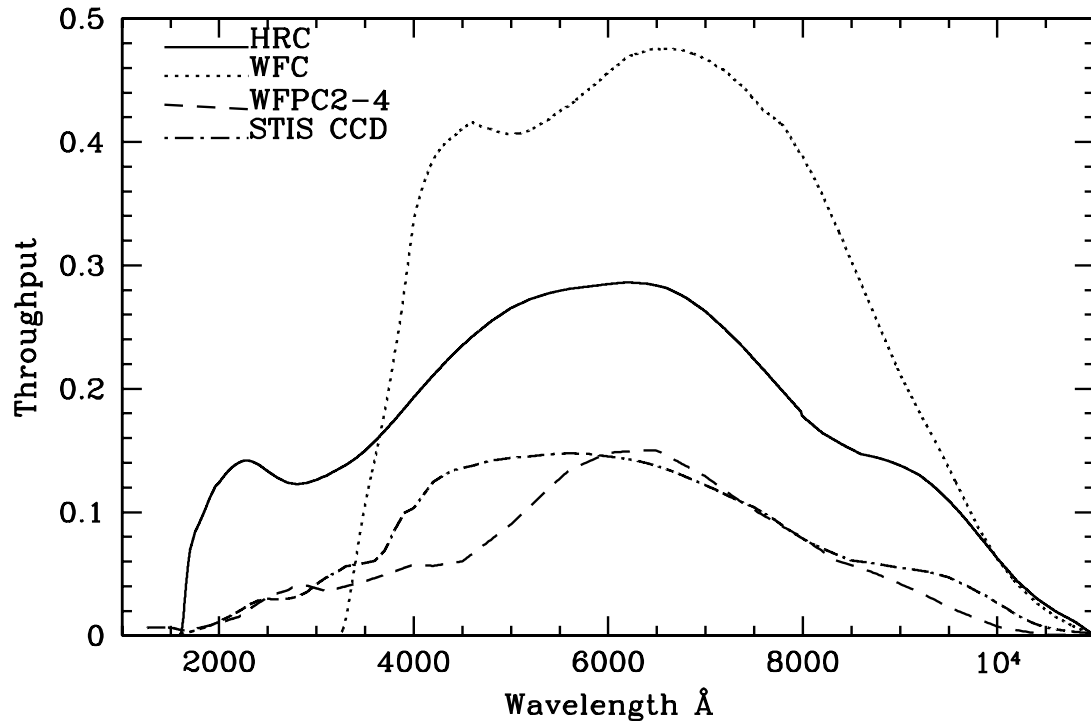


Table 5.5: V detection limits for ACS, HRC, and SBC direct imaging.

| Camera | Filter | V limit (S/N = 5, exposure time = 1 hour) | | |
|--------|--------|---|-------------|------------|
| | | O5 V (Kurucz model) | A0 V (Vega) | G2 V (Sun) |
| WFC | F606W | 27.8 | 27.8 | 28.0 |
| WFC | F814W | 26.7 | 27.0 | 27.7 |
| HRC | F330W | 26.8 | 24.8 | 24.1 |
| HRC | F606W | 27.3 | 27.3 | 27.5 |
| SBC | F125LP | 27.8 | 23.2 | 13.5 |

5.2.4 Signal-To-Noise Ratios

In Chapter 10, we present, for each imaging mode, plots of exposure time versus magnitude to achieve a desired signal-to-noise ratio. These plots, which are referenced in the individual imaging-mode sections below, are useful for getting an idea of the exposure time you need to accomplish your scientific objectives. More accurate estimates require the use of the ACS Exposure Time Calculator (<http://www.stsci.edu/hst/acs/software>).

5.2.5 Saturation

Both CCD and SBC imaging observations are subject to saturation at high total accumulated counts per pixel. For the CCDs, this is due either to the depth of the full well or to the 16 bit data format. For the SBC, this is due to the 16 bit format of the buffer memory (see Section 4.3.1 and Section 4.5.2).

5.3 Wide Field Optical CCD Imaging

The Wide Field Channel of ACS was designed primarily for high throughput observations at visible wavelengths. The use of protected silver mirror coatings, the small number of reflections, and the use of a red sensitive CCD have provided the high throughput required for this camera at the expense of a 3700 Å blue cutoff. The WFC detectors are two butted 2K by 4K thinned, backside-illuminated, SITE CCDs with a red optimized coating and long- λ halo fix. The plate scale is 0.050 arcseconds per pixel, which provides a good compromise between adequately sampling the PSF and a wide field of view. The WFC PSF is critically sampled at 11,600 Å and undersampled by a factor 3 at the blue end of the WFC sensitivity range (3700 Å). We expect that it will be possible to achieve a final reconstructed FWHM of 0.100 to 0.140 arcseconds for well-dithered observations. Because the WFC PSF FWHM is largely dependent on the blurring caused by CCD charge diffusion, dithering will not be able to recover the full resolution of the optical system. See Section 7.4 for more discussion of how to use dithered observations to optimally sample the PSF.

The optical design of the camera introduces a two-component geometric distortion. The detectors themselves are at an angle with respect to the optical axis. This produces an 8% stretching of one pixel diagonal compared to the other. As a result, WFC pixels project on the sky as rhombuses rather than squares. These effects are purely geometrical and are routinely corrected in the ACS data reduction pipeline. The second component of geometric distortion is more complex. This distortion causes up to $\pm 9\%$ variation in effective pixel area and needs to be taken into account when doing accurate photometry or astrometry as the effective area of the detector pixels varies nonlinearly with field position.

5.3.1 Filter Set

WFPC2 and Johnson-Cousins filters

All of the most commonly used WFPC2 filters are included in the ACS filter set. In addition to a medium and a broad V band filter (F550M and F606W), there is a complete Johnson-Cousins *BVI* set (F435W, F555W, F814W).

Sloan Digital Sky Survey filters

The Sloan Digital Sky Survey (SDSS) *griz* filter set (F475W, F625W, F775W, F850LP) is designed to provide high throughput for the wavelengths of interest and excellent rejection of out-of-band wavelengths. The filters were designed to provide wide, non-overlapping filter bands that cover the entire range of CCD sensitivity from blue to near-IR wavelengths.

Narrow Band filters

The H α (F658N), [OIII] (F502N), and [NII] (F660N) narrow band filters are full-size, and can be used with both the WFC and HRC.

Ramp filters

ACS includes a complete set of ramp filters that provide full coverage of the WFC wavelength range at 2% and 9% bandwidth. Each ramp filter consists of three segments. The inner and outer filter segments can be used with the WFC only, while the middle segments can be used by both WFC and HRC. Unlike the WFPC2, where the desired wavelength is achieved by offsetting the telescope, the wavelength of ACS ramps is selected by rotating the filter while the target is positioned in one of the pre-defined apertures. The monochromatic field of view of the ramp filters is approximately 40 by 80 arcseconds. Details of how to use the ramp filters are given in Section 7.7.2.

Polarizer filters

The WFC/HRC filter wheels contain polarizers with pass directions spaced by 60°, optimized for both the UV (POL0UV, POL60UV, and POL120UV) and the visible (POL0V, POL60V, and POL120V). All the polarizer filters are sized for the HRC field of view. They induce vignetting when used with the WFC, for which the FOV will be about 72 by 72 arcseconds. More information on the use of the polarizers is given in Chapter 6.

Grism and Prism

The CCD channels also have a grism (G800L) for use with both WFC and HRC from 5500 Å to 11,000 Å, and a prism (PR200L) for use with the HRC from 1600 Å to 3500 Å. These are described more fully in Chapter 6.

5.4 High-Resolution Optical and UV Imaging

The High Resolution Channel of ACS is the prime ACS camera for near-UV imaging. HRC provides high throughput in the blue and a better sampling of the PSF than either the WFC or other CCD cameras on HST. The HRC pixel size critically samples the PSF at 6300 \AA and is undersampled by a factor 3.0 at the blue end of its sensitivity range (2000 \AA). With this capability, the HRC functionally replaces the Faint Object Camera as the instrument able to critically sample the PSF in the V band. For this reason, most of the usage of HRC will be for UV and blue imaging. HRC can also be convenient for imaging in the red when the PSF sampling is important. As an example, better PSF sampling is probably important for accurate stellar photometry in crowded fields. We expect that the photometric accuracy achievable by the HRC will be higher than that achievable with the WFC. Well-dithered observations with the HRC should lead to a reconstructed PSF FWHM of 0.03 arcsec at $\sim 4000 \text{ \AA}$, increasing towards longer wavelengths. HRC also includes a coronagraph that is discussed in Chapter 6. The HRC CCD presents a long wavelength halo problem similar to the STIS CCD since the front-side metallization correcting the halo problem for the WFC CCDs was implemented only after the HRC CCD had been procured. Although most of the HRC imaging is likely to occur in the UV, users should be cautioned to take into account the effects of the long wavelength halo when using the HRC in combination with near-IR filters (See Section 5.6.5).

5.4.1 Filter Set

The HRC-specific filters are mostly UV and blue. The set includes UV and visible polarizers (discussed in Chapter 6), a prism (PR200L, discussed in Chapter 6), three medium-broad UV filters (F330W, F250W, and F220W) and two narrow band filters (F344N and F892N). Use of the UV filters with the WFC is not supported because of the uncertainty of the WFC silver coating transmission below 4000 \AA .

All broad, medium and narrow band WFC filters can be used with the HRC whenever a better PSF sampling is required. In general, the throughput of WFC is higher than that of HRC where their sensitivity overlaps. Only some of the WFC ramp segments can be used with the HRC since only the middle segment overlaps with the HRC FOV. In particular, HRC can use the FR459M and FR914M broad ramps, and the FR505N [OIII], FR388N [OII], and FR656N (H α) narrow ramps.

5.4.2 Multiple Electron Events

Like the STIS CCD but unlike WFPC2, the HRC CCD is directly sensitive to UV photons and for this reason is much more effective in detecting them. However, whenever a detector has non-negligible sensitivity over more than a factor two in wavelength, it becomes energetically possible for a UV photon to generate more than one electron and be counted more than once. This effect has been seen for STIS and also during the ground testing of the HRC detector. The effect is only important shortward of 3200 Å, and reaches a magnitude of approximately 1.7 e⁻/photon at 2000 Å. Multiple counting of photons has to be taken into account when estimating the detector QE and the noise level of a UV observation since multiple photons cause a distortion in the Poisson distribution of electrons.

5.4.3 Red Leaks

When designing a UV filter, a high suppression of off-band transmission, particularly in the red, has to be traded with overall in-band transmission. The very high blue quantum efficiency of the HRC compared to WFPC2 makes it possible to obtain an overall red leak suppression comparable to that of the WFPC2 while using much higher transmission filters. In Cycle 14 we obtained new calibration data to check the impact of red leaks on observations. The results are described in [ACS ISR 2007-003](#). In Table 5.6 we show the ratio of in-band versus total flux for a few UV and blue HRC filters, where the cutoff point between in-band and out-of-band flux is defined as the filter's 1% transmission point. The same ratio is also listed for the equivalent filters in WFPC2. Correction factors for different stellar spectral types and non-stellar spectra can be found in the ISR. Clearly, red leaks are not a problem for F330W, F435W, and F475W. Red leaks are more important for F250W and F220W. In particular, accurate UV photometry of objects with the spectrum of an M star will require correction for the redleak in F250W and will be essentially impossible in F220W. For the latter filter a red leak correction will also be necessary for K and G stars.

Table 5.6: In-band flux as a percentage of the total flux.

| Stellar type | WFPC2 F218W | HRC F220W | WFPC2 F255W | HRC F250W | WFPC2 F300W | HRC F330W | WFPC2 F439W | HRC F435W | WFPC2 F450W | HRC F475W |
|--------------|-------------|-----------|-------------|-----------|-------------|-----------|-------------|-----------|-------------|-----------|
| O5 V | 99.8 | 99.6 | 99.6 | 99.7 | 99.9 | 99.9 | 99.9 | 99.9 | 99.9 | 99.9 |
| B1 V | 99.7 | 99.6 | 99.6 | 99.7 | 99.9 | 99.9 | 99.9 | 99.9 | 99.9 | 99.9 |
| A1 V | 99.4 | 98.8 | 99.2 | 99.0 | 99.2 | 99.9 | 99.9 | 99.9 | 99.9 | 99.9 |
| F0 V | 98.5 | 97.0 | 98.8 | 98.3 | 98.8 | 99.9 | 99.9 | 99.9 | 99.9 | 99.9 |
| G2 V | 92.5 | 88.7 | 97.4 | 97.1 | 97.4 | 99.9 | 99.9 | 99.9 | 99.8 | 99.9 |
| K0 V | 71.7 | 60.6 | 95.0 | 95.2 | 95.0 | 99.9 | 99.9 | 99.9 | 99.8 | 99.9 |
| M2 V | 0.03 | 1.5 | 45.5 | 62.4 | 45.4 | 99.9 | 99.9 | 99.9 | 99.6 | 99.9 |

5.5 Ultraviolet Imaging with the SBC

The Solar Blind Channel is the ACS camera optimized for UV imaging. The SBC uses the same optical train as the HRC and is comparable in performance to the FUV MAMA of STIS. The use of the repeller wire increases the quantum efficiency of the detector by $\sim 30\%$, but adds a halo to the PSF. Bright object limits are discussed in detail in Section 7.2.

5.5.1 Filter Set

Several filters are available for use with the SBC, including a Lyman α narrow band filter (F122M), a long pass quartz filter (F150LP), MgF₂ filter (F115LP), and a CaF₂ filter (F125LP). The SBC also includes two additional long pass filters (F140LP and F165LP) as well as prisms (discussed in Chapter 6). A list of filters is given in Table 5.3

5.5.2 Red Leaks

The visible light rejection of the SBC is excellent, but users should be aware that stars of solar type or later will have a significant fraction of the detected flux coming from outside the nominal wavelength range of the detector. This is discussed in greater detail in Section 4.4.2.

Table 5.7: Visible-light rejection of the SBC F115LP imaging mode.

| Stellar type | Percentage of all detected photons which have $\lambda < 1800 \text{ \AA}$ | Percentage of all detected photons which have $\lambda < 3000 \text{ \AA}$ |
|--------------|--|--|
| O5 | 99.5 | 100 |
| B1 V | 99.4 | 100 |
| A0 V | 98.1 | 100 |
| G0 V | 72.7 | 99.8 |
| K0 V | 35.1 | 94.4 |

5.5.3 SBC Imaging Filter Shifts

The SBC focal surface, like that of the HRC, is tilted significantly with respect to the chief ray. Because the MAMA detector is a STIS spare, its window is approximately parallel to the MCP surface and the whole detector must tilt to achieve good focus over the field. Because the window is therefore tilted, "lateral color" is introduced, which would result in dispersion-induced degradation of the PSF, so the filters are canted in the opposite direction to that of the window to ameliorate the color. The filter thickness is matched to the mean index of refraction over its bandpass to maintain focus. These result in unavoidable image location offsets between filters. In contrast, the WFC and HRC filters and windows are normal to the chief ray and the detector surfaces are tilted within their housings to match the focal surface tilt. In Table 5.8, we list the shifts for each SBC imaging filter with respect to the F115LP filter. No pointing compensations are made for these offsets.

Table 5.8: Shifts between SBC imaging filters.

| Spectral Element | Offset (pixels) in the x,y directions |
|------------------|---------------------------------------|
| F115LP | 0,0 |
| F122M | 0,0 |
| F125LP | -5,15 |
| F140LP | -7,21 |
| F150LP | -3,11 |
| F165LP | -4,12 |

5.6 ACS Point Spread Functions

The ACS point spread function has been studied in ground test measurements, and by using on-orbit data and models generated by the **Tiny TIM** software (<http://www.stsci.edu/software/tinytim/tinytim.html>) developed by J. Krist and R. Hook. As with other HST instruments, the ACS point spread function is affected by both optical aberrations and geometric distortions. Point sources imaged with WFC and HRC experience blurring due to charge diffusion into adjacent pixels because of CCD subpixel variations, which reduces the limiting magnitudes that can be reached by WFC/HRC. The SBC PSF and the long-wavelength HRC PSF are also affected by a halo produced by the detectors themselves.

5.6.1 CCD Pixel Response Function

The sharpness of the CCD PSF is somewhat degraded by charge diffusion into adjacent pixels. The effect is usually described in terms of the pixel response function (PRF), which gives the distribution of flux from within the pixel into adjacent pixels. Charge diffusion results in ~ 0.5 magnitude loss in the WFC limiting magnitude at short wavelengths (the worst case). At longer wavelengths and at all wavelengths for the HRC the reduction in the limiting magnitude is ~ 0.2 magnitudes or less. Due to variations in the CCD thickness, charge diffusion is not constant over the field of view. At different wavelengths, the CCD pixel response functions can be represented by the following kernels (for the center of the field):

Figure 5.8: Kernels representing CCD pixel functions for HRC and WFC.

$$K_{HRC} = \begin{bmatrix} 0.02 & 0.07 & 0.02 \\ 0.07 & 0.64 & 0.07 \\ 0.02 & 0.07 & 0.02 \end{bmatrix}, \quad K_{WFC} = \begin{bmatrix} 0.04 & 0.11 & 0.04 \\ 0.11 & 0.40 & 0.11 \\ 0.04 & 0.11 & 0.04 \end{bmatrix}$$

at $\lambda = 4000 \text{ \AA}$,

$$K_{HRC} = \begin{bmatrix} 0.02 & 0.06 & 0.02 \\ 0.06 & 0.68 & 0.06 \\ 0.02 & 0.06 & 0.02 \end{bmatrix}, \quad K_{WFC} = \begin{bmatrix} 0.03 & 0.10 & 0.03 \\ 0.10 & 0.48 & 0.10 \\ 0.03 & 0.10 & 0.03 \end{bmatrix}$$

at $\lambda = 5500 \text{ \AA}$, and

$$K_{HRC} = \begin{bmatrix} 0.02 & 0.04 & 0.02 \\ 0.04 & 0.76 & 0.04 \\ 0.02 & 0.04 & 0.02 \end{bmatrix}, \quad K_{WFC} = \begin{bmatrix} 0.02 & 0.07 & 0.02 \\ 0.07 & 0.64 & 0.07 \\ 0.02 & 0.07 & 0.02 \end{bmatrix}$$

at $\lambda = 8000 \text{ \AA}$.

More details on ACS CCD charge diffusion are given in [ACS ISR 2006-01](#). For details on CTE-induced photometric losses for ACS/WFC and techniques to correct for them, see [ACS ISR 2006-01](#).

5.6.2 Model PSFs

Table 5.9 and Table 5.10 give ACS model PSFs in the central 5×5 pixel region in two wavelength bands (filters). Numbers listed are the fraction of the total energy received in each pixel. The models have been generated using **Tiny TIM**, taking into account the HST optical aberrations and obscurations as well as the CCD pixel response function. Field dependent geometrical distortions are included. The real PSF will also differ from the model because of the jitter in the HST pointing, HST focus variation (focus breathing), and other instrumental effects, some of which are briefly discussed below. For further details on the PSF variations and an effective procedure to model them, see [ACS ISR 2006-01](#). The SBC PSF is shown Figure 5.10.

Table 5.9: Model ACS CCD PSFs.

| WFC model PSF, filter F435W | | | | | WFC model PSF, filter F814W | | | | |
|-----------------------------|------|------|------|------|-----------------------------|------|------|------|------|
| 0.00 | 0.01 | 0.01 | 0.01 | 0.00 | 0.01 | 0.01 | 0.02 | 0.01 | 0.01 |
| 0.01 | 0.04 | 0.07 | 0.05 | 0.02 | 0.01 | 0.03 | 0.07 | 0.03 | 0.02 |
| 0.02 | 0.08 | 0.17 | 0.08 | 0.02 | 0.02 | 0.07 | 0.18 | 0.07 | 0.02 |
| 0.01 | 0.04 | 0.08 | 0.04 | 0.01 | 0.01 | 0.03 | 0.07 | 0.03 | 0.01 |
| 0.00 | 0.01 | 0.02 | 0.01 | 0.00 | 0.01 | 0.02 | 0.02 | 0.01 | 0.00 |
| HRC model PSF, filter F435W | | | | | HRC model PSF, filter F814W | | | | |
| 0.01 | 0.01 | 0.01 | 0.01 | 0.01 | 0.00 | 0.01 | 0.02 | 0.01 | 0.00 |
| 0.02 | 0.03 | 0.06 | 0.03 | 0.01 | 0.01 | 0.04 | 0.05 | 0.04 | 0.01 |
| 0.01 | 0.06 | 0.16 | 0.06 | 0.01 | 0.02 | 0.05 | 0.08 | 0.05 | 0.02 |
| 0.01 | 0.03 | 0.07 | 0.03 | 0.01 | 0.01 | 0.04 | 0.05 | 0.04 | 0.01 |
| 0.01 | 0.02 | 0.01 | 0.01 | 0.01 | 0.00 | 0.01 | 0.02 | 0.01 | 0.00 |

Table 5.10: Model ACS SBC PSFs.

| SBC PSF at 120 nm | | | | | SBC PSF at 160 nm | | | | |
|-------------------|------|------|------|-------|-------------------|-------|-------|-------|-------|
| <0.01 | 0.01 | 0.01 | 0.01 | <0.01 | <0.01 | <0.01 | <0.01 | <0.01 | <0.01 |
| 0.01 | 0.02 | 0.03 | 0.02 | 0.01 | <0.01 | 0.02 | 0.04 | 0.02 | <0.01 |
| 0.01 | 0.03 | 0.15 | 0.03 | 0.01 | <0.01 | 0.04 | 0.20 | 0.04 | <0.01 |
| 0.01 | 0.02 | 0.03 | 0.02 | 0.01 | <0.01 | 0.02 | 0.04 | 0.02 | <0.01 |
| <0.01 | 0.01 | 0.01 | 0.01 | <0.01 | <0.01 | <0.01 | <0.01 | <0.01 | <0.01 |

5.6.3 Encircled Energy

In general, the ACS channels encircled energy distribution has been found to be within the original instrument specifications. Figure 5.9 and Figure 5.10 show the ACS encircled energy curves derived from on-orbit images. Tabulated values of the encircled energy for most filters are available in Sirianni et al. (2005PASP 117.1049).

5.6.4 Geometric Distortions

Geometric distortions produce a significant impact on the shape of the PSF in all three of the ACS channels, as can readily be seen in Figure 5.11 and Figure 5.12, which display WFC and HRC PSF images. The log stretch enhances the spider diffraction patterns, which the distortion renders non-perpendicular, and the outer Airy rings, which appear elliptical. The distortion owes primarily to the tilt of the focal surface to the chief ray at the large OTA field angles of the ACS apertures. The linear, field-independent approximation for the WFC produces a difference in plate scale of about 8% between the two diagonals of the field and, in the HRC and SBC, about a 16.5% difference in scale between orthogonal directions rotated about 20° from the aperture edges. Field-dependent distortions, measured as actual vs. predicted distances from field center, amount to about 2% peak in the WFC and about 1% in the HRC and SBC.

The distortions render the pixels, as projected on the sky, trapezoidal in shape and their area varies over the field by about 19% and 3.5% in the WFC and HRC/SBC, respectively. These variations have significant ramifications concerning appropriate techniques for flat-fielding and photometric calibration, especially when complicated by resampling in order to combine dithered image sets. Related issues are the manner in which the halation effects of the HRC and SBC detectors are removed and the treatment of spectra from the prisms and grism, which are not subject to the same distortion effects.

More details concerning geometric distortions in ACS can be found in [ACS ISR 2002-02](#) and [ACS ISR 2004-15](#). An introduction to *calacs*, and to *multidrizzle* which applies corrections for geometric distortion, is available on-line at:

<http://www.stsci.edu/hst/acs/analysis/multidrizzle>.

Figure 5.9: Encircled energy for the CCD channels.

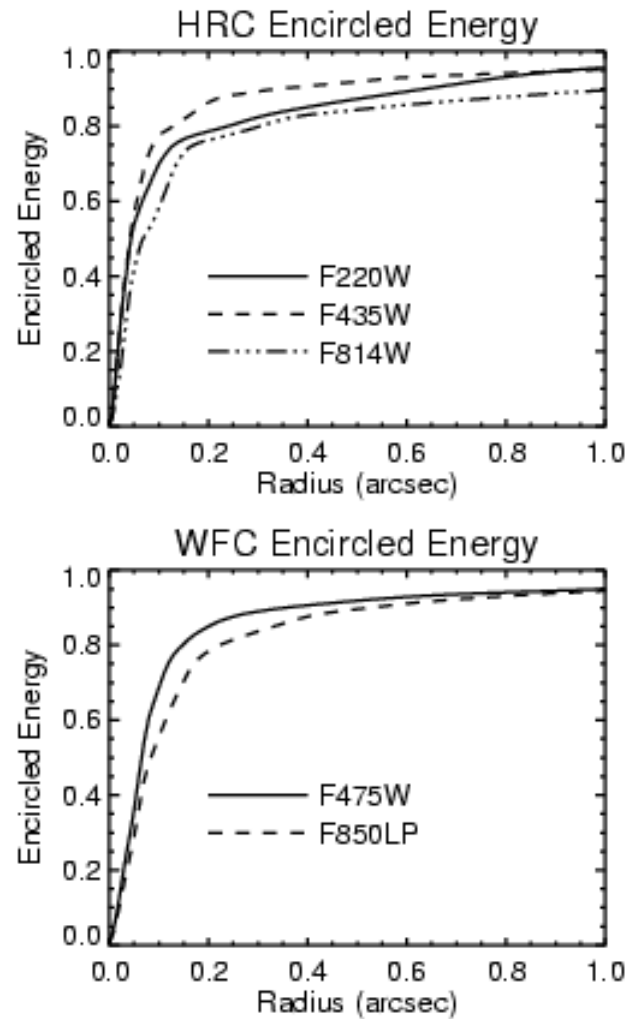


Figure 5.10: Encircled energy for the SBC.

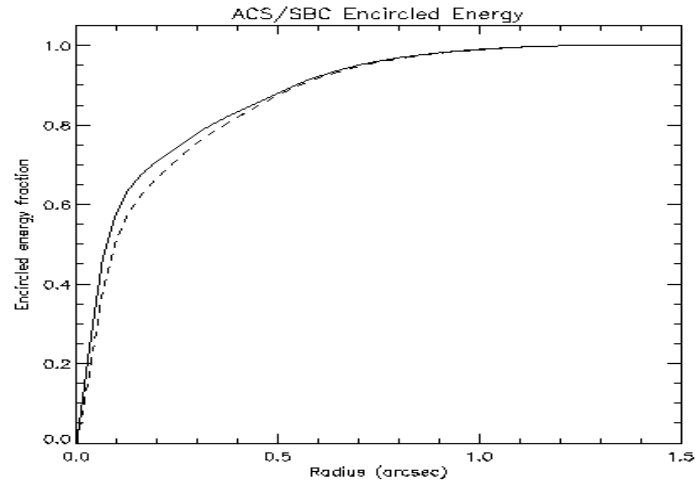


Figure 5.11: ACS WFC PSF - F625W.

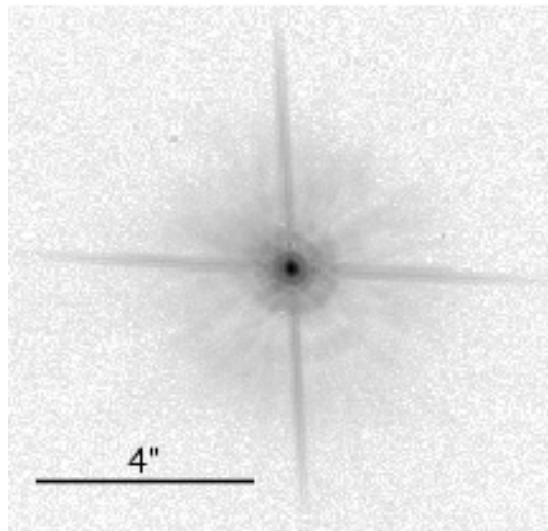
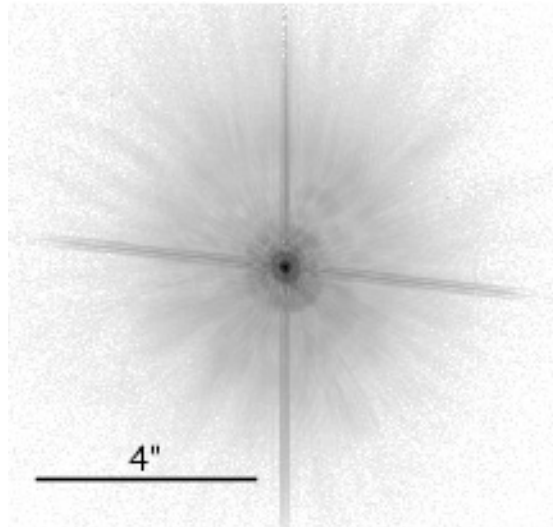


Figure 5.12: ACS HRC PSF - F625W.



5.6.5 PSFs at Red Wavelengths and the UV

The CCDs used in the HRC and WFC suffer from a halo that is caused by very red photons passing through the device and being scattered back into the detector by the mounting substrate. This creates a large halo in HRC images beyond 7000 Å and WFC images past 9000 Å. At 8000 Å in the HRC, the halo contains about 10% of the light. At 10,000 Å, it contains about 30% and increases the surface brightness of the PSF wings by over an order of magnitude, overwhelming the PSF diffraction rings and spikes. A discussion of this may be found in Gilliland & Riess, (2002) *HST Calibration Workshop* at:

http://www.stsci.edu/hst/HST_overview/documents/calworkshop/workshop2002/CW2002_Papers/CW02_gilliland.

In the F850LP filter, in particular, extremely red stars show a progressive loss of flux in small to moderate sized apertures as a function of color. A paper by Sirianni et al. (2005, astro-ph/0507614) is available at:

<http://adcam.pha.jhu.edu/instrument/photometry/sirianni.pdf>

See also Bohlin ACS ISR 2007-06. These papers provide a detailed recipe to correct for this effect. This halo effect is only partially treated by the [Exposure Time Calculator](#). Observers can use *synphot* (see Section 9.3.2) to accurately calculate the photometry of red sources in the SDSS z-filter.

Long wavelength photons that pass through the CCD can also be scattered by the electrode structure on the back side of the device and will create two spikes that extend roughly parallel to the x-axis. These spikes are seen at wavelengths longer than 9500 Å in both the HRC and WFC (see Figure 5.13 and Figure 5.14).

Figure 5.13: ACS WFC PSFs (10" x10"). FR914M images are saturated.

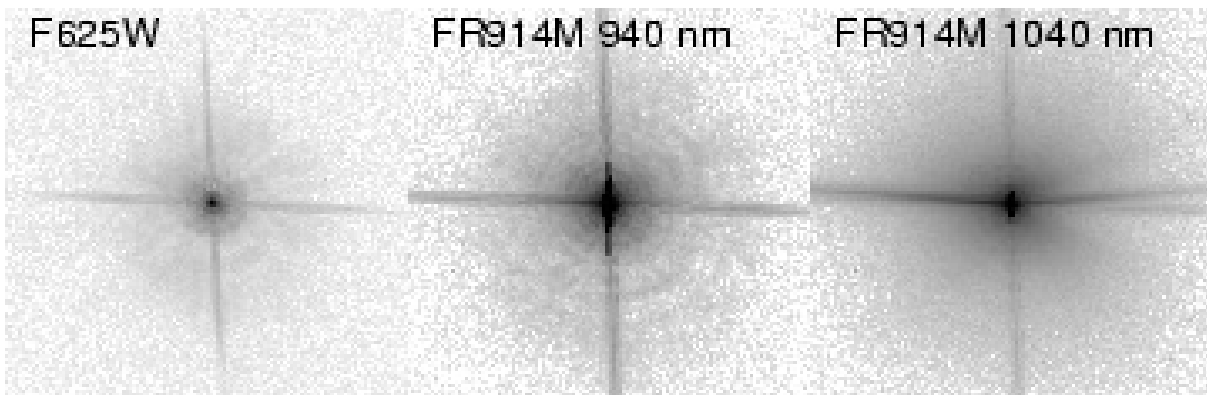
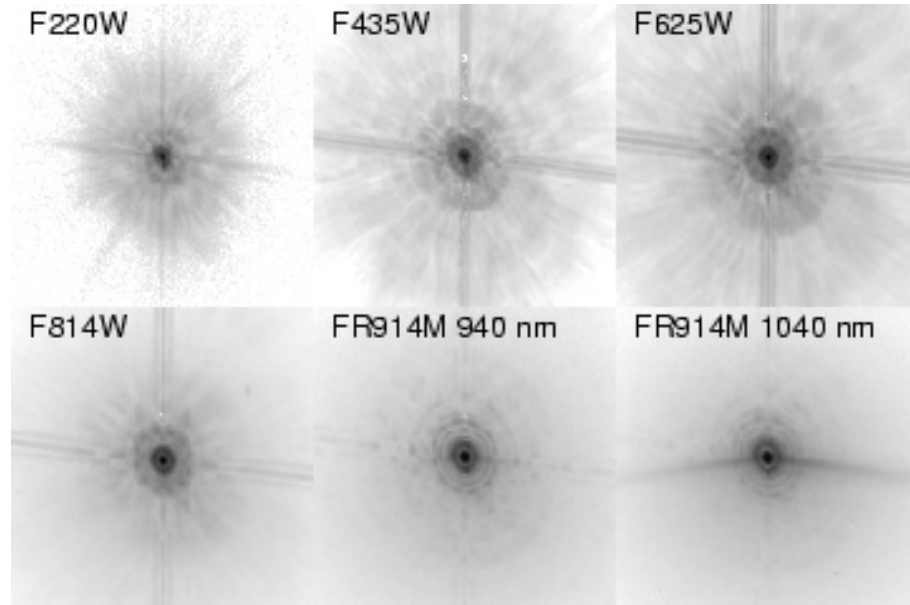


Figure 5.14: ACS HRC PSFs (3.25" x3.25").



In the UV the core of the PSF becomes rather asymmetrical due to midfrequency optical surface errors. In the SBC, a halo is created by charge migration at the microchannel plate surface. This effect, seen previously in STIS MAMA images, broadens the PSF core and redistributes a small portion of flux into a broad halo that can be approximated by a Gaussian with FWHM ~ 20 pixels. The peak flux for a point source centered on a pixel is reduced by 30% to 40% depending on wavelength.

The encircled energy curves presented in this handbook and incorporated into the ETC include all of the scattering effects discussed here.

5.6.6 Residual Aberrations

Residual aberration levels at the center of the field in each camera are $1/30$ wave (HRC) and $1/20$ wave (WFC) rms at 5500\AA (excluding defocus). Coma and astigmatism are minimized at the field center of each camera. The ACS PSF varies far less over the field of view than those of WFPC2 and STIS. WFPC2 especially suffers from a variable obscuration pattern that significantly alters the PSF structure depending on field position. Lacking the additional obscurations present in WFPC2, ACS PSF variations are instead due to changes in aberrations and charge diffusion.

At the extreme corners of the WFC field, increased astigmatism slightly elongates the PSF core. The axis of elongation rotates by 90° if the system passes through focus due to breathing. This may affect ellipticity measurements of small galaxies with bright cores at the field edges. Focus

variations in the WFC, which alter the amount of light in the peak, are largely due to detector surface height irregularities and amount to the equivalent of 5 microns of breathing (1/18 wave rms). The largest focus offset is along the gap between the two CCDs. Variations in the width of the PSF core are dominated by changes in CCD charge diffusion, which is dependent on the thickness of the detector (12 to 17 microns for the WFC). The PSF FWHM in F550M, for example, can vary by 20% (0.10 to 0.13 arcseconds) over the field.


The PSFs in the HRC and SBC are reasonably constant over their fields. The HRC FWHM is 0.060 to 0.073 arcseconds in F550M. More details on ACS PSF field variations are provided in [ACS ISR 2003-06](#). The [Tiny Tim](#) PSF simulator includes field dependent aberrations and charge diffusion and may be used to estimate the impact of these variations.



CHAPTER 6:

Polarimetry, Coronagraphy and Prism/Grism Spectroscopy

In this chapter. . .



| |
|------------------------------------|
| 6.1 Polarimetry / 79 |
| 6.2 Coronagraphy / 85 |
| 6.3 Grism/Prism Spectroscopy / 104 |

6.1 Polarimetry

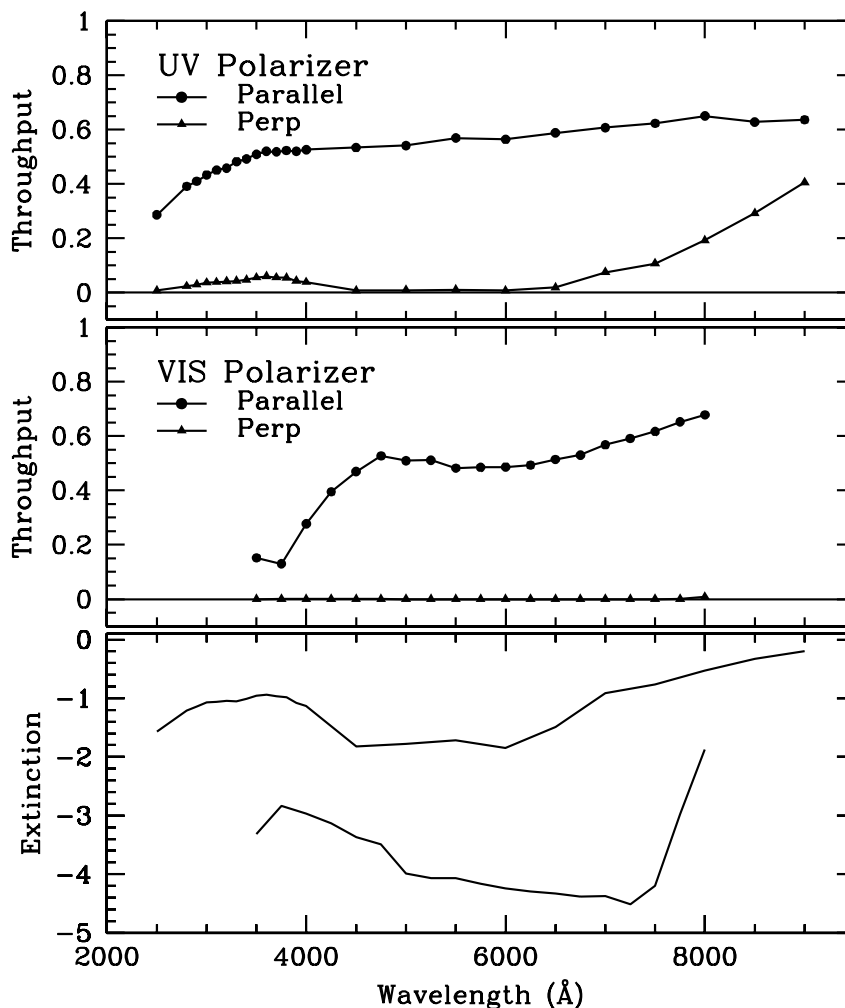
The ACS has an imaging polarimetric capability. Polarization observations require a minimum of three images taken using polarizing optics with different polarization characteristics in order to solve for the source polarization unknowns (polarization degree, position angle, and total intensity). To do this, ACS offers two sets of polarizers, one optimized for the blue (POLUV) and the other for the red (POLV). These polarizers can be used in combination with most of the ACS filters (see Table 6.2) allowing polarization data to be obtained in both the continuum and in line emission; and to perform rudimentary spectropolarimetry by using the polarizers in conjunction with the dispersing elements. (Due to the large number of possibilities in combination with ramp and dispersing elements, and heavy calibration overheads, observers wishing to use those modes should request additional calibration observations). For normal imaging polarization observations, the target remains essentially at rest on the

detector with a suitable filter in beam, and an image is obtained with each of the appropriate polarizing elements in turn. The intensity changes between the resulting images provide the polarization information.

Each set of polarizers comprises three individual polarizing filters with relative position angles 0° , 60° , and 120° . The polarizers are designed as aplanatic optical elements and are coated with “Polacoat 105UV” for the blue optimized set, and HN32 polaroid for the red set. The blue/near-UV optimized set is also effective all through the visible region, giving a useful operational range from approximately 2000 \AA to 8500 \AA . The second set is optimized for the visible region of the spectrum and is fully effective from 4500 \AA to about 7500 \AA .

The relative performance of the UV-optimized versus the visible optimized polarizers is shown in Figure 6.1.

Figure 6.1: Throughput and rejection of the ACS polarizers.



In the top two boxes, the upper curve is the parallel transmission, while the lower curve is the perpendicular transmission. The bottom panel shows the logarithm of the ratio of perpendicular to parallel transmission.

The visible polarizers clearly provide superior rejection for science in the 4500 Å to 7500 Å bandpass, while the UV optimized polarizers deliver lower overall rejection across a wider range from 2000 Å to 7500 Å. While performance of the polarizers begins to degrade at wavelengths longer than about 7500 Å, useful observations should still be achievable to approximately 8500 Å in the red. In this case, allowance for imperfect rejection of orthogonally polarized light should be made at the analysis stage.

Imperfections in the flat fields of the POLVIS polarizer set have been found which may limit the optimal field of view somewhat. Potential users are encouraged to check [ACS ISR 2005-10](#) the STScI [ACS Web site](#) for the latest information.

To first approximation, the ACS polarizers can be treated as three essentially perfect polarizers. The Stokes parameters (I, Q, U) in the most straightforward case of three images obtained with three perfect polarizers at 60° relative orientation, can be computed using simple arithmetic. Using *im1*, *im2*, and *im3* to represent the images taken through the polarizers POL0, POL60, and POL120 respectively, the Stokes parameters are as follows:

$$Q = \frac{2}{3}(2im1 - im2 - im3)$$

$$U = \frac{2}{\sqrt{3}}(im3 - im2)$$

$$I = \frac{2}{3}(im1 + im2 + im3)$$

These values can be converted to the degree of polarization P and the polarization angle θ , measured counterclockwise from the x axis as follows:

$$P = \frac{\sqrt{Q^2 + U^2}}{I}$$

$$\theta = \frac{1}{2}\tan^{-1}(U/Q)$$

A more detailed analysis, including allowance for imperfections in the polarizers may be found in Sparks & Axon, 1999 *PASP*, **111**, 1298. They find that the important parameter in experiment design is the product of expected polarization degree and signal-to-noise. A good approximation for the case of three perfect polarizers oriented at the optimal 60° relative

position angles (as in ACS) is that the error on the polarization degree P (which lies in the range 0 for unpolarized to 1 for fully polarized) is just the inverse of the signal-to-noise per image. Specifically, they found

$$\log\left(\frac{\sigma_P}{P}\right) = -0.102 - 0.9898 \log(P \langle S/N \rangle_i)$$

where $\langle S/N \rangle_i$ is the signal-to-noise of the i^{th} image; and

$$\log \sigma_\theta = 1.514 - 1.068 \log(P \langle S/N \rangle_i)$$

The above discussion is for ideal polarizers with no instrumental polarization. Of course, the reality is that the polarizer filters, especially the UV polarizer, has significant leakage of cross-polarized light. The instrumental polarization of the HRC ranges from a minimum of 4% in the red to 14% in the far-UV, while that of the WFC is $\sim 2\%$ (see [ACS ISR 2004-09](#)). Other effects, such as phase retardance in the mirrors, may be significant as well. Please consult the *ACS Data Handbook* at:

http://www.stsci.edu/hst/acs/documents/handbooks/DataHandbookv4/ACS_longdnhbcover.html,

the STScI Web pages, and ISRs for more detailed information at:

<http://www.stsci.edu/hst/acs/documents/isrs>.

The implementation of the ACS polarizers is designed for ease of use. The observer merely selects the camera (either HRC or WFC) and the spectral filter, and then takes images stepping through the three filters of either the VIS set (POL0V, POL60V, POL120V) or the UV set (POL0UV, POL60UV, POL120UV). Once the camera and polarizer are specified, the scheduling system automatically generates slews to place the target in the optimal region of the field of view.

Since the ACS near-UV and visible filter complement is split between two filter wheels, there are restrictions on which filters the polarizer sets can be combined with. The choices available were determined by the relative performance of the polarizers and the near-UV limitations of the WFC resulting from the silver mirror coatings.

The near-UV optimized polarizers are mounted on Filter Wheel 1 and may be crossed with the near-UV filter complement, which are mounted on Filter Wheel 2. The visible optimized polarizers are mounted on Filter Wheel 2 and can be crossed with filters on Filter Wheel 1, namely the primary broadband filters, and discrete narrowband filters $H\alpha$, [OII], and their continuum filters. Due to the calibration overhead required, we do not plan to support the use of ramp filters with either polarizer set. GOs are required to include calibration observations if they plan to use the ramp filters with the polarizers.

The polarizer sets are designed for use on the HRC where they offer a full unvignetted field of view, 29×26 arcseconds with any of the allowable filter and coronagraph combinations including those ramps and spectroscopic elements that may also be used on the HRC (although see above re. additional calibrations).

The same allowable combinations, either UV or visible optimized, may also be used on the WFC where an unvignetted field of view of diameter 70 arcseconds is obtained. This does not fill the field of view of the WFC due to the small size of the polarizing filters. However, it does offer an area approximately five times larger than that obtained on the HRC. In order to avoid the gap between the WFC CCDs, and to optimize the readout noise and CTE effects, the scheduling system will automatically slew the target to roughly pixel (3096,1024) on the WFC1 CCD whenever the WFC aperture is selected in conjunction with one of the polarizers. Also, to reduce camera overhead times, only a 2048 x 2048 subimage centered on the target location will be readout from WFC1 (see Table 6.1).

Occasionally observers will ask to obtain non-polarized images at the same physical location on the detector as their polarized images. This is straightforward for the HRC; one merely takes the exposure without the polarizer filter. However, for the WFC it is more complicated because specifying WFC together with a polarizer automatically invokes a large slew, whereas no slew is performed when the polarizer filter is omitted. To obtain a non-polarizer image at the same physical detector location as the polarizer image in the WFC, one needs to specify the aperture as WFC1-2K instead of WFC (see Table 6.1).

Table 6.1: Examples of polarizer and non-polarizer exposures in a Phase II proposal.

| Aperture | Filters | Comment |
|----------|----------------|---|
| HRC | F606W, POL0V | 1024 x 1024 image centered at usual HRC aperture. |
| HRC | F606W, POL60V | Same but with POL60V. |
| HRC | F606W, POL120V | Same but with POL120V. |
| HRC | F606W | Non-polarizer image centered at same detector location as polarizer exposure. |
| WFC | F606W, POL0V | Target automatically placed at WFC1 pixel (3096,1024); 2048 x 2048 image. |
| WFC | F606W, POL60V | Same but with POL60V. |
| WFC | F606W, POL120V | Same but with POL120V. |
| WFC1-2K | F606W | Non-polarizer image at same detector location. Target at WFC1 pixel (3096,1024); 2048 x 2048 image. |

Table 6.2: Filters that can be used in conjunction with the ACS polarizers.

| Polarizer set | Filters | Filter comments |
|---------------|---------|-----------------|
| POL0UV | F220W | HRC NUV short |
| POL60UV | F250W | HRC NUV long |
| POL120UV | F330W | HRC U |
| | F435W | Johnson B |
| | F814W | Broad I |
| POL0V | F475W | SDSS g |
| POL60V | F606W | Johnson V |
| POL120V | F625W | SDSS r |
| | F658N | H α |
| | F775W | SDSS i |

The filters specified in Table 6.2 are those that we expect users to choose for their polarization observations. We will calibrate the most popular of these filters. Filter combinations not on this list will most probably not be calibrated, so potential users who have a strong need for such a polarizer/filter combination should include any necessary calibrations in their proposals.

We anticipate that the most accurate polarization observations will be obtained in the visible band (i.e., F606W) with the HRC and the visible polarizers. This mode has the advantages of a very high rejection of perpendicular polarization, and known mirror coatings with readily modeled properties. The WFC may be capable of similar accuracy to the HRC; however, its proprietary mirror coatings will make modeling of the polarization properties, and hence calibration, much more difficult (e.g., unknown phase retardance effects in the WFC IM3 mirror are a concern).

Polarimetry in the UV will be more challenging for a number of reasons. The UV polarizer has relatively poor rejection in the UV, and the instrumental polarization of the HRC, which is 4% to 7% in the visible, rises to 8% to 9% in the UV, and reaches 14% at 2200 Å (see [ACS ISR 2004-09](#)). Far-UV polarimetry will be especially challenging since the polarizer properties were not well-characterized shortwards of 2800 Å, and appear to change rapidly with wavelength. Moreover, the low UV transmission of the UV polarizer, and the poor polarization rejection in the far-red, work together to exacerbate red leaks which are normally seen in the far-UV spectral filters.

The polarizer filters contribute a weak geometric distortion which rises to about 0.3 pixels near the edges of the HRC field-of-view. This is caused by a weak positive lens in the polarizers, which is needed to maintain proper focus when multiple filters are in the beam. In addition, the visible polarizer has a weak ripple structure which is related to manufacture of its polaroid material; this contributes an additional ± 0.3 pixel distortion with a very complex structure (see [ACS ISR 2004-10](#) and [ACS ISR 2004-11](#)). All these geometric effects are correctable with the drizzle software. However, astrometry will likely be less accurate in the polarizers due to residual errors and imperfect corrections.

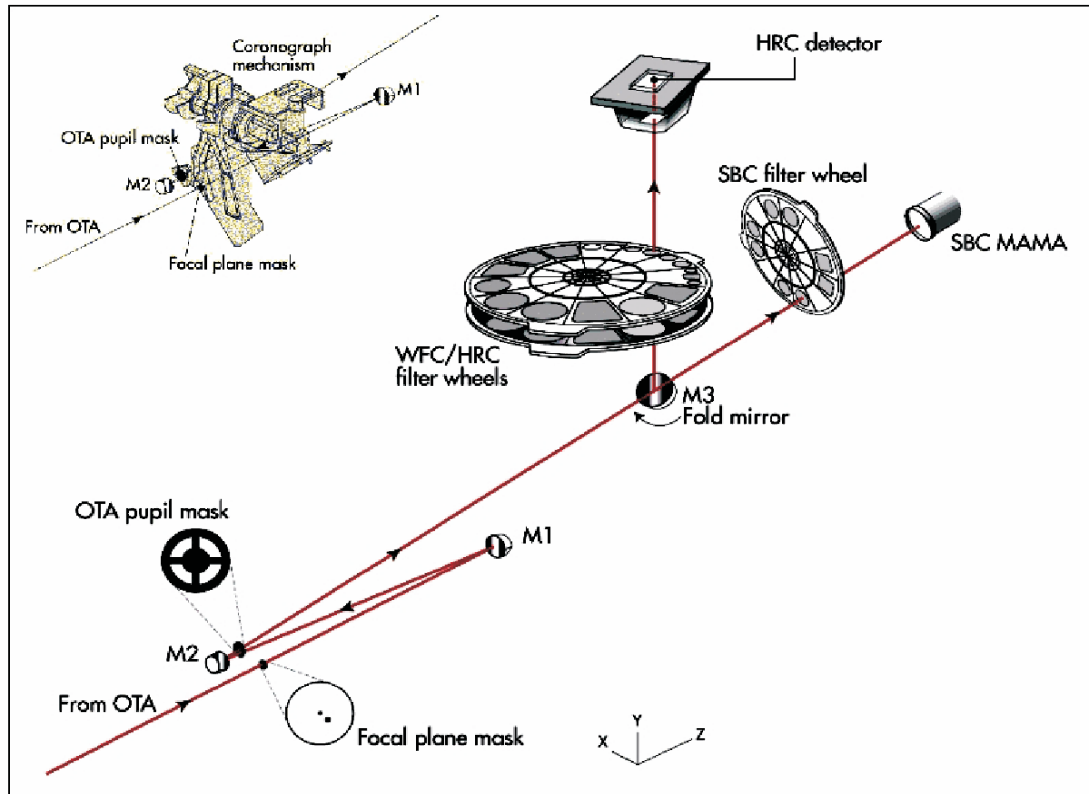
Bubbles in the Visible Polarizers

The POL0V and POL60V filters contain bubbles which impact the PSF and flat fields. These bubbles are far out of focus, and hence appear as large patterns (400 pixels diameter in WFC, 370 pixels in HRC) of concentric bright and dark rings, and streaks in the flats. The worst case is the HRC in the POL60V filter, where the amplitude reaches $\pm 4\%$ in the flats; the affected region for this case is roughly centered at pixel (835,430). Other combinations involving the POL0V filter or the WFC show more minor effects, with amplitudes typically $\pm 1\%$. Observers requiring precision polarimetry would do well to avoid these regions of the field of view. While the polarizer flats attempt to correct these features (see [ACS ISR 2005-10](#)), the corrections are likely to be imperfect and depend somewhat on the illumination provided by the target (i.e., stellar vs. extended target, etc.). The locations of these features and their effects can be discerned more accurately by examining the "pfl" flats for the respective spectral filter crossed with the visual polarizers.

6.2 Coronagraphy

The ACS High Resolution Camera has a user-selectable coronagraphic mode for imaging faint objects (circumstellar disks, substellar companions) near bright point sources (stars or luminous quasar nuclei). The coronagraph suppresses the diffraction spikes and rings of the occulted source below the level of the scattered light, most of which is caused by surface errors in the HST optics. The coronagraph was added after ACS construction began, at which point it was impossible to insert it into the aberration-corrected beam. Instead, the system is deployed into the aberrated beam, which is subsequently corrected by the ACS optics. Although it is not as efficient as a corrected-beam coronagraph (especially for imaging close to the occulted source) the HRC coronagraph significantly improves the high-contrast imaging capabilities of HST. Care must be taken, however, to design an observation plan that properly optimizes the coronagraph's capabilities and accounts for its limitations.

Figure 6.2: Schematic layout of the ACS HRC coronagraph.



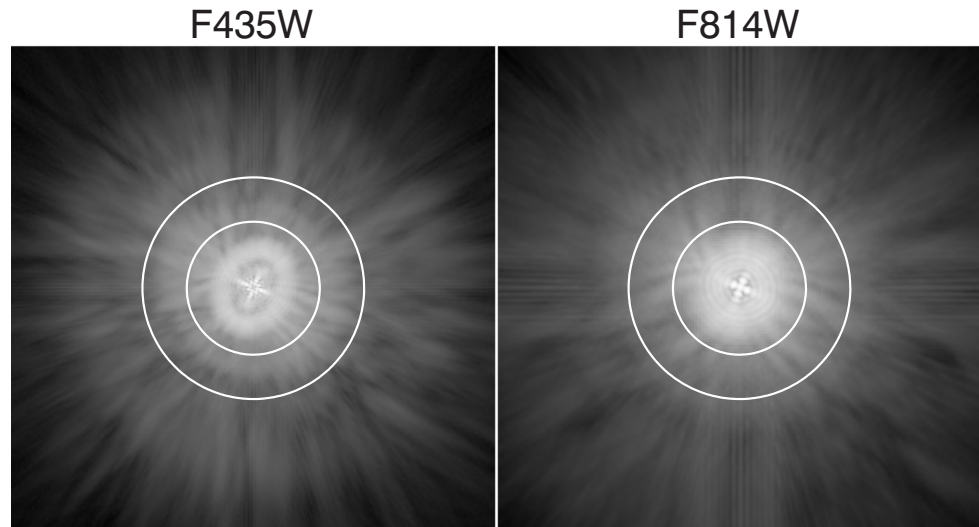
The upper left inset shows a schematic of the coronagraph mechanism that can be flipped in-and-out of the HRC optical path.

6.2.1 Coronagraph Design

A schematic layout of the ACS coronagraph is shown in Figure 6.2. The aberrated beam from the telescope first encounters one of two occulting spots. The beam continues to the M1 mirror, which forms an image of the HST entrance pupil on the M2 mirror, which corrects for the spherical aberration in the HST primary mirror. The coronagraph's Lyot stop is placed in front of M2. A fold mirror directs the beam onto the CCD detector. The field is 29×26 arcseconds with a mean scale of 0.026 arcseconds/pixel. Geometric distortion results in effectively non-square pixels. The coronagraph can be used over the entire HRC wavelength range of $\lambda = 2000 \text{ \AA}$ to $10,000 \text{ \AA}$ using a variety of broad-to-narrowband filters.

The occulting spots are placed in the plane of the circle of least confusion of the converging aberrated beam. The balance of defocus and spherical aberration at this location allows maximal occulted flux and minimal spot radius. The angular extent of the PSF in this plane necessitates larger spots than would be used in an unaberrated beam (Figure 6.3).

Figure 6.3: Simulated point spread functions at the plane of the occulting spots through filters F435W and F814W, shown with logarithmic intensity scaling.



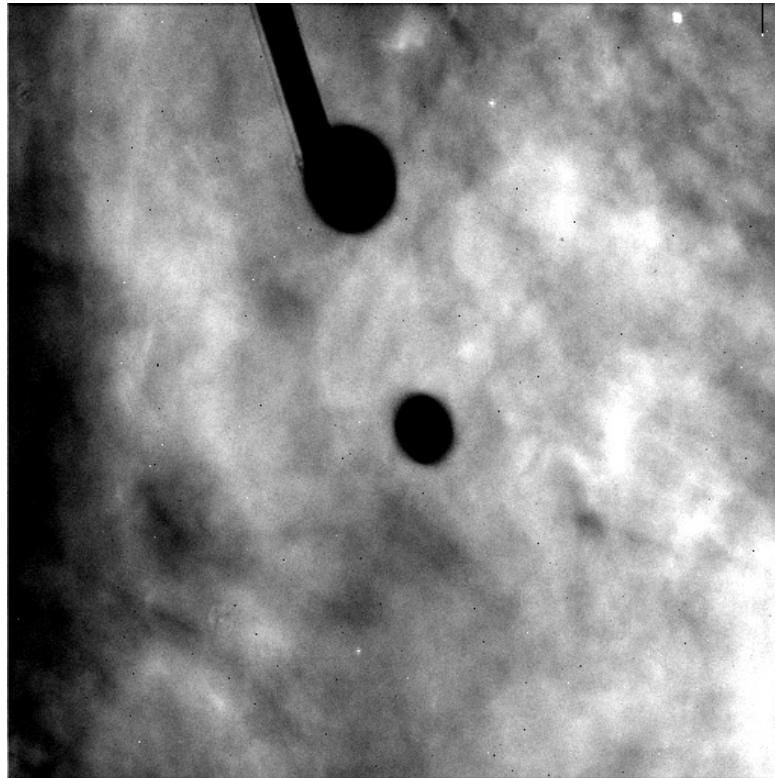
The elliptical, cross-shaped patterns in the cores are due to astigmatism at the off-axis ACS aperture. The astigmatism is corrected later by the ACS optics. The sizes of the two occulting spots ($D=1.8$ arcseconds and 3.0 arcseconds) are indicated by the white circles.

The occulting spots are solid (unapodized) metallic coatings deposited on a glass substrate that reduces the throughput by 4.5%. The smaller spot is 1.8 arcseconds in diameter and is at the center of the field. Its aperture name is CORON-1.8. The second spot, 3.0 arcseconds in diameter, is near the edge of the field (Figure 6.4) and is designated as aperture CORON-3.0. The smaller spot is used for the majority of the coronagraphic observations, as it allows imaging closer to the occulted source. The larger spot may be used for very deep imaging of bright targets with less saturation around the spot than would occur with the smaller spot. Its position near the edge of the field also allows imaging of material out to 20 arcseconds from the occulted source.

The Lyot stop is located just in front of the M2 aberration correction mirror, where an image of the HST primary is formed. The stop is a thin metal mask that covers all of the diffracting edges in the HST OTA (outer aperture, secondary mirror baffle, secondary mirror support vanes, and primary mirror support pads) at the reimaged pupil. The sizes of the Lyot stop and occulting spots were chosen to reduce the diffracted light below the level of the scattered light, which is unaltered by the coronagraph. The smaller aperture and larger central obscuration of the Lyot stop reduce the throughput by 48% and broaden the field PSF. The spots and Lyot stop are located on a panel attached to the ACS calibration door mechanism, which allows them to be flipped out of the beam when not in use. The inside surface of this door can be illuminated by a lamp to provide flat field calibration images for direct imaging. However, this configuration prevents the acquisition of internal coronagraphic flat fields.

In addition to the occulting spots and Lyot stop there is a 0.8 arcseconds \times 5 arcseconds occulting finger (OCCULT-0.8) permanently located at the window of the CCD dewar. It does not suppress any diffracted light because it occurs after the Lyot stop. Its intended purpose was to allow imaging closer to stars than is possible with the occulting spots while preventing saturation of the detector. However, because the finger is located some distance from the image plane, there is significant vignetting around its edges, which reduces its effectiveness. It was originally aligned with the center of the 3.0 arcsecond spot, but shifting of the spots during launch ultimately placed the finger near the edge of the spot. Because of vignetting and the sensitivity of the occulted PSF to its position behind the finger, unocculted saturated observations of sources will likely be more effective than those using the occulting finger.

Figure 6.4: Region of the Orion Nebula imaged with the coronagraph and filter F606W.



The silhouettes of the occulters can be seen against the background nebulosity. The 1.8 arcsecond spot is located at the center and the 3.0 arcsecond spot towards the top. The finger is aligned along one edge of the larger spot. This image has not been corrected for geometric distortion, so the spots appear elliptical.

6.2.2 Acquisition Procedure and Pointing Accuracy

The bright point source must be placed precisely behind the occulting spot to ensure the proper suppression of the diffracted light. The absolute pointing accuracy of HST is about 1 arcsecond, which is too crude to ensure accurate positioning behind the spot. An on-board acquisition procedure is used to provide better alignment. The observer must request an acquisition image immediately before using the coronagraph and must specify a combination of filter and exposure time that provides an unsaturated image of the source. To define an acquisition image in APT, specify HRC-ACQ as the aperture and ACQ as the opmode.

Acquisition images are taken with the coronagraph deployed. The bright source is imaged within a predefined 200 x 200 pixel (5 x 5 arcseconds) subarray near the small occulting spot. Two identical exposures are taken, each of the length specified by the observer (rather than each being half the length specified, as they would be for a conventional CR-SPLIT). From these two images, the on-board computer selects the minimum value for each pixel as a crude way of rejecting cosmic rays. The result is then smoothed with a 3 x 3 pixel boxcar and the maximum pixel in the subarray is identified. The centroid of the unsmoothed image is then computed within a 5 x 5 pixel box centered on this pixel. Based on this position, the telescope is then slewed to place the source behind the occulting spot.

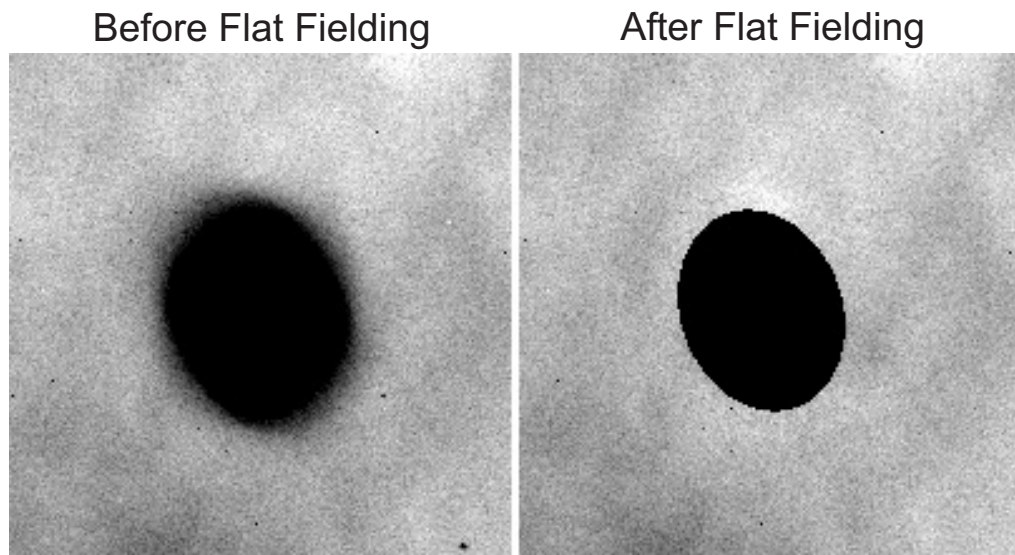
Because the coronagraph is deployed during acquisition, throughput is decreased by 52.5% relative to a non-coronagraphic observation. Also, the Lyot stop broadens the PSF, resulting in a lower relative peak pixel value (see Section 6.2.6). Care must be taken to select a combination of exposure time and filter that avoids saturating the source but provides enough flux for a good centroid measurement. A peak pixel flux of 2000 e⁻ to 50,000 e⁻ is desirable. The HRC saturation limit is ~140,000 e⁻. Narrowband filters can be used, but for the brightest targets crossed filters are required. Allowable filter combinations for acquisitions are F220W+F606W, F220W+F550M, and F220W+F502N, in order of decreasing throughput. Be warned that the calibration of these filter combinations is poor, so estimated count rates from *synphot* or the APT ETC may be high or low by a factor of two.

Multiple on-orbit observations indicate that the combined acquisition and slew errors are on the order of ±0.25 pixels (±6 milliarcseconds). While small, these shifts necessitate the use of subpixel registration techniques to subtract one coronagraphic PSF from another (Section 6.2.5). The position of the spots relative to the detector also varies over time. This further alters the PSF, resulting in subtraction residuals.

6.2.3 Vignetting and Flat Fields

ACS coronagraphic flat fields differ from the standard flats because of the presence of the occulting spots and alteration of the field vignetting by the Lyot stop. The large angular size of the aberrated PSF causes vignetting beyond one arcsecond of the spot edge (Figure 6.4), which can be corrected by dividing the image by the spot pattern (Figure 6.5). To facilitate this correction, separate flat fields have been derived that contain just the spot patterns (spot flats) and the remaining static features (P-flats). For a full discussion see [ACS ISR 2004-16](#).

Figure 6.5: Region of the Orion Nebula around the $D = 1.8$ arcseconds spot.



(Left) The spot edge appears blurred due to vignetting. The image has not been geometrically corrected. (Right) The same region after the image has been corrected by dividing the flat field. The interior of the spot has been masked.

The ACS data pipeline will divide images by the P-flat. P-flats specific to the coronagraph have been derived from either ground-based or on-orbit data for filters F330W, F435W, F475W, F606W, and F814W. Other filters use the normal flats, which may cause some small-scale errors around dust diffraction patterns. The pipeline then divides images by the spot flat, using a table of spot positions versus date to determine the proper shift for the spot flat. However, there is a lag in determining the spot position, so it may be a month after the observation before the pipeline knows where the spot was on that date. So, coronagraph users should note that their data may be calibrated with an incorrect spot flat if they extract their data from the archive soon after they were taken. (Spot flats for the filters listed above are available for download from the [ACS reference files Web page](#). For other filters, the available spot flat closest in wavelength should be used. The spot

flat must be shifted by an amount listed on the reference files page to account for motions of the occulting spots.)

Because coronagraphic P-flats and spot flats exist only for the few filters listed above, observers are encouraged to use those filters. It is unlikely that coronagraphic flat fields for other filters will be available in the future.

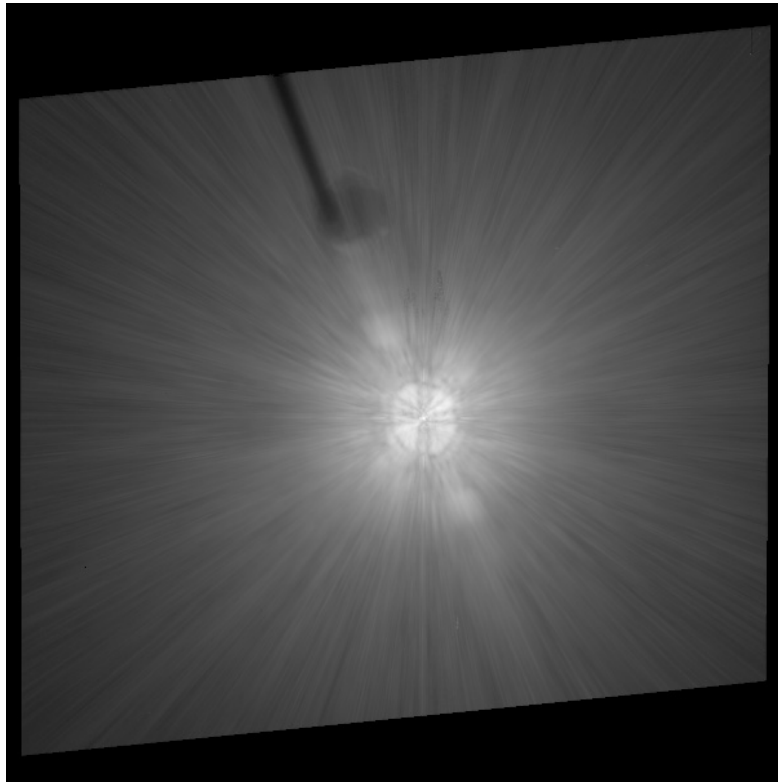
6.2.4 Coronagraphic Performance

Early in Cycle 11, coronagraphic performance verification images were taken of the $V = 0$ star Arcturus (Figure 6.6 and Figure 6.7). This star has an angular diameter of 25 milliarcseconds and is thus unresolved by the coronagraph. The coronagraphic image of a star is quite unusual. Rather than appearing as a dark hole surrounded by residual light, as would be the case in an aberration-free coronagraph, the interior of the spot is filled with a diminished and somewhat distorted image of the star. This image is caused by the M2 mirror's correction of aberrated light from the star that is not blocked by the spot. The small spot is filled with light, while the large one is relatively dark. Broad, ring-like structures surround the spots, extending their apparent radii by about 0.5 arcseconds. These rings are due to diffraction of the wings of the aberrated PSF by the occulting spot itself. Consequently, coronagraphic images of bright stars may saturate at the interior and edges of the spot within a short time. Within the small spot, the brightest pixels will saturate in less than one second for a $V = 0.0$ star, while pixels at edge of the larger spot will saturate in about 14 seconds.

The measured radial surface brightness profiles (Figure 6.8) show that the coronagraph is well aligned and operating as expected. The light diffracted by the HST obscurations is suppressed below the level of the scattered light – there are no prominent diffraction spikes, rings, or ghosts beyond the immediate proximity of the spots. At longer wavelengths ($\lambda > 6000 \text{ \AA}$) the diffraction spikes appear about as bright as the residual scattered light because the diffraction pattern is larger and not as well suppressed by the coronagraph. The spikes are more prominent in images with the large spot than the small one because the Lyot stop is not located exactly in the pupil plane but is slightly ahead of it. Consequently, the beam can “walk” around the stop depending on the field angle of the object. Because the large spot is at the edge of the field, the beam is slightly shifted, allowing more diffracted light to pass around the edges of the stop.

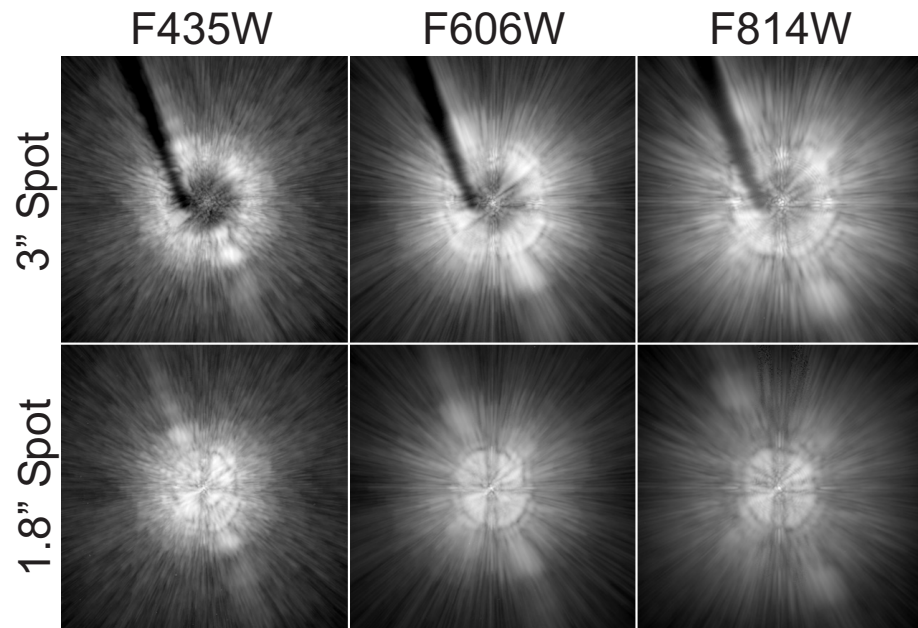
The coronagraphic PSF is dominated by radial streaks that are caused primarily by scattering from zonal surface errors in the HST mirrors. This halo increases in brightness and decreases in size towards shorter wavelengths. One unexpected feature is a diagonal streak or “bar” seen in both direct and coronagraphic images. It is about 5 times brighter than the mean azimuthal surface brightness in the coronagraphic images. This structure was not seen in the ground-test images and is likely due to scattering introduced by the HST optics. There appears to be a corresponding feature in STIS as well.

Figure 6.6: Geometrically corrected (29 arcseconds across) image of Arcturus observed in F814W behind the 1.8 arcseconds spot.



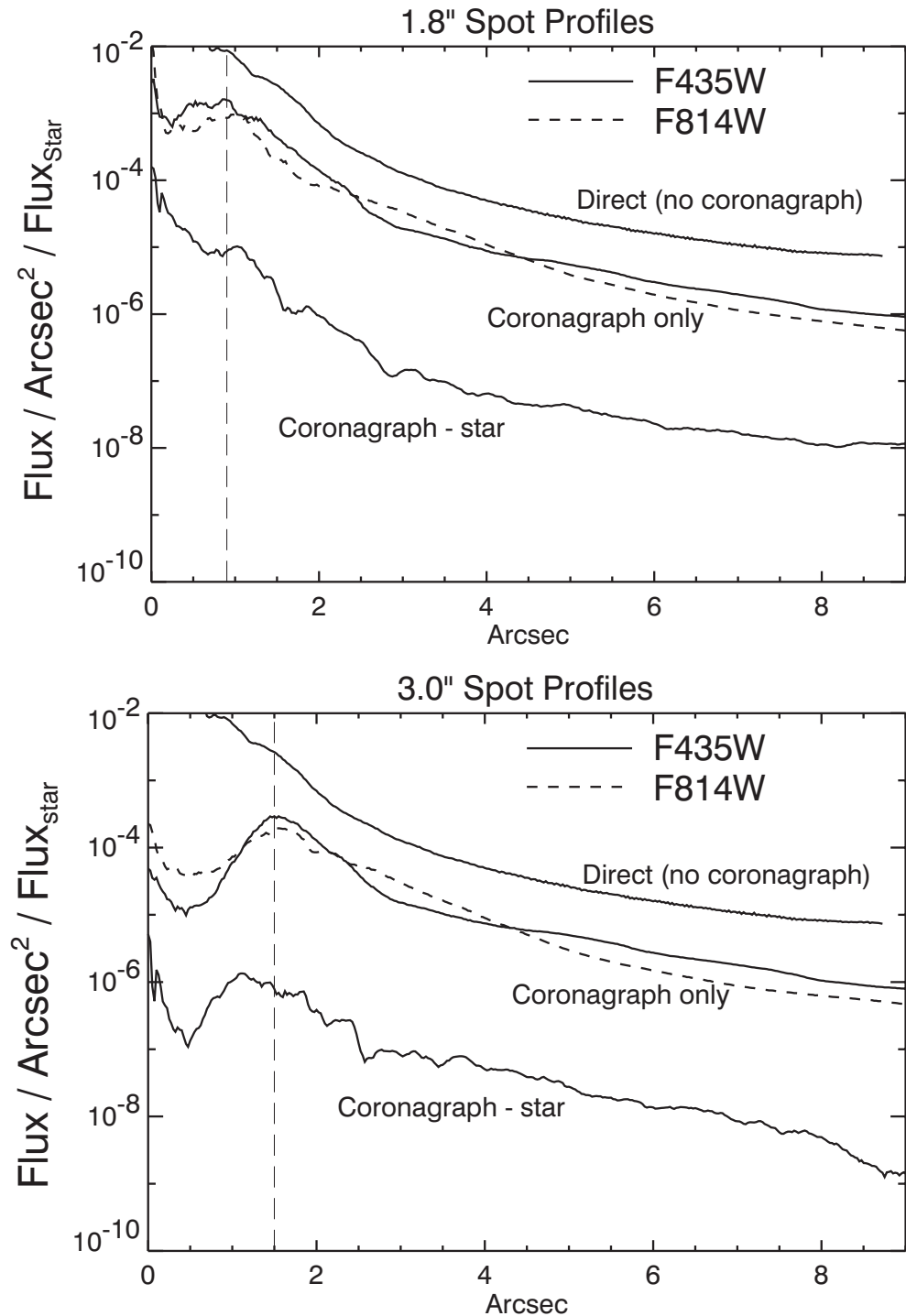
This is a composite of short, medium, and long (280 seconds) exposures. The “bar” can be seen extending from the upper left to lower right. The shadows of the occulting finger and large spot can be seen against the scattered light background. Logarithmic intensity scale.

Figure 6.7: Regions around the occulting spots in different filters.



The occulting finger can be seen in the 3 arcseconds spot images. Logarithmic intensity scaled.

Figure 6.8: Surface brightness plots derived by computing the median value at each radius.



The brightness units are relative to the total flux of the star. The direct profile is predicted; the coronagraphic profiles are measured from on-orbit images of Arcturus. "Coronagraph-star" shows the absolute median residual level from the subtraction of images of the same star observed in separate visits.

6.2.5 Subtraction of the coronagraphic PSF

While the coronagraph suppresses the diffracted light from a bright star, the scattered light still overwhelms faint, nearby sources. It is possible to subtract most of the remaining light using an image of another occulted star. PSF subtraction has been successfully used with images taken by other HST cameras, with and without a coronagraph. The quality of the subtraction depends critically on how well the target and reference PSFs match.

As mentioned above, for any pair of target and reference PSF observations, there is likely to be a difference of 5 to 20 milliarcseconds between the positions of the stars. Because the scattered light background is largely insensitive to small errors in star-to-spot alignment (it is produced before the coronagraph), most of it can be subtracted if the two stars are precisely registered and normalized. Due to the numerous sharp, thin streaks that form the scattered light background, subtraction quality is visually sensitive to registration errors as small as 0.03 pixels (0.75 milliarcseconds). To achieve this level of accuracy, the reference PSF may be iteratively shifted and subtracted from the target until an offset is found where the residual streaks are minimized. This method relies on the judgment of the observer, as any circumstellar material could unexpectedly bias a registration optimization algorithm. A higher-order sampling method, such as cubic convolution interpolation, should be used to shift the reference PSF by subpixel amounts; simpler schemes such as bilinear interpolation degrade the fine PSF structure too much to provide good subtractions.

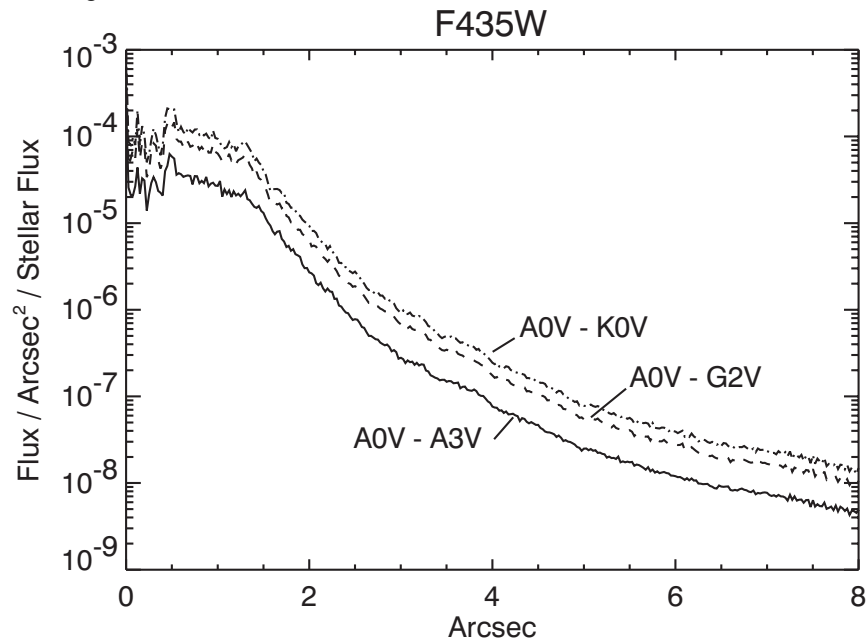
Normalization errors as small as 1% to 4% between the target and reference stars may also create significant subtraction residuals. However, derivation of the normalization factors from direct photometry is often not possible. Bright, unocculted stars will be saturated in medium or broadband filters at the shortest exposure time (0.1 seconds). An indirect method uses the ratio of saturated pixels in unocculted images (the accuracy improves with greater numbers of saturated pixels). A last-ditch effort would rely on the judgment of the observer to iteratively subtract the PSFs while varying the normalization factor.

In addition to registration offsets, positional differences can alter the diffraction patterns near the spots' edges. The shape and intensity of these rings are very sensitive to the location of the star relative to the spot. They cannot be subtracted by simply adjusting the registration or normalization. These errors are especially frustrating because they increase the diameter of the central region where the data are unreliable. The only solution to this problem is to observe the target and reference PSF star in adjacent orbits without flipping the masks out of the beam between objects.

Color differences between the target and reference PSFs can be controlled by choosing an appropriate reference star. As wavelength increases, the speckles that make up the streaks in the coronagraphic PSF

move away from the center while their intensity decreases (Figure 6.7). The diffraction rings near the spot edges will expand as well. These effects can be seen in images through wideband filters – a red star will appear to have a slightly larger PSF than a blue one. Thus, an M-type star should be subtracted using a similarly red star – an A-type star would cause significant subtraction residuals. Even the small color difference between A0 V and B8 V stars, for example, may be enough to introduce bothersome errors (Figure 6.9).

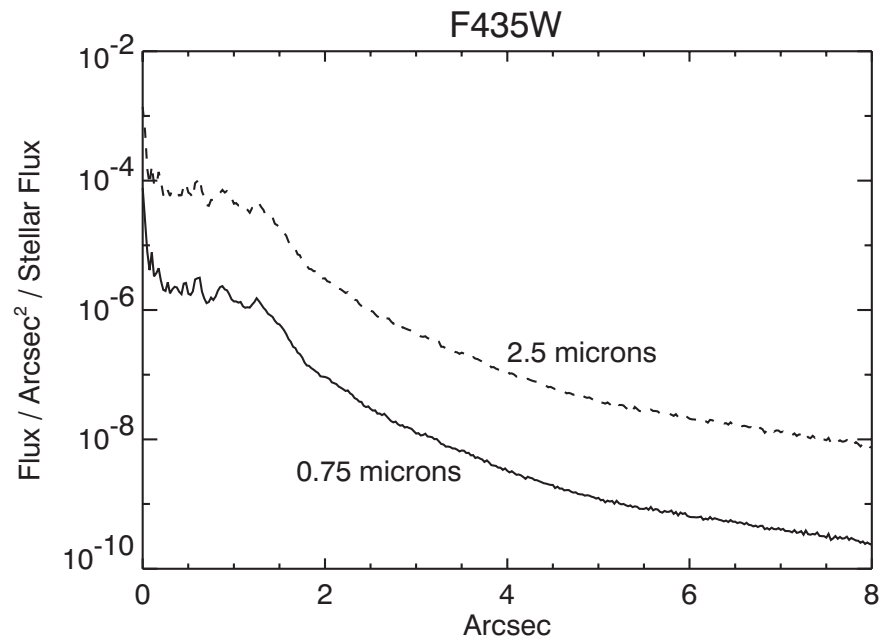
Figure 6.9: Predicted absolute mean subtraction residual levels for cases where the target and reference stars have mismatched colors.



The brightness units are relative to the total flux of the target star.

A focus change can also alter the distribution of light in the PSF. HST's focus changes over time scales of minutes to months. Within an orbit, the separation between the primary and secondary mirrors varies on average by $3 \mu\text{m}$, resulting in $1/28$ wave rms of defocus @ $\lambda = 5000 \text{ \AA}$. This effect known as *breathing* is caused by the occultation of the telescope's field of view by the warm Earth, which typically occurs during half of each 96-minute orbit. This heats HST's interior structure, which expands. After occultation the telescope gradually shrinks. Changes relative to the sun (mostly anti-sun pointings) cause contraction of the telescope, which gradually expands to "normal" size after a few orbits. The main result of these small focus changes is the redistribution of light in the wings of the PSF (Figure 6.10).

Figure 6.10: Predicted absolute mean subtraction residual levels for cases where the target and reference stars are imaged at different breathing-induced focus positions.



The offset (0.75 or 2.5 mm) from perfect focus (0 mm) is indicated with respect to the change in primary-secondary mirror separation. The typical breathing amplitude is 3 to 4 mm within an orbit. The brightness units are relative to the total flux of the target star.

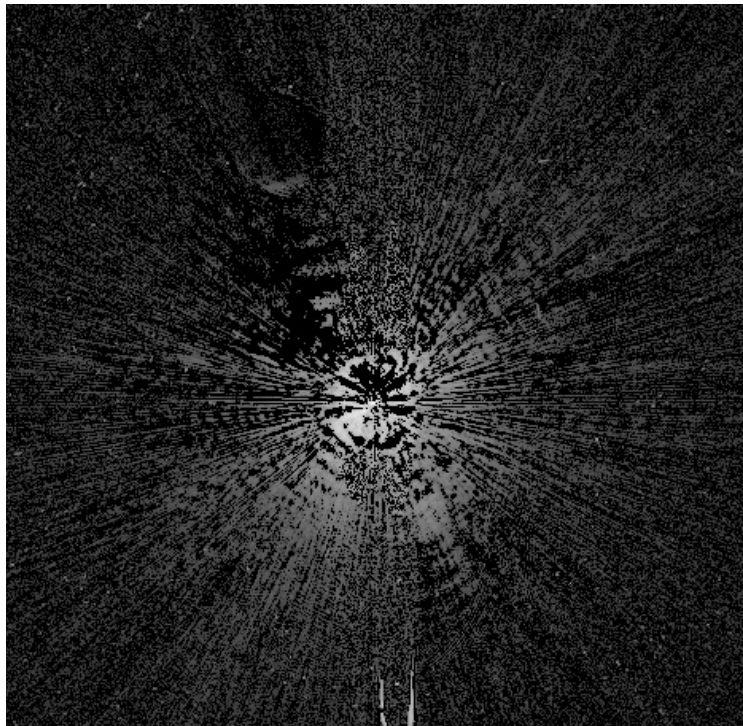
Plots of the azimuthal median radial profiles after PSF subtraction are shown in Figure 6.8. In these cases, images of Arcturus were subtracted from similar images of the star taken a day later. The images were registered as previously described. Combined with PSF subtraction, the coronagraph reduces the median background level by 250x to 2500x, depending on the radius and filter. An example of a PSF subtraction is shown in Figure 6.11. The mean of the residuals is not zero. Because of PSF mismatches, one image will typically be slightly brighter than the other over a portion of the field (Figure 6.12). The pixel-to-pixel residuals can be more than 10x greater than the median level (Figure 6.13). Note that these profiles would be worse if there were color differences between the target and reference PSFs.

One way to avoid both the color and normalization problems is to take images of the target at two different field orientations, and subtract one from the other. This technique, known as *roll subtraction*, can be done either by requesting a roll of the telescope about the optical axis (up to 30°) between orbits or by revisiting the target at a later date when the default orientation of the telescope is different. Roll subtraction only works when the nearby object of interest is not azimuthally extended. It is the best technique for detecting point source companions or imaging strictly edge-on disks (e.g. Beta Pictoris). It can also be used to reduce the

pixel-to-pixel variations in the subtraction residuals by rotating and co-adding the images taken at different orientations. (This works for extended sources if another PSF star is used.) Ideally, the subtraction errors will decrease as the square root of the number of orientations.

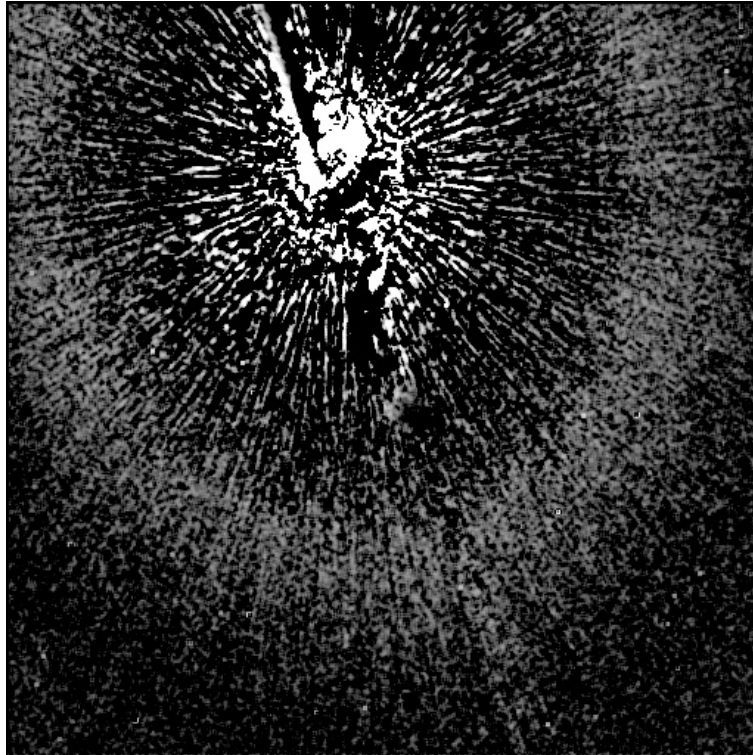
The large sizes of the occulting spots severely limit how close to the target one can image. It may be useful to combine coronagraphic imaging with direct observations of the target, allowing the central columns to saturate. Additional observations at other rolls would help. PSF subtraction can then be used to remove the diffracted and scattered light.

Figure 6.11: Residual errors from the subtraction of one image of Arcturus from another taken in a different visit (filter = F435W, $D = 1.8$ arcseconds spot).



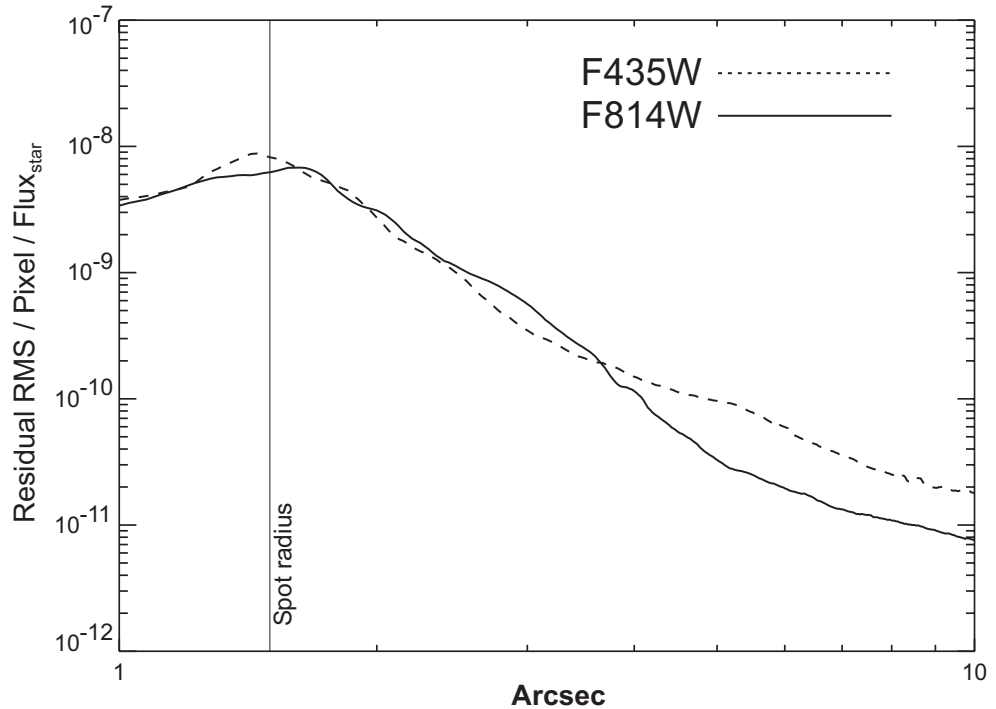
The image is 29 arcseconds across and has not been geometrically corrected. Logarithmic intensity scaled.

Figure 6.12: Subtraction of Arcturus from another image of itself taken during another visit using the large ($D = 3.0$ arcseconds) spot and F435W filter.



The image has been rebinned, smoothed, and stretched to reveal very low level residuals. The broad ring at about 13 arcseconds from the star is a residual from some unknown source – perhaps it represents a zonal redistribution of light due to focus differences (breathing) between the two images. The surface brightness of this ring is 20.5 magnitudes/arcsecond² fainter than the star. The diameter, brightness, and thickness of this ring may vary with breathing and filter. The image has not been geometrically corrected.

Figure 6.13: Plots of the azimuthal RMS subtraction residual levels at each radius for the large (3 arcseconds) spot.

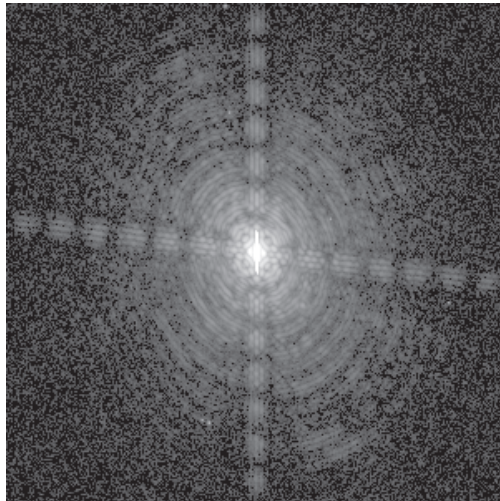


The flux units are counts per pixel relative to the total unocculted flux from the central source. These plots were derived from Arcturus-Arcturus subtractions represent the best results one is likely to achieve. The undistorted HRC scale assumed here is 25 milliarcseconds/pixel.

6.2.6 The Off-Spot PSF

Objects that are observed in the coronagraphic mode but that are not placed behind an occulting mask have a PSF that is defined by the Lyot stop. Because the stop effectively reduces the diameter of the telescope and introduces larger obscurations, this "off-spot" PSF is wider than normal, with more power in the wings and diffraction spikes (Figure 6.14). In addition, the Lyot stop and occulting spot substrate reduce the throughput by 52.5%. In F814W, the "off-spot" PSF has a peak pixel containing 4.3% of the total (reduced) flux and a sharpness (including CCD charge diffusion effects) of 0.010. (Compare these to 7.7% and 0.026, respectively, for the normal HRC PSF.) In F435W, the peak is 11% and the sharpness is 0.025 (compared to 17% and 0.051 for the normal F435W PSF). Observers need to take the reduced throughput and sharpness into account when determining detection limits for planned observations. [Tiny Tim](#) can be used to compute off-spot PSFs.

Figure 6.14: Image of Arcturus taken in coronagraphic mode with the star placed outside of the spot.



The coronagraphic field PSF has more pronounced diffraction features (rings and spikes) than the normal HRC PSF due to the effectively larger obscurations introduced by the Lyot stop. The central portion of this image is saturated. It was taken through a narrowband filter (F660N) and is not geometrically corrected.

6.2.7 Occulting Spot Motions

STScI measures the positions of the occulting spots at weekly intervals using Earth flats. These measurements show that the spots move over daily to weekly time scales in an unpredictable manner. The cause of this motion is unknown. The spot positions typically vary by ~ 0.3 pixels (8 milliarcseconds) over one week, but they occasionally shift by 1 to 5 pixels over 1 to 3 weeks. During a single orbit, however, the spots are stable to within ± 0.1 pixel when continuously deployed and they recover their positions within ± 0.25 pixel when repeatedly stowed and deployed.

After the acquisition exposure, a coronagraphic target is moved to a previously measured position of an occulting spot. Unfortunately, ACS's configuration prevents automatic determination of the spot's position before a coronagraphic exposure, as can be done with NICMOS. Furthermore, unlike STIS, the target cannot be dithered until the flux around the occulter is minimized. Instead, STScI uploads the latest measured spot positions (which may be several days old) a few orbits before each coronagraphic observation. After acquisition, the target is moved to this appropriate spot position via a USE OFFSET special requirement. This procedure adds approximately 40 seconds to each visit and is required for all coronagraphic observations.

The uncertainties in the day-to-day spot positions can cause star-to-spot registration errors that affect coronagraphic performance. If the star is offset from the spot center by more than 3 pixels, then one side of the coronagraphic PSF will be brighter than expected and may saturate earlier

than predicted. A large offset will also degrade the coronagraphic suppression of the diffraction pattern. Most importantly, slight changes in the spot positions can alter the coronagraphic PSFs of the target and reference stars enough to cause large PSF-subtraction residuals. Consequently, an observer cannot rely on reference PSFs obtained from other programs or at different times.

To reduce the impact of spot motion, observers should obtain a reference PSF in an orbit immediately before or after their science observation. A single reference PSF can be used for two science targets if all three objects can be observed in adjacent orbits and they have similar colors. (Note that SAA restrictions make it difficult to schedule programs requiring more than five consecutive orbits.) Otherwise, each target will require a distinct reference PSF. Additional orbits for reference PSFs must be included in the Phase 1 proposal.

6.2.8 Planning ACS Coronagraphic Observations

Exposure Time Estimation

Estimating the exposure times for coronagraphic observations is similar to estimating those for direct observations, except that the background signal from the occulted source must be considered. Generally, most coronagraphic observations are limited by the wings of the coronagraphic PSF. The [APT Exposure Time Calculator](#) includes a coronagraphic mode for estimating exposure times. They can be determined using the Web-based version of the [ACS Exposure Time Calculator](#). The following steps are required:

- Determine which occulting mask to use
- Calculate the count rate for the circumstellar/circumnuclear science target
- Calculate the count rate for the bright source to be occulted
- Calculate the background signal from the wings of the occulted source's PSF at the location of the target.
- Verify that background+target does not saturate at this location in the desired exposure time t_{exp}
- Calculate the signal-to-noise ratio Σ , given by:

$$\Sigma = \frac{Ct}{\sqrt{Ct + N_{\text{pix}}(B_{\text{sky}} + B_{\text{det}} + B_{\text{PSF}})t + N_{\text{pix}}N_{\text{read}}R^2}}$$

Where:

- C = the signal from the science target in electrons/sec.
- N_{pix} = the total number of detector pixels summed to achieve C .
- B_{sky} = the sky background in counts/sec/pixel.

- B_{det} = the detector dark current in counts/sec/pixel.
- B_{PSF} = the background in counts/sec/pixel from the wings of the occulted source's PSF at the distance of the science target.
- N_{read} = the number of CCD readouts.
- t = the integration time in seconds.
- R is the readout noise of the HRC CCD = $4.7e^-$.

As an example we will determine the S/N achieved in detecting a M6 V star with a V magnitude of 20.5 at a distance of 4.25 arcseconds from a F0 V star with a V magnitude of 6, for an exposure time of 1000 seconds with the F435W filter. Using the [ACS Exposure Time Calculator](#) and considering the case for the 3.0 arcseconds occulting mask:

- M6V star count rate = $3.7 e^-/\text{second}$ for a 5×5 aperture (including 47.5% throughput of coronagraph)
 Sky count rate = $0.0025 e^-/\text{second/pixel}$
 Detector dark rate = $0.0037 e^-/\text{second/pixel}$
- F0V count rate = $3.3 \times 10^7 e^-/\text{second}$ for a 101×101 aperture (101×101 aperture used to estimate total integrated flux)
- At a distance 4.25 arcseconds from the central star, from Figure 6.8, the fraction of flux per 0.026×0.026 arcseconds pixel in the PSF wings is 5×10^{-9} .
 $B_{\text{PSF}} = 3.3 \times 10^7 * 5 \times 10^{-9} = 0.165 e^-/\text{second/pixel}$
- Using the equation above we find the signal-to-noise for a 1000 seconds exposure is 40. Note that a M6 V star with a V magnitude of 20.5 observed with the HRC in isolation would yield a S/N of 93.

Observing sequence for point source companions

The best way to detect faint stellar or substellar companions is to use roll subtraction to avoid color differences between the target and reference PSFs. This also provides duplicate observations that make it easier to verify true companions from noise. It is best to roll the telescope between visits and repeat the image sequence in a new orbit. This way, you can better match the breathing cycle of the telescope than if you rolled the telescope in the middle of an orbital visibility window. You can force this to happen by selecting both orientation and time-sequencing constraints in the visit special requirements. Remember that the off-spot coronagraphic PSF is somewhat broader than the normal HRC PSF, which may influence your assumed signal-to-noise ratio. Off-spot PSF models can be generated with the [Tiny Tim](#) PSF software. You can estimate the residual background noise level using Figure 6.13.

Suggested point-source companion observing sequence:

1. Obtain an acquisition image
2. Execute coronagraphic image sequence.

3. Request telescope roll offset (use **ORIENT q₁ TO q₂ FROM n** special requirement in visit).
4. Obtain another acquisition.
5. Repeat image sequence.
6. Repeat 3 to 5 as necessary.

Observing sequence for extended sources (e.g. circumstellar disks and AGN host galaxies)

When imaging extended objects, the remaining scattered light must be subtracted using an image of a reference star that matches the color of your target as closely as possible. To reduce the impact of photon noise in the subtracted images, the reference star should be much brighter than the target source. If possible, select a reference star that is nearby ($< 20^\circ$ from the target) and request that it be observed immediately before or after the target source. This strategy reduces the chances of large focus differences between the two visits. To better discriminate between subtraction artifacts and real circumstellar emission, obtain images of the target at two or more telescope orientations. (There is no need to get reference PSF images at different rolls.) Estimate the residual background noise level using Figure 6.13.

Suggested extended source observing sequence:

1. Obtain direct images of the science target in each filter to derive flux normalization factors
2. Obtain an acquisition image of the science target.
3. Take coronagraphic image sequence of science target.
4. Request a new telescope orientation.
5. Repeat steps 2 to 3.
6. In a new visit immediately before or after the science observation, point at the reference star.
7. Obtain an acquisition image of reference star.
8. Take coronagraphic image sequence of reference star.
9. Obtain direct images of the reference star in each filter to derive flux normalization factors.

Note that the order of the observations places direct imaging before or after coronagraphic imaging. This reduces cycling of the coronagraphic mechanism. Because the occulting spots are large, you may wish to image closer to the source using additional direct observations without the coronagraph. Multiple roll angles are necessary in this case because portions of the inner region will be affected by saturated columns and diffraction spikes. Direct observations of the reference star will be required as well to subtract both the diffracted and scattered light. Color and focus

mismatches between the target and reference PSFs will be even more important in the direct imaging mode than with the coronagraph because the diffracted light is not suppressed. However, there are no mismatches caused by star-spot alignment to worry about.

6.2.9 Choice of Filters for Coronagraphic Observations

All HRC filters are available for coronagraphic observations. However, only a few (F435W, F475W, F606W, and F814W) are well characterized in this mode. The first three have produced good results and can be considered “safe” choices. Filter F814W is problematic, however. Its PSF is relatively large so less light from the bright source is blocked by the occulting spot. The coronagraphic PSF is therefore more sensitive to spot shifts and star-to-spot misalignments. Mismatches between target and reference PSFs may cause significant PSF subtraction residuals. Also, F814W images suffer from the red halo (see Section 5.6.5), which affects coronagraphic observations because the central spot is filled with light that will be scattered to large radii. Color differences between the target and reference stars will cause differences in the halo pattern, altering the local background level in unpredictable ways. If multicolor images are needed, it is safer to choose F435W and F606W rather than F606W and F814W. However for red objects it may not be feasible to choose a blue filter due to low flux levels, in which case F814W must be used.

6.3 Grism/Prism Spectroscopy

The ACS filter wheels include four dispersing elements for low resolution slitless spectrometry over the field of view of the three ACS channels. One grism (G800L) provides low resolution spectra over the 5500 Å to 10,500 Å range for both the WFC and HRC. A prism (PR200L) in the HRC covers the range 1700 Å to beyond 3900 Å (although reliable wavelength and flux calibration is only guaranteed to 3500 Å). In the SBC a LiF prism covers the wavelength range 1150 Å to ~1800 Å (PR110L) and a CaF₂ prism is useful over the 1250 Å to ~1800 Å range (PR130L). Table 6.3 summarizes the essential features of the four ACS dispersers in the five available modes. The grism provides first order spectra with almost constant dispersion as a function of wavelength but with second order overlap beyond about 10,000 Å; the prisms however have non-linear dispersion with maximum resolution at shorter wavelengths but much lower resolving power at longer wavelengths. The two-pixel resolution is listed for each grism or prism at a selected wavelength in Table 6.3. The pixel scale for the prism spectra is given at the selected wavelength. The tilt of the spectra to the detector X axis (close to the spacecraft V2 axis) is also listed.

Table 6.3: Optical parameters of ACS dispersers.

| Disperser | Channel | Wavelength range (Å) | Resolving power | Å/pixel | Tilt ¹ (deg) |
|-----------|---------|-----------------------------|-----------------|-------------------|-------------------------|
| G800L | WFC | 1st order: 5500 to 10500 | 100 @ 8000 Å | 39.8 ² | -2 |
| G800L | WFC | 2nd order: 5000 to 8500 | 200 @ 8000 Å | 20.7 ² | -2 |
| G800L | HRC | 1st order: 5500 to 10500 | 140 @ 8000 Å | 23.9 ³ | -38 |
| G800L | HRC | 2nd order: 5500 to 8500 | 280 @ 8000 Å | 12.0 ³ | -38 |
| PR200L | HRC | 1700 to 3900 | 59 @ 2500 Å | 21.3 | -1 |
| PR110L | SBC | 1150 to 1800 | 79 @ 1500 Å | 9.5 | 0 |
| PR130L | SBC | 1250 to 1800 | 96 @ 1500 Å | 7.8 | 0 |

1. Tilt with respect to the positive X-axis of the data frame.

2. The dispersion varies over the field by $\pm 11\%$; the tabulated value refers to the field center.

3. The dispersion varies over the field by $\pm 2\%$; the tabulated value refers to the field center.

6.3.1 WFC G800L

The G800L grism and the WFC provide two-pixel resolving power from 69 (at 5500 Å) to 131 (at 10,500 Å) for first order spectra over the whole accessible field of 202 x 202 arcseconds. Table 6.3 lists the linear dispersion, but a second order dispersion solution provides a better fit. Figure 6.15 shows the wavelength extent and sensitivity for the zeroth, first, and second order spectra when used with the WFC. Figure 6.16 shows the same plot in pixel extent. The 0 position refers to the position of the direct image and the pixel size is 0.05 arcseconds. Note that there is contamination of the 1st order spectrum above 10,000 Å by the second order. The total power in the zeroth order is 2.5% of that in the first order, so locating the zeroth order may not be an effective method of measuring the wavelengths of weak spectra. The default method will be to obtain a matched direct image-grism pair. There is also sensitivity of about a percent of first order in the third and fourth orders, and about half a percent in the negative orders. The full extent of the spectrum of a bright source (orders -2, -1, 0, 1, 2, 3) is 1200 pixels (60 arcseconds). The higher orders are not in focus and the spectral resolution of these orders is therefore less than what would be predicted from the nominally higher dispersion.

Figure 6.15: Sensitivity versus wavelength for WFC G800L.

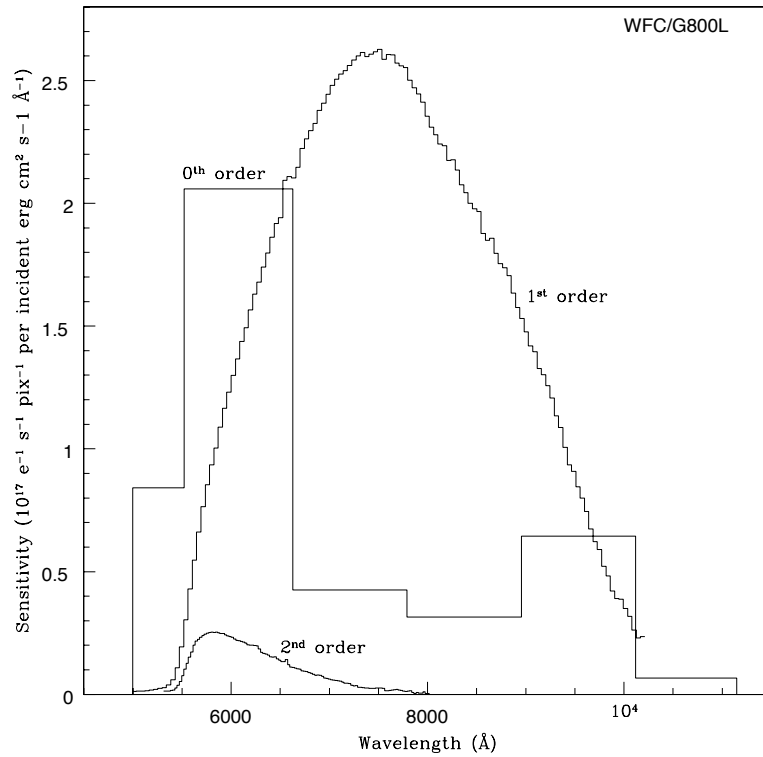


Figure 6.16: Sensitivity versus pixel position for WFC G800L.

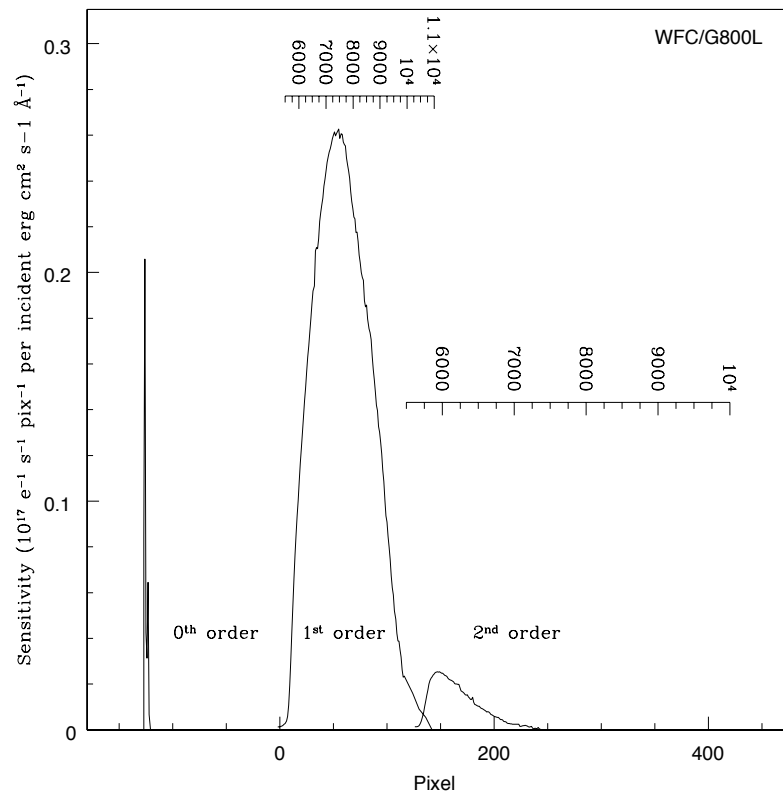


Figure 6.17 shows the full spectrum extent for a 60 second exposure of the white dwarf GD153 ($V = 13.35$) with the individual orders indicated. When bright objects are observed, the signal in fainter orders may be mistaken for separate spectra of faint sources and in crowded fields, many

orders from different objects can overlap. The wavelength solution is field dependent on account of the tilt of the grism to the optical axis, and the linear dispersion varies by $\pm 11\%$ from center to corner. This field dependence has been calibrated to allow wavelength determination to better than 0.5 pixels over the whole field.

Figure 6.17: Full dispersed spectrum for white dwarf GD153 with WFC/G800L.



The numbers indicate the different grism orders.

6.3.2 HRC G800L

When used with the HRC, the G800L grism provides higher spatial resolution (0.028 arcseconds) pixels than the WFC and also higher spectral resolution. However, the spectra are tilted at -38° to the detector X axis. Figure 6.18 shows the wavelength extent and sensitivity in the zero, first and second orders, with the pixel extent shown in Figure 6.19. Figure 6.20 shows the observed spectrum of the standard star GD153. Again there is contamination of the first order spectrum by the second order beyond 9500 Å. The total extent of the spectrum (orders -1 and +2) in Figure 6.20 covers about 70% of the 1024 detector pixels. In addition, a much greater number of spectra will be formed by objects situated outside the HRC direct image, or will have their spectra truncated by the chip edges, than for the WFC. The variation of the grism dispersion over the HRC field is about $\pm 2\%$ from center to corner and has been calibrated.

Figure 6.18: Sensitivity versus wavelength for HRC G800L.

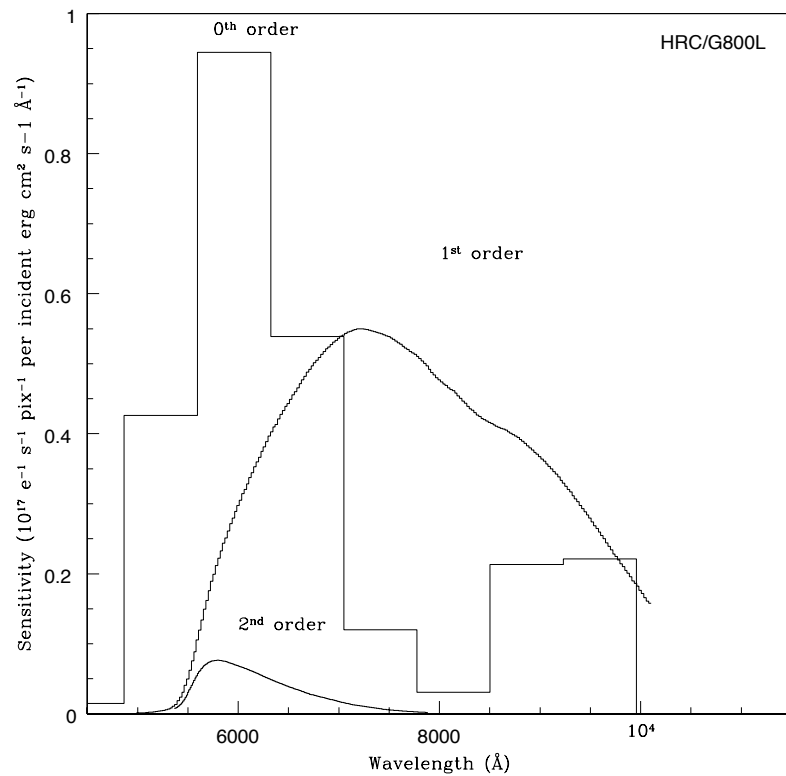


Figure 6.19: Sensitivity versus pixel position for HRC G800L.

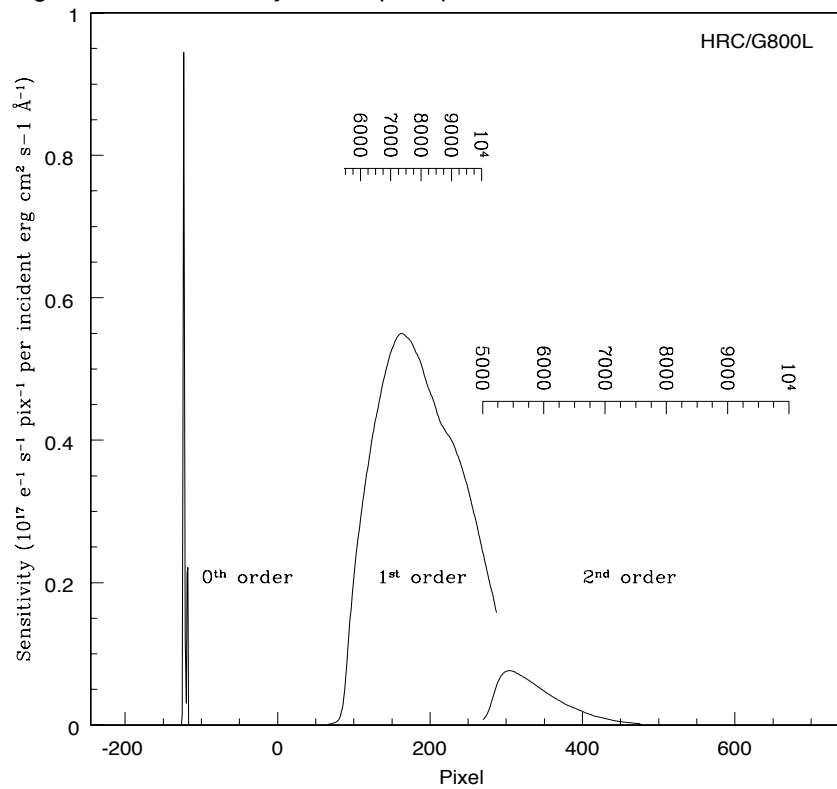
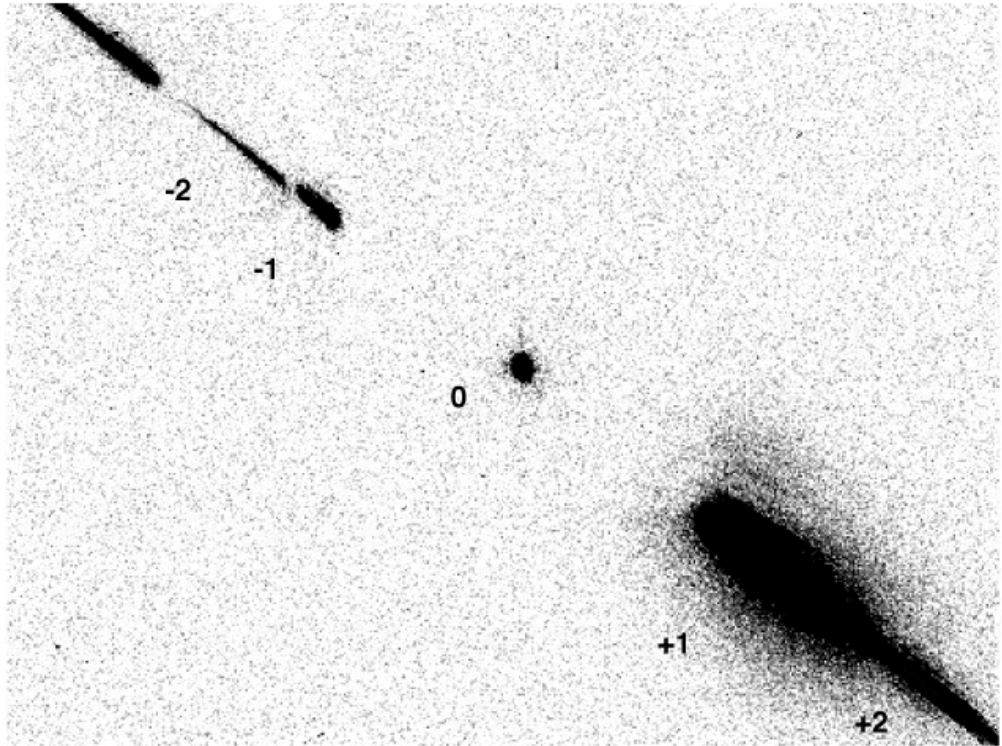


Figure 6.20: Full dispersed spectrum of white dwarf GD153 with HRC/G800L.



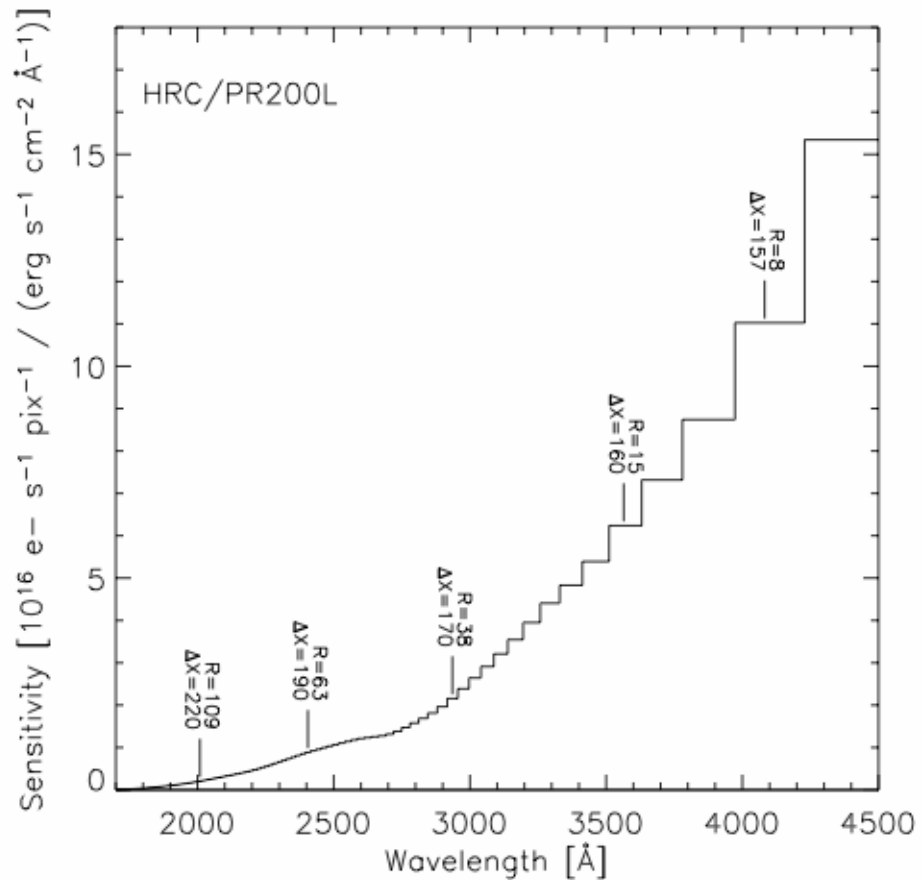
The numbers indicate the different grism orders.

6.3.3 HRC PR200L

The maximum dispersion of the prism is 5.3 \AA at 1800 \AA . At 3500 \AA , the dispersion drops to 105 \AA/pix and is 563 \AA/pix at 5000 \AA . The result is a pile-up of the spectrum to long wavelengths with 8 pixels spanning 1500 \AA . For bright objects, this effect can lead to blooming of the HRC CCD from filled wells; the overfilled pixels bleed in the detector Y direction, and thus can affect other spectra. Figure 6.21 shows the sensitivity versus wavelength for PR200L and the wavelength extent of the pixels is indicated. The variation of the dispersion across the detector for PR200L amounts to about $\pm 4\%$ (corner to corner) at 2000 \AA . The tilt of the prism causes a deviation of about 300 pixels between the position of the direct object and the region of the dispersed spectrum on the CCD, while simultaneously vignetting this same amount from the low-x side of the HRC image. We have therefore defined a new prism aperture with a recentered reference point. Because of this and the real deflection caused by the prism, the telescope has to be shifted by 7.4 arcseconds to place the target at the new center. The use of this special aperture and the associated pointing correction takes place automatically when the prism PR200L is chosen. Users specify HRC as the aperture in conjunction with the filter PR200L. The current calibration of the wavelength solution used in the aXe data reduction software (see Section 6.3.7) assumes the use of these

apertures. The numbers in Figure 6.21 indicate the resolving power (R) and the offset between the direct and prism images in pixels (Δx) as functions of wavelength. These offsets and the wavelength calibration take into account the use of the two different pointings for direct and prism observations.

Figure 6.21: Sensitivity versus wavelength for HRC/PR200L.



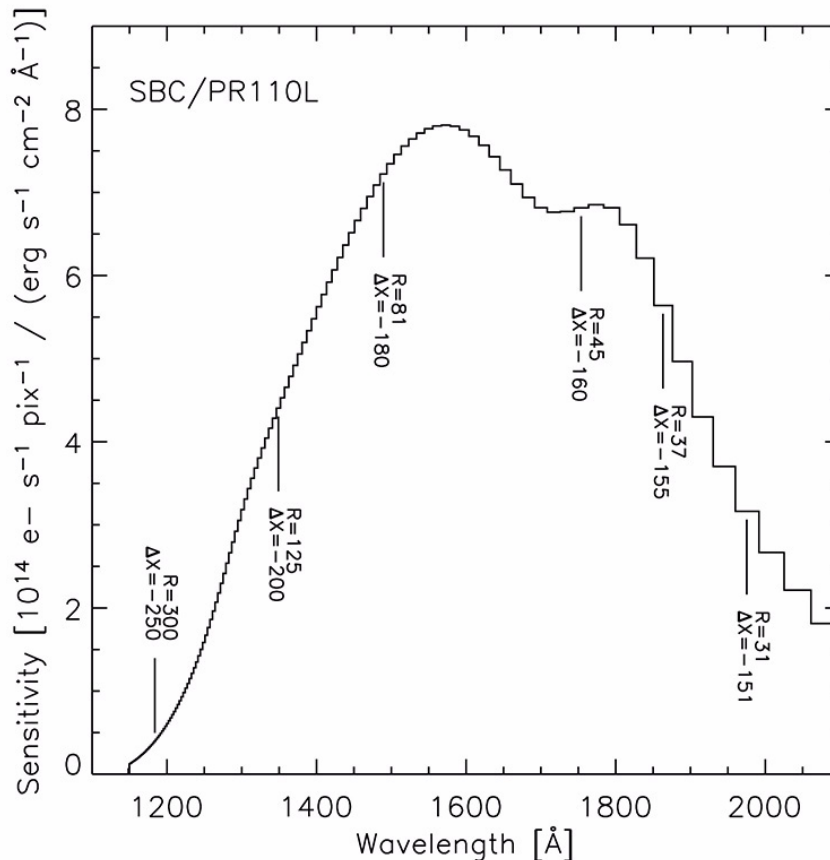
The numbers indicate the resolving power (R) and the offset from the direct image in pixels (Δx) as functions of wavelength.

6.3.4 SBC PR110L

The PR110L prism is sensitive to below 1200 Å and includes the geo-coronal Lyman-alpha line, so it is subject to high background. The dispersion at Lyman-alpha is 2.6 Å per pixel. Figure 6.22 shows the sensitivity with wavelength and the wavelength width of the pixels. The long wavelength efficiency decline of the CsI MAMA detector beyond ~1800 Å occurs before the long wavelength pile-up. However, recent prism observations of flux standards and a G-type star indicate that the system throughput is increased by a factor of approximately 1000 at 4000 Å with respect to the curve in Figure 4.17. For stars redder than about F-type this will result in significantly increased counts between 2000 and 6000 Å,

peaking at about 3500 Å. For a G-type star this peak can be a factor of ~3 times larger than the maximum count rate in the UV. The dispersion at 1800 Å is 21.6 Å/pixel. The detected counts in the spectrum must be within the MAMA Bright Object Protection Limits (BOP) (see Section 4.6). These limits must include the contribution of the geo-coronal Lyman-alpha flux per SBC pixel. The numbers in Figure 6.22 indicate the resolving power (R) and the offset from the direct image in pixels (Δx) as functions of wavelength. As for the HRC, the prisms deflect the SBC image, although this time the vignetting is on the +x part of the image. Users specify SBC as the aperture in conjunction with the filter PR110L and the correct prism aperture will automatically be used. The current wavelength calibration used in aXe (see Section 6.3.7) assumes these default apertures. In Figure 6.23 a direct image and a PR110L exposure of the standard star WD1657+343 are shown, as an example.

Figure 6.22: Sensitivity versus wavelength for SBC PR110L.



The numbers indicate the resolving power (R) and the offset from the direct image in pixels (Δx) as functions of wavelength.

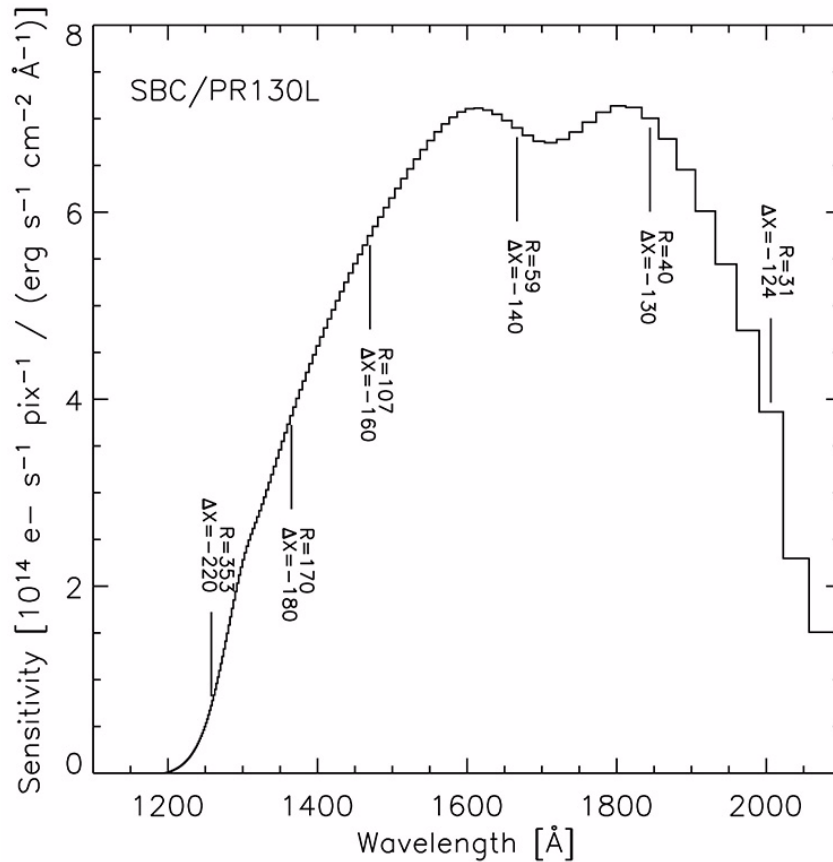
Figure 6.23: Sum of direct (F122M) and PR110L prism exposure of the standard star WD1657+343. The direct image exposure was scaled prior to combination for representation purposes.



6.3.5 SBC PR130L

The short wavelength cut-off of the PR130L prism at 1250 \AA excludes the geocoronal Lyman-alpha line, making it the disperser of choice for faint object detection in the 1250 \AA to 1800 \AA window. The dispersion varies from 1.65 \AA/pixel at 1250 \AA to 20.2 \AA/pixel at 1800 \AA . Figure 6.24 shows the sensitivity versus wavelength, with the resolving power (R) and the offset from the direct image in pixels (Δx) as functions of wavelength. Bright Object Protection considerations similar to the case of PR110L also apply to the use of this prism, except that the background count rate is lower (see Section 4.6). As for the other prisms, the direct and dispersed images use different apertures with a small angle maneuver between them.

Figure 6.24: Sensitivity versus wavelength for SBC/PR130L.



The numbers indicate the resolving power (R) and the offset from the direct image in pixels (Δx) as functions of wavelength.

6.3.6 Observation Strategy

The normal observing technique for all ACS spectroscopy is to obtain a direct image of the field followed by the dispersed grism/prism image. This combination allows the wavelength calibration of individual target spectra by reference to the corresponding direct images. For WFC and HRC, the scheduling system automatically inserts a default direct image for each specified spectroscopic exposure, which for G800L consists of a 3 minute F606W exposure, and for PR200L, a 6 minute F330W exposure. If the observer wishes to eliminate the default image, the supported Optional Parameter AUTOIMAGE=NO can be specified. Then a direct image with a different filter and/or exposure time can be specified manually, or no direct image at all in the case of repeated spectroscopic exposures within an orbit, or if no wavelength calibration is required. For the SBC prisms, there is no default direct image because of the Bright Object Protection requirements (Section 7.2); the direct image must always be specified manually, and it

must satisfy the BOP limits, which will be more stringent than for the dispersed image.

Because of the offset between the direct imaging and prism aperture definitions, the `SAME POS AS` option will generally not have the desired effect for prism spectroscopy (PR110L, PR130L, and PR200L). Users who wish to specify offsets from the field center by means of the `POS-TARG` option should do so by explicitly specifying the same `POS-TARG` for the direct imaging and prism exposures.

Table 6.4 lists the V detection limits for the ACS grism/prism modes for unreddened O5 V, A0 V, and G2 V stars, generated using the [Exposure Time Calculator](#). WFC and HRC values used the parameters `CR-SPLIT=2` and `GAIN=2`. An average sky background was used in these examples. However, limiting magnitudes are sensitive to the background levels; for instance, the limiting magnitude of an A0 V in the WFC using the F606W filter changes by ± 0.4 magnitudes at the background extremes.

Table 6.4: V detection limits for the ACS grism/prism modes.

| Mode | V limit (S/N = 5, exposure time = 1 hour) | | | Wavelength of reference (Å) |
|------------|--|-------------|------------|--------------------------------|
| | O5 V (Kurucz model) | A0 V (Vega) | G2 V (Sun) | |
| WFC/G800L | 24.2 | 24.4 | 24.9 | 7000 |
| HRC/G800L | 23.4 | 23.6 | 24.2 | 7000 |
| HRC/PR200L | 25.6 | 22.7 | 18.8 | 2500 |
| SBC/PR110L | 24.9 | 20.9 | 9.3 | 1500 |
| SBC/PR130L | 25.6 | 21.5 | 9.9 | 1500 |

Chapter 9 provides details of the calculations. Depending on the wavelength region, the background must also be taken into account in computing the signal-to-noise ratio. The background at each pixel consists of the sum of all the dispersed light in all the orders from the background source. For complex fields, the background consists of the dispersed spectrum of the unresolved sources; for crowded fields, overlap in the spectral direction and confusion in the direction perpendicular to the dispersion may limit the utility of the spectra.

The [ACS Exposure Time Calculator](#) supports all the available spectroscopic modes of the ACS and is available for more extensive calculations at http://apt.stsci.edu/webetc/acs/acs_spec_etc.jsp. The current version employs the on-orbit determinations of the dispersion solution and sensitivity where available.

For more detailed simulations of ACS spectra, an image-spectral simulator, called [SLIM](#) is available. This tool allows synthetic target fields to be constructed and dispersed images from spectrum templates to be

formed. **SLIM** can simulate spectra for all the ACS spectral modes. The simulator runs under Python and an executable version is available at:

<http://www.stecf.org/instruments/ACSgrism/slim/>.

The software uses a Gaussian PSF but this has been found to be an adequate representation to the **Tiny Tim** model of the ACS PSF. A detailed description of the tool and examples of its use are given by Pirzkal et. al. ([ACS ISR 01-03](#)).

6.3.7 Extraction and Calibration of Spectra

Since there is no slit in the ACS, the Point Spread Function of the target modulates the spectral resolution. In the case of extended sources it is the extension of the target in the direction of dispersion which sets the achievable resolution. Simulations show that for elliptical sources, the spectral resolution depends on the orientation of the long axis of the target to the dispersion direction and is described in more detail in [ACS ISR 2001-02](#). The dispersion of the gratings and prisms is well characterized, but for the wavelength zero point it is important to know the position of the target in the direct image. For the gratings, the zeroth order will generally be too weak to reliably set the wavelength zero point. Given the typical spacecraft jitter, wavelength zero points to ± 0.4 pixels should be routinely achievable using the direct image taken just before or after the slitless spectrum image.

The jitter information can be used to obtain more accurate coordinates for the center of the FOV. These in turn allow one to determine better relative offsets between the direct and the spectroscopic images.

The wavelength extent of each pixel for the WFC and HRC G800L modes in the red is small enough that fringing can modulate the spectra. For the HRC, the peak-to-peak fringe amplitude is about 30% at 9500Å, and is about 25% for the WFC chips. Modelling of the fringing for WFC and HRC chips is described in [ACS ISR 2003-12](#). In practice, for observations of point sources, and even more so for extended sources, the detectable fringing is significantly reduced by the smoothing effect that the PSF, together with the intrinsic object size, has on the spectrum in the dispersion direction. No fringing has been detected in observed continuum spectra to an upper limit of about 2%. For objects with narrow emission lines the fringing can be significantly larger and thus the observed line flux can be affected.

Because the STSCI pipeline does not provide an extracted spectral count rate vs. wavelength, an extraction software package, **axE**, is available to extract, wavelength calibrate, flat field, and flux calibrate ACS grism and prism spectra. Full details can be found at:

<http://www.stecf.org/instruments/ACSgrism/axe/>

The package is also available in **STSDAS**.

Observing Techniques

In this chapter . . .

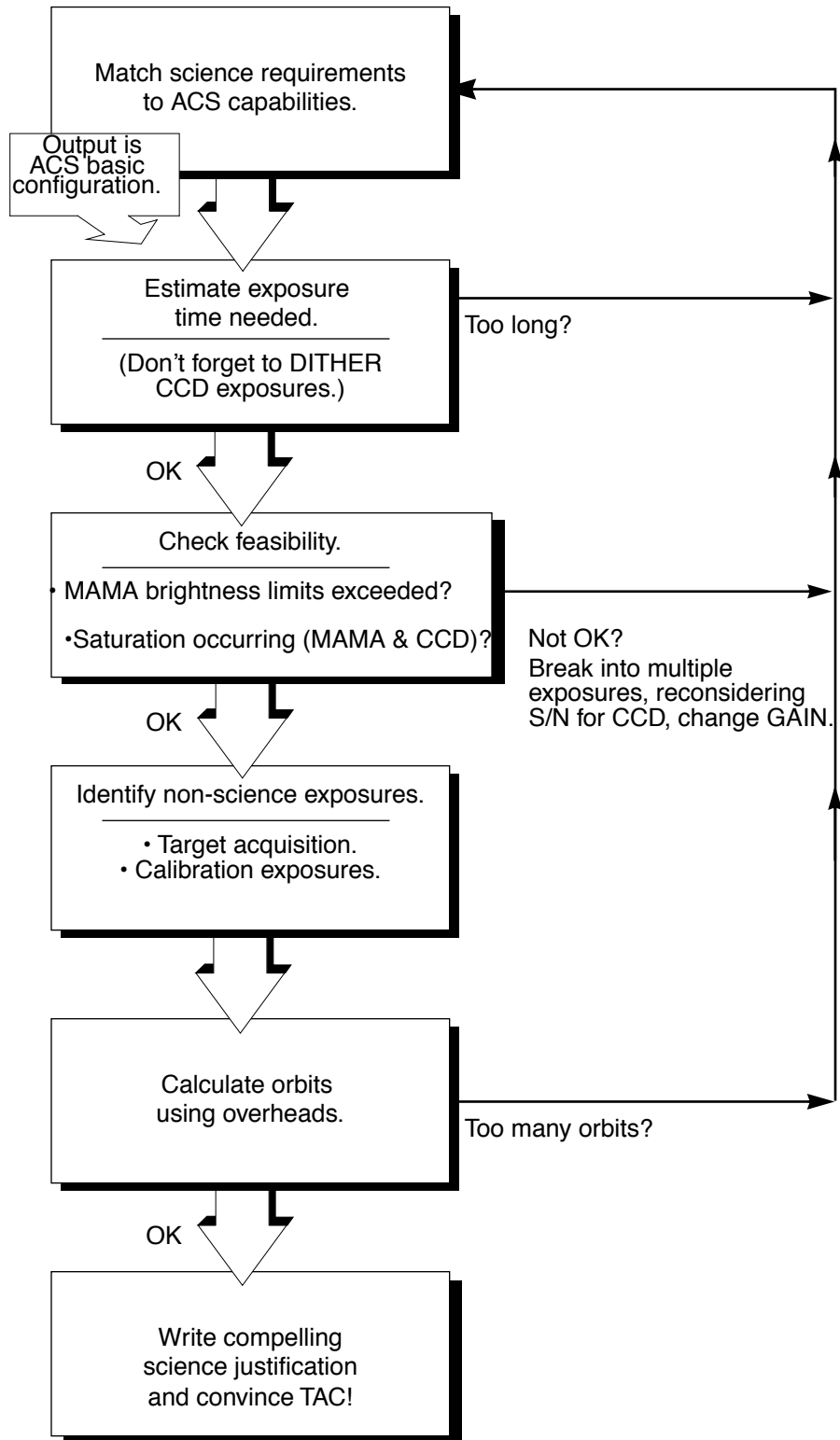
| |
|--|
| 7.1 Designing an ACS Observing Proposal / 117 |
| 7.2 SBC Bright Object Protection / 125 |
| 7.3 Operating Modes / 132 |
| 7.4 Patterns and Dithering / 137 |
| 7.5 A Road Map for Optimizing Observations / 138 |
| 7.6 CCD Gain Selection / 140 |
| 7.7 ACS Apertures / 142 |
| 7.8 Specifying Orientation on the Sky / 152 |
| 7.9 Parallel Observations / 156 |
| 7.10 Pointing Stability for Moving Targets / 162 |

7.1 Designing an ACS Observing Proposal

In this section, we describe the sequence of steps you will need to take when designing your ACS observing proposal. The process is an iterative one, as trade-offs are made between signal-to-noise ratio and the limitations of the instrument itself. The basic sequence of steps in defining an ACS observation are:

- Identify science requirements and select the basic ACS configuration to support those requirements.
- Estimate exposure time to achieve the required signal-to-noise ratio, determine GAIN selection, CR-SPLIT, dithering, and mosaic strategy, and check feasibility, including saturation and bright-object limits.
- Identify any additional target acquisition (coronagraph) and calibration exposures needed.
- Calculate the total number of orbits required, taking into account the overheads.

Figure 7.1: Defining an ACS observation.



7.1.1 Identify Science Requirements and Define ACS Configuration

First and foremost, of course, you must identify the science you wish to achieve with ACS. Basic decisions you will need to make are:

- Nature of target
- Filter selection

As you choose your science requirements and work to match them to the instrument's capabilities, keep in mind that those capabilities differ greatly depending on whether you are observing in the optical or near-UV with the CCD, or in the far-UV using the MAMA detector. Trade-offs are described in Table 7.1.

Table 7.1: Science decision guide.

| Decision | Choices | Tradeoffs |
|--------------------|---|--|
| Field of view | Camera Filter selection | WFC: 202 x 202 arcseconds HRC: 29 x 26 arcseconds SBC: 35 x 31 arcseconds |
| Spectral response | Camera Filter selection | WFC: 3700-11,000 Å HRC: 2000-11,000 Å SBC: 1150-1700 Å |
| Spatial resolution | Camera | WFC: ~50 milliarcsecond pixels HRC: ~27 milliarcsecond pixels SBC: ~32 milliarcsecond pixels |
| Filter selection | Camera | WFC: broad, medium & narrow band, ramps HRC: Visible, UV, ramp middle sections |
| Spectroscopy | Camera Spatial resolution Field of view Wavelength range | Grism (G800L): WFC and HRC Prism (PR200L): HRC Prism (PR110L, PR130L): SBC |
| Polarimetry | Filters | UV polarizers combine with Wheel 2 filters VIS polarizers combine with Wheel 1 filters |
| Coronagraphy | Filter selection | Coronagraphic imaging available with HRC only |

Imaging

For imaging observations, the base configuration is detector (Configuration), operating mode (MODE=ACCUM), and filter. Chapter 5 presents detailed information about each ACS imaging mode.

Special Uses

We refer you to Chapter 6 if you are interested in any of the following special uses of ACS: slitless spectroscopy, polarimetry, and coronagraphy.

7.1.2 Use of Available-but-Unsupported Capabilities

A set of core ACS capabilities to support scientific observations has been established. In addition there are a few capabilities with ACS, some of which are mentioned in this Handbook, for which limited access is available. These capabilities are “available-but-unsupported,” but, in consultation with an ACS Instrument Scientist, may be requested. These include a few apertures, limited interest optional parameters, some GAIN options, and filterless (CLEAR) operation. If you find that your science cannot be obtained using fully supported modes, or that it would be much better with use of these special cases, then you may wish to consider use of an unsupported mode.

Use of unsupported modes comes at a price; they should only be used if the technical requirements and scientific justifications are particularly compelling. The following caveats apply:

- Calibrations for available-but-unsupported modes will not be provided by STScI. It is the observer’s responsibility to obtain such calibrations as needed.
- STScI adopts a policy of shared risk with the observer for the use of these modes. Requests to repeat failed observations taken with unsupported capabilities will not be honored if the failure is related to use of this capability.
- User support from STScI will be more limited.

Phase I proposals that include use of unsupported ACS capabilities must include the following:

- Justification of why supported modes don’t suffice.
- A request for any observing time needed for calibration purposes.
- Justification for added risk of use in terms of scientific payback.
- Demonstration that the observers are able to analyze such data.

During the Phase II proposal submission process, use of available-but-unsupported modes requires formal approval from the AWT at STScI. To request permission for use of an available-but-unsupported mode, please send a brief e-mail to your Program Coordinator (PC) that addresses the above four points. The PC will relay the request to the contact scientist or relevant ACS instrument scientist, who will decide whether the use will be allowed. This procedure ensures that any potential technical problems have been taken into account. Note also that archival research may be hindered by use of these modes. As a result, requests for use of unsupported modes which do not adequately address the above four points, or which will result in only marginal improvements in the quality of the data obtained, may be denied, even if the request was included in your approved Phase I proposal.

The current list of available-but-unsupported items are:

- Targets: BIAS
- Optional parameters: SIZEAXIS1, SIZEAXIS2, CENTERAXIS1, CENTERAXIS2, COMPRESSION, AMP, FLASHEXP, WFC: GAIN=4,8, HRC: GAIN=1,8
- Spectral elements: CLEAR (both WFC and HRC)
- ACQ mode: optional parameter GAIN

7.1.3 Determine Exposure Time and Check Feasibility

Once you've selected your basic ACS configuration, the next steps are:

- Estimate the exposure time needed to achieve your required signal-to-noise ratio, given your source brightness. (You can use the [ACS Exposure Time Calculator](#) for this; see also Chapter 9 and the plots in Chapter 10).
- For observations using the CCD detectors, ensure that for pixels of interest, you do not exceed the per pixel saturation count limit of the CCD full well or the 16 bit word size at the GAIN setting you choose.
- For observations using the MAMA detector, ensure that your observations do not exceed brightness (count rate) limits.
- For observations using the MAMA detector, ensure that for pixels of interest, your observations do not exceed the limit of 65,535 accumulated counts per pixel per exposure imposed by the ACS 16 bit buffer.

To determine your exposure-time requirements, consult Chapter 9 where an explanation of how to calculate a signal-to-noise ratio and a description of the sky backgrounds are provided. To assess whether you are close to the brightness, signal-to-noise, and dynamic-range limitations of the detectors, refer to Chapter 4.

If you find that the exposure time needed to meet your signal-to-noise requirements is too great, or that you are constrained by the detector's brightness or dynamic-range limitations, you will need to adjust your base ACS configuration. Table 7.2 summarizes the options available to you and steps you may wish to take as you iterate to select an ACS configuration which is both suited to your science and is technically feasible.

Table 7.2: Science feasibility guide.

| Action | Outcome | Recourse |
|--|---|---|
| Estimate exposure time. | If too long, re-evaluate instrument configuration. | Consider use of an alternative filter. |
| Check full-well limit for CCD observations. | If full well exceeded and you wish to avoid saturation, reduce time per exposure. | Divide total exposure time into multiple, short exposures. ¹ Consider use of different Gain. |
| Check bright-object limits for MAMA observations. | If source is too bright, re-evaluate instrument configuration. | Consider the use of an alternative filter or change detectors and wavelength regime. |
| Check 65,535 counts-per pixel limit for MAMA observations. | If limit exceeded, reduce time per exposure. | Divide total exposure time into multiple, short exposures |

1. Splitting CCD exposures affects the exposure time needed to achieve a given signal-to-noise ratio because of the readnoise.

7.1.4 Identify Need for Additional Exposures

Having identified a sequence of *science* exposures, you need to determine what additional exposures you may require to achieve your scientific goals. Specifically:

- For coronagraphy, determine what filter and target-acquisition exposure will be needed to acquire your target in the target acquisition aperture. This target acquisition zeroes out the position errors inherent in the guide stars.
- If the success of your science program requires calibration to a higher level of precision than is provided by STScI calibration data, and if you are able to justify your ability to reach this level of calibration accuracy yourself, you will need to include the necessary calibration exposures in your program, including the orbits required for calibration in your total orbit request.

7.1.5 Data Volume Constraints

If ACS data are taken at the highest possible rate for more than a few orbits or in the Continuous Viewing Zone (CVZ), it is possible to accumulate data faster than it can be transmitted to the ground. High data volume proposals will be reviewed and, on some occasions, users may be requested to break the proposal into different visits. Consider using sub-arrays, or take other steps to reduce data volume.

7.1.6 Determine Total Orbit Request

In this step, you place all of your exposures (science and non-science, alike) into orbits, including tabulated overheads, and determine the total number of orbits required. Refer to Chapter 8 when performing this step. If you are observing a small target and find your total time request is significantly affected by data-transfer overheads (which will be the case *only* if you are taking many separate exposures under 339 seconds with the WFC), you can consider the use of CCD subarrays to lessen the data volume. Subarrays are described in Section 7.3.1 (WFC), Section 7.3.2 (HRC), and in Section 8.2.1.

At this point, if you are happy with the total number of orbits required, you're done! If you are unhappy with the total number of orbits required, you can adjust your instrument configuration, lessen your acquisition requirements, or change your target signal-to-noise or wavelength requirements, until you find a combination which allows you to achieve your science goals.

7.1.7 Charge Transfer Efficiency

All CCDs operated in a radiative environment are subject to a significant degradation in charge transfer efficiency (CTE). The degradation is due to radiation damage of the silicon, inducing the creation of traps that impede an efficient clocking of the charge on the CCD. Since reading out the ACS WFC requires 2048 parallel transfers and 2048 serial transfers, it is not surprising that CTE effects have begun to manifest themselves since first years of ACS operation.

Initial expectations for growth of CTE for the Wide Field Camera have proven to be pessimistic. Multiple iterations of special programs designed to track the growth of CTE over time show that the degradation proceeds linearly with time. Projected to early 2009 (7 years on orbit) a star with 100 total electrons, a nominal sky background of 30 electrons, and a placement at row 1024 (center) in one of the WFC chips would experience a loss of about 4% to 7% for an aperture of 5 pixel radius. A target placed at the WFC aperture reference point, near the maximum number of parallel shifts during readout, would have approximately twice the loss. Expected absolute errors after calibration of science data, at these low-loss levels, is expected to be of order 25% the relative loss. Since projection to 2009 involves a substantial extrapolation, reaching this level of accuracy for corrections will require new calibrations.

The aperture WFC1-CTE is available to mitigate CTE loss. This aperture has the same area as the WFC1 aperture except that the reference position is 200 pixels from the upper right corner of chip 1, in both the chips x- and y- direction. Therefore, WFC1-CTE is not appropriate for highly extended targets.

As the CTE effects continue to worsen in future cycles, users may want to consider using the post-flash capability (currently an “available-but-unsupported” mode) to add a background level to their images. This causes the Poisson noise from the background level to increase and imposes a non-uniform background, but to-date only marginally improves the CTE performance of the detector. In some cases adopting a broader filter (e.g. F606W) to obtain a higher background and higher source counts may be useful. At present, we do not recommend the use of the post-flash capability for any applications, but we will continue to track this carefully. An exception might be for astrometry (see [ACS ISR 2007-04](#)) of relatively bright objects for which proposers may wish to consider use of post-flash.

7.1.8 Image Anomalies

The ACS was designed with a requirement that no single straylight feature may contain more than 0.1% of the detected energy in the object producing it. This goal has generally been met, but during the extensive ground and SMOV test programs a few exceptions have been identified (Hartig et al. 2002, Proc SPIE 4854) such as the WFC elliptical haloes and the F660N ghosts.

While some of these anomalies exceed the specified intensity, some judicious planning of your science observations is recommended to help alleviate their effect on your data, especially if bright sources are expected in the field of view. For instance, the impact of diffraction spikes (which for ACS lie along x and y axes) and of CCD blooming (which occurs along the y direction) due to saturation of a bright star(s), can be reduced by choosing an ORIENT which prevents the source of interest from being connected to the bright star along either of these axes. Alternatively, a suitable ORIENT could move the bright star(s) into the interchip gap or off the field of view altogether. Similarly, the impact of WFC elliptical haloes can be minimized by avoiding a bright star in the quadrant associated with amplifier D.

SBC observations of bright objects may show optical ghosts possibly due to reflection between the back and front sides of the filter.

More details about the ACS image anomalies can be found in the ACS Data Handbook and at

http://www.stsci.edu/hst/acs/performance/anomalies/ACS_ghosts.pdf

http://www.stsci.edu/hst/acs/performance/anomalies/ACS_scatter.pdf

http://www.stsci.edu/hst/acs/performance/anomalies/acs_sbc_opticalghosts.html

7.2 SBC Bright Object Protection

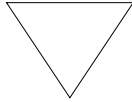
7.2.1 How Do You Determine if You Violate a Bright Object Limit for SBC Exposures?

High global and local count rates can cause catastrophic damage to the SBC detector. Therefore, targets should be checked to verify that their fluxes do not exceed the defined SBC safety limits. As a first step, you can check your source V magnitude and peak flux against the bright-object screening magnitudes in Table 7.4 for your chosen observing configuration. In many cases, your source properties will be much fainter than these limits, and you need not worry further.

However, the magnitudes in this table are hard screening limits that correspond to the count rate limits in Table 7.3 and the output of the [ACS Exposure Time Calculator](#). In earlier editions of this Handbook, these magnitudes were made fainter by arbitrary 1 or 2 magnitude pads, depending on the spectral-type range, which have now been removed. If your target is near these limits (within 2 magnitudes or a factor of 6.3 of the flux limits), then you need to carefully consider whether your source will be observable in the chosen configuration. Remember that the limits in these tables assume zero extinction. Thus, you will want to correct the limits appropriately for your source reddening due to interstellar dust.

You can use the information presented in Section 9.2 to calculate peak and global count rates. You can also use the [ACS Exposure-Time Calculator](#) to calculate the expected count rate from your source. The ETC has a host of template stellar spectrograms. If you have a spectrum of your source (e.g., from IUE, FOS, GHRS, or STIS) you can also use it directly in the calculator. As implied by the footnotes to Table 7.4, the model spectra in the ETC cannot be used for bright-object checking at the solar spectral type and later; the UV spectra of such stars are dominated by emission lines and continua not reproduced by the models. For these types, more realistic theoretical or observational input spectra (e.g., from the IUE or HST archives) must be used. The calculator will evaluate the global and per pixel count rates, and will warn you if your exposure exceeds the absolute bright-object limits. We recommend you use the [ACS Exposure Time Calculator](#) if you have *any doubt* that your exposure may exceed the bright-object MAMA limits.

7.2.2 Policy and Observers' Responsibility in Phase I and Phase II



It is the responsibility of the observer to ensure that observations do not exceed the bright-object count rate limits stated in Table 7.3. Please address this issue in your Phase I proposal.

It is your responsibility to ensure that you have checked your planned observations against the brightness limits prior to proposing for Phase I. If your proposal is accepted and we, or you, subsequently determine in Phase II that your source violates the absolute limits, then you will either have to change the configuration or target, if allowed, or lose the granted observing time. We request that you address the safety of your SBC targets and fields (i.e., all objects that will fall on the detector at the specified pointings and orientations) in your Phase I proposal. APT provides tools for this purpose, and you may consult with an ACS Instrument Scientist via the helpdesk if needed. For SBC target-of-opportunity proposals, please include in your Phase I proposal an explanation of how you will ensure your target can be safely observed.

In Phase II, proposers of SBC observations are required to check their targets and fields in detail for excessively bright sources, by the Phase II deadline. The relevant policies and procedures are described here.

STScI has developed bright object tools (BOT) to conduct detailed field checking prior to SBC program implementation. These tools are based on automated analysis of the fields by means of data from the second Guide Star Catalogue (GSC2) and displays of the Digital Sky Survey (DSS). GSC2 provides two magnitudes (photographic J and F), hence one color, for most fields down to about 22nd mag, which, combined with conservative spectral-type vs. color relationships, supports Exposure Time Calculator (ETC) determinations of safety or otherwise for individual objects. In the best cases, these procedures allow expeditious safety clearing, but in some cases the GSC2 is inadequate because of crowding or absence of one of the filters, for instance. Then supplementary information must be provided by the proposers to support the bright object protection (BOP) process. The target should always be checked directly in the ETC with the more detailed information generally available for it, rather than relying on its field report data.

STScI will check all targets and fields before any SBC observations are cleared. However, by policy GOs must provide screened, safe targets for SBC programs, and supplementary data as needed to verify target and field safety. The APT/BOT, including an Aladin interface, makes the BOP procedures accessible for GO use. Extensive help files and training movies

are available. While the procedures may appear complex on first exposure, their convenience and straightforward application rapidly become apparent. All SBC proposers must conduct BOP reviews of their targets and fields in conjunction with their Phase II preparations. Thus, they will become aware of any problems earlier, such as the need for supplementary data, which may otherwise entail lengthy implementation delays following the Phase II deadline. (An exception is moving target fields, which must be cleared after the scheduling windows have been established.) To assist with these procedures, a Contact Scientist (CS) who is an SBC/BOP specialist will be assigned to each SBC program, to interact with the GO as necessary and requested during the Phase II preparations, and through program execution.

Briefly, for a single default SBC pointing with unconstrained orientation, a field of 70 arcseconds in diameter must be cleared. The APT/BOT automatically reports on all GSC2 stars within that field. If any displacements from the default pointing (e.g., POS TARGs, patterns, or mosaics) are specified, the field to be cleared increases commensurately. POS TARG vectors and the enlarged, rotated field circles are conveniently displayed in APT/Aladin. No unsafe or unknown star may lie within 5 arcseconds of the detector edge at any orientation. Conversely, POS TARGs and orientation restrictions may be introduced to avoid bright objects in the fields. In case a single guide-star implementation becomes necessary, the field to be cleared increases to 140 arcseconds in diameter, but usually that will not become known until scheduling is attempted after the Phase II deadline.

An SBC GO must send his/her CS, by the Phase II deadline, ETC calculations for each discrete target, and reports on any unsafe or unknown stars from APT/BOT for each field, either showing that the observations are in fact safe, or documenting any unresolved issues. In the latter case, including inadequacy of BOT/GSC2 to clear the observations, other photometric or spectroscopic data sources must be sought by the GO to clear the fields. Many of these are available directly through the APT/Aladin interface (although automatic BOP calculations are available only with GSC2), including the STScI Multimission Archive (MAST), which contains the IUE and GALEX in addition to the HST data. An existing UV spectrogram of the target or class may be imported directly into the ETC; IUE data must be low resolution, large aperture for BOP. The NOMAD, SIMBAD, and NED compilations are often useful as well. In worst cases, new ground based data or WFPC2 UV exposures may be required to clear the fields for BOP; in general, the latter must be covered by the existing Phase I time allocation.

If a given star has only a V magnitude, it must be treated as an unreddened O5 star. (The older Kurucz O5 model with higher T_{eff} in the ETC should be used for BOP purposes.) If one color is available, it may be processed as a reddened O5 (which will always have a greater UV flux than

an unreddened star of the same color). If two colors are available, then the actual spectral type and reddening can be estimated separately. Many, usually faint, stars are reported as "unknown" by the APT/BOT because of only one or neither magnitude available. They must also be cleared. In the former case, Table 7.5 with the J and F O5 limits for each SBC configuration will be useful. These values have been calculated from the relationships in Appendix 2 of [ACS TIR 2007-01](#). In the latter case, stars with neither magnitude available that appear fainter than those below the F limit in the (red) DSS display can be ignored.

It is not expected that all such issues will be resolved by the Phase II deadline, but they should at least be identified and have planned resolutions by then. Another possible resolution is a change to a less sensitive SBC configuration. Any SBC targets or fields that cannot be demonstrated to be safe to a reasonable level of certainty in the judgement of the CS will not be observed. It is possible that equivalent alternative targets may be approved upon request in that case; but any observations that trigger the onboard safety mechanisms will not be replaced.

A related issue is SBC pointing specification changes after the targets and fields have been cleared by the STScI BOP review. Any such changes must be approved by the ACS Team on the basis of a specific scientific justification and a new BOP review by the GO, which may be submitted via the CS if absolutely necessary. However, in general such requests should be avoided by ensuring that submitted SBC specifications are final, to prevent a need for multiple BOP reviews.

GOs planning SBC observations of unpredictably variable targets, such as cataclysmic variables, are reminded of the special BOP procedures in effect for them, which are detailed in [ACS ISR 2006-04](#).

Table 7.3: Absolute SBC count rate screening limits for nonvariable and variable objects.

| Target | Limit type | Screening limit |
|-----------------------------------|------------|------------------------|
| Nonvariable | Global | 200,000 counts/second |
| Nonvariable | Local | 50 counts/second/pixel |
| Irregularly variable ¹ | Global | 80,000 counts/second |
| Irregularly variable ¹ | Local | 20 counts/second/pixel |

1. Applies to the brightest state of the target.

The limits for irregular variable sources are a factor 2.5 more conservative than for sources with predictable fluxes. Predictable variables are treated as nonvariable for this purpose. Examples of sources whose variability is predictable are Cepheids or eclipsing binaries. Irregularly variable sources are, for instance, cataclysmic variables or AGN.

Table 7.4: Bright limit V-band magnitudes for observations with the SBC filters and prisms (no reddening).

| Spectral type | Log T _{eff} | F122M | F115LP | F125LP | F140LP | F150LP | F165LP | PR110L | PR130L |
|---------------------|----------------------|-------|--------|--------|--------|--------|--------|--------|--------|
| O5 V | 4.648 | 16.1 | 19.2 | 19.0 | 18.5 | 18.0 | 16.6 | 15.8 | 15.5 |
| B1 V | 4.405 | 15.2 | 18.4 | 18.2 | 17.7 | 17.1 | 15.7 | 15.0 | 14.7 |
| B3 V | 4.271 | 14.3 | 17.6 | 17.5 | 17.0 | 16.4 | 15.2 | 14.2 | 14.0 |
| B5 V | 4.188 | 13.5 | 17.0 | 16.9 | 16.5 | 15.9 | 14.7 | 13.7 | 13.4 |
| B8 V | 4.077 | 12.0 | 15.9 | 15.9 | 15.5 | 15.0 | 13.8 | 12.7 | 12.5 |
| A1 V | 3.965 | 9.4 | 14.0 | 13.9 | 13.8 | 13.6 | 12.6 | 11.1 | 11.0 |
| A3 V | 3.940 | 8.2 | 13.0 | 13.0 | 12.9 | 12.8 | 12.2 | 10.5 | 10.3 |
| A5 V | 3.914 | 6.8 | 11.9 | 11.9 | 11.9 | 11.9 | 11.6 | 9.9 | 9.8 |
| F0 V | 3.857 | 4.8 | 10.0 | 10.0 | 10.0 | 10.0 | 9.8 | 8.2 | 8.2 |
| F2 V | 3.838 | 4.0 | 9.0 | 9.0 | 9.0 | 9.0 | 9.0 | 7.5 | 7.5 |
| F5 V | 3.809 | 2.1 | 7.4 | 7.4 | 7.4 | 7.4 | 7.3 | 5.9 | 5.8 |
| F8 V | 3.792 | 0.9 | 6.2 | 6.2 | 6.2 | 6.1 | 6.1 | 4.7 | 4.7 |
| G2 V ² | --- | 2.2 | 5.6 | 5.2 | 5.1 | 5.0 | 4.7 | 3.1 | 3.1 |
| G8 V ³ | --- | --- | 5.1 | 5.0 | 4.8 | 4.6 | 3.9 | 2.1 | 2.0 |
| K2 V ⁴ | --- | --- | 5.1 | 5.1 | 4.8 | 4.5 | 3.6 | 3.1 | 3.0 |
| KM III ⁵ | --- | --- | 3.7 | 3.7 | 3.2 | 2.8 | 1.8 | 1.6 | 1.1 |
| Binary ⁶ | --- | 14.4 | 17.5 | 17.3 | 16.8 | 16.3 | 14.9 | 14.1 | 13.8 |

- O5 V through F8 V values are based on Kurucz models.
- The magnitudes listed for G2 V are for the Solar template in the [ACS Exposure Time Calculator](#).
- The magnitudes listed for G8 V are from IUE data for the star Tau Ceti.
- The magnitudes listed for K2 V are from IUE data for the star Epsilon Eri.
- The magnitudes listed for KM III are from IUE data for 9 stars of these types.
- System made of a late-type star with an O5 companion contributing 20% to the total light in the V band. In the UV, the O5 component dominates and sets the same magnitude limit for companion types A to M.

Table 7.5: Bright limit J- and F-band magnitudes of an unreddened O5 star for observations with the SBC filters and prisms.

| Band | F122M | F115LP | F125LP | F140LP | F150LP | F165LP | PR110L | PR130L |
|------|-------|--------|--------|--------|--------|--------|--------|--------|
| J | 15.8 | 18.9 | 18.7 | 18.2 | 17.7 | 16.3 | 15.5 | 15.2 |
| F | 16.3 | 19.4 | 19.2 | 18.7 | 18.2 | 16.8 | 16.0 | 15.7 |

In some cases, the 2MASS JHK may be the only photometry available for an otherwise "unknown" star. It is possible to estimate V and E(B-V)

from those data on the assumption of a reddened O5 star, and thus determine its countrates in the ETC. F. Martins & B. Plez, *A&A*, 457, 637 (2006), derive $(J-H)_0 = -0.11$ for all O stars; and $(V-J)_0 = -0.67$, $(V-H)_0 = -0.79$ for early O types. (The K band should be avoided for BOP because of various instrumental and astrophysical complications.) M.S. Bessell & J.M. Brett, *PASP*, 100, 1134 (1988), Appendix B, give relationships between the NIR reddenings and $E(B-V)$. These data determine the necessary parameters. Note that the ETC also supports direct entry of observed J, H magnitudes with $E(B-V)$.

Policy on Observations Which Fail Because they Exceed Bright-Object Limits

If your source passes screening, but causes the automatic flight checking to shutter your exposures or shut down the detector voltage causing the loss of your observing time, *then that lost time will not be returned to you*; it is the observer's responsibility to ensure that observations do not exceed the bright-object limits.

7.2.3 Bright-Object Protection for Solar System Observations

Observations of planets with the SBC require particularly careful planning due to very stringent overlight limits. In principle, Table 7.3 and Table 7.4 can be used to determine if a particular observation of a solar-system target exceeds the safety limit. In practice, the simplest and most straightforward method of checking the bright object limits for a particular observation is to use the [ACS Exposure-Time Calculator](#). With a user-supplied input spectrum, or assumptions about the spectral energy distribution of the target, the ETC will determine whether a specified observation violates any bright object limits.

Generally speaking, for small ($< \sim 0.5$ to 1 arcseconds) solar-system objects the local count rate limit is the more restrictive constraint, while for large objects ($> \sim 1$ to 2 arcseconds) the global limit is more restrictive.

As a first approximation, small solar system targets can be regarded as point sources with a solar (G2 V) spectrum, and if the V magnitude is known, Table 7.3 and Table 7.4 can be used to estimate whether an observation with a particular ACS prism or filter is near the bright-object limits. V magnitudes for the most common solar-system targets (all planets and satellites, and the principal minor planets) can be found in the *Astronomical Almanac*. This approximation should provide a conservative estimate, particularly for the local limit, because it is equivalent to assuming that all the flux from the target falls on a single pixel, which is an overestimate, and because the albedos of solar-system objects in the UV are almost always significantly less than their values in the visible part of

the spectrum. A very conservative estimate of the global count rate can be obtained by estimating the peak (local) count rate assuming all the flux falls on one pixel, and then multiplying by the number of pixels subtended by the target. If these simple estimates produce numbers near the bright-object limits, more sophisticated estimates may be required to provide assurance that the object is not too bright to observe in a particular configuration.

For large solar-system targets, checking of the bright-object limits is most conveniently done by converting the integrated V magnitude (V_0 , which can be found in the *Astronomical Almanac*) to V magnitude/arcseconds² as follows:

$$V/(\text{arcsec}^2) = V_0 - 2.5\log(1/\text{area})$$

where *area* is the area of the target in arcseconds². This surface brightness and the diameter of the target in arcseconds can then be input into the [ETC](#) (choose the solar template spectrum for the spectral energy distribution) to test whether the bright-object limits are satisfied.

7.2.4 Prime and Parallel Observing with the SBC

STScI will perform screening of all SBC exposures prior to scheduling. Targets not established as safe for the configuration in which they are being observed will not be scheduled. Observations that pass screening but are lost in orbit due to a bright-object violation will not be rescheduled. Observers are responsible for ensuring that their observations do not violate the SBC count-rate limits.

To ensure that STScI can adequately screen observations, special constraints are imposed on parallel observing with the SBC. In particular:

- No pure parallels are allowed using the SBC.
- Coordinated parallels are allowed with the SBC only if an exact spacecraft orientation (**ORIENT**) is requested, and the RA and Declination of the parallel field are determined. Note that the specification of an exact **ORIENT** usually limits the scheduling of observations each year. The observer is responsible for ensuring that observations do not violate the SBC count rate limits both for coordinated parallel SBC observations and for prime observations.
- **SNAPSHOT** observations with the SBC are not allowed

Table 7.6: Bright object protection policy for SBC observations.

| Type of observing | Policy |
|----------------------|--|
| Prime | Allowed if target passes screening |
| Snapshots | Not allowed |
| Coordinated parallel | Allowed only if ORIENT is exactly specified and field passes screening |
| Pure parallel | Not allowed |

Targets that are one magnitude or more fainter than the magnitude limits in the screening tables generally automatically pass screening. For a target that is within one magnitude of the screening limits, observers must provide a calibrated spectrum of the source at the intended observing wavelength. If such a spectrum is not available, the prospective GO must request an orbit in Phase I for a pre-qualification exposure, during which the target spectrum must be determined by observation in an allowed configuration.

Please note that if you are proposing SBC target-of-opportunity observations, we ask you to provide an explanation in your Phase I proposal of how you will ensure that your target can be safely observed.

7.3 Operating Modes

ACS supports two types of operating modes:

- **ACCUM** for each of the cameras. This is the standard data taking mode used by observers.
- **ACQ** (acquisition). This is the mode used to acquire a target for coronagraphic observations. ACQ is only available with the HRC.

7.3.1 WFC ACCUM Mode

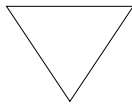
In this mode the WFC CCD accumulates signal during the exposure in response to photons. The charge is read out at the end of the exposure and translated by the A-to-D converter into a 16 bit data number (DN), ranging from 0 to 65,535. The number of electrons per DN can be specified by the user as the GAIN value. The full well of the WFC CCD is about 85,000 electrons and consequently, all GAIN values larger than 1 will allow the observer to count up to the full well capacity. For GAIN=1 only 75% of full well capacity is reached when the DN value saturates at 65,535. The read-out noise of the WFC CCD is about 5 electrons rms and thus it is critically sampled even at GAIN=2. WFC can make use of a

user-transparent, lossless, on-board compression algorithm, the benefits of which will be discussed in the context of parallel observations. The algorithm is more effective with higher GAIN values (i.e. when the noise is undersampled).

Fifteen supported apertures, (see Table 7.7) are accessible to WFC users. WFC1-FIX and WFC2-FIX select the geometric centers of the two WFC camera chips. WFCENTER corresponds to the geometric center of the combined WFC field, and will be useful for facilitating mosaics and obtaining observations at multiple orientations. WFC, WFC1, and WFC2 are located near the field of view center and the centers of chips 1 and 2, respectively. Their locations were chosen to be free of detector blemishes and hot pixels, and they are the preferred apertures for typical observations. See Section 7.7 for more details about ACS apertures, including subarray apertures.

Usually each CCD is read from two amplifiers to minimize charge transfer efficiency (CTE) problems and read-out time. As a result, the two 2K by 2K portions in a single chip may have slightly different read-out noise. The WFC chips have both physical and virtual overscans that can be used to estimate the bias level and the read-out noise on each single image.

The ACS internal buffer can store only a single full frame WFC image. When this image is compressed, and depending on the compression factor, the buffer can store additional HRC and SBC images. As a consequence of the implementation of the compression strategy, under no circumstance can more than one full frame WFC image be stored in the buffer. Note that the adopted policy is not to compress primary WFC observations. The present flight software does not allow reading an ACS frame directly into the HST on-board recorder. Images have to be first stored in the internal buffer. When more than one WFC image is obtained during an orbit a buffer dump must occur during the visibility period so as to create space in the buffer for a new WFC image.



If each exposure is longer than approximately 339 seconds, buffer dumps can occur during the integration of the following image with no impact on observing efficiency.

Conversely, short, full frame, integrations with the WFC during the same orbit will cause buffer dumps to be interleaved with observations and will negatively affect the observing efficiency. See Chapter 8 for more details about ACS overheads.

WFC CCD Subarrays

It is possible to read-out only a portion of a detector with subarrays, which have a smaller size than the full frame. Subarrays are used to reduce

data volume, to store more frames in the internal buffer (thus avoiding the efficiency loss due to buffer dumps), or to read only the relevant portion of the detector when imaging with ramp filters or with HRC filters (which produce a vignetted field of view on WFC). WFC subarrays have some limitations:

1. They can be specified only on a single WFC chip;
2. They may have physical but no virtual overscan;
3. They cannot include the CCD edge (i.e. the maximum subarray size is 4140 by 2046); and
4. They are read through a single amplifier and may take longer to read-out than a full-frame image, depending on size and location.

Users can use WFC subarrays either by specifying a supported pre-defined subarray (which is recommended) or by defining their own general subarrays. For supported subarrays, the dark, flat, and bias frames used for calibration will simply be extracted from available full-frame images. Tests have shown that this does not degrade the quality of the dark, flat-field or bias corrections, as compared to full-frame data. However, this is true only for subarrays that fall entirely within a single amplifier quadrant and include a corner section with the overscan (true for all the supported subarrays). Users who define general subarrays that cross amplifier boundaries or do not include a corner (not advised) must request their own subarray bias images, and these will typically be scheduled during the following occultation. In some special cases where a general subarray is cleverly defined so as to include a physical overscan region, no separate bias frames are needed.

Pre-defined subarrays are the appropriate choice for observing a small target when lessening the data volume is desired. These supported subarrays for WFC are invoked by using the named apertures WFC1-1K, WFC1-2K, and WFC1-512. On WFC1, at the amplifier B corner there are square apertures WFC1-512, WFC1-1K, and WFC1-2K with light collecting areas being squares with sides of length 512, 1024, and 2048 pixels. A 2048 pixel aperture is available at the amplifier D corner of WFC2 called WFC2-2K. These all incorporate 22 columns of the physical overscan pixels. These have been chosen bearing in mind that as charge transfer efficiency degrades with radiation damage to the detectors, there is an advantage in being close to the readout amplifier. The reference pixel and extent of the subarrays are listed in Table 7.7. More information about pre-defined subarray apertures can be found in Section 7.7

To define a general subarray, the available-but-unsupported parameters SIZEAXIS1, SIZEAXIS2, CENTERAXIS1, and CENTERAXIS2 can be used. More practical information about defining subarrays can be found at <http://www.stsci.edu/hst/acs/faqs/subarrays.html>. When polarizers or the small HRC filter F892N are used with the WFC, the aperture WFC

must be selected and a subarray is forced by the system. If the user chooses to use a polarizer with a ramp filter, then they may select an available-but-unsupported ramp aperture, but a subarray is still read out.

Ramp Filters

Unlike WFPC2, ACS ramp filter observations at different wavelengths are obtained at the same location on the CCD, thus simplifying data processing. In practice the observer specifies a ramp filter and a central wavelength; the filter wheel is automatically rotated to place the central wavelength at the reference point of the relevant aperture. The different ramp apertures and their reference points on the WFC chips are shown in Table 7.7 and Figure 7.4. To select the desired wavelength, the ramp filter is rotated to move the appropriate part of the filter over the specified pointing. Observations with different ramp filters do not generally occur at the same pointing. The precise location where a given observation will be performed can be found from Table 7.7 where for each ramp filter we list the fiducial pointing for the inner IRAMP, middle MRAMP, and outer ORAMP filter segment. The inner segment corresponds to the WFC1 chip, while the outer segment corresponds to the WFC2 chip. The middle segment can be used with either of the WFC chips but is used by default with WFC1. For any ramp filter observation three ramp filters will end up in the FOV even though the target is properly positioned only for the requested one. Or, if desired, the user can define a general subarray to readout only a portion of the chip. Table 5.1 and Table 5.2 can be used to determine the remaining two ramp filter segments which can be of interest for serendipitous observations. While all fifteen ramp segments can be used with the WFC, only the five middle ramp segments are available with the HRC. Ramps used with the HRC cover the region over the HRC chip defined by the HRC aperture (Table 7.9). Please refer to Section 7.7.2 and Section 5.3.1 for further information.

7.3.2 HRC ACCUM Mode

In this mode the HRC CCD accumulates signal during the exposure in response to photons. The charge is read out at the end of the exposure, and translated by the A-to-D converter into a 16 bit data number (DN) ranging from 0 to 65,535. The number of electrons per DN can be specified by the user as the GAIN value. The full well of the HRC CCD is about 155,000 electrons. In order not to overflow the 16 bit pixel word size, one needs to use GAIN=4. In many applications GAIN=2 is adequate since it still allows critical sampling of the read-out noise of HRC (about 4.7 electrons rms) and, for this reason, it is the default GAIN ratio. For typical HRC observations the observer should specify the HRC aperture which is approximately located at the center of the field of view in a location free of detector blemishes and hot pixels. The HRC-FIX aperture is located at the geometric center of the field-of-view. Additional apertures

are used for coronagraphic observations - see Table 7.9 for more details of HRC apertures.

Up to 16 HRC images can be stored in the ACS buffer. Alternatively, HRC images can share the buffer with some SBC images and/or a single compressed WFC image. The number of HRC images will depend in the latter case on the WFC compression factor.

HRC CCD Subarrays

Similarly to the WFC, a subarray is obtained when only a portion of the detector is read-out and transmitted to the ground. Generally the smaller size of the HRC CCD reduces the usefulness of subarrays. However, subarrays are used during on-board coronagraphic target acquisition, which is similar to the STIS target acquisition and cannot be changed. A square subarray of 512 x 512 pixels in the C Amp readout corner and a 512 pixel square aperture centered on the 1.8 arcseconds coronagraphic spot are available. In addition, on an available-but-unsupported basis, nearly arbitrary sizes and locations for subarrays can be specified. When coupling use of subarrays with PATTERNS or POS TARGs, the issue arises of whether to keep the subarray fixed in pixel space, or have it track and stay centered on the target. With PATTERNS, the subarray stays fixed in pixel space. When using POS TARGs, the observer can decide which mode to adopt.

7.3.3 SBC ACCUM Mode

The SBC ACCUM mode accumulates photons into a 1024 by 1024 array, with 16 bits per pixel. The data are sent to the onboard recorder via the internal ACS memory buffer at the end of the exposure. ACCUM is the only mode available for SBC observations; the Time Tag mode of the STIS MAMAs is not available on ACS. The minimum SBC exposure time is 0.1 seconds and the maximum is 1.0 hour. The minimum time between SBC exposures is 40 seconds. Note that the SBC, like the STIS MAMAs, has no read-out noise. As a consequence there is no scientific driver for longer exposure times apart from the small overhead between successive images, described in Section 8.2.

Up to 16 SBC images can be stored in the internal buffer. SBC images can also share the buffer with HRC images and/or a single, compressed WFC image.

7.3.4 HRC ACQ Mode

The HRC target acquisition mode is used to place a target under the occulting finger or the coronagraphic mask. Observations through two (non-polarizer) filters are allowed in ACQ images to cut down the flux to acceptable levels for very bright targets. Due to the optical design of HRC the simultaneous use of two filters leads to a degraded imaging quality but

which is still acceptable for a successful target acquisition. The ACS IDT has identified a number of filter combinations that effectively act as neutral density filters, and allow the observer to acquire a very bright target that would otherwise saturate the CCD. These filter pairs are F220W+F606W, F220W+F550M, and F220W+F502N in order of decreasing transmission. A more complete description of the target acquisition procedure is given in Section 6.2.2.

7.4 Patterns and Dithering

A number of different patterns are available for ACS to support dithered observations, i.e., observations where the pointing is shifted between frames. The size of the offsets can be very different depending on the purpose of offsetting the pointing between exposures. In particular, it is useful to distinguish between *mosaicing* and *dithering*. Mosaicing is done with the aim of increasing the area covered by a particular set of exposures, while providing a seamless joining of contiguous frames. Dithering is done for a variety of reasons, such as:

- better removal of detector blemishes,
- straightforward removal of hot pixels,
- improving the PSF sampling,
- improving the photometric accuracy by averaging over flat fielding errors and
- obtaining a contiguous field of view for the WFC (filling in the inter-chip gap).

Patterns have been defined to allow ACS users to easily carry out both mosaicing and dithering. Using patterns allows exposures to be automatically associated in *calacs* pipeline processing with the following restrictions: only pattern exposures obtained within a single visit, and those patterns where the cumulative offset is under the ~ 100 arcsecond guide star limitation, can be associated. For the latter, these patterns include the dither patterns for all three cameras, the HRC and SBC mosaic patterns, the 2-point ACS-WFC-MOSAIC-LINE pattern, and all patterns designed with POS TARGs. These are described in detail on the ACS Dither Web page:

<http://www.stsci.edu/hst/acs/proposing/dither>.

The plate scale for the WFC varies by about $\pm 5\%$, so a one pixel dither near the center will be 0.95 or 1.05 pixels near the corners. For this reason, dither patterns should strike a balance between being large enough to reject detector artifacts, and being as compact as possible to maintain the integrity of the pattern over the entire field-of-view. Large displacements will have varying sub-pixel properties across the image.

In addition to the plate scale variation associated with the significant ACS geometric distortion, there can also be a temporal variation of overall image alignment. Some CR-SPLIT images taken during SMOV testing, in which the two components were separated by the scheduling system across orbital occultations (about a one hour gap), showed registration differences of about 0.5 pixels corner-to-corner. Thus, to combine multiple images to create oversampled images at the resolution ACS is capable of providing, the user may need to allow for the general problem of combining distorted, misregistered images. A variety of tools are being made available within STSDAS and **pyraf** to assist with these tasks including *pydrizzle* and *multidrizzle*. See the [ACS Drizzle Web](#) page and the *ACS Data Handbook*.

Additional information on dithering, and processing drizzled data using *multidrizzle* can be obtained from the *Dither Handbook*

7.5 A Road Map for Optimizing Observations

Dithering and CR-SPLITting more than the minimum recommended values tends to yield higher quality images with fewer residual detector defects, hot pixels or CR signatures in the final combined image. Dithering is recommended over CR-SPLITS since it allows the removal of both detectors artifacts (hot pixels, bad columns, etc.) and cosmic rays. Unfortunately, splitting a given exposure time into several exposures reduces its signal-to-noise when a noise-limited image is read-out. WFC images longer than about 500 seconds are background limited, while shorter exposures and narrow band images are read-out noise limited for all practical exposure times. Thus, the optimal number of CR-SPLITS and dithering positions is a result of a trade-off between completeness of the hot pixel elimination, CR-rejection, final image quality, and optimal S/N. A schematic flow chart of this trade-off is given in Figure 7.2. The main steps in this, possibly iterative, process are the following:

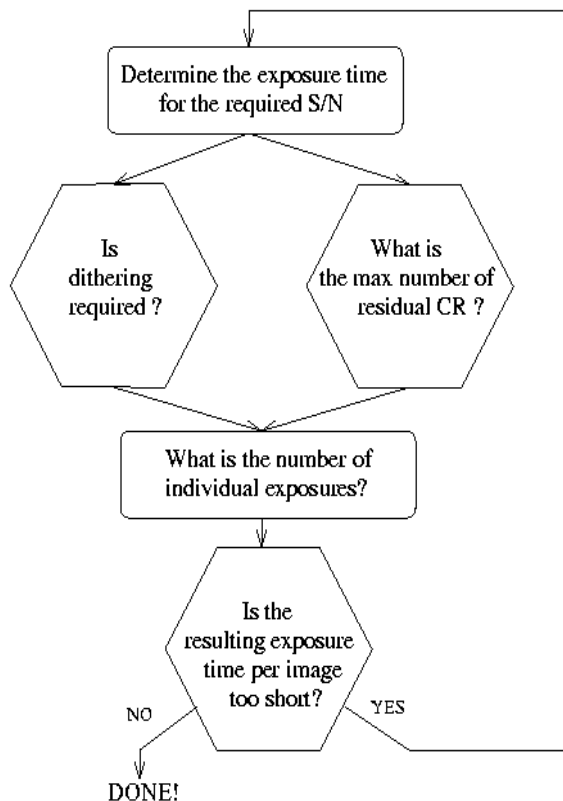
1. Determine the exposure time required to achieve the desired S/N
2. Determine the maximum number of acceptable residual CR in the final combined image. This number depends critically on the scientific objective. For example, for a survey of distant galaxies or a globular cluster color magnitude diagram, a few residual CR will not compromise the scientific output of the observations. In contrast, for a search for an optical counterpart of some radio or gamma ray selected object even one residual CR would not be acceptable over the region of interest. In this latter case, since we expect about ~4% to 7% of the pixels to be affected by CR hits during a one orbit exposure on the WFC, the requirement that no pixel in the final image is affected by CR hits would force one to use at least 4 sub-exposures.

For an experiment in which the number of allowed false alarms is zero (e.g., a search for cosmological supernovae), observers may wish to consider using at least twice the number of sub-exposures required to formally avoid coincidences. Note also that given the large number of pixels in the WFC even a few thousand residual CR hits would correspond to only a small fraction of the total number of pixels. In general, the number of pixels affected by coincident CR hits for a given total exposure time and number of sub-exposures N will be:

$$\left(0.05 \times \frac{\text{ExposureTime}}{2400s \times N}\right)^N \times 4096^2$$

3. Determine whether dithering is required. CR-SPLITs have no effect on hot pixels, which result from CCD radiation damage and which persist for about weeks or indefinitely. If such features would critically affect the science, then dithering is required to remove them. For some imaging programs the spatial resolution provided by the WFC and the presence of some detector defects and hot pixels in the final image are acceptable. For such observations, dithering would not be required and one would simply split the exposure time for CR correction. For observations where several orbits worth of data are obtained with each filter, the best strategy is to observe using a sub-pixel dither pattern *without* obtaining multiple images at each position. Since each CR will now influence more than one output pixel the requirement on the number of separate exposures is more stringent than in the simple CR-SPLIT case. If the total exposure time with each filter is short, one will have to compromise between S/N and image quality. In general, dithering with sub-pixel steps increases the number of individual exposures required to eliminate CR hits. Given that the geometric distortion of WFC makes any dithering step non-integer somewhere in the field of view (unless the dither steps are very small, < 2 pixels), the size of the high image quality field of view also comes into play. If the high quality area is small, one may make do with integer pixel dithers. In this case a few CR-SPLITs may be obtained at each dithering position and the combined images may then be combined together using *drizzle* or *multidrizzle*. On the edges of the field the CR-rejection quality will be lower than in the field center. A minimum of 4 images for a two position dither, and 8 for a four position dither are then required.
4. Once the required number of individual exposures has been established on the basis of CR rejection and dithering requirements, the observer will need to verify whether the resulting read-out noise affects the achieved S/N.

Figure 7.2: Schematic flow-chart of the CR-split vs. dithering vs. S/N trade-off.



7.6 CCD Gain Selection

As quantified in Table 4.1 both the WFC and HRC CCDs have selectable gain values near 1, 2, 4, and 8 electrons per digital number. Various factors should influence the gain selected in Phase II for your science program: level of support and calibrations provided, influence of associated readout noise on data quality, dynamic range on the bright end, and data compressibility for WFC in limited applications.

7.6.1 WFC Gain

GAINS 1 and 2 are fully supported for the WFC, since GAIN=1 provides the smallest readout noise, while GAIN=2 (or higher) is needed to sample the available full well depth. It is the goal, now closely achieved, to provide equal calibration support for data taken in these two supported gains, although more calibration data will be taken in the default GAIN=2 setting. Calibration support will not be provided for the

“available-but-unsupported” GAIN=4 and 8 settings; users proposing their use should provide special justification and discussion of calibrations to be used. Note that WFC auto-parallel data is taken with GAIN=2.

While the readout noise is lower at GAIN=1, the advantage over GAIN=2 ($< 0.3 e^-$ extra rms) is modest. GAIN=2 has the offsetting advantage of completely sampling the full well depth of nearly 85,000 e^- , thus providing a > 0.3 magnitudes dynamic range extension before saturation is reached. The latter could be advantageous even for programs in which the prime targets are very faint, if serendipitous objects in the field of view can be used to support image-to-image registration solutions as needed for optimal dithered image combinations. Furthermore, charge is conserved even beyond filling the full well depth; for point sources at GAIN=2 it is possible to obtain valid aperture photometry several magnitudes beyond saturation by summing over all pixels bled into. Both GAINs 1 and 2 provide better than critical sampling of the readout noise supporting robust background sky-level determination even at low values. Evidence also suggests that a minor electronic cross-talk feature is relatively less pronounced with GAIN=2 than GAIN=1 (see [ACS ISR 2004-13](#)).

The large pixel count for WFC can create data rate problems if images are acquired as quickly as possible over multiple orbits. The available-but-unsupported mode COMPRESSION is more effective when the noise is undersampled which could result in special circumstances for which the GAIN values of 4 or 8 are preferred.

7.6.2 HRC Gain

GAINs 2 and 4 are fully supported for the HRC, and analogous to the supported WFC values provide a low readout noise case and a GAIN that provides sampling of the physical full well depth.

GAIN=4 on the HRC, which is needed if high dynamic range on the bright end is desired, does not provide critical sampling of the readout noise. Not only is the readout noise penalty in going from GAIN=2 to 4 non-trivial, but background estimation will be less robust without critical noise sampling. As with WFC, when the full well depth is sampled with GAIN=4 the detector response remains accurately linear up to and even well beyond saturation. Compression is not an issue for the small HRC images, therefore use of the unsupported GAIN=8 is not anticipated. GAIN=1 is available-but-unsupported, but the very modest improvement of readout noise in comparison to GAIN=2 ($< 0.2 e^-$ higher rms) seems unlikely to present compelling need for its use.

7.7 ACS Apertures

As discussed in Section 3.3, the ACS consists of three cameras: the WFC, the HRC, and the SBC. The WFC is constructed of two CCDs each nominally 2048 by 4096 pixels, with their long sides adjacent to form a roughly square array, 4096 pixels on a side. The HRC CCD and the SBC MAMA detectors are each 1024 pixels square.

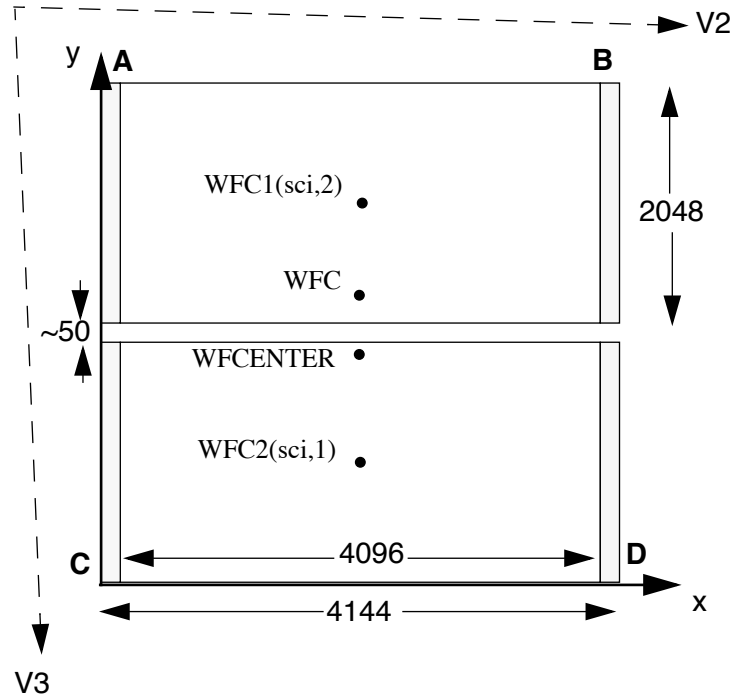
7.7.1 WFC Apertures

The active image area of each WFC detector is 4096 by 2048. The mean scale is 0.049 arcseconds/pixel, and the combined detectors cover an approximately square area of 202 arcseconds on a side. In establishing reference pixel positions we have to consider the overscan pixel areas which extend 24 pixels beyond the edges in the long direction. So each CCD must be regarded as a 4144 by 2048 pixel area. The gap between the two CCDs is equivalent to 50 pixels. In Figure 7.3 the letters A, B, C, and D show the corner locations of the four readout amps.

We define apertures named WFC1 and WFC2 which represent the two CCDs, with their reference points near the geometric center of each chip. The positions have been moved about 50 pixels from the center line to avoid a discontinuity at the amplifier readout boundary. However, we keep two other apertures named WFC1-FIX and WFC2-FIX at the original central locations (2072,1024). For extended sources, choosing new positions may not be of any advantage and it may be more effective to use these fixed positions.

The aperture WFC encompasses both detectors, and has its reference point near the overall center but about 10 arcseconds away from the interchip gap. This has been chosen to be position (2124,200) on the WFC1 CCD. Again, this has been moved away from the center line, but the reference point for WFC-FIX remains at (2073,200). Selection of WFC1, WFC2 or WFC only changes the pixel where the target will be positioned. In all three cases data is normally delivered in a file containing two imsets, one for each detector. See the *ACS Data Handbook* for details of the ACS data format. Reading out a subarray, which consists of part of only one of the chips, is done only if requested.

Figure 7.3: WFC aperture definitions.



WFCENTER is similar to WFC, but is placed at the center of the combined WFC full field. The center is defined as the average of the four corners in the distortion corrected space. Because of the scale variation this does not appear at the center in pixel space, but rather is on WFC2 about 20 pixels from the edge. Selection of WFCENTER can be of use in obtaining observations with maximum overlap at unique orientations and for mosaics.

For sets of observations which take place over a substantial part of a year, the telescope roll limitations will require measurements to be taken over most of the angular range. On sky, the WFC aperture is roughly square, and it is natural to design observations in steps of 90° to consistently cover the same area. There will be some region at the edges not covered at all four orientations. However, a square area of side 194.8 arcseconds centered on WFCENTER, and with edges parallel to the V2 and V3 axes, is overlapped at all four positions. In designing a mosaic which combines observations at 90° steps, a translation of about 190 arcseconds between pointings would provide continuous coverage.

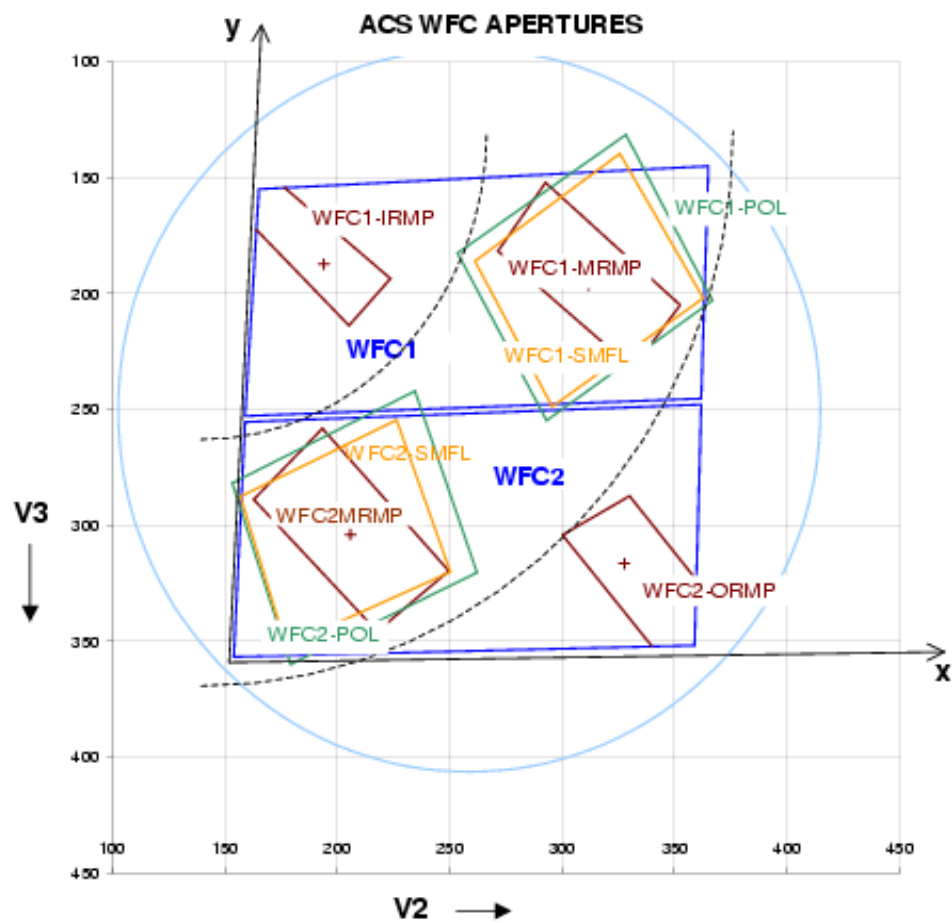
7.7.2 Ramp Filter Apertures

WFC Ramp Filter Apertures

There are five ramp filters. Each ramp filter consists of three segments (inner, middle, outer) that can be rotated across the WFC field of view as

indicated in Figure 7.4. The IRAMP filters can only be placed on WFC1 in a location which will define the aperture WFC1-IRAMP and the ORAMP filters only on WFC2 creating the aperture WFC2-ORAMP. The MRAMP filters can lie on WFC1 or WFC2 with corresponding apertures WFC1-MRAMP and WFC2-MRAMP. The approximate aperture locations are indicated in Figure 7.4, while actual data obtained during ground calibrations are overlaid on an image of a ramp filter in Figure 7.5. Operationally, a fixed reference point will be defined for each detector and filter combination. Then the ramp filter will be rotated to place the required wavelength at the reference position.

Figure 7.4: Schematic WFC apertures and ramp filters.



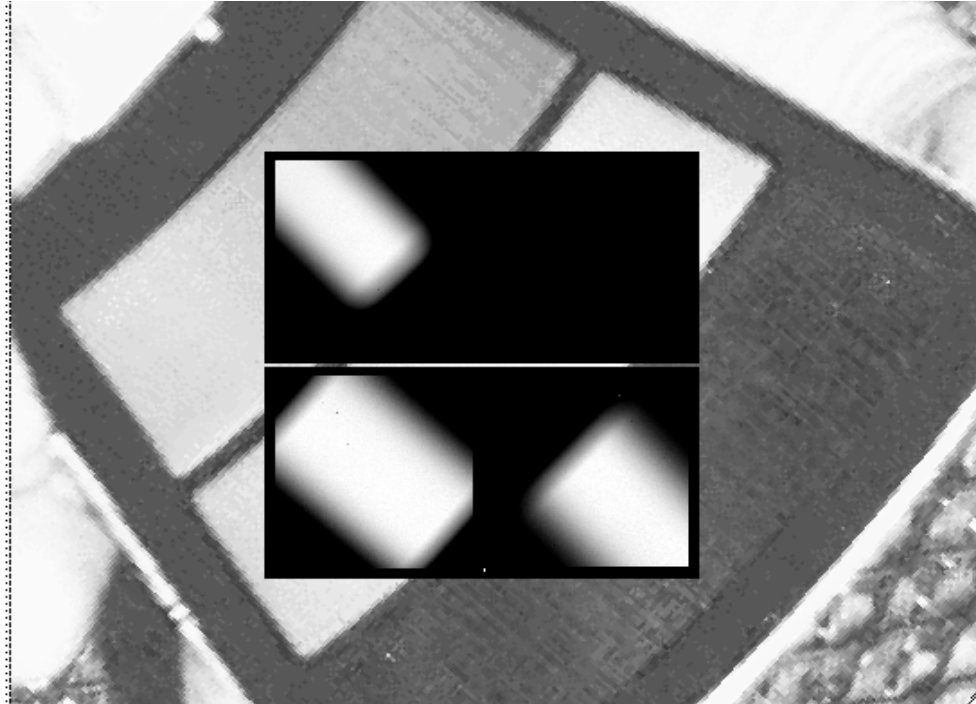
Shown are the approximate active areas defined by the filters. The actual readout areas are the quadrants for the polarizers and small (HRC) filters, and either the quadrant or the full chip for the ramp filters.

The reference positions for all defined apertures are given in Table 7.7 in pixels, and in the telescope V2,V3 reference frame where values are measured in arcseconds. The values given here are based on in-flight calibration results. The x and y axis angles are measured in degrees from the V3 axis towards the V2 axis. This is in the same sense as measuring from North to East on the sky. The “extent” of the ramp filter apertures given in Table 7.6 are the FWHM of the monochromatic patches (visible in

Figure 7.4) measured from a small sample of ground calibration data. To use a ramp filter in a Phase II program, specify the filter name, the central wavelength, and the aperture. The scheduling software will then automatically rotate the filter to the appropriate wavelength, and point at the reference point of the aperture chosen.

The aperture chosen may either be the full chip or just the quadrant on which the ramp filter lies. This second choice was new as of Cycle 15, and requires that the aperture be specified. The apertures matching each filter are given in Table 7.7. Those with names ending in Q are the quadrants. It will normally be preferable to choose the quadrant aperture to save data volume and buffer dumping time. All listed apertures will be supported and may also be used with non-ramp filters. A target may thereby be put at the same position using a ramp and a non-ramp filter.

Figure 7.5: Monochromatic patches in ground calibration data showing actual aperture sizes through ramp filters (superimposed on photo of ramp filters).



HRC Ramp Filter Apertures

Only the middle segments of the five ramp filters can be used with the HRC. They are FR914M, FR459M, FR505N, FR388N and FR656N. All five middle segments can be used with any of the HRC apertures listed in Table 7.8 (see Table 7.9 for the aperture reference positions). There are no special ramp apertures with the HRC because when a ramp filter is used with the HRC it covers the entire region over the HRC chip. This region is defined by the HRC aperture in Table 7.9. To use the HRC-512 or HRC-SUB1.8 subarray apertures with a ramp filter, POS TARGs will have to be used to align the aperture correctly.

As with the WFC, to use a ramp filter specify the filter name, the wavelength and the aperture in the Phase II proposal. The fixed reference

point is defined operationally depending on the detector, aperture and filter combination. Please refer to Section 7.3.1, Section 5.3.1, and [ACS ISR 02-01](#) for further information.

7.7.3 The Small Filter Apertures

When a filter designed for the HRC is used with the WFC, it only covers a small area on either WFC1 or WFC2. The projected filter position may be placed on either chip by selection of the filter wheel setting. Figure 7.4 shows how the filter projection may be placed so as to avoid the borders of the chips. When a WFC observation is proposed using a HRC filter spacecraft commanding software automatically uses internal built-in apertures designed for these observing scenarios, called WFC1-SMFL and WFC2-SMFL. Reference positions at or near the center of these apertures are defined so that a target may be placed in the region covered by the chosen filter.

The axis angles given in Table 7.7 do not refer to the edges of the apertures as drawn, but rather to the orientation of the x and y axes at the WFC reference pixel. These angles vary slightly with position due to geometric distortion.

For the polarizers and F892N used with WFC, the default will be to read out a subarray. The subarray will be a rectangular area with sides parallel to the detector edges which encompasses the indicated filtered areas. For ramp filters the default will be to readout the entire WFC detector, unless a polarizer is used with the ramp filter, in which case a subarray is readout. Users cannot override the small filter subarrays.

Table 7.7: WFC aperture parameters.

| APT Aperture Name | Readout area | Extent (arcsec) | Reference pixel | Reference V2,V3 (arcsec) | x-axis angle (degrees from V3 through V2) | y-axis angle |
|-------------------|--------------|-----------------|-------------------------------|--------------------------|---|--------------|
| WFC | 4096 × 4096 | 202 × 202 | (2124,200) <i>on WFC1</i> | (262,239) | 92.2 | 177.5 |
| WFC-FIX | 4096 × 4096 | 202 × 202 | (2073,200) | (261,198) | 92.5 | 177.3 |
| WFCENTER | 4096 × 4096 | 202 × 202 | (2114,2029) <i>on WFC2</i> | (261,252) | 92.1 | 177.5 |
| WFC1 | 4096 × 4096 | 202 × 202 | (2124, 1024) | (263,198) | 92.5 | 177.4 |
| WFC1-FIX | 4096 × 4096 | 202 × 202 | (2072, 1024) | (261,198) | 92.5 | 177.4 |
| WFC2 | 4096 × 4096 | 202 × 202 | (2124, 1024) | (259,302) | 91.7 | 177.8 |
| WFC2-FIX | 4096 × 4096 | 202 × 202 | (2072, 1024) | (257,302) | 91.7 | 177.8 |
| WFC1-IRAMP | 4096 × 4096 | 25 × 65 | (680,1325) | (194,187) | 93.1 | 176.6 |
| WFC1-MRAMP | 4096 × 4096 | 35 × 80 | (3096,1024) | (312,196) | 92.2 | 177.8 |

Table 7.7: WFC aperture parameters.

| APT Aperture Name | Readout area | Extent (arcsec) | Reference pixel | Reference V2,V3 (arcsec) | x-axis angle | y-axis angle |
|--------------------------|--------------|-----------------|-----------------|--------------------------|------------------------------|--------------|
| | | | | | (degrees from V3 through V2) | |
| WFC2-MRAMP | 4096 × 4096 | 40 × 80 | (1048,1024) | (206,304) | 91.9 | 177.5 |
| WFC2-ORAMP | 4096 × 4096 | 35 × 65 | (3494,708) | (328,316) | 91.4 | 178.2 |
| WFC1-SMFL ¹ | 2048 × 2048 | 70 × 80 | (3096,1024) | (312,196) | 92.2 | 177.8 |
| WFC2-SMFL ¹ | 2048 × 2048 | 70 × 80 | (1048,1024) | (206,304) | 91.9 | 177.5 |
| WFC1-POL0UV ² | 2048 × 2048 | 90 × 80 | (3096,1024) | (312,196) | 92.1 | 177.8 |
| WFC1-POL0V ² | 2048 × 2048 | 90 × 80 | (3096,1024) | (312,196) | 92.2 | 177.8 |
| WFC2-POL0UV ² | 2048 × 2048 | 90 × 80 | (1048,1024) | (206,304) | 91.9 | 177.5 |
| WFC2-POL0V ² | 2048 × 2048 | 90 × 80 | (1048,1024) | (206,304) | 91.9 | 177.5 |
| WFC1-512 | 512 × 512 | 25 × 25 | (3864,1792) | (352,158) | 92.1 | 178.0 |
| WFC1-1K | 1024 × 1024 | 50 × 50 | (3608,1536) | (338,170) | 92.1 | 177.9 |
| WFC1-2K | 2048 × 2048 | 101 × 101 | (3096,1024) | (312,196) | 92.2 | 177.8 |
| WFC2-2K | 2048 × 2048 | 101 × 101 | (1048,1024) | (206,304) | 91.9 | 177.5 |
| WFC1-IRAMPQ | 2048 × 2048 | 25 × 65 | (680,1325) | (194,187) | 93.1 | 176.6 |
| WFC1-MRAMPQ | 2048 × 2048 | 35 × 80 | (3096,1024) | (312,196) | 92.2 | 177.8 |
| WFC2-MRAMPQ | 2048 × 2048 | 40 × 80 | (1048,1024) | (206,304) | 91.9 | 177.5 |
| WFC2-ORAMPQ | 2048 × 2048 | 35 × 65 | (3494,708) | (328,316) | 91.4 | 178.2 |
| WFC1-CTE | 4096 × 2048 | 202 × 101 | (3920,1848) | (354,155) | 92.1 | 178 |

1. Apertures are automatically created by commanding software when a HRC filter is used in WFC observations. (Apertures are not listed in the APT aperture pull-down menu.)

2. Apertures are automatically created by commanding software when a polarizer filter is used. Same parameters apply for POL60 and POL120 in V and UV. (Apertures are not listed in the APT aperture pull-down menu.)

3. Extent (arcsec) is the smaller of actual pixel domain readout and the area actively exposed to sky. For RAMP associated apertures the leading dimension is size yielding coverage at the specified wavelength.

Table 7.8: Ramp filter apertures.

| Detector | Filter | Ramp Segment | Full-frame apertures | Quadrant or subarray aperture |
|----------|---------|--------------|--------------------------|---|
| WFC | FR423N | Inner | WFC1-IRAMP | WFC1-IRAMPQ |
| | FR716N | | | |
| | FR853N | | | |
| | FR5551N | | | |
| | FR647M | | | |
| | FR388N | Middle | WFC1-MRAMP WFC2-MRAMP | WFC1-MRAMPQ WFC2-MRAMPQ |
| | FR656N | | | |
| | FR459M | | | |
| | FR505N | | | |
| | FR914M | | | |
| | FR462N | Outer | WFC2-ORAMP | WFC2-ORAMPQ |
| | FR782N | | | |
| | FR931N | | | |
| | FR1016N | | | |
| | FR601N | | | |
| HRC | FR914M | Middle | HRC HRC-FIX | HRC-CORON1.8 HRC-CORON3.0 HRC-OCCULT08 HRC-ACQ HRC-SUB1.8 |
| | FR459M | | | |
| | FR505N | | | |
| | FR388N | | | |
| | FR656N | | | |

7.7.4 Polarizer Apertures

Apertures have been provided for use with the polarizer sets similar to the SMFL apertures. These apertures are selected automatically when a polarizing spectral element is used, and a single WFC chip quadrant readout is obtained. The aperture parameters given in Table 7.7 are valid for all three polarizing filters in each polarizer set, UV or visible, to the stated significant figures.

7.7.5 HRC Apertures

The HRC has an area of 1062 by 1024 including 19 physical overscan pixels at each end in the x direction. The active area is 1024 by 1024 pixels. The mean scales along the x and y directions are 0.028 and 0.025 arcseconds/pixel, thus providing a field of view of about 29 by 26 arcseconds in extent. The anisotropy and variation of scales is discussed in Section 10.3 of this handbook. The reference point for the aperture labelled HRC-FIX, and initially for HRC, is at the geometric center, (531,512). As with the WFC apertures, there may be reason to move the HRC reference point later.

The HRC is equipped with two coronagraphic spots, nominally 1.8 and 3.0 arcseconds in diameter and a coronagraphic finger, 0.8 arcseconds in width. Apertures HRC-CORON1.8, HRC-CORON3.0, and HRC-OCCULT0.8 are defined to correspond to these features. The

coronagraphic spots are only in the optical train and thus in the data if HRC-CORON1.8 or HRC-CORON3.0 are specified and their positions are shown in Figure 7.6 (left panel). In addition we define a target acquisition aperture, HRC-ACQ designed for acquiring targets which are subsequently automatically placed behind a coronagraphic spot or the occultation finger. The coronagraphic spots are only in the optical train if HRC-CORON1.8 or HRC-CORON3.0 are specified and their positions are shown in Figure 7.6 -- left panel. The positions of the coronagraphic spots have been found to fluctuate. Observations will need to incorporate a `USE OFFSET` special requirement to allow current values to be inserted at the time of the observation (see the *Phase II Proposal Instructions*).

A substantial region masked out by the occulting finger will be present in the HRC data (Figure 7.6 -- right panel). The occulting finger is not retractable -- it will be in every HRC exposure. However as with any other detector feature or artifact, the "lost" data can be recovered by combining exposures which were suitably shifted with respect to each other. A dither pattern, `ACS-HRC-DITHER-LINE` has been defined for this purpose and spans the area flagged for the HRC occulting finger (~1.6 arcseconds or ~56 pixels wide), with an extra ~0.3 arcseconds or ~10 pixels of overlap. More details can be found in the *Phase II Proposal Instructions*.

Use of the prism PR200L requires specifying aperture HRC, but results in a reference point of [671,512] to optimally center the target coordinates within the somewhat vignetted prism field of view. Although the HRC direct imaging and PR200L prism apertures have the same name in APT, they are actually distinct, and HST executes a small angle maneuver between observations of a given target with them, to compensate for the positional deflection by the prism. One consequence is that the Special Requirement `SAME POS AS` cannot be used among mixed direct and prism exposures, as always with different apertures.

Figure 7.6: HRC coronagraphic finger and spots (left), coronagraphic finger always in data (right)

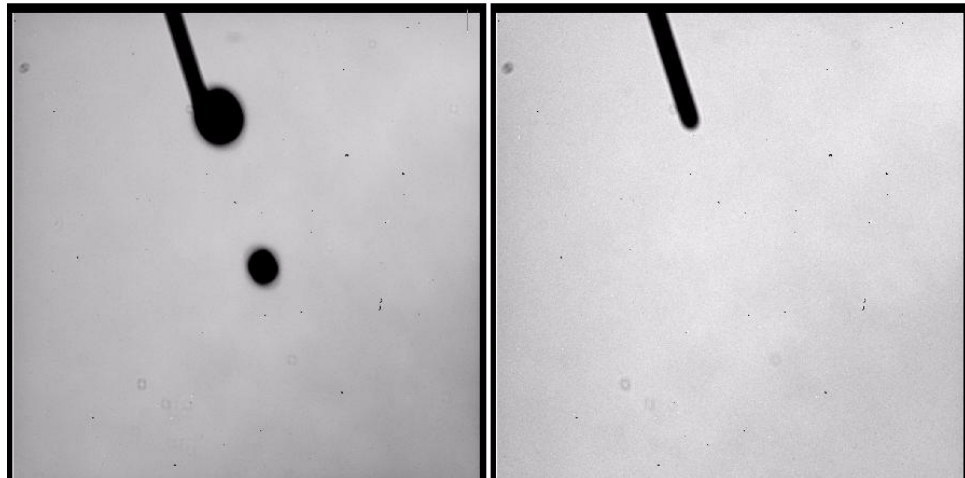


Table 7.9: HRC aperture parameters.

| APT Aperture Name | Active area | Extent (arcsec) | Reference pixel | Reference V2,V3 (arcsec) | x-axis angle | y-axis angle |
|------------------------|-------------|-----------------|------------------------|--------------------------|--------------|--------------|
| HRC | 1024 × 1024 | 29 × 26 | (531, 512) | (206,472) | -84.1 | 0.1 |
| HRC-FIX | 1024 × 024 | 29 × 26 | (531, 512) | (206,472) | -84.1 | 0.1 |
| HRC-CORON1.8 | 200 × 200 | 6 × 5 | (564,466) ¹ | (205,471) ¹ | -84.1 | 0.1 |
| HRC-CORON3.0 | 200 × 200 | 6 × 5 | (467,794) ¹ | (208,479) ¹ | -84.2 | 0.1 |
| HRC-OCCULT0.8 | 200 × 200 | 6 × 5 | (443,791) | (209,477) | -84.2 | 0.2 |
| HRC-ACQ | 200 × 200 | 6 × 5 | (735,575) | (200,474) | -84.1 | 0.0 |
| HRC-512 | 512 × 512 | 15 × 13 | (276,256) | (214,465) | -84.1 | 0.2 |
| HRC-SUB1.8 | 512 × 512 | 15 × 13 | (570,468) | (205,471) | -84.1 | 0.1 |
| HRC-PRISM ² | 744 × 1024 | 21 × 26 | (671,512) | (214,471) | -84.2 | 0.2 |

1. These values fluctuate and will be updated at the time of the observation.

2. HRC-PRISM is automatically created by commanding software when spectral element PR200L and aperture HRC are selected in APT.

7.7.6 SBC Apertures

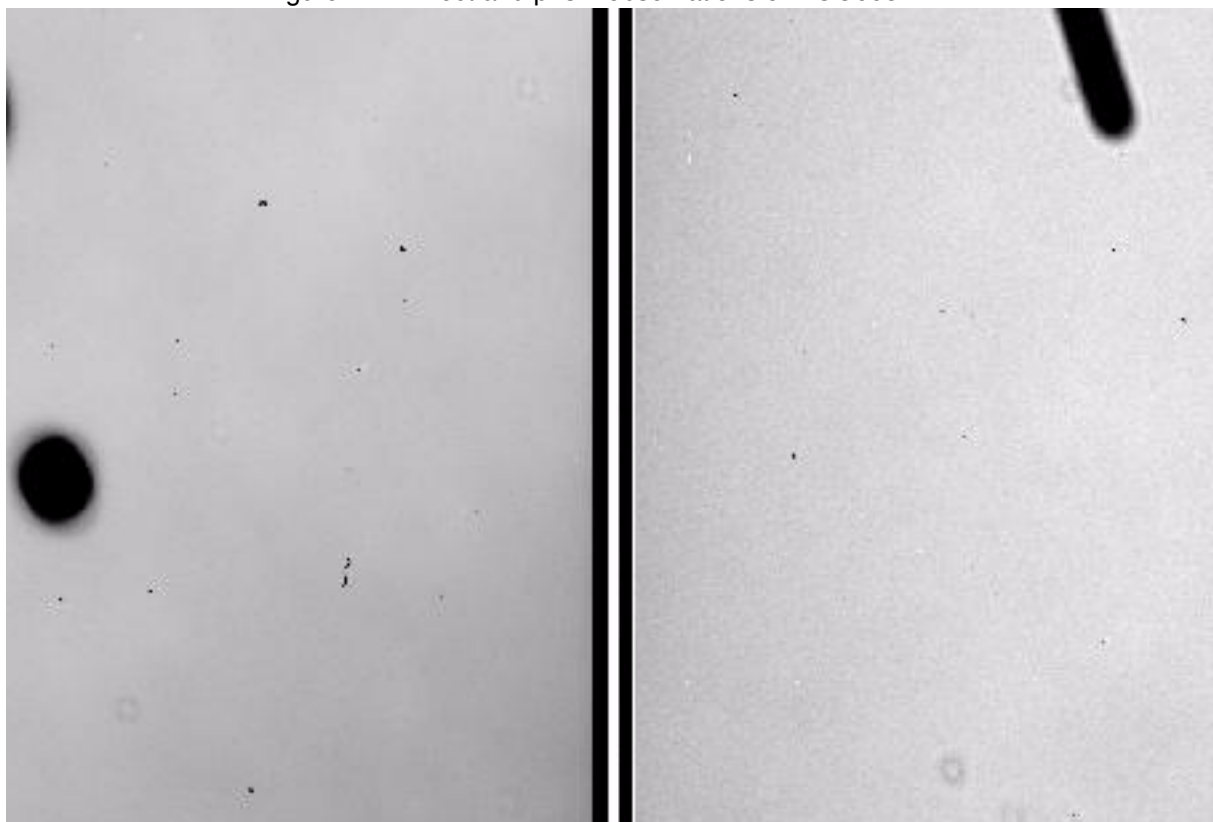
The SBC aperture is 1024 pixels square. There are no overscan pixels to consider. The x and y scales are 0.034 and 0.030 arcseconds/pixel leading to a coverage on the sky of 35 by 31 arcseconds. The reference point has been moved to (512,400) to place targets further from a bad anode which disables several rows of the detector near $y = 600$. As with the CCDs we maintain an SBC-FIX aperture which will always have position (512,512). MAMA detectors slowly lose efficiency with each exposure, therefore the SBC reference point may be shifted again if the chosen position shows this effect to a measurable degree.

The (512,512) reference point falls near to the same position in (V2,V3) as the HRC, namely (205, 470), and the x and y axis angles are -85.4° and -0.9° .

Use of either prism PR110L or PR130L requires use of aperture SBC and results in a reference point of [425,400] to optimally center the target coordinates with respect to vignetting on the right side of the field and to avoid a set of bad rows at 599 to 605.

Although the SBC direct imaging and prism apertures have the same name in APT, they are actually distinct, and HST executes a small angle maneuver between observations of a given target with them, to compensate for the positional deflection by the prisms. One consequence is that the Special Requirement SAME POS AS cannot be used among mixed direct and prism exposures. Figure 7.7 shows a direct and prism observation of the same field. The prism now is vignitted on the positive x side. The reference points and the small angle maneuver place the same target near the reference point of each view.

Figure 7.7: Direct and prism observations of NGC6681.



Direct and prism observations of NGC6681. The reference point is defined to be at the center of each aperture in the x direction but below the center in the y direction to avoid the bad rows.

Table 7.10: SBC aperture parameters

| APT Aperture Name | Active area | Extent (arcsec) | Reference pixel | Reference V2,V3 (arcsec) | x-axis angle | y-axis angle |
|------------------------|-------------|-----------------|-----------------|--------------------------|--------------|--------------|
| SBC | 1024 × 1024 | 34 × 31 | (512, 400) | (205, 467) | -84.7 | -0.2 |
| SBC-FIX | 1024 × 1024 | 34 × 31 | (512, 512) | (205, 470) | -84.7 | -0.2 |
| SBC-PRISM ¹ | 1024 × 1024 | 28 × 31 | (425, 400) | (203, 467) | -84.7 | -0.2 |

1. SBC-PRISM is automatically created by commanding software when spectral elements PR110L and PR130L, and aperture SBC, are selected in APT.

7.8 Specifying Orientation on the Sky

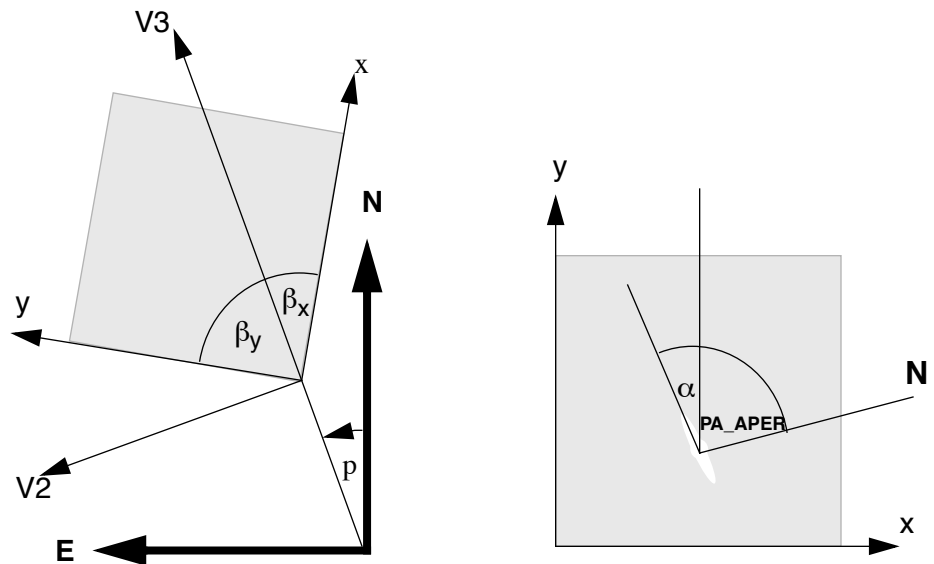
Determining the orientation of an image requires knowledge of the telescope roll and the angle of the aperture relative to the HST coordinate frame. A target may need to be oriented in a preferred direction on a detector, particularly when spectroscopy is to be performed.

To specify an ORIENT in Phase II, note that this parameter is just the usual PA (Position Angle) of the HST U3 axis (= -V3, see below); see

Figure 3.1 and Figure 7.9 in this Handbook, as well as the *Phase II Proposal Instructions*. APT provides a convenient interactive display of the aperture and orientations in your field. The ORIENT parameter is related to the following discussion of ACS geometry.

All HST aperture positions and orientations are defined within an orthogonal coordinate system labeled V1,V2,V3, in which V1 is nominally along the telescope roll axis. Apertures are therefore in the V2,V3 plane. (For more information about HST instrument aperture locations and axes in the HST FOV, please visit the Observatory Support Web page section on apertures at: <http://www.stsci.edu/hst/observatory/apertures>.) The V3 position angle p is defined as the angle of the projection of the V3 axis on the sky, measured from North towards East with the aperture denoting the origin. This is almost identical to the telescope roll angle. (There is a small difference between roll angles measured at the V1 axis and those measured at the aperture. This can amount to several tenths of a degree depending on the target declination.) When the position angle is zero, V3 points North and V2 points East. In the V2V3 coordinate system, as shown in Figure 7.9, aperture orientations are defined by β_x and β_y , the angles their x and y axes make with the V3 axis, measured in an anti-clockwise direction. (The value of β_x as illustrated in Figure 7.8, would be considered negative.) Hence, the angles these axes make with North are found by adding the axis angles to the position angle.

Figure 7.8: Aperture and image feature orientation.

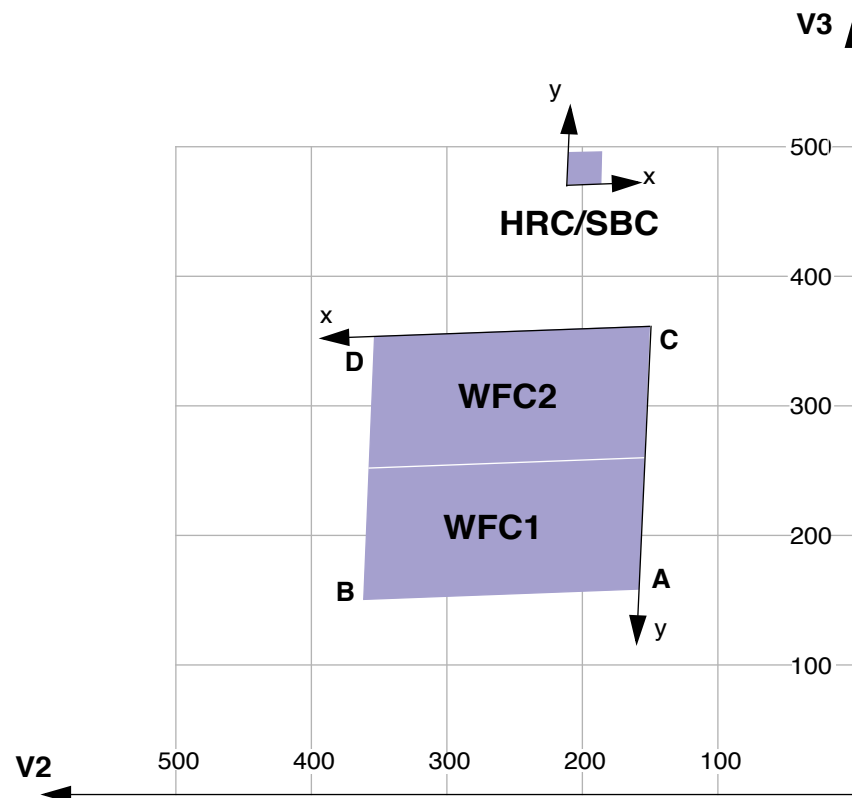


The science image header supplies the value of ORIENTAT, the angle the detector y axis makes with North, which is equal to $p + \beta_y$. Another angle keyword supplied is PA_APER which is the angle the aperture y axis makes with North. Both angles are defined at the aperture so using them

does not involve the displacement difference. Normally the aperture and detector y axes are parallel, and so $PA_APER = ORIENTAT$. Several STIS slit apertures were not aligned parallel to the detector axes, so this distinction was meaningful, but ACS has no slit apertures so this difference will probably not arise. In any case, we recommend using PA_APER .

Beyond establishing the direction of the aperture axes, it will often be necessary to know the orientation of a feature, such as the plane of a galaxy, within an image. Conversely, we need to know what direction within an image corresponds to North. To this end we define a feature angle α within the aperture as measured on the science image, anti-clockwise from the y-axis so that it is in the same sense as the previously defined angles. For an orthogonal set of aperture axes the direction of this feature would be $PA_APER + \alpha$ and the image direction of North would be the value of α which makes this angle zero, namely $-PA_APER$, still measured in an anti-clockwise direction from the y axis.

Figure 7.9: ACS apertures in the V2/V3 reference frame.



The readout amplifiers (A,B,C,D) are indicated on the figure. The WFC data products from the calibration pipeline will be oriented so that WFC1 (chip 1, which uses amps A and B) is on top. The HRC data products will also be oriented such that amps A and B are on top, but they will be inverted from WFC images with respect to the sky.

The x and y axes projected on the sky are not necessarily orthogonal. For all instruments prior to the ACS the departure from orthogonality has

been negligible, but for the ACS the angle between the axes is about 85° . Figure 7.9 realistically represents the alignment of the ACS apertures and shows that the apertures are not square. The x and y axes indicated are those that will be used for the science images. The V2,V3 coordinates can be calculated from the x, y coordinates according to

$$V2 = V2_0 + s_x \sin \beta_x x + s_y \sin \beta_y y$$

$$V3 = V3_0 + s_x \cos \beta_x x + s_y \cos \beta_y y$$

where s_x and s_y are scales in arcseconds per pixel along the image x and y axes. $V2_0$ and $V3_0$ are the coordinates of the aperture origin, but they do not enter into the angle calculations. Figure 7.9 shows that a rotation from x to y is in the opposite sense to a rotation from V2 to V3. This will be the arrangement for ACS apertures. This is significant in defining the sense of the rotation angles. For a direction specified by displacements Δx and Δy in the image, the angle α is $\arctan(-\Delta x/\Delta y)$.

Because of the oblique coordinates, the angle α_s on the sky will not be equal to α . To calculate the sky angle, it is convenient to define another set of orthogonal axes x_s, y_s , similar to the V2V3 but rotated so that y_s lies along y, and x_s is approximately in the x direction. Let $\omega = \beta_y - \beta_x$ be the angle between the projected detector axes and for simplicity let their origins be coincident. Then the transformation is

$$x_s = s_x \sin \omega x$$

$$y_s = s_x \cos \omega x + s_y y$$

By comparing differentials and defining α_s as $\arctan(-\Delta x_s/\Delta y_s)$ we find

$$\tan \alpha_s = \frac{s_x \sin \omega \sin \alpha}{s_y \cos \alpha - s_x \cos \omega \sin \alpha}$$

The equation as written will place the angle in the proper quadrant if the ATAN2 Fortran function or the IDL ATAN function is used. To get the true angle East of North, for a feature seen at angle α in the image, calculate α_s and add to PA_APER.

The inverse relation is

$$\tan \alpha = \frac{s_y \sin \alpha_s}{s_x \sin(\alpha_s + \omega)}$$

To find the value of α corresponding to North we need the value of α_s such that $\text{PA_APER} + \alpha_s = 0$. So substitute $-\text{PA_APER}$ for α_s in the equation to get the angle α in the image which corresponds to North. The values of the scales and axis angles for all instruments are maintained on an [Observatory Science Group Web page](#).

For the ACS apertures, the values in Table 7.11 have been derived from results of operating the ACS in the Refractive Aberrated Simulator. These should not be considered as true calibrations but they indicate some

aperture features, such as the non-orthogonality of the aperture axes, and the x and y scale differences for HRC and SBC.

Table 7.11: Plate scales and axis angles for the 3 ACS channels.

| | s_x | s_y | β_x | β_y | $\beta_y - \beta_x$ |
|-----|--------------|-------|-----------|-----------|---------------------|
| | arcsec/pixel | | degrees | | |
| WFC | .0494 | .0494 | 92.2 | 177.528 | 85.3 |
| HRC | .0284 | .0248 | -84.1 | 0.081 | 84.2 |
| SBC | .0338 | .0301 | -84.7 | -0.2 | 84.5 |

7.8.1 Determining Orientation for Phase II

A particular orientation is specified in an HST Phase II proposal using yet another coordinate system: U2,U3. These axes are opposite to V2 and V3, so, for example, $U3 = -V3$. The angle `ORIENT`, used in a Phase II proposal to specify a particular spacecraft orientation, is the position angle of U3 measured from North towards East. The direction of the V3 axis with respect to North is $PA_APER - \beta_y$ and so

$$ORIENT = PA_APER - \beta_y \pm 180^\circ.$$

The IRAF task *rotate* in the package *images.geom* takes a drizzled image and rotates it counter-clockwise by a specified angle. To orient the image so that its y axis becomes North, the angle to specify is `PA_APER`. The x axis of the coordinate system will then point East. Orientations can be checked by using [APT](#).

7.9 Parallel Observations

7.9.1 Parallel Observing

Parallel observing allows HST to operate several other instruments while the prime instrument is executing its observations. While the primary instrument observes a fixed target at user-specified coordinates, the parallel instrument observes at coordinates 5 to 10 arcminutes away, depending on the parallel instrument. The HST field of view following SM4 (Figure 3.1) shows the general locations of the instrument apertures adjacent to one another on the sky. Accurate relative positions for all instruments can be found on STScI's [Observatory Web page](#) in the [Pointing section](#).

The recommended method of determining the field of view for any instrument is to use `APT`. A Digital Sky Survey (or user supplied) image of

the primary target area is displayed with an HST field of view overlay. Any desired coordinate and ORIENT combination for the primary target will then display the possible pointings of any instrument operated in parallel. If the primary exposure will execute at a known (absolute) orientation, APT will display the exact field of view for any instrument executed in parallel. If the primary exposure will execute at a random (nominal) orient or range of orient values, APT allows the HST field of view to be rotated interactively about the primary pointing. APT can be a valuable resource for parallel observing programs, especially those designed for, or restricted to specific pointings for the parallel FOV.

Certain operating limits are in place to restrict use of configurations, modes, parameters, elements, and requirements allowed for each instrument while used in parallel. Details on these limits are documented in the *Call for Proposals* and *Primer*. General information on ACS specific parallel operations are documented in the following sections for each of the three types of ACS parallel observing: coordinated, auto, and pure.

ACS Coordinated Parallels

Coordinated parallel observations are specified in the same Phase II observing program as the primary observations via the prime and parallel group containers in APT. A single ACS channel may be used for a coordinated parallel observation, with, and only with, another instrument. Unlike NICMOS, coordinated parallels cannot be used to operate any of the ACS channels simultaneously. ACS exposures may not be used as both the prime and parallel exposures within the same parallel container. In order to operate ACS channels simultaneously, the use of ACS auto-parallels is described in the following section.

In order to protect the ACS SBC detector from inadvertent over illumination, the ACS/SBC configuration may be used as a coordinated parallel only if an exact spacecraft orientation (ORIENTATION) is specified, the coordinates of the parallel field are determined, and the parallel target or field passes the same bright-object screening applied to SBC primary observations. The APT will greatly assist in defining this type of ACS parallel program.

It is expected that users will frequently wish to employ ACS and WFC3 in parallel. Because users will also generally want to dither their observations, exposures of these two cameras will generally be taken synchronously. However, both ACS and WFC3 images must be loaded transferred from the camera buffers to the solid state data recorders (SSDRs). The ACS buffer can only hold one image, while the WFC3 can hold two optical images (and roughly the same number of NIR images, as each NIR image is expected to use multiple reads). However images from these cameras cannot be transferred to the SSDRs simultaneously, and each transfer takes about 350 seconds. We presently expect that it will be possible to take at least three images per orbit in each of the two cameras, and four exposures per orbit may also be feasible. Members of the ACS and

WFC3 teams are actively pursuing this question, and more detailed information on planning parallel ACS and WFC3 observations will be made available to the community before the Cycle 17 proposal deadline.

ACS Auto-Parallels

The ACS auto-parallel capability is intended to increase the scientific return of the instrument by adding exposures with the parallel detector while interfering as little as possible with the observer's primary program. When either the WFC or HRC is the primary channel, and the exposure in that channel meets the requirements stated below, an auto-parallel observation will be automatically scheduled in the parallel channel during Phase II processing. Parallel detector exposures will be added automatically with the longest possible exposure time that does not interfere with the primary program. In order for an auto-parallel to be scheduled, the *primary* observation must meet the specifications that depend primarily on the exposure time and the filter selection of the primary exposure.

The user has three control options: This is done by selecting the PAREXP optional parameter. A user may either choose to explicitly add the auto-parallels by choosing PAREXP=MULTIPLE; choose to have no auto-parallels added by selecting PAREXP=NONE; or leave the special requirement set to the default, DEF. When DEF is selected, auto-parallels will be added according to the same primary exposure requirements as those for the MULTIPLE option. When MULTIPLE is selected an auto-parallel will be added for each CR-SPLIT part of the primary exposure (see Figure 7.10). There is a simple algorithm that the Phase II software follows in order to determine if an auto-parallel is feasible:

1. The primary exposure must be for an external target, in ACCUM mode, and either in the WFC or HRC channel. It is not possible to observe simultaneously with the HRC and SBC since they share the same optical train up to the flip mirror. Simultaneous operation of the WFC and SBC is not supported.
2. The primary exposure must be taken with a filter from the list of primary/auto-parallel filter combinations (Table 7.12). The WFC and HRC share the same filter wheels and their optical paths are not diametrically opposite each other. In addition, the filters in the filter wheel are not evenly spaced around the wheel. Therefore, only certain parallel/auto-parallel combinations are physically possible. If a filter does not appear in the table, an auto-parallel is not physically possible.
3. The primary exposure time must be greater than the minimum exposure time, defined in Table 7.13. These values are calculated such that all of the commanding associated with the auto-parallel is scheduled during the exposure time of the primary CR-SPLIT portion.

4. The primary exposure is not allowed to have any EXPAND, MIN DUR, MAX DUR, or RT ANALYSIS special requirements.

Table 7.12: Filter combinations for auto-parallels in the two cases of (i) HRC camera prime and (ii) WFC camera prime.

| HRC primary | WFC auto-parallel | WFC primary | HRC auto-parallel |
|-------------|-------------------|-------------|-------------------|
| CLEAR | CLEAR | CLEAR | CLEAR |
| F892N | F775W | F475W | F850LP |
| F606W | F625W | F658N | F550M |
| F502N | F550M | G800L | F625W |
| G800L | F850LP | F502N | F775W |
| F555W | F606W | F606W | F555W |
| F775W | F502N | F850LP | G800L |
| F625W | G800L | F550M | F502N |
| F550M | F658N | F625W | F606W |
| F850LP | F475W | F775W | F892N |
| F330W | F660N | F660N | F330W |
| F250W | F814W | F814W | F250W |
| F220W | F435W | F435W | F220W |

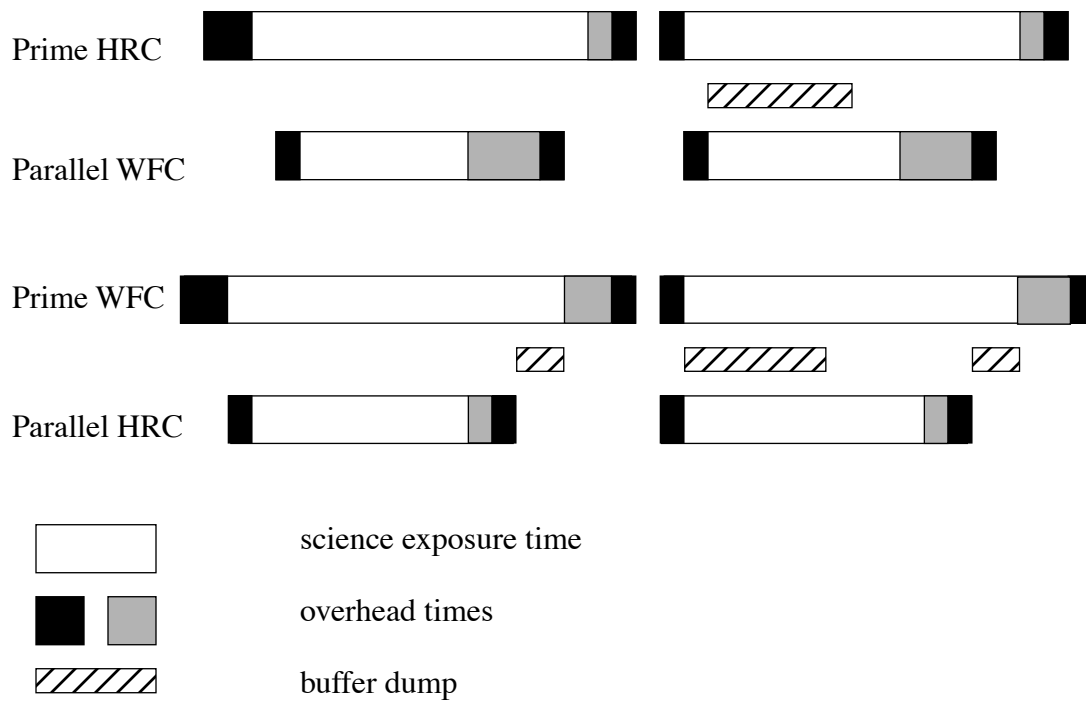
Note that since the WFC and HRC apertures are not opposite each other on the filter wheels, filter pairs in columns 1 and 2 do not map to columns 3 and 4.

Table 7.13: Minimum primary exposure time (seconds) to attach an auto-parallel for CR-SPLIT=n.

| Primary exposure type | Multiple auto-parallel scenario (n ≥ 1) |
|-----------------------|---|
| HRC | n × 495 |
| WFC compressed | n × 406 |
| WFC uncompressed | n × 465 |

(if CR-SPLIT=NO then n=1, if CR-SPLIT is not specified n=2.)

Figure 7.10: Scheduling of auto-parallel.

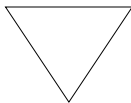


There are a few things to remember about auto-parallels:

- In order to avoid the addition of serial buffer dumps in the primary program, group short HRC exposures and long WFC exposures separately. It takes approximately 349 seconds to dump a WFC image from the buffer. When WFC is the parallel camera, this buffer dump can occur during the following exposure if its exposure time is greater than ~ 339 seconds, otherwise a serial buffer dump must be added. This can be avoided by scheduling long WFC full-frame exposures together.
- auto-parallels will not be assigned when the number of exposure iterations specified for the primary exposure is greater than one. It is assumed that the observer will use exposure iterations to obtain coarse time resolution. These exposures will in most cases be too short for auto-parallel observations.

The following policies will be in effect for Auto-Parallel observations:

- Auto-Parallel observations are the property of the PI of the program using the prime ACS detector.
- Auto-Parallel observations are not available for independent scheduling.
- There are some fairly severe timing constraints under which Auto-Parallel observations may be added. The scheduling system will add parallels only if it can do so without affecting the prime science.
- If WFC data are taken in parallel with prime HRC observations, the GAIN setting will be 2 (see Section 4.3). For HRC parallels added to prime WFC exposures the GAIN will be 2.
- WFC Auto-parallel observations are subject to compression of one quadrant at a level that can occasionally result in some data loss. Such observations will not be repeated.



This data loss will be considered routine and it will be the policy of STScI not to repeat observations scheduled as auto-parallels which exhibit partial data loss due to the data compression.

ACS Pure Parallels

In ACS pure parallel observations, an observation is taken with ACS on an essentially random area of the sky while another instrument is making prime observations. No SBC pure parallels will be allowed due to bright object concerns.

Unlike the previous two types of parallel programs, pure parallels contain only parallel visits. Use of the GO/PAR proposal category will make any visit in the program a pure parallel.

The ACS default (archival) pure parallel program continued to execute for the community until midway through Cycle 13 when all of the "Default" HST archival pure parallel programs were discontinued to prolong the lifetime of transmitters on HST. This non-proprietary data came from programs 9575, 9584, and 9701. A list of all pure parallel datasets in the HST archive is at:

<http://www.stsci.edu/instruments/parallels/retrieve.html>.

Observers can request ACS pure parallels; however, there are many constraints which can render pure parallels unselectable in any given orbit. Pure parallels will always be given lower priority than primaries, and are thus scheduled only on a non-interference basis.

ACS Auto-Parallels with ACS Coordinated and ACS Pure Parallels

ACS auto-parallels can be added to ACS pure and ACS coordinated parallels by default if scheduling constraints allow. However auto-parallels cannot be added to observations that make use of EXPAND or MAX DUR special requirements. Therefore ACS pure parallels can either be crafted to expose for the maximum duration allowed in each individual orbit by using EXPAND/MAX DUR or have auto-parallels added, but not both.

7.10 Pointing Stability for Moving Targets

Observations of Solar System targets are subject to some special limitations on the achievable pointing stability during a visit. These limitations apply to both two-gyro and three-gyro operations.

For moving targets, the HST ground system assumes that the position of the target as seen from the center of the earth can be approximated as a linear function of time. This is done using rates of motion calculated from the object's ephemeris for a time near the start of each orbit. If the target's geocentric ephemeris departs significantly from this linear approximation over the course of an orbit, this can lead to small but noticeable pointing offsets. If you think this may adversely affect your science, please consult with your PC about possible strategies for ameliorating this effect.

The correction for the variable parallax to a solar system object due to HST's orbit around the Earth is calculated on-orbit using the best ephemeris for HST's orbit that was available at the time the detailed weekly schedule was created. However, the real position of HST along its orbit often differs by up to 1 to 2 seconds (7 to 15 kilometers) from the predicted ephemeris position. This leads to small errors in the phasing of the

calculated parallax correction. For example, when observing a Solar System object at a distance of 0.5 AU from the Earth, this can cause typical pointing offsets over the course of an orbit of order 20 to 40 milliarcseconds. As these offsets depend on unpredictable changes in HST's orbit, such drifts are unavoidable when observing near-Earth objects.

Overheads and Orbit-Time Determination

In this chapter. . .

8.1 Overview / 165

8.2 ACS Exposure Overheads / 166

8.3 Orbit Use Determination Examples / 170

8.1 Overview

After you establish a set of scientific exposures, as well as any additional target acquisition or calibration exposures required for your program, you are ready to determine the total number of orbits to request. Generally, this straightforward exercise involves compiling the overheads for individual exposures, packing exposure plus overhead time into individual orbits, and tallying up the results to determine the total number of orbits needed. It may be an iterative process as you refine your exposures to better use the orbit visibility times.

The Phase I Call for Proposals (http://www.stsci.edu/hst/hst/proposing/documents/cp/cp_cover.html) includes proposal instructions that provide information on the Observatory policies and practices with respect to orbit time requests. The HST Primer (<http://www.stsci.edu/hst/proposing/docs/proposing/documents/cp/primer.pdf>) provides specific advice on orbit determination. Below, we provide a summary of the ACS specific overheads, and give several examples that illustrate how to calculate your orbit requirements for a Phase I Proposal.

8.2 ACS Exposure Overheads

Exposure overheads are summarized in Table 8.1 and Table 8.2. All numbers given are approximate; they do not make detailed differentiations between overheads for different ACS modes and configurations. These overhead times are to be used (in conjunction with the actual exposure times and the instructions in the *HST Primer* to estimate the total number of orbits for your proposal. After your HST proposal is accepted, you will be asked to submit a Phase II proposal to support scheduling of your approved observations. At that time you will be presented with actual, up-to-date overheads by the APT scheduling software. *Allowing sufficient time for overhead in your Phase I proposal is important; additional time to cover unplanned overhead will not be granted later.*

The following list presents important points for each type of overhead:

- **Generic (Observatory Level) Overheads:**
 - The first time you acquire an object you must include overhead for the guide-star acquisition (6 minutes).
 - In subsequent contiguous orbits you must include the overhead for the guide-star reacquisition (6 minutes); if you are observing in the Continuous Viewing Zone (see the *Phase I Proposal Instructions*), no guide-star *reacquisitions* are required.
 - Allocate some time for each deliberate movement of the telescope; e.g., if you are performing a target acquisition exposure on a nearby star and then offsetting to your target, or if you are taking a series of exposures in which you move the target on the detector, you must allow time for the moves (20 seconds to 60 seconds, depending on the size of the slew (see Table 8.1 and Table 8.2).

Table 8.1: Science exposure overheads: general.

| Action | Overhead |
|------------------------------------|---|
| Generic (observatory level) | |
| Guide-star acquisition | Initial acquisition overhead = 6 minutes. Reacquisitions on subsequent orbits = 6 minutes per orbit. |
| Spacecraft moves | For offsets less than 1.5 arcminutes and more than 10 arcseconds = 1 minute. For offsets between 10 arcseconds and 1 arcseconds = 0.5 minutes. For offsets less than 1 arcseconds in size = 20 seconds. |

Table 8.2: ACS science exposure overhead times (minutes).

| Exposure type | WFC | HRC | SBC |
|---|-----|-------------------------|-----|
| <i>Mode: ACCUM</i> | | | |
| Single exposure or the first exposure in a series of identical exposures. | 4.0 | 2.5 | 1.7 |
| Subsequent identical exposures in series (within an orbit). | 2.5 | 1.0 | 0.7 |
| Additional overhead for each serial buffer dump (added when WFC exposures are less than 339 seconds long, or the buffer fills with short HRC or SBC exposures). | 5.8 | 5.8 | 5.8 |
| Predefined imaging exposure for prism spectroscopy. | N/A | 8.5 | N/A |
| Predefined imaging exposure for grism spectroscopy. | 7 | 5.5 | N/A |
| <i>Mode: ACQ</i> | | | |
| For the specified acquisition exposure time, $tacq$, the total acquisition time is: | N/A | $3.5 + (2 \times tacq)$ | N/A |
| <i>Additional overheads</i> | | | |
| Additional overhead if switching over from HRC to SBC within an orbit. | | 10.7 | |

- ***Onboard Target-Acquisition Overheads:***

- On board target acquisitions only need to be done to place the target under one of the coronagraphic spots.
- An on board target acquisition needs to be done only once for a series of observations in contiguous orbits (i.e., once per visit).
- The drift rate induced by the Observatory is less than 10 milliarcseconds per hour. Thermal drifts internal to ACS are even less.

- ***Scientific Exposures:***

- The overhead times are dominated by the time to move the filter wheel, the CCD readout time, and any necessary serial buffer dumps. Again, it should be stressed that in Phase II, the overheads will frequently be less, but it is important to plan Phase I using the conservative overheads given in Table 8.2 to ensure adequate time for the proposal's scientific goals.

- *Spectroscopy:*

- Each CCD spectroscopic observation is preceded by an imaging exposure used for calibration, with exposure times of 3 and 6 minutes, respectively, for grism and prism observations. SBC prism exposures are not preceded by an automatic calibration exposure. Technically this is an individual single exposure requiring all regular science exposure overheads. For the observer, however, it represents an additional overhead in the observation time budget, so it has been included in the table of instrument overhead times for science exposures. However, if the observing program is already taking an appropriate broadband image, the automatic imaging and associated overheads preceding the spectroscopic grism or prism observations can be avoided by invoking the Optional Parameter `AUTOIMAGE=NO` during the Phase II preparations. More details can be found in the *Phase II Proposal Instructions*.

Note that identical exposures are generated automatically if the observer specifies the proposal optional parameters `CR-SPLIT` (for $n > 1$), or `PATTERN`, or if `Number_of_Iterations > 1`. If it is not specified, `CR-SPLIT` defaults to $n = 2$. In general, identical exposures are defined here as exposures of the same target, with the same detector and filter(s). For identical exposures in `PATTERNS`, this also involves slews and therefore slew overheads.

For `ACQ` mode, the overhead includes double the specified exposure time. The reason for having two acquisition images is to eliminate possible image defects which can interfere with target acquisition. The flight software ensures that two images are taken, so the user does not need to specify that in the proposal.

The overhead time for serial buffer dumps arises in certain cases from the overheads associated with the onboard data management and switching over the cameras. The on-board buffer memory can hold no more than one WFC image. The next WFC image can be placed into the buffer only after the buffer has dumped the previous image, which takes 349 seconds.



If the next exposure time is longer than 339 seconds (for WFC) or 346 seconds (for HRC; 16 HRC images may be taken before a buffer dump is triggered), the buffer dump will occur during that exposure, and no overhead is imposed. However, if the next exposure time is shorter than 339 seconds (WFC) or 346 seconds (HRC), then the dump must occur between the two exposures.

Sequences of many short HRC or SBC exposures can also lead to serial dumps when the buffer becomes full. In this case the buffer dump time becomes an overhead to be included into the orbit time budget. This overhead can severely constrain the number of short exposures one can squeeze into an orbit. Subarrays can be used to lower the data volume for some applications.

For operational reasons related to power constraints and SAA avoidance, respectively, the HRC and SBC cannot be powered up simultaneously, and once on, the SBC must remain on for a minimum of 2 hours. These constraints affect programs using both cameras as follows. (1) Although not recommended, both may be used within a single orbit, but then the HRC observations must always be done first. Moreover, there is a 12 minute overhead penalty for the reconfiguration. If the buffer is full or will be before the end of the visibility period, then an additional 6 minute overhead is incurred for the switch. (2) Even if the two cameras are used in separate, consecutive orbits, either the HRC must be scheduled first, or the SBC must be used for a minimum of two orbits before the HRC is activated.

8.2.1 Subarrays

At the end of each exposure, data are read out into ACS's internal buffer memory where they are stored until they are dumped into HST's solid state data recorder. The ACS internal buffer memory holds 34 MB or the equivalent of 1 full WFC frame, or 16 HRC or SBC frames. Thus, after observing a full WFC frame, the internal buffer memory must be dumped before the next exposure can be taken. The buffer dump takes 349 seconds and may not occur while ACS is being actively commanded. Of this time, 339 seconds (for one WFC image) or 346 seconds (for 16 HRC images) is spent dumping the image. The buffer dump cannot be done during the next exposure if the latter is shorter than 339 seconds. If, however, the next exposure is less than 339 seconds the buffer dump will create an extra 5.8 minutes of overhead.

If your science program is such that a smaller FOV can be used, then one way of possibly reducing the frequency and hence overheads associated with buffer dumps is to use WFC subarrays. With subarrays, only the selected region of the detector is read out at a normal speed and stored in the buffer, and a larger number of frames can be stored before requiring a dump. Using subarrays not only reduces the amount of time spent dumping the buffer but in some cases may reduce the readout time. See Chapter 7 for a discussion of some of the limitations of subarrays. If the user elects to define a subarray of arbitrary size and location, allowed on an available-but-unsupported basis, then matching bias frames will not be automatically provided by STScI. Any bias frames specified by the user will typically be scheduled during the following occultation (i.e., they do not add to the overheads during visibility time). Dark frames and flat fields

will be extracted from full frame images. In some special cases where a general subarray is cleverly defined so as to include a physical overscan region, no separate bias frames are needed.

8.3 Orbit Use Determination Examples

The easiest way to learn to compute total orbit time requests is to work through a few examples. Below we provide five different examples:

- Example 1 is a simple WFC image in one filter.
- Example 2 is a set of short WFC exposures that may require large overheads associated with buffer dumps.
- Example 3 is a one-orbit coronagraphic observation in two filters.
- Example 4 is a two-orbit observation using dithering.
- Example 5 is a one orbit WFC grism spectroscopic observation.

These examples represent fairly typical uses of ACS.

8.3.1 Sample Orbit Calculation 1:

Consider a target to be imaged with WFC in a given filter in one orbit. Using the [Exposure Time Calculator \(ETC\)](#), we find that we need 2400 seconds of exposure time to reach the desired level of signal-to-noise ratio. Given that the observation must be split into a series of two exposures by CR-SPLIT (CR-SPLIT=2), we map the overheads and the science exposure times onto the orbit as follows:

Table 8.3: Orbit calculation for example 1.

| Action | Time (minutes) | Explanation |
|--|----------------|--|
| <i>Orbit 1</i> | | |
| Initial guide-star acquisition | 6 | Needed at start of observation of a new target |
| WFC overhead for the first exposure | 4.0 | Includes filter change, camera set-up, and readout |
| First science exposure | 20.0 | |
| WFC overhead for the subsequent science exposure in the series | 2.5 | Includes readout |
| The next science exposure in the series | 20.0 | |
| Total time for science exposures | 40.0 | |
| Total used time in the orbit | 52.6 | |

Thus, the two WFC exposures totaling 2400 seconds make full use of the typically available time in one orbit. The exposure times can be adjusted if the actual target visibility time differs from the derived total used time.

8.3.2 Sample Orbit Calculation 2:

This example illustrates the impact of short WFC exposures on the useful time in the orbit. We have one orbit to observe a target with WFC in two filters, so the observation consists of two series, each with two identical CR-SPLIT exposures. The ETC has shown that at the minimally accepted signal-to-noise ratio the exposure time must be 540 seconds for each of the filters, so each of the CR-SPLITS must be at least 270 seconds long. For the target declination, we find that the visibility time is 55 minutes. The time budget for the orbit is then as follows:

Table 8.4: Orbit calculation for example 2.

| Action | Time (minutes) | Explanation |
|---|--------------------------|---|
| <i>Orbit 1</i> | | |
| Initial guide-star acquisition | 6 | Needed at start of observation of a new target |
| WFC overhead for the first exposures in two series | $2 \times 4 = 8$ | Includes filter change, camera set-up, and readout |
| WFC overhead for subsequent exposures in each of the two series | $2 \times 2.5 = 5$ | Includes readout |
| Additional overhead for all but the last exposures in the orbit | $5.8 \times 3 = \sim 17$ | Needed to dump the buffer because the next exposure is too short (> 339 seconds) to accommodate the dump time. |
| Science exposures | $4 \times 4.5 = 18$ | |
| Total time for science exposures | 18 | |
| Total used time in the orbit | 54 | |

Comparing with the previous example, we see that although with the adopted minimum exposure times we can squeeze the observation into one orbit, the efficiency of the orbit use is very low because of the large overheads associated with buffer dumps. However, if we increase each of the four exposure times so that they are larger than 339 seconds, we avoid these additional overheads. This would free ~ 17 minutes of the orbit time for science, which allows us to almost double the science exposure time (35 minutes instead of 18 minutes) and thus significantly improve signal-to-noise.

Similarly, a subarray can be used to readout only a fraction of the detector, allowing more frames to be stored in the buffer before requiring a dump. In this example, using four WFC1-1K subarrays for 4 short ($t < 339$ seconds) exposures would save 176 seconds in readout time and 1047 seconds in dump time. This frees up ~ 20 minutes of orbit time to be used for science.

8.3.3 Sample Orbit Calculation 3:

This example demonstrates the orbit calculation for a coronagraphic observation. We want to obtain coronagraphic images of a star in two filters, F250W and F606W. The ETC has shown that the exposure times adequate for our scientific goals are 5 minutes in F606W and 30 minutes in F250W. From the orbit visibility table (see the [HST Primer](#)) we find that at the target declination of 15° the target visibility time is 52 minutes. With CR-SPLIT=2, we thus have to accommodate in that period 35 minutes of four science exposures grouped in two series. The orbit calculation goes like this:

Table 8.5: Orbit calculation for example 3.

| Action | Time (minutes) | Explanation |
|---|------------------------------|--|
| <i>Orbit 1</i> | | |
| Initial guide-star acquisition | 6 | Needed at start of observation of a new target |
| Target acquisition | $3.5 + (2 \times 0.1) = 3.7$ | Point-source acquisition on target |
| HRC overhead for the first exposures in the series | $2 \times 2.5 = 5$ | Includes filter change, camera set-up, and readout |
| HRC overhead for the subsequent exposures in the series | $2 \times 1 = 2$ | Includes readout |
| Science exposures in F606W | $2 \times 2.5 = 5$ | |
| Science exposures in F250W | $2 \times 15 = 30$ | |
| Total time for science exposures | 35 | |
| Total used time in the orbit | ~ 52 | |

The derived total used time in the orbit shows that our target can indeed be imaged in the selected filters in one orbit. Since there remains 3 minutes of unused time, we can adjust our exposure times to make full use of the available time.

8.3.4 Sample Orbit Calculation 4:

This example illustrates the orbit calculation for a WFC observation with the ACS box pattern, which implements imaging at four offset pointings. The goal of the observation is to obtain a dithered image of a field in such a way that would allow us to bridge the 50 pixel interchip gap between the WFC CCDs in the combined image. Given the WFC plate scale of 0.05 arcseconds/pixel, this requires that the offsets in the dithering pattern are larger than 2.5 arcseconds. Each offset will then take 0.5 minutes to move the spacecraft from one pointing in the pattern to another. We have determined that the exposure time necessary to reach the desired signal-to-noise ratio is 80 minutes. The visibility time at our target declination is 58 minutes. In this observation we do not want to rely on cosmic ray removal provided by the dithering data reduction package, and set `CR-SPLIT=2` to be able to remove cosmic rays from the four individual images separately. As a result, the orbit calculation will involve a series of 8 exposures (two exposures at each of the four pointings in the dithering pattern) split across two orbits:

Table 8.6: Orbit calculation for example 4.

| Action | Time (minutes) | Explanation |
|---|----------------------|---|
| Orbit 1 | | |
| Initial guide-star acquisition | 6 | Needed at start of observation of a new target |
| WFC overhead for the first exposures in the series | 4 | Includes filter change, camera set-up, and readout |
| WFC overhead for the subsequent 3 exposures in the series | $3 \times 2.5 = 7.5$ | Includes readout |
| Spacecraft slew | 0.5 | To offset from the first to the second pointing |
| Four science exposures | $4 \times 10 = 40$ | Exposures at the first two pointings in the dither pattern |
| Total time for science exposures | 40 | |
| Total used time in the orbit | 58 | |
| Orbit 2 | | |
| Guide-star re-acquisition | ~6 | Needed at start of a new orbit to observe the same target |
| WFC overhead for the remaining exposures in the series | $4 \times 2.5 = 10$ | Includes readout |
| Spacecraft slews | $2 \times 0.5 = 1$ | To offset to the third and fourth pointings |
| Four science exposures | $4 \times 10 = 40$ | Exposures at the second two pointings in the dither pattern |
| Total time for science exposures | 40 | |
| Total used time in the orbit | 57 | |

The total used time in the first orbit comes out a little bit larger than the visibility time. However, given the conservative nature of the adopted overhead times as well as a bit of flexibility in the adopted signal-to-noise ratio, the difference is not significant. It should be remembered that the purpose of the above exercises is to estimate how many orbits to request for our science program rather than to exactly design the observation.

8.3.5 Sample Orbit Calculation 5:

This example illustrates the orbit calculation for a simple 30 minutes WFC grism spectroscopic observation broken down by CR-SPLIT=2 into a series of two exposures.

Table 8.7: Orbit calculation for example 5.

| Action | Time (minutes) | Explanation |
|--|----------------------|--|
| <i>Orbit 1</i> | | |
| Initial guide-star acquisition | 6 | Needed at start of observation of a new target |
| Predefined imaging exposure for grism spectroscopy | 7 | Needed to co-locate the targets and their spectra in the FOV |
| WFC overhead for the first science exposure in the series | 4.0 | Includes filter change, camera set-up, and readout |
| WFC overhead for the subsequent science exposure in the series | 2.5 | Includes readout |
| Two science exposures | $2 \times 15.0 = 30$ | |
| Total science exposure time | 30.0 | |
| Total used time in the orbit | 49.5 | |

Unlike similar imaging exposures, here we have to take into account an additional imaging exposure before the sequence of spectroscopic exposures, which takes 10 minutes off the available orbit time.

Exposure-Time Calculations

In this chapter...

| |
|--|
| 9.1 Overview / 175 |
| 9.2 Determining Count Rates from Sensitivities / 176 |
| 9.3 Computing Exposure Times / 182 |
| 9.4 Detector and Sky Backgrounds / 185 |
| 9.5 Extinction Correction / 190 |
| 9.6 Exposure-Time Examples / 191 |
| 9.7 Tabular Sky Backgrounds / 195 |

9.1 Overview

In this chapter we explain how to use sensitivities and throughputs to determine the expected count rate from your source and how to calculate exposure times to achieve a given signal-to-noise ratio for your ACS observations taking all background contributions into account. At the end of this chapter you will find examples to guide you through specific cases.

9.1.1 The ACS Exposure Time Calculator

The ACS Exposure-Time Calculator ([ETC](#)) is available to help with proposal preparation at:

http://www.stsci.edu/hst/acs/software/etcs/ETC_page.html.

This [ETC](#) calculates count rates for given source and background parameters, signal-to-noise ratios for a given exposure time, or count rates and exposure time for a given signal-to-noise ratio for imaging,

spectroscopic, and coronagraphic observations. A variety of apertures are now available, both circular and square, allowing the user to either select a radius in arcseconds or a size in pixels. The current default are a 0.2 arcseconds radius for both the WFC and the HRC, and a 0.5 arcseconds radius for SBC observations, which enclose approximately 80% of the PSF flux. Square and circular apertures are available between 0.1 and 2.0 arcseconds. For extended sources the S/N calculation is based on counts summed over one resolution element of 2 x 2 pixels, as the source size is assumed to be larger than the ACS resolution. A calibrated spectrum of your source can be provided directly to the [Exposure Time Calculator](#). The [ETC](#) also determines peak per-pixel count rates and total count rates to aid in feasibility assessment. Warnings appear if the source exceeds the local or global brightness limits for SBC observations (see Section 7.2). The [ETC](#) has online help for its execution and interpretation of results. Alternatively, users can use *synphot* in [STSDAS](#) to calculate count rates and the wavelength distribution of detected counts.

9.2 Determining Count Rates from Sensitivities

In this Chapter, specific formulae appropriate for imaging and spectroscopic modes are provided to calculate the expected count rates and the signal-to-noise ratio from the flux distribution of a source. The formulae are given in terms of sensitivities, but we also provide transformation equations between the throughput (QT) and sensitivity (S) for imaging and spectroscopic modes.

Throughputs are presented in graphical form as a function of wavelength for the prisms and for the imaging modes in Chapter 10. Given your source characteristics and the sensitivity of the ACS configuration, calculating the expected count rate over a given number of pixels is straightforward, since the ACS PSF is well characterized. The additional required information is the encircled energy fraction (ϵ_f) in the peak pixel, the plate scale, and the dispersions of the grisms and prisms. This information is summarized in Table 9.1, Table 9.2, and Table 9.3.

Table 9.1: Useful quantities for the ACS WFC.

| Filter | Pivot λ (Å) | $\int Q_{\lambda} T_{\lambda} d\lambda/\lambda$ | AB mag zero point | $\int S_{\lambda} d\lambda$ | encircled energy | Flux in central pixel | Background sky rate |
|--------|---------------------|---|-------------------|-----------------------------|------------------|-----------------------|---------------------|
| F435W | 4317.4 | 0.0744 | 25.67 | 3.18E18 | 0.85 | 0.22 | 0.0284 |
| F475W | 4744.3 | 0.1070 | 26.07 | 5.53E18 | 0.86 | 0.21 | 0.0609 |
| F502N | 5023.0 | 0.0032 | 22.27 | 1.88E17 | 0.86 | 0.21 | 0.0020 |
| F550M | 5581.2 | 0.0362 | 24.89 | 2.59E18 | 0.85 | 0.22 | 0.0280 |
| F555W | 5359.6 | 0.0775 | 25.72 | 5.11E18 | 0.86 | 0.21 | 0.0545 |
| F606W | 5917.7 | 0.1573 | 26.49 | 1.26E19 | 0.85 | 0.22 | 0.1358 |
| F625W | 6310.5 | 0.0915 | 25.90 | 8.37E18 | 0.85 | 0.22 | 0.0825 |
| F658N | 6583.9 | 0.0050 | 22.75 | 5.00E17 | 0.85 | 0.22 | 0.0045 |
| F660N | 6599.4 | 0.0019 | 21.67 | 1.87E17 | 0.85 | 0.22 | 0.0017 |
| F775W | 7693.0 | 0.0731 | 25.65 | 9.93E18 | 0.85 | 0.20 | 0.0780 |
| F814W | 8059.8 | 0.0948 | 25.94 | 1.41E19 | 0.83 | 0.19 | 0.1044 |
| F850LP | 9054.8 | 0.0352 | 24.86 | 6.63E18 | 0.73 | 0.14 | 0.0415 |
| F892N | 8914.9 | 0.0036 | 22.37 | 6.48E17 | 0.77 | 0.15 | 0.0039 |
| G800L | 7480.7 | 0.1591 | 26.50 | 2.04E19 | 0.86 | 0.17 | 0.1526 |
| CLEAR | 6269.8 | 0.3833 | 27.45 | 3.46E19 | ---- | 0.10 | 0.3580 |

Table 9.2: Useful quantities for the ACS HRC.

| Filter | Pivot λ (Å) | $\int Q_{\lambda} T_{\lambda} d\lambda/\lambda$ | AB mag zero point | $\int S_{\lambda} d\lambda$ | encircled energy | Flux in central pixel | Background sky rate |
|--------|---------------------|---|-------------------|-----------------------------|------------------|-----------------------|---------------------|
| F220W | 2255.3 | 0.0106 | 23.55 | 1.23E17 | 0.79 | 0.17 | 0.0001 |
| F250W | 2715.8 | 0.0123 | 23.72 | 2.09E17 | 0.82 | 0.16 | 0.0003 |
| F330W | 3362.7 | 0.0172 | 24.08 | 4.47E17 | 0.84 | 0.16 | 0.0006 |
| F344N | 3433.7 | 0.0017 | 21.59 | 4.67E16 | 0.84 | 0.16 | 0.0001 |
| F435W | 4311.0 | 0.0436 | 25.09 | 1.86E18 | 0.86 | 0.17 | 0.0043 |
| F475W | 4775.7 | 0.0650 | 25.53 | 3.40E18 | 0.85 | 0.17 | 0.0120 |
| F502N | 5022.9 | 0.0021 | 21.82 | 1.24E17 | 0.85 | 0.17 | 0.0003 |
| F550M | 5579.8 | 0.0234 | 24.42 | 1.67E18 | 0.85 | 0.15 | 0.0048 |
| F555W | 5356.0 | 0.0503 | 25.25 | 3.31E18 | 0.85 | 0.16 | 0.0099 |
| F606W | 5888.0 | 0.0983 | 25.98 | 7.82E18 | 0.85 | 0.14 | 0.0238 |
| F625W | 6295.5 | 0.0557 | 25.36 | 5.07E18 | 0.84 | 0.13 | 0.0148 |
| F658N | 6583.7 | 0.0030 | 22.18 | 2.98E17 | 0.83 | 0.13 | 0.0008 |
| F660N | 6599.1 | 0.0011 | 21.11 | 1.11E17 | 0.83 | 0.13 | 0.0003 |
| F775W | 7665.1 | 0.0380 | 24.94 | 5.13E18 | 0.78 | 0.11 | 0.0111 |
| F814W | 8115.3 | 0.0521 | 25.29 | 7.88E18 | 0.76 | 0.10 | 0.0161 |
| F850LP | 9145.2 | 0.0228 | 24.39 | 4.37E18 | 0.68 | 0.08 | 0.0075 |
| F892N | 8916.1 | 0.0022 | 21.87 | 4.09E17 | 0.73 | 0.09 | 0.0007 |
| G800L | 7506.4 | 0.0924 | 25.91 | 1.20E19 | 0.81 | 0.07 | 0.0250 |
| PR200L | 5650.2 | 0.2756 | 27.10 | 2.02E19 | 0.80 | 0.16 | 0.0624 |
| CLEAR | 5472.0 | 0.3205 | 27.26 | 2.20E19 | ---- | 0.12 | 0.0683 |

Table 9.3: Useful quantities for the ACS SBC.

| Filter | Pivot λ (Å) | $\int Q_{\lambda} T_{\lambda} d\lambda/\lambda$ | AB mag zero point | $\int S_{\lambda} d\lambda$ | encircled energy | Flux in central pixel | Background sky rate |
|--------|---------------------|---|-------------------|-----------------------------|------------------|-----------------------|---------------------|
| F115LP | 1406.1 | 0.0147 | 23.92 | 6.70E16 | 0.83 | 0.11 | 0.0238 |
| F122M | 1273.8 | 0.0010 | 20.95 | 3.56E15 | 0.82 | 0.09 | 0.0042 |
| F125LP | 1437.5 | 0.0122 | 23.71 | 5.80E16 | 0.83 | 0.12 | 0.0027 |
| F140LP | 1527.0 | 0.0069 | 23.09 | 3.68E16 | 0.84 | 0.13 | 0.0000 |
| F150LP | 1610.7 | 0.0038 | 22.45 | 2.27E16 | 0.84 | 0.14 | 0.0000 |
| F165LP | 1757.9 | 0.0010 | 21.02 | 7.29E15 | 0.85 | 0.16 | 0.0000 |
| PR110L | 1429.4 | 0.0120 | 23.69 | 5.62E16 | 0.86 | 0.26 | 0.0129 |
| PR130L | 1438.8 | 0.0120 | 23.68 | 5.66E16 | 0.87 | 0.28 | 0.0027 |

In each Table, the following quantities are listed:

- The pivot wavelength, a source-independent measure of the characteristic wavelength of the bandpass, defined such that it is the same if the input spectrum is in units of F_{λ} or F_{ν} :

$$\lambda_p = \sqrt{\frac{\int Q(\lambda)T(\lambda)d\lambda}{\int Q(\lambda)T(\lambda)((d\lambda)/\lambda)}}$$

- The integral $\int Q_{\lambda} T_{\lambda} d\lambda/\lambda$, used to determine the count rate when given the astronomical magnitude of the source.
- The ABmag zero point, defined as the AB magnitude of a source with a constant F_{ν} that gives 1 count/second with the specified configuration.
- The sensitivity integral, defined as the count rate that would be observed from a constant F_{λ} source with flux 1 erg/cm²/second/Å.
- The encircled energy, defined as the fraction of PSF flux enclosed in the default photometry aperture 0.2 arcseconds for the WFC and HRC, and 0.5 arcseconds for the SBC. These correspond approximately to 5 × 5, 9 × 9, and 15 × 15 box-sizes respectively.
- The fraction of PSF flux in the central pixel, useful for determining the peak count rate to check for overflow or bright object protection possibilities.
- The sky background count rate, which is the count rate that would be measured with average zodiacal background, and average earthshine. It does not include the contribution from the detectors, tabulated separately in Table 3.1

Here, we describe how to determine two quantities:

1. The counts/second (C) from your source over some selected area of N_{pix} pixels, where a signal of an electron on a CCD is equivalent to one count.
2. The peak counts/second/pixel (P_{cr}) from your source, which is useful for avoiding saturated CCD exposures, and for assuring that SBC observations do not exceed the bright-object limits.

We consider the cases of point sources and diffuse sources separately in each of the imaging and spectroscopy sections following.

9.2.1 Imaging

Point Source

For a point source, the count rate, C , can be expressed as the integral over the bandpass of the filter:

$$C = A \int F_{\lambda} \frac{\lambda}{hc} Q_{\lambda} T_{\lambda} \varepsilon_f d\lambda = \int F_{\lambda} S_{\lambda} \varepsilon_f d\lambda$$

Where:

- A is the area of the unobstructed 2.4 meter telescope (i.e., 45,239 cm²)
- F_{λ} is the flux from the astronomical source in erg/second/cm²/Å
- h is Planck's constant
- c is the speed of light
- The factor λ/hc converts ergs to photons.
- $Q_{\lambda} T_{\lambda}$ is the system fractional throughput, i.e., the probability of detecting a count per incident photon, including losses due to obstructions of the full 2.4 meter OTA aperture. It is specified this way to separate out the instrument sensitivity Q_{λ} and the filter transmission T_{λ} .
- ε_f = the fraction of the point source energy encircled within N_{pix} pixels.
- S_{λ} is the total imaging point source sensitivity with units of counts/second/Å per incident erg/second/cm²/Å.

The peak counts/second/pixel from the point source, is given by:

$$C_{peak} = \int F_{\lambda} S_{\lambda} \varepsilon_f(1) d\lambda$$

Where:

- F_λ , and S_λ are as above.
- $\varepsilon_f(1)$ is the fraction of energy encircled within the peak pixel.

Again, the integral is over the bandpass.

If the flux from your source can be approximated by a flat continuum ($F_\lambda = \text{constant}$) and ε_f is roughly constant over the bandpass, then:

$$C = F_\lambda \varepsilon_f \int S_\lambda d\lambda$$

We can now define an equivalent bandpass of the filter (B_λ) such that:

$$\int S_\lambda d\lambda = S_{peak} B_\lambda$$

Where:

- S_{peak} is the peak sensitivity.
- B_λ is the effective bandpass of the filter.

The count rate from the source can now be written as:

$$C = F_\lambda \varepsilon_f S_{peak} B_\lambda$$

In Tables 9.1 to 9.3, we give the value of $\int S_\lambda d\lambda$ for each of the filters. Alternatively, we can write the equation in terms of V magnitudes:

$$C = 2.5 \times 10^{11} \varepsilon_f \left(\int QT d\lambda / \lambda \right) \times 10^{-0.4(V + AB_v)}$$

where V is the visual magnitude of the source, the quantity under the integral sign is the mean sensitivity of the detector+filter combination, and is tabulated in Tables 9.1 to 9.3, and AB_v is the filter-dependent correction for the deviation of the source spectrum from a constant F_v spectrum. This latter quantity is tabulated for several different astronomical spectra in Tables 10.1 to 10.3 in Chapter 10.

Diffuse Source

For a diffuse source, the count rate, C , per pixel, due to the astronomical source can be expressed as:

$$C = \int I_\lambda S_\lambda m_x m_y d\lambda$$

Where:

- I_λ = the surface brightness of the astronomical source, in $\text{erg/second/cm}^2/\text{\AA}/\text{arcseconds}^2$.
- S_λ as above.
- m_x and m_y are the plate scales along orthogonal axes.

Emission Line Source

For a source where the flux is dominated by a single emission line, the count rate can be calculated from the equation

$$C = 2.23 \times 10^{12} \cdot (QT)_\lambda \cdot F(\lambda) \cdot \lambda$$

where C is the observed count rate in counts/second, (QT) is the system throughput at the wavelength of the emission line, $F(\lambda)$ is the emission line flux in units of erg/cm²/second, and λ is the wavelength of the emission line in Angstroms. $(QT)_\lambda$ can be determined by inspection of the plots in Chapter 10. See Section 9.6.4 for an example of emission-line imaging using ACS.

9.2.2 Spectroscopy

Point Source

For a point source spectrum with a **continuum flux distribution**, the count rate, C , is per pixel in the dispersion direction, and is integrated over a fixed extraction height N_{spix} in the spatial direction perpendicular to the dispersion:

$$C = F_\lambda S'_\lambda \varepsilon'_{Nspix} = F_\lambda A \frac{\lambda}{hc} T_\lambda \varepsilon'_{Nspix} d$$

Where:

- S'_λ is the total point source sensitivity in units of counts/second per incident erg/second/cm²/Å; and $S_\lambda = S'_\lambda \cdot d$
- d is the dispersion in Å/pixel.
- ε'_{Nspix} is the fraction of the point source energy within N_{spix} in the spatial direction.
- the other quantities are defined above.

For an **unresolved emission line** at $\lambda = L$ with a flux of F_L in erg/second/cm² the total counts recorded over the N_{spix} extraction height is:

$$C = F_\lambda S'_\lambda / d$$

These counts will be distributed over pixels in the wavelength direction according to the instrumental line spread function.

In contrast to the case of imaging, sensitivity S_λ , the spectroscopic point source sensitivity calibration ($S_\lambda \times \varepsilon_{Nspix}$) for a default extraction height of N_{spix} is measured directly from observations of stellar flux standards after insertion of ACS into HST. Therefore, the accuracy in laboratory

determinations of T_λ for the ACS prisms and grisms is NOT crucial to the final accuracy of their sensitivity calibrations.

The peak counts/second/pixel from the point source, is given by:

$$P_{cr} = \varepsilon'_f(1)F_\lambda S'_\lambda$$

Where:

- $\varepsilon'_f(1)$ is the fraction of energy contained within the peak pixel.
- the other quantities are as above.

9.3 Computing Exposure Times

To derive the exposure time to achieve a given signal-to-noise ratio, or to derive the signal to noise ratio in a given exposure time, there are four principal ingredients:

- Expected counts C from your source over some area.
- The area (in pixels) over which those counts are received (N_{pix}).
- Sky background (B_{sky}) in counts/pixel/second.
- The detector background, or dark, (B_{det}) in counts/second/pixel and the readnoise (R) in counts of the CCD.
- Section 9.4 provides the information for determining the sky-plus-detector background.

9.3.1 Calculating Exposure Times for a Given signal-to-noise

The signal-to-noise ratio, Σ is given by:

$$\Sigma = \frac{Ct}{\sqrt{Ct + N_{pix}(B_{sky} + B_{det})t + N_{pix}N_{read}R^2}}$$

Where:

- C = the signal from the astronomical source in counts/second, or electrons/second from the CCD. The actual output signal from a CCD is C/G where G is the gain. You must remember to multiply by G to compute photon events in the raw CCD images.
- G = the gain is always 1 for the SBC, and $\sim 1, 2, 4,$ or 8 for the CCDs, depending on GAIN.

- N_{pix} = the total number of detector pixels integrated over to achieve C .
- B_{sky} = the sky background in counts/second/pixel.
- B_{det} = the detector dark current in counts/second/pixel.
- R = the readnoise in electrons; = 0 for SBC observations, 5.0 and 4.7 for WFC and HRC respectively
- N_{read} = the number of CCD readouts.
- t = the integration time in seconds.

This equation assumes the optimistic (and often realistic) condition that the background zero point level under the object is sufficiently well known (and subtracted) to not significantly contribute; in crowded fields this may not be true.

Observers using the CCD normally take sufficiently long integrations that the CCD readnoise is not important. This condition is met when:

$$Ct + N_{pix}(B_{sky} + B_{det})t > 2N_{pix}N_{read}R^2$$

For the CCD in the regime where readnoise is not important and for all SBC observations, the integration time to reach a signal-to-noise ratio Σ , is given by:

$$t = \frac{\Sigma^2[C + N_{pix}(B_{sky} + B_{det})]}{C^2}$$

If your source count rate is much brighter than the sky plus detector backgrounds, then this expression reduces further to:

$$t = \frac{\Sigma^2}{C}$$

i.e., the usual result for Poisson statistics of $\Sigma = \sqrt{totalcounts}$.

More generally, the required integration time to reach a signal-to-noise ratio Σ is given by:

$$t = \frac{\Sigma^2[C + N_{pix}(B_{sky} + B_{det})] + \sqrt{\Sigma^4[C + N_{pix}(B_{sky} + B_{det})]^2 + 4\Sigma^2C^2[N_{pix}N_{read}R^2]}}{2C^2}$$

9.3.2 Exposure Time Estimates for Red Targets in F850LP

At wavelengths greater than 7500 Å (HRC) and about 9000 Å (WFC) ACS CCD observations are affected by a red halo due to light scattered off

the CCD substrate. An increasing fraction of the light as a function of wavelength is scattered from the center of the PSF into the wings. This problem affects particularly the very broad z-band F850LP filter, for which the encircled energy depends on the underlying spectral energy distribution the most. In the currently available **ETC**, the treatment of such an effect has been ameliorated but not solved. The encircled energy fraction is calculated at the effective wavelength which takes into account the source spectral distribution. This fraction is then multiplied by the source counts. (The effective wavelength is the weighted average of the system throughput AND source flux distribution integrated over wavelength). However, this does not account for the variation in enclosed energy with wavelength.

As a consequence, in order to obtain correct estimated count rates for red targets, observers are advised to use the *synphot* package in IRAF/STSDAS for which the proper integration of encircled energy over wavelength has now been incorporated. To quantify this new **synphot** capability, we compare the ETC results with **synphot** for a set of different spectral energy distributions and the observation mode WFC/F850LP. In Table 9.4, the spectral type is listed in the first column. The fraction of light with respect to the total integrated to infinity is listed in the other two columns, for the ETC and **synphot** calculations respectively. These values are derived for a 0.2 arcseconds aperture for the ETC calculations and **synphot**.

Table 9.4: Encircled energy comparison for WFC/F850LP.

| Spectral type | APT ETC | Synphot |
|---------------|---------|---------|
| O | 0.76 | 0.74 |
| M | 0.71 | 0.7 |
| L | 0.69 | 0.68 |
| T | 0.61 | 0.6 |

The **ETC** results are off by 3% (O star), 2% (M star), 2% (L star), and 1% (T star). If this small effect is relevant to particular observations, then the *synphot* software package can be used. To learn how to use the **synphot** tool, we refer to the instructions provided in the April 2003 STAN, <http://www.stsci.edu/hst/acs/documents/newsletters/stan0302.html>, and in ACS ISR 2003-08.

9.4 Detector and Sky Backgrounds

When calculating expected signal-to-noise ratios or exposure times, the background from the sky, and the background from the detector must be taken into account.

9.4.1 Detector Backgrounds

See Table 3.1 for readnoise and dark current characteristics of the detectors, including variations by amplifier and GAIN for the CCDs.

9.4.2 Sky Background

The sources of sky background which will affect ACS observations include:

- Earth shine (ES).
- Zodiacal light (ZL).
- Geocoronal emission (GC).

The background in counts/second/pixel for **imaging observations** can be computed as:

$$B_{sky} = \int I_{\lambda} S_{\lambda} m_x m_y d\lambda$$

Where:

- I_{λ} is the surface brightness of the sky background, in erg/second/cm²/Å/arcseconds².
- S_{λ} is the point source sensitivity for the imaging mode.
- m_x and m_y are the plate scales along orthogonal axes.

The image of the sky through a disperser is not uniform, since some wavelengths fall off the detector for regions of sky near the edge of the field of view (FOV). Since the ACS grism spectra are of order 200 pixels long, the regions of lower sky will be strips at the long and short wavelength edges of the FOV. The maximum width of the strips from where the signal starts to decline to the edge, where the signal is down by roughly 2x, is about half the total length of a spectrum of a point source, i.e., roughly 100 pixels in the case of a sky background with a **continuum** of wavelengths. In the case of the HRC, the sky for the dispersed mode will not have the low background strips, since the FOV is not masked to the detector size. These small strips of lower sky background in the SBC and the WFC are ignored in the following formulae. Furthermore in the SBC

and the WFC, since the spectra do not lie along the direction of the anamorphic distortion, the plate scales of m_x and m_y above must be replaced by the plate scales m_s and m_λ in the orthogonal spatial and dispersion directions, respectively. Interior to the strips, a point on the detector sees a region of sky over the full wavelength coverage of the disperser. Thus, for **spectroscopic observations**:

$$B_{sky}^\lambda = \int I_\lambda S'_\lambda m_s m_\lambda d\lambda$$

For a **monochromatic** sky emission line at $\lambda = L$ like Lyman- α , which will dominate the background through the LiF prism:

$$B_{sky}^L = I_L S'_L m_s m_\lambda / d$$

where

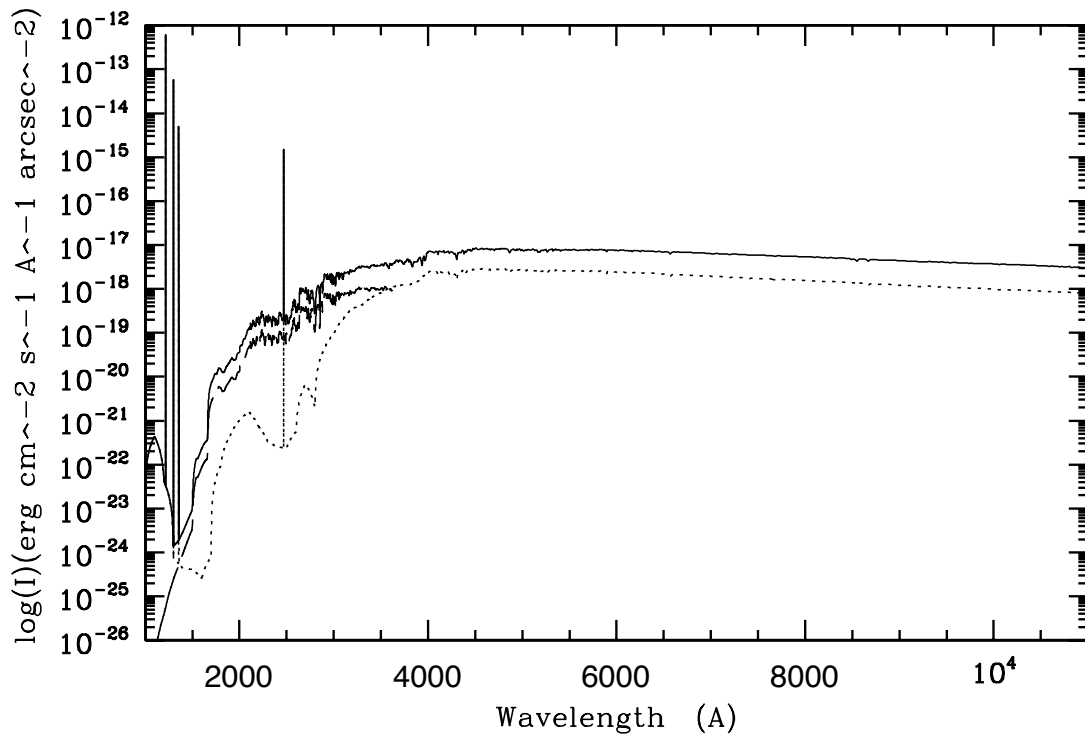
- I_L is the monochromatic intensity of a line at wavelength L in erg/second/cm²/ arcseconds².

The total sky background is:

$$B_{sky} = B_{sky}^\lambda + B_{sky}^L$$

Figure 9.1 and Table 9.7 show “high” sky background intensity as a function of wavelength, identifying the separate components which contribute to the background. The “shadow” and “average” values of the Earthshine contribution in the [ACS Exposure Time Calculator](#) correspond, respectively, to 0 and 50% of the “high” values in Figure 9.1 and Table 9.7. “Extremely high” Earthshine corresponds to twice the “high” value. For the zodiacal sky background, the values in Figure 9.1 and Table 9.7 and the ETCs correspond to the high value of $m_v = 22.1$ from Table 9.5, while the “low” and “average” zodiacal light is scaled to $m_v = 23.3$ and 22.7, respectively.

Figure 9.1: High sky background intensity as a function of wavelength.



The zodiacal contribution (ZL) is at ecliptic latitude and longitude of $30^\circ, 180^\circ$, and corresponds to $m_v = 22.1$ per square arcseconds. The Earthshine (ES) is for a target which is 38° from the limb of the sunlit Earth. Use Figure 9.2 to estimate background contributions at other angles. The day-time geocoronal line intensities are in $\text{erg}/\text{cm}^2/\text{second}/\text{arcseconds}^2$ (see Table 9.6).

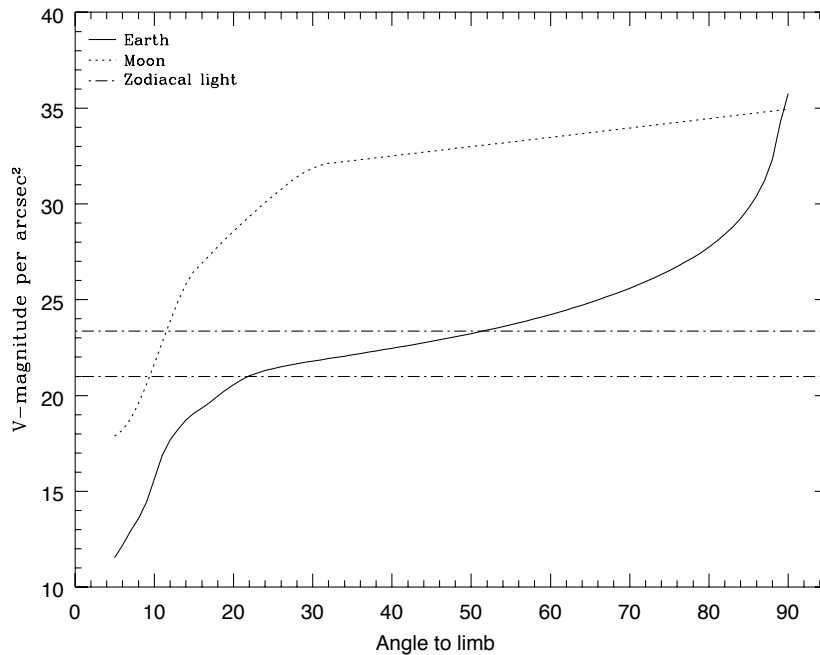
Background Variations and LOW-SKY

In the ultraviolet, the background contains bright airglow lines, which vary from day to night and as a function of HST orbital position. The airglow lines may be the dominant sky contributions in the UV both for imaging-mode and spectroscopic observations. Away from the airglow lines, at wavelengths shortward of $\sim 3000 \text{ \AA}$, the background is dominated by zodiacal light, where the small area of sky that corresponds to a pixel of the high resolution HST instrumentation usually produces a signal that is much lower than the intrinsic detector background. The contribution of zodiacal light does not vary dramatically with time, and varies by only a factor of about three throughout most of the sky. Table 9.5 gives the variation of the zodiacal background as a function of ecliptic latitude and longitude. For a target near ecliptic coordinates of $(50,0)$ or $(-50,0)$, the zodiacal light is relatively bright at $m_v = 20.9$, i.e. about 9 times the faintest values of $m_v = 23.3$. Deep imaging applications must carefully consider expected sky values!

On the other hand, Earthshine varies strongly depending on the angle between the target and the bright Earth limb. The variation of the Earthshine as a function of limb angle from the sunlit Earth is shown in Figure 9.2. This figure also shows the contribution of the moon, which is

typically much smaller than the zodiacal contribution, for which the upper and lower limits are shown. For reference, the limb angle is approximately 24° when the HST is aligned toward its orbit pole (i.e., the center of the CVZ), this limb angle corresponds to "Extremely High" Earthshine. The Earthshine contribution shown in Figure 9.1 and Table 9.7 corresponds to a limb angle of 30° , High Earthshine.

Figure 9.2: Background contributions in V magnitude per arcseconds² due to the zodiacal light, Moon, and the sunlit Earth, as a function of angle between the target and the limb of the Earth or Moon.



The two zodiacal light lines show the extremes of possible values.

For observations taken longward of 3500 \AA , the Earthshine dominates the background at small ($< 22^\circ$) limb angles. In fact, the background increases exponentially for limb angles $< 22^\circ$. The background near the bright limb can also vary by a factor of ~ 2 on timescales as short as two minutes, which suggests that the background from Earthshine also depends upon the reflectivity of the terrain over which HST passes during the course of an exposure. Details of the sky background as it affects ACS, as well as STIS, are discussed by Shaw, et al. (STIS ISR 98-21). The impact of Earthshine on ACS observations is discussed by Biretta, et al., (ACS ISR 03-05).

Table 9.5: Approximate zodiacal sky background as a function of ecliptic latitude and ecliptic longitude (in V magnitudes per square arcseconds).

| Ecliptic longitude (degrees) | Ecliptic latitude (degrees) | | | |
|------------------------------|-----------------------------|------|------|------|
| | 0 | 30 | 60 | 90 |
| 180 | 22.1 | 22.7 | 23.2 | 23.3 |
| 145 | 22.4 | 22.9 | 23.3 | 23.3 |
| 110 | 22.3 | 22.9 | 23.3 | 23.3 |
| 50 | 20.9 | 22.2 | 22.9 | 23.3 |

Observations of the faintest objects may need the special requirement **LOW-SKY** in the Phase II observing program. **LOW-SKY** observations are scheduled during the part of the year when the zodiacal background light is no more than 30% greater than the minimum possible zodiacal light for the given sky position. **LOW-SKY** in the Phase II scheduling also invokes the restriction that exposures will be taken only at angles greater than 40° from the bright Earth limb to minimize Earthshine and the UV airglow lines. The **LOW-SKY** special requirement limits the times at which targets within 60° of the ecliptic plane will schedule, and limits visibility to about 48 minutes per orbit. The use of **LOW-SKY** must be requested and justified in the Phase I Proposal.

The **ETC** provides the user with the flexibility to separately adjust both the zodiacal (low, average, high) and Earthshine (shadow, average, high, extremely high) sky background components in order to determine if planning for use of **LOW-SKY** is advisable for a given program. However, the absolute sky levels that can be specified in the **ETC** may not be achievable for a given target; e.g., as shown in Table 9.5 the zodiacal background minimum for an ecliptic target is $m_v = 22.4$ which is still brighter than both the low and average options with the **ETC**. By contrast, a target near the ecliptic pole would always have a zodiacal = low background in the **ETC**. The user is cautioned to carefully consider sky levels as the backgrounds obtained in HST observations can cover significant ranges.

Geocoronal Emission and Shadow

Background due to geocoronal emission originates mainly from hydrogen and oxygen atoms in the exosphere of the Earth. The emission is concentrated in the four lines listed in Table 9.6. The brightest line is Lyman- α at 1216 Å. The strength of the Lyman- α line varies between about 2 and ~30 kilo-Rayleighs (i.e., between 6.1×10^{-14} and 6.1×10^{-13} erg /second/cm²/arcseconds² where 1 Rayleigh = 10^6 photons/second/cm per 4π steradian) depending on the position of HST with respect to the day-night terminator and the position of the target relative to the Earth

limb. The next strongest line is the OI line at 1304 Å, which rarely exceeds 10% of Lyman- α . The typical strength of the OI 1304 Å line is about 1 kilo-Rayleighs (which corresponds to about 2.85×10^{-14} erg/second/cm²/arcseconds²) on the daylight side and about 75 times fainter on the night side of the HST orbit. OI 1356 Å and OI 2471 Å lines may appear in observations on the daylight side of the orbit, but these lines are ~10 times weaker than the OI 1304 Å line. The width of the lines also vary with temperature, the line widths given in Table 9.6 are representative values assuming a temperature of 2000 °K.

Except for the brightest objects (e.g., planets), a filter or prism mode which does not transmit at Lyman- α should be employed. To minimize geocoronal emission the special requirement SHADOW can be requested. Exposures using this special requirement are limited to roughly 25 minutes per orbit, exclusive of the guide-star acquisition (or reacquisition), and can be scheduled only during a small percentage of the year. SHADOW reduces the contribution from the geocoronal emission lines by roughly a factor of ten while the continuum Earthshine is set to zero. SHADOW requirements must be included and justified in your Phase I proposal (see the *Call for Proposals*).

Table 9.6: Geocoronal emission lines.

| Wavelength (Å) | ID | Line width (Å) | Intensity | | | |
|-------------------|--------------|----------------------|--------------------|--|--------------------|--|
| | | | Day | | Night | |
| | | | kilo- Rayleighs | erg/s/cm ² /arcsec ² | kilo- Rayleighs | erg/s/cm ² /arcsec ² |
| 1216 | Ly- α | 0.04 | ~20 | 6.1×10^{-13} | 2 | 6.1×10^{-14} |
| 1304 | OI | 0.013 | ~2 | 5.7×10^{-14} | 0.013 | 3.8×10^{-16} |
| 1356 | OI | 0.013 | ~0.2 | $\sim 5 \times 10^{-15}$ | ~0.001 | $\sim 3 \times 10^{-17}$ |
| 2471 | OI | 0.023 | <0.2 | $< 3 \times 10^{-15}$ | <0.001 | $< 1.5 \times 10^{-17}$ |

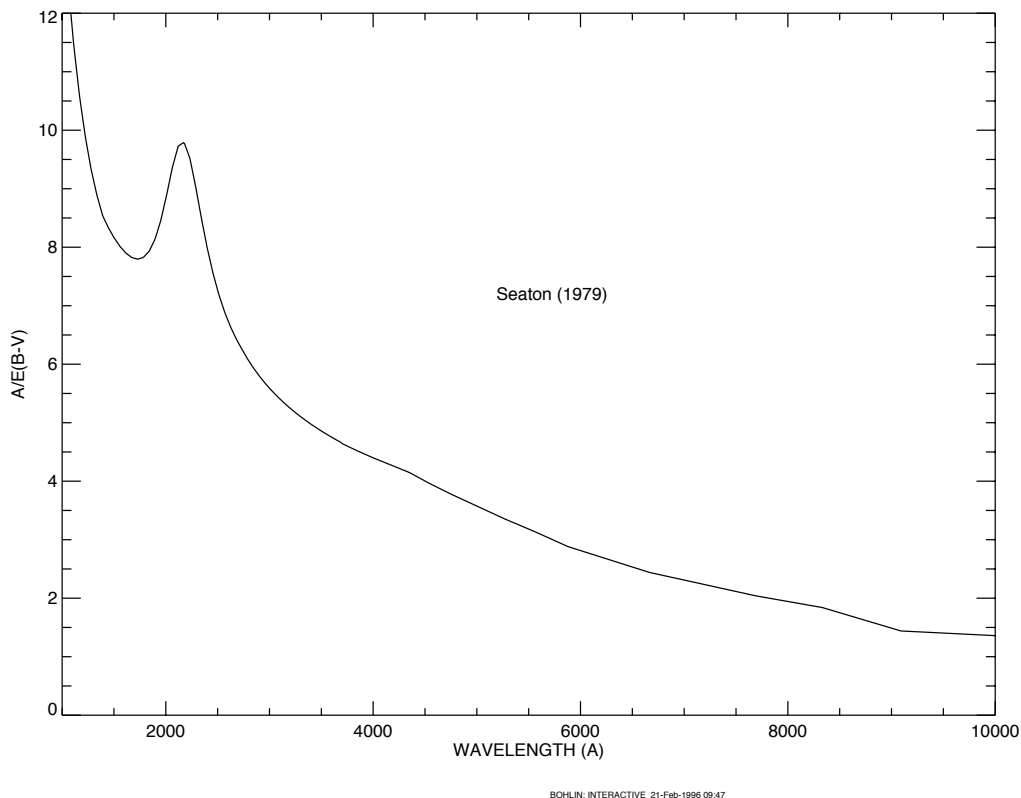
9.5 Extinction Correction

Extinction can dramatically reduce the counts expected from your source, particularly in the ultraviolet. Figure 9.3 shows the average $A_V / E(B-V)$ values for our galaxy, taken from (Seaton, *MNRAS*, **187**, 73P, 1979). Large variations about the average are observed (Witt, Bohlin, Stecher, *ApJ*, **279**, 698, 1984).

Extinction curves have a strong metallicity dependence, particularly in the UV wavelengths. Sample extinction curves can be seen in Koornneef and Code, *ApJ*, **247**, 860 1981 (LMC); Bouchet et al., *A&A*, **149**, 330 1985

(SMC); and Calzetti, Kinney and Storchi-Bergmann, *ApJ*, **429**, 582, 1994, and references therein. At lower metallicities, the 2200 Å bump which is so prominent in the galactic extinction curve disappears; and $A_V/E(B-V)$ may increase monotonically at UV wavelengths.

Figure 9.3: Extinction versus wavelength.



9.6 Exposure-Time Examples

In the following you will find a set of examples for the three different channels and for different types of sources. The examples were chosen in order to present typical objects for the three channels and also to present interesting cases as they may arise with the use of ACS.

9.6.1 Example 1: WFC Imaging a Faint Point Source

What is the exposure time needed to obtain a signal-to-noise of 10 for a point source of spectral type F2 V, normalized to $V = 26.5$, when using the WFC, F555W filter? Assume a GAIN of 1 and a photometry box size of 11 x 11 pixels, and average sky values.

The [ACS Exposure Time Calculator \(ETC\)](#) gives a total exposure time of 4410 seconds to obtain this S/N in a single exposure. Since such an exposure would be riddled with cosmic rays and essentially useless, it is necessary to specify how many exposures to split the observation into. ACS WFC observations generally should be split if the exposure time is larger than about 5 minutes, but for multi-orbit observations, splitting into 2 exposures per orbit is generally sufficient.

For a typical object visibility of 53 minutes, after applying the requisite overheads, there is time for two 1200 seconds exposures per orbit. The required exposure time can thus be reached in 4 exposures, but re-running the ETC using `CR-SPLIT=4` raises the required exposure time to 5303 seconds (because of the extra noise introduced by the four extra readouts). To achieve the required exposure time would require `CR-SPLIT=5`, or three orbits.

Using the pencil and paper method, Table 9.1 gives the integral $QTd\lambda/\lambda$ as 0.0775, and the AB_v correction term can be retrieved from Table 10.1 as 0.040. According to Figure 5.9, a circular aperture of radius 0.3 arcseconds (which has an area of 116 pixels, close to the 121 pixel box specified) encloses about 90% of the light from a star. The count rate is then $2.5 \times 10^{11} * 0.0775 * 0.9 * 10^{-0.4(26.5+0.040)} = 0.423$ counts/second, which agrees with the [ETC](#)-returned value of 0.42. The exposure time can then be found by using the equation

$$t = \frac{\Sigma^2 [C + N_{pix}(B_{sky} + B_{det})]}{C^2}$$

to give $t = 4172$ seconds, which is close to the [ETC](#)-derived value of 4410 seconds. We have inserted the background rate from Table 9.1 ($B_{sky} = 0.055$) and Table 9.5 ($B_{det} = 0.0032$), and assumed that the noise on the background is much greater than the readout noise.

Note that this can be greatly shortened by specifying a smaller analysis box (for example, 5 x 5) and using `LOW-SKY`. Dropping the aperture size to 5 x 5 at average sky which still encloses 81% of the light requires 1532 seconds. Including both the smaller 5 x 5 box and `LOW-SKY` (Zodiacal = `LOW`, Earthshine = `AVERAGE`), using the [ETC](#) gives the required exposure time as only 1306 seconds (using `CR-SPLIT=1`), or 1540 seconds with `CR-SPLIT=2`. The `LOW-SKY` visibility per orbit is 47 minutes, which allows a total on-target exposure time of 2000 seconds in one orbit with `CR-SPLIT=2`.

Note also that the count rate from WFC2 would be 0.167 electrons/second, a factor of 2.5 lower.

9.6.2 Example 2: SBC Objective Prism Spectrum of a UV Spectrophotometric Standard Star

What is the peak count rate using the PR110L prism in the SBC for the HST standard star HS2027+0651 ($V = 16.9$) that was used for the STIS prism calibration (this spectrum is not in the ETC list, therefore we quote below the flux which could be found by dearchiving the STIS spectrum)?

The sensitivity peaks in the 1500 Å to 1600 Å region. To find the count rate at 1537 Å, inspection of Figure 6.22 gives the sensitivity of 9.9×10^{14} counts/second per $\text{erg}/\text{cm}^2/\text{s}/\text{Å}$. Multiplying by the stellar flux of 5.3587×10^{-14} gives 53.0 counts/second, summed in the cross dispersion direction. For the fraction of light in the central pixel $\epsilon = 0.31$, the brightest pixel at 1437.6 Å is 17.6 counts/second/pixel, well below the bright object limit.

The SBC has no readout noise, and the dark current rate is negligible, while the main sky contribution for PR110L is from Lyman- α . For daytime Ly- α intensity of $20\text{kR} = 6.1 \times 10^{-13} \text{ ergs}/\text{cm}^2/\text{second}/\text{arcseconds}^2$, $S' = 1.7 \times 10^{14}$, and d , the dispersion in Å/pixel, is 2.58. Therefore, the background count rate is $6.1 \times 10^{-13} * 1.7 \times 10^{14} * 0.032^2 / 2.58 = 0.041$ counts/second/pixel. This value varies somewhat over the field, as the plate scale varies from the nominal 0.032 arcseconds/pixel. For faint source spectroscopy, it is better to use PR130L, which is on a CaF₂ substrate to block Ly- α .

9.6.3 Example 3: WFC VIS Polarimetry of the Jet of M87

What signal-to-noise ratio is reached in three one orbit exposures (~2400 seconds each) for M87, when using the WFC, F555W for one orbit each in the three VIS polarizers? Gain is 2, box size is 5 x 5 pixels, CR-SPLIT=2, and average sky.

If the M87 jet region has $\mu_V = 17$ magnitudes/arcseconds², using the ETC with a flat continuum spectral distribution and an exposure time of 2400 seconds (CR-SPLIT=2), gives $S/N = 131.6$ for an observation with each VIS polarizer filter (which is an average of the polarizer at the 3 available position angles 0°, 60°, and 120°). If the polarization P is 20%, then $P * S/N = 26.3$, so using

$$\log\left(\frac{\sigma_P}{P}\right) = -0.102 - 0.9898 \log(P \langle S/N \rangle_i)$$

from Chapter 6, $\sigma_P/P = 0.031$, or $\sigma_P = 6.2 \times 10^{-3}$, which is the error on the fractional polarization. The error on the position angle should be ~1.0° using the formula, again from Chapter 6, of

$$\log \sigma_\theta = 1.514 - 1.068 \log(P \langle S/N \rangle_i)$$

9.6.4 Example 4: SBC imaging of Jupiter's Aurora at Lyman-alpha

What signal-to-noise ratio is reached in a one orbit exposure (2000 seconds) observing Jupiter's aurora in Ly- α using the SBC and F122M filter?

The equation from the Section, "Emission Line Source," on page 181 can be used to calculate the expected count rate. The aurora is variable, up to $\sim 100\text{kR}$. The value of (QT) for the SBC+F122M filter at 1216 \AA is 0.0009, from inspection of Figure 10.106 on page 236. For a surface brightness of $40\text{kR} = 1.22 \times 10^{-12} \text{ erg/cm}^2/\text{second}/\text{arcseconds}^2$ (See "Geocoronal Emission and Shadow" on page 189 for conversion), the total counts per pixel are given by the following calculation:

$$2.23 \times 10^{12} * 0.009 * 1.22 \times 10^{-12} * 1216 * (0.032)^2 * 2000 = 61.0.$$

The background contributions are the detector dark of $1.2 \times 10^{-5} \text{ counts/pixel/second}$ (which can be ignored in this case) and a sky background which is dominated by geocoronal Lyman- α . During the daytime, the geocoronal background is 20kR , or 30.5 counts, while at night the background drops to one tenth of this, or 3.05 counts.

Finally, we calculate the signal-to-noise ratio Σ for a 2×2 pixel resolution element: in the daytime, $\Sigma = 61.0 \cdot 4 / \sqrt{(61.0 + 30.5) \cdot 4} = 12.7$, while at night, $\Sigma = 61.0 \cdot 4 / \sqrt{(61.0 + 3.05) \cdot 4} = 15.2$

9.6.5 Example 5: Coronagraphic imaging of the Beta-Pictoris Disk

In the final example we shall consider the case where we are trying to determine the S/N achieved on the Beta Pictoris disk, assuming a disk surface brightness of R magnitude of 16 arcseconds² at a distance of 6 arcseconds from the central star with a V magnitude of 3.9, for an exposure time of 1000 seconds with an F435W filter. Assume that the star and disk have an A5 V-type spectrum. Using the [ACS Exposure Time Calculator](#) and considering the case for the 3.0 arcseconds occulting mask:

- Disk count rate = $4.98 \text{ e}^-/\text{second}$ for a 2×2 aperture (including 47.5% throughput of coronagraph)
Sky count rate = $0.010 \text{ e}^-/\text{second}/\text{pixel}$,
Detector dark rate = $0.015 \text{ e}^-/\text{second}/\text{pixel}$
- In 1000 seconds, this gives $4,980 \text{ e}^-/2 \times 2$ aperture in the disk region.
- Central star count rate = $3.63 \times 10^8 \text{ e}^-/\text{second}$ for a 101×101 aperture (101×101 aperture used to estimate total integrated flux)

- At a distance 6 arcseconds from the central star, the fraction of flux per square arcsecond in the PSF wings is 2.6×10^{-6} .
 $B_{\text{PSF}} = 3.63 \times 10^{11} * 2.6 \times 10^{-6} = 943.8 \text{ e}^-$ per square arcsecond. The counts collected in 4 pixels are $4 \times 0.027^2 \times (943.8) = 2.752$.
- The S/N in a 2×2 box is then $4980 / \sqrt{4980 + 2.8} \cong 70.5$.

9.7 Tabular Sky Backgrounds

We provide Table 9.7 of the “high” sky background numbers as plotted in Figure 9.1. See the text and the caption in Figure 9.1 for more details. These high sky values are defined as the earthshine at 38° from the limb and the high zodiacal light of $m_v = 22.1$ magnitude/arcseconds².

Table 9.7: High sky backgrounds.

| Wavelength | Earthshine | Zodiacal light | Total background |
|------------|--|--|--|
| Å | erg/sec/cm ² /Å/arcsec ² | erg/sec/cm ² /Å/arcsec ² | erg/sec/cm ² /Å/arcsec ² |
| 1000. | 2.41E-23 | 1.26E-28 | 2.41E-23 |
| 1100. | 4.38E-22 | 1.02E-26 | 4.38E-22 |
| 1200. | 4.01E-23 | 1.05E-25 | 4.02E-23 |
| 1400. | 4.29E-25 | 2.50E-24 | 2.93E-24 |
| 1500. | 4.16E-25 | 9.12E-24 | 9.54E-24 |
| 1600. | 2.55E-25 | 2.30E-22 | 2.30E-22 |
| 1700. | 7.89E-23 | 7.06E-21 | 7.14E-21 |
| 1800. | 9.33E-23 | 1.50E-20 | 1.51E-20 |
| 1900. | 4.39E-22 | 2.20E-20 | 2.24E-20 |
| 2000. | 1.01E-21 | 3.49E-20 | 3.59E-20 |
| 2100. | 1.60E-21 | 1.21E-19 | 1.23E-19 |
| 2200. | 7.49E-22 | 2.16E-19 | 2.17E-19 |
| 2300. | 3.32E-22 | 1.75E-19 | 1.75E-19 |
| 2400. | 2.50E-22 | 1.79E-19 | 1.79E-19 |
| 2500. | 2.39E-22 | 2.47E-19 | 2.47E-19 |
| 2600. | 5.62E-22 | 2.93E-19 | 2.94E-19 |
| 2700. | 6.77E-21 | 9.95E-19 | 1.00E-18 |
| 2800. | 2.03E-21 | 2.82E-19 | 2.91E-19 |
| 2900. | 4.32E-20 | 2.04E-18 | 2.08E-18 |

Table 9.7: High sky backgrounds.

| Wavelength | Earthshine | Zodiacal light | Total background |
|-------------------|--|--|--|
| Å | erg/sec/cm ² /Å/arcsec ² | erg/sec/cm ² /Å/arcsec ² | erg/sec/cm ² /Å/arcsec ² |
| 3000. | 9.34E-20 | 1.20E-18 | 1.29E-18 |
| 3100. | 2.07E-19 | 1.46E-18 | 1.67E-18 |
| 3200. | 3.60E-19 | 2.25E-18 | 2.61E-18 |
| 3400. | 6.40E-19 | 2.81E-18 | 3.45E-18 |
| 3500. | 8.20E-19 | 2.73E-18 | 3.55E-18 |
| 3600. | 1.06E-18 | 2.68E-18 | 3.74E-18 |
| 3700. | 1.22E-18 | 3.25E-18 | 4.47E-18 |
| 3800. | 1.23E-18 | 3.05E-18 | 4.28E-18 |
| 3900. | 1.52E-18 | 3.27E-18 | 4.79E-18 |
| 4000. | 2.38E-18 | 4.54E-18 | 6.92E-18 |
| 4250. | 2.33E-18 | 4.48E-18 | 6.81E-18 |
| 4500. | 2.78E-18 | 5.32E-18 | 8.10E-18 |
| 5000. | 2.55E-18 | 4.92E-18 | 7.47E-18 |
| 5250. | 2.69E-18 | 5.28E-18 | 7.97E-18 |
| 5500. | 2.56E-18 | 5.20E-18 | 7.76E-18 |
| 5750. | 2.56E-18 | 5.33E-18 | 7.89E-18 |
| 6000. | 2.40E-18 | 5.11E-18 | 7.51E-18 |
| 6250. | 2.27E-18 | 4.94E-18 | 7.21E-18 |
| 6500. | 2.20E-18 | 4.88E-18 | 7.08E-18 |
| 6750. | 2.07E-18 | 4.69E-18 | 6.76E-18 |
| 7000. | 1.90E-18 | 4.40E-18 | 6.30E-18 |
| 7250. | 1.85E-18 | 4.34E-18 | 6.19E-18 |
| 7500. | 1.73E-18 | 4.13E-18 | 5.86E-18 |
| 7750. | 1.63E-18 | 3.95E-18 | 5.58E-18 |
| 8000. | 1.57E-18 | 3.85E-18 | 5.42E-18 |
| 8250. | 1.48E-18 | 3.68E-18 | 5.16E-18 |
| 8500. | 1.37E-18 | 3.46E-18 | 4.83E-18 |
| 8750. | 1.31E-18 | 3.36E-18 | 4.67E-18 |

Imaging Reference Material

In this chapter. . .

| | |
|---|-------------------------------------|
| 10.1 Introduction / 198 | HRC/F550M / 222 |
| 10.2 Using the Information in this Chapter / 198 | HRC/F555W / 223 |
| WFC/F435W / 201 | HRC/F606W / 224 |
| WFC/F475W / 202 | HRC/F625W / 225 |
| WFC/F502N / 203 | HRC/F658N / 226 |
| WFC/F550M / 204 | HRC/F660N / 227 |
| WFC/F555W / 205 | HRC/F775W / 228 |
| WFC/F606W / 206 | HRC/F814W / 229 |
| WFC/F625W / 207 | HRC/F850LP / 230 |
| WFC/F658N / 208 | HRC/F892N / 231 |
| WFC/F660N / 209 | HRC/G800L / 232 |
| WFC/F775W / 210 | HRC/PR200L / 233 |
| WFC/F814W / 211 | HRC/CLEAR / 234 |
| WFC/F850LP / 212 | SBC/F115LP / 235 |
| WFC/G800L / 213 | SBC/F122M / 236 |
| WFC/CLEAR / 214 | SBC/F125LP / 237 |
| HRC/F220W / 215 | SBC/F140LP / 238 |
| HRC/F250W / 216 | SBC/F150LP / 239 |
| HRC/F330W / 217 | SBC/F165LP / 240 |
| HRC/F344N / 218 | SBC/PR110L / 241 |
| HRC/F435W / 219 | SBC/PR130L / 242 |
| HRC/F475W / 220 | 10.3 Distortion in the ACS / 246 |
| HRC/F502N / 221 | |

In this Chapter, we provide imaging reference material, in support of the information presented in Chapter 9.

10.1 Introduction

This chapter provides reference material to help you select your filter and detector configuration, and determine your observing plan (e.g., total required exposure time, and number of exposures). This chapter is, for the most part, organized by *filter* and *detector*. For each imaging mode the following are provided:

- Plots of integrated system throughput as a function of wavelength.
- Plots of the time needed to achieve a desired signal-to-noise ratio vs. magnitude for all filters for a point source and a one arcseconds² extended source.
- Tables of color corrections AB_v to go from Johnson V magnitude to AB magnitude.

10.2 Using the Information in this Chapter

10.2.1 Sensitivity Units and Conversions

This chapter contains plots of throughputs for each imaging mode. "Determining Count Rates from Sensitivities" in Section 9.2 explains how to use these throughputs to calculate expected count rates from your source.

The first figure for each imaging mode gives the integrated system throughput. This is the combination of the efficiencies of the detector and of the optical elements in the light path. The throughputs in this handbook are based in part on ground test data. Although, at the time of writing the overall detector efficiency curve and most filter throughputs have been adjusted based on in-flight data. The throughput is defined as the number of detected counts/second/cm² of telescope area relative to the incident flux in photons/cm²/second. For the CCD, "counts" is the number of electrons detected. For the MAMA, "counts" is the number of valid events processed by the detector electronics after passing through the various pulse-shape and anti-coincidence filters. In both cases the detected counts obey Poisson statistics. The throughput includes all obscuration effects in the optical train (e.g., due to the HST secondary).

To recalculate the throughput with the most recent CCD QE tables in *synphot*, you can create total-system-throughput tables (instrument plus OTA) using the *synphot calcband* task. *calcband* takes any valid obsmode command string as input and produces an *STSDAS* table with two columns of data called "wavelength" and "throughput" as its output. For example, to

evaluate the throughput for the F475W filter and the WFC detector, chip 1, you would use the command *calcband acs,wfc1,f475w sdssg_thpt*. The resulting throughput table is stored in *sdssg_thpt*.

The ramp filters are not included in this chapter because the passband will change depending on the chosen central wavelength. The width of the passband and available range of central wavelengths for each ramp segment are listed in Table 5.2. Additionally, the passband for a ramp segment can be plotted with *synphot* using the following command *calcband acs,wfc1,fr388n#3880 sdssg_thpt* where the #3880 is the desired central wavelength in Angstroms.

10.2.2 Signal-to-Noise

For each imaging mode, plots are provided to estimate the signal-to-noise ratio (S/N) for a representative source. The first figure shows S/N for point sources (GAIN=1). The second figure shows S/N for uniform extended sources of area 1 arcseconds².

The different line styles in the S/N figures delineate regions where different sources of noise dominate. A particular source of noise (readnoise for example) is presumed to dominate if it contributes more than half the total noise in the observations.

The point- and extended-source S/N figures are shown for average and low sky levels. For point sources, an aperture size of 5 x 5 pixels has been used for the WFC, 9 x 9 pixels for HRC, and 15 x 15 pixels for the SBC S/N evaluation. For extended sources, a 1 arcseconds² aperture was used. For the CCD the readnoise has been computed assuming a number of readouts NREAD= integer ($t / 1000$ seconds), where t is the exposure time, with a minimum NREAD=2. That is, each exposure has a minimum CR-SPLIT=2. Different line styles in the figures are used to indicate which source of noise dominates.

To the left of the vertical line in the SBC S/N plots, the count rate from the source exceeds the 150 counts/second/pixel local count rate limit. This is computed from the model PSF, which gives 14% to 22% of the flux in the central pixel.

In situations requiring more detailed calculations (non-stellar spectra, extended sources, other sky background levels, unknown target V magnitude, etc.), the ACS [Exposure-Time Calculator](#) should be used.

Follow these steps to use the signal-to-noise plots:

1. Determine the AB magnitude of your source at the wavelength of interest. There are several ways to do this.
 - Examine Table 10.1, 10.2, or 10.3 and find AB_V for the desired spectral type and filter. Sum the V magnitude of the target and AB_V derived from the table.

- Alternatively, compute $ABMAG (=V+ABv)$ from the source flux, using the relation $ABMAG = -2.5 \log f_{\nu} - 48.60$, or $ABMAG = -2.5 \log f_{\lambda} - 5 \log \lambda - 2.406$.
- 2. Find the appropriate plot for the filter in question, and locate $V+AB_{\nu}$ on the horizontal axis. Then read off the signal-to-noise ratio for the desired exposure time, or vice-versa.

The “x” characters at the top of each plot indicate the onset of saturation, in the case of the CCD. The “x” shows where the total number of counts exceeds the 16 bit buffer size of 65,535.

Note that the plots show the S/N as a function of source magnitude for exposure times as short as 0.1 seconds, although the minimum exposure time for the WFC CCD channel is 0.5 seconds.

10.2.3 Point Spread Functions

All information about the PSF are based on the modeled encircled energy data presented in ACS Point Spread Functions in Section 5.6

WFC/F435W

Description

Johnson B filter.

Figure 10.1: Integrated system throughput for WFC/F435W.

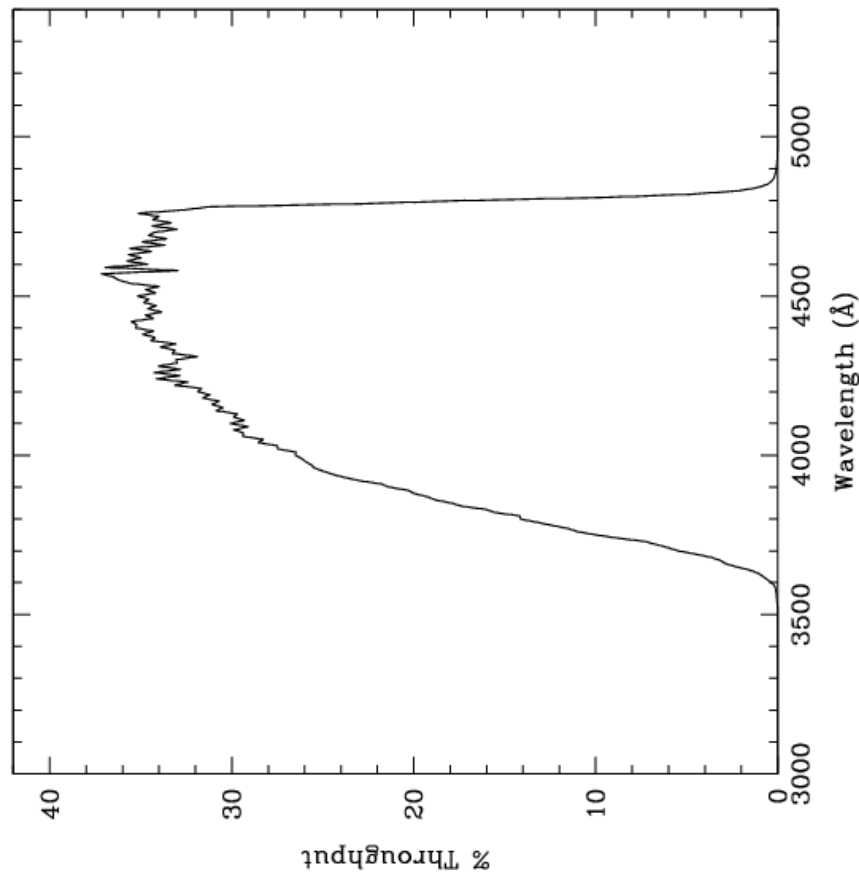


Figure 10.2: Point source S/N vs. $V+AB_V$ for the WFC/F435W filter. Top curves are for low sky; bottom curves are for average sky.

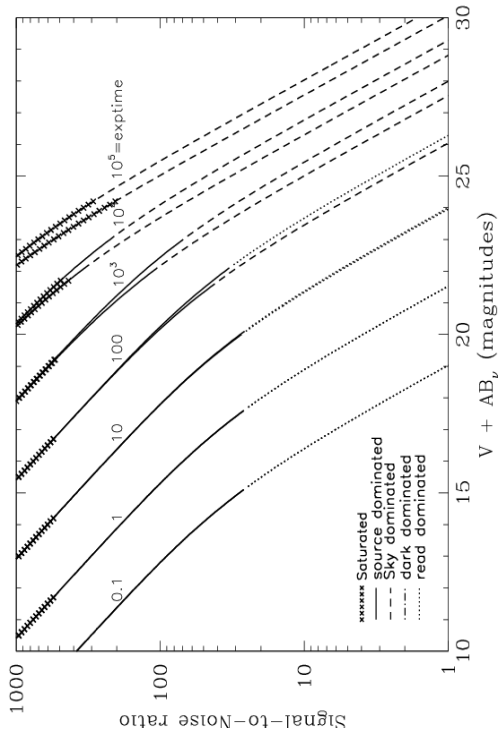
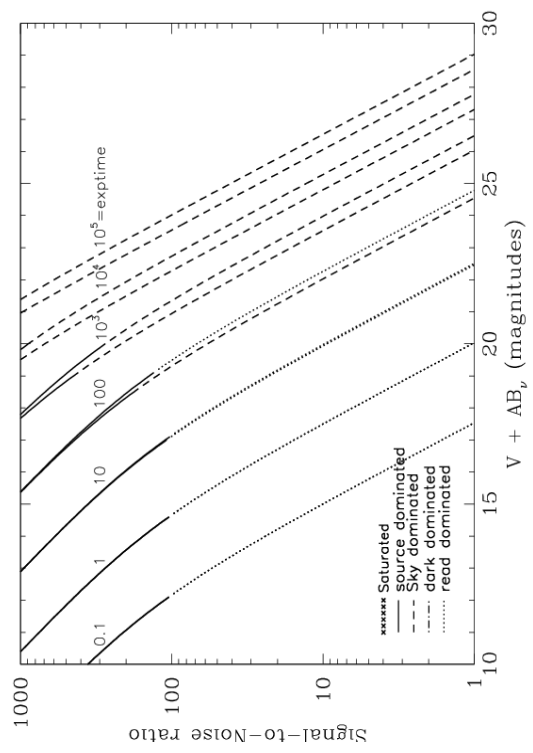


Figure 10.3: Extended source S/N vs. $V+AB_V$ for the WFC/F435W filter. Top curves are for low sky and bottom curves are for average sky for a 1 arcsec² area.



WFC/F475W

Description

Sloan Digital Sky Survey g filter.

Figure 10.4: Integrated system throughput for WFC/F475W.

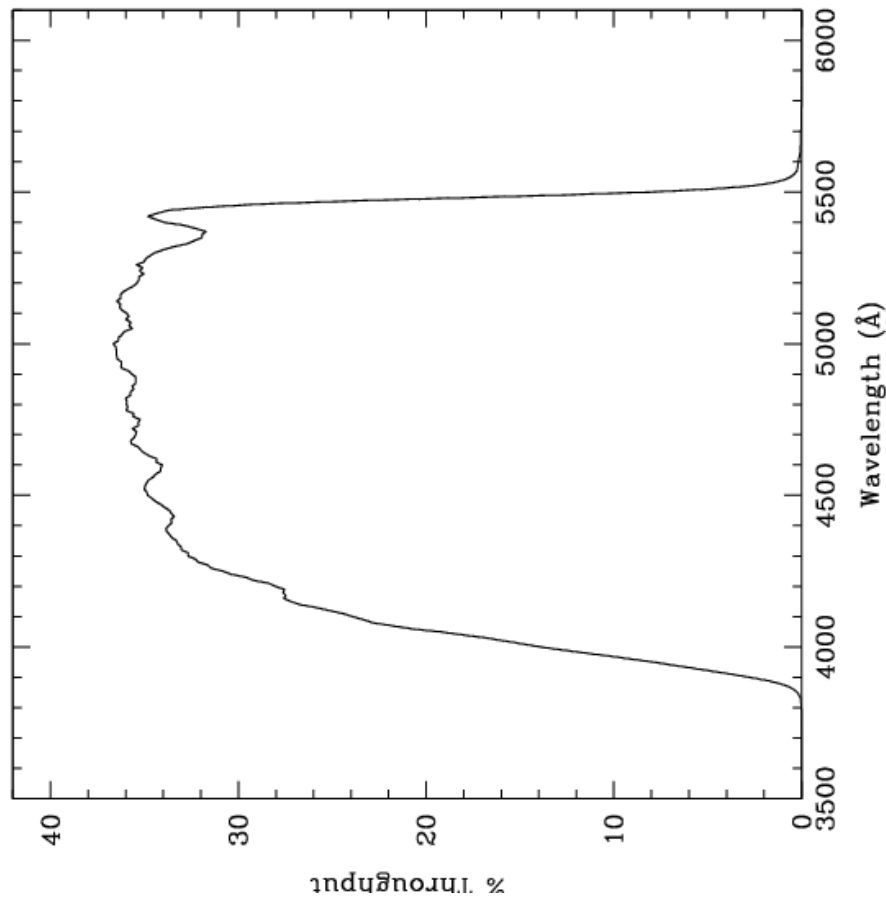


Figure 10.5: Point source S/N vs. $V+AB_V$ for the WFC/F475W filter. Top curves are for low sky; bottom curves are for average sky.

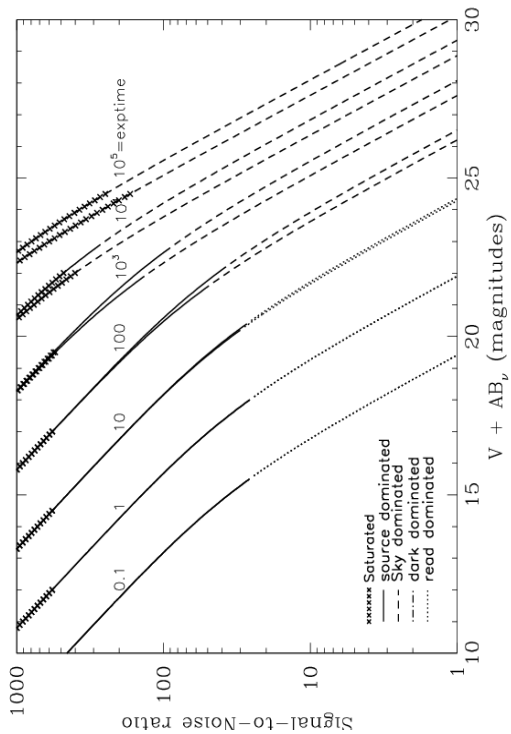
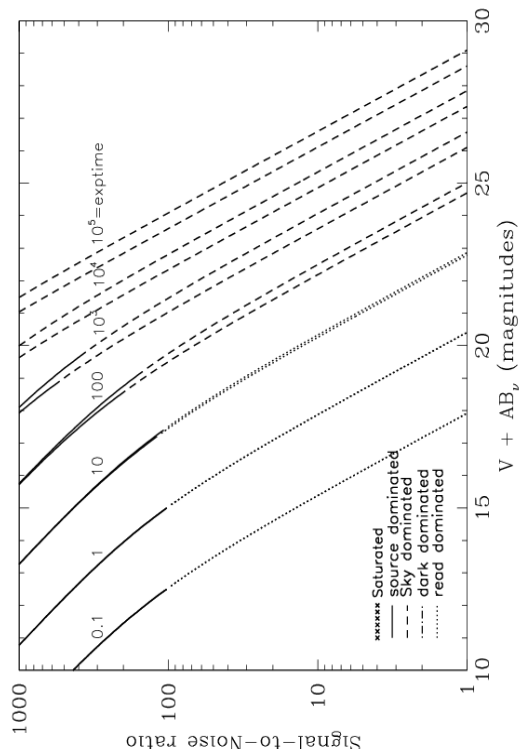


Figure 10.6: Extended source S/N vs. $V+AB_V$ for the WFC/F475W filter. Top curves are for low sky and bottom curves are for average sky for a 1 arcsec² area.



WFC/F502N

Description

OIII filter.

Figure 10.7: Integrated system throughput for WFC/F502N.

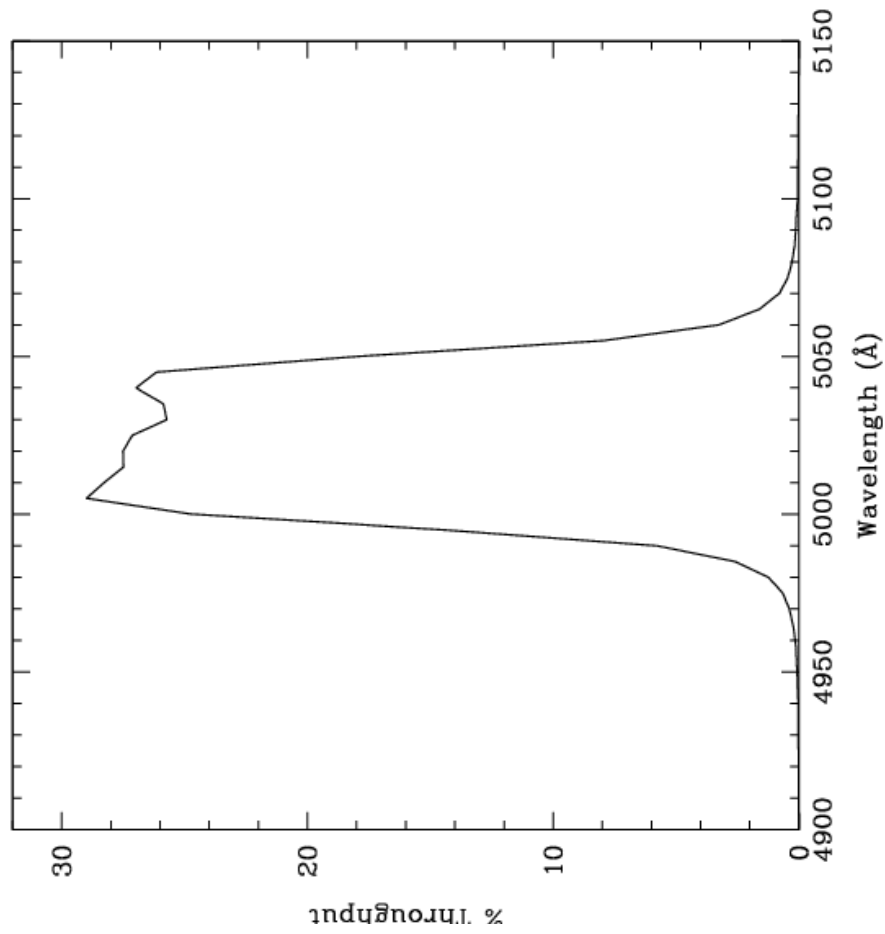


Figure 10.8: Point source S/N vs. $V+AB_V$ for the WFC/F502N filter. Top curves are for low sky; bottom curves are for average sky.

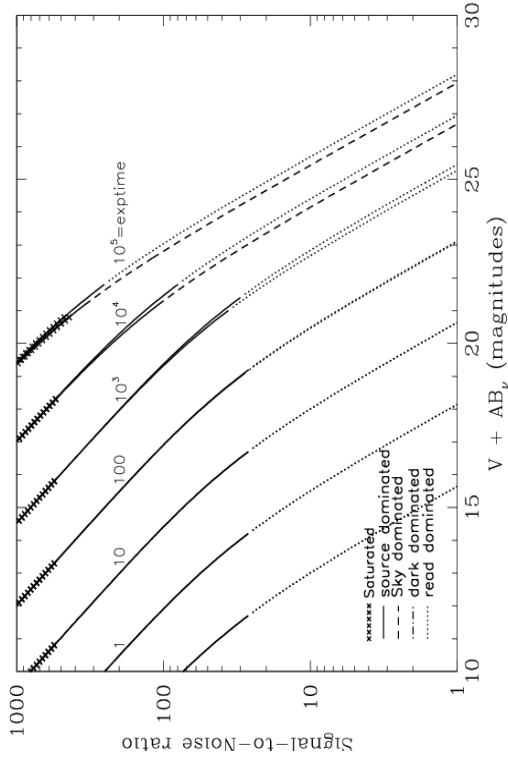
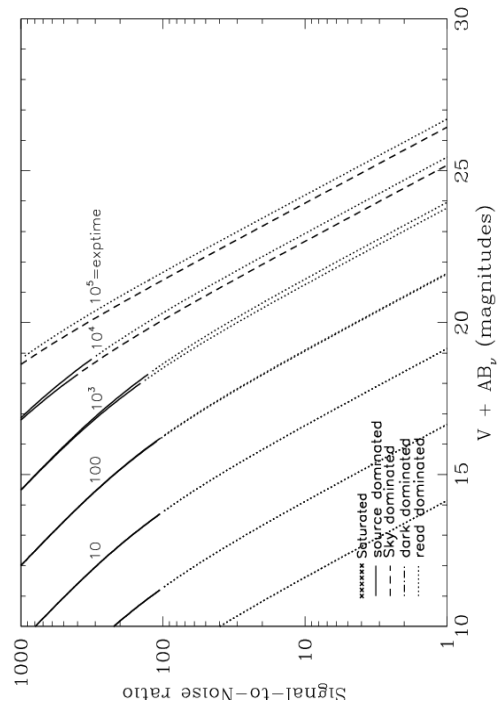


Figure 10.9: Extended source S/N vs. $V+AB_V$ for the WFC/F502N filter. Top curves are for low sky and bottom curves are for average sky for a 1 arcsec² area.



WFC/F550M

Description

Narrow V filter.

Figure 10.10: Integrated system throughput for WFC/F550M.

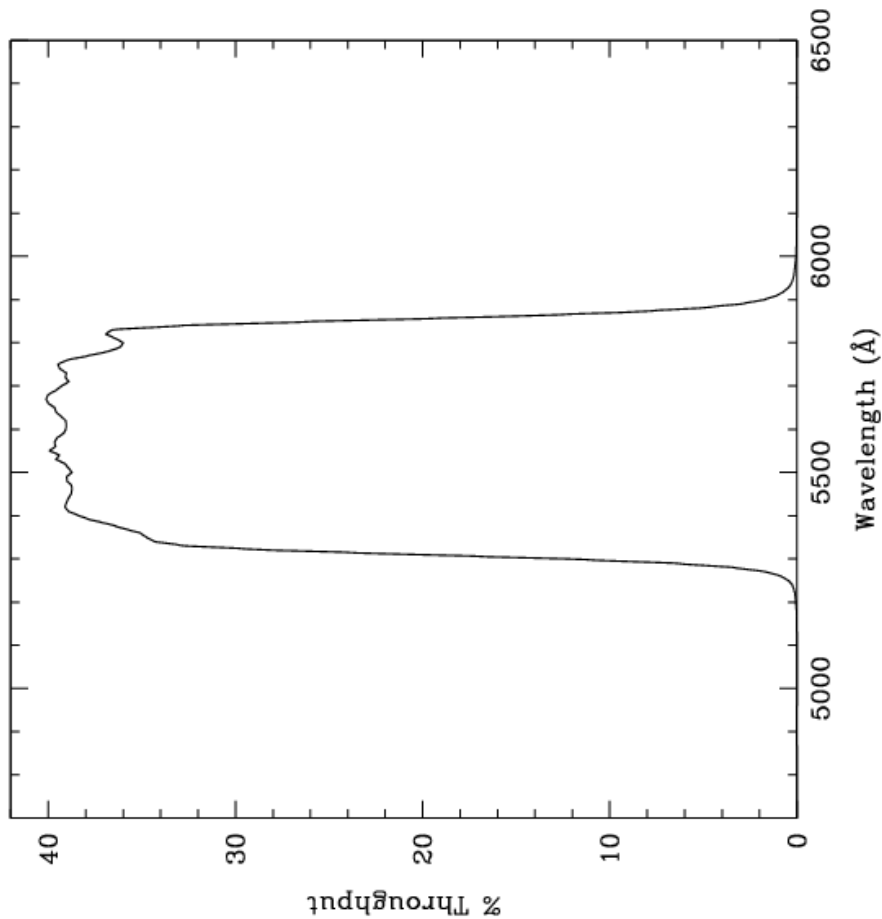


Figure 10.11: Point source S/N vs. $V+AB_V$ for the WFC/F550M filter. Top curves are for low sky; bottom curves are for average sky.

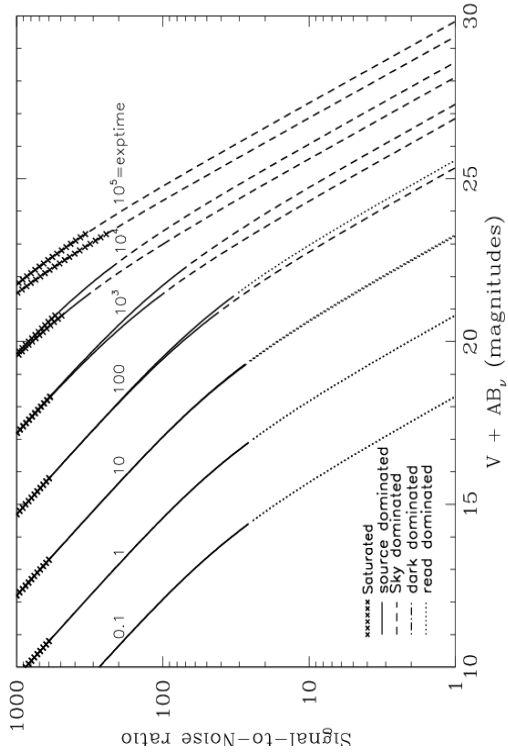
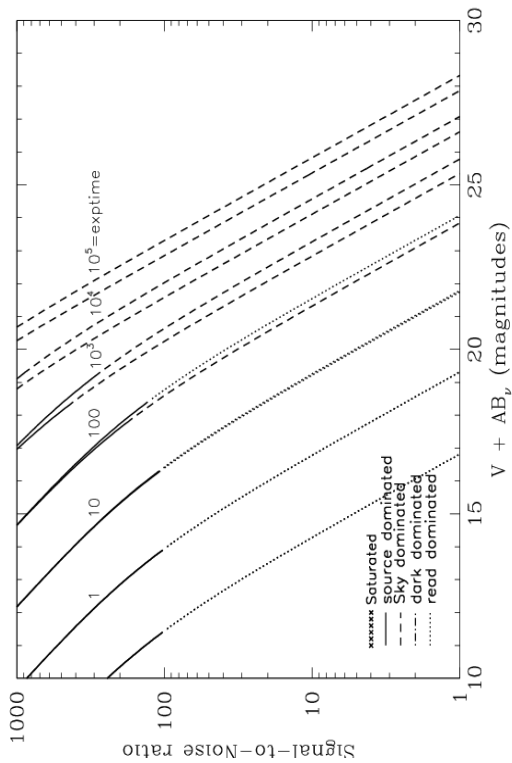


Figure 10.12: Extended source S/N vs. $V+AB_V$ for the WFC/F550M filter. Top curves are for low sky and bottom curves are for average sky for a 1 arcsec^2 area.



WFC/F555W

Description

Johnson V filter.

Figure 10.13: Integrated system throughput for WFC/F555W.

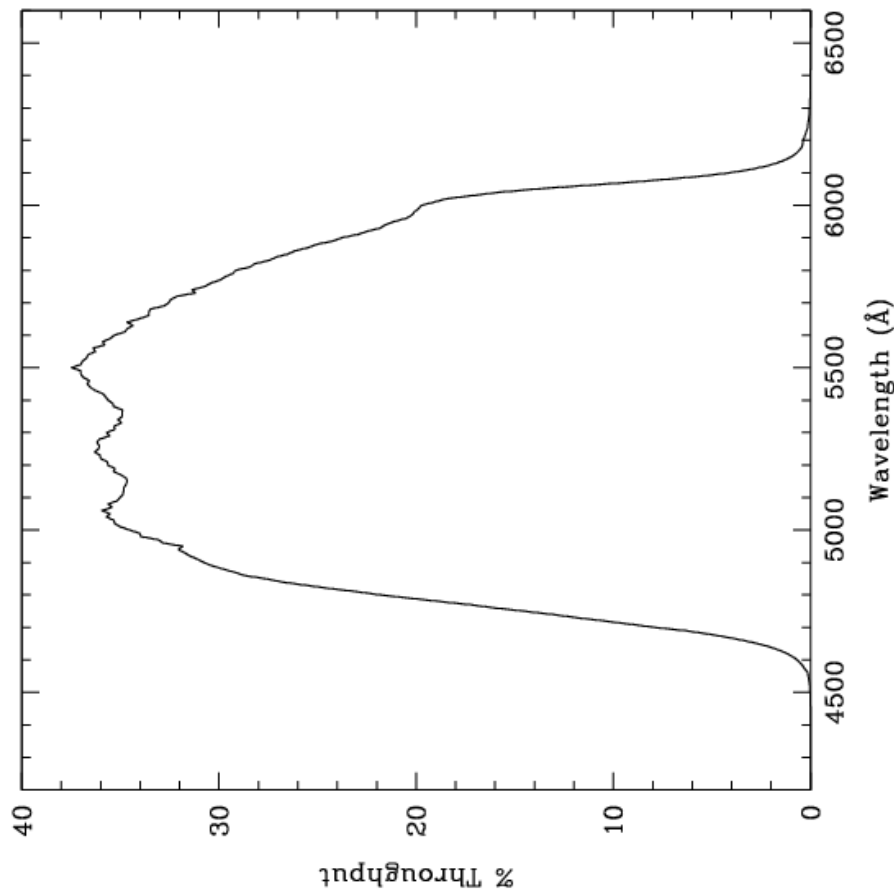


Figure 10.14: Point source S/N vs. $V + AB_V$ for the WFC/F555W filter. Top curves are for low sky; bottom curves are for average sky.

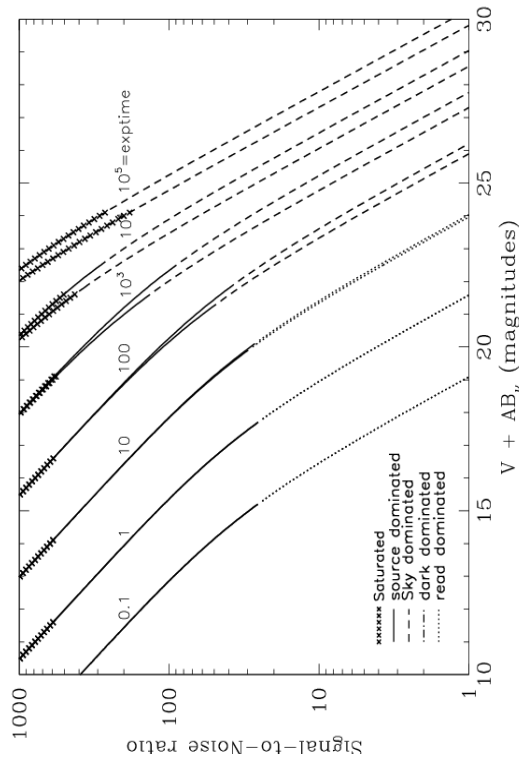
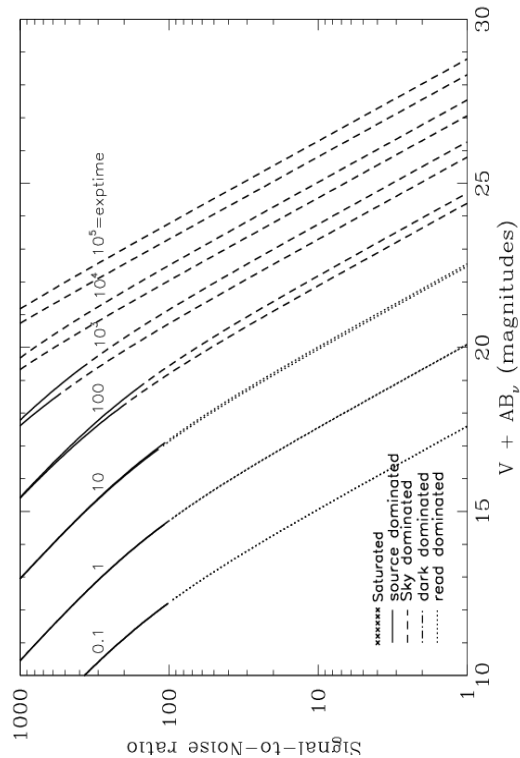


Figure 10.15: Extended source S/N vs. $V + AB_V$ for the WFC/F555W filter. Top curves are for low sky and bottom curves are for average sky for a 1 arcsec^2 area.



WFC/F606W

Description

Broad V filter.

Figure 10.16: Integrated system throughput for WFC/F606W.

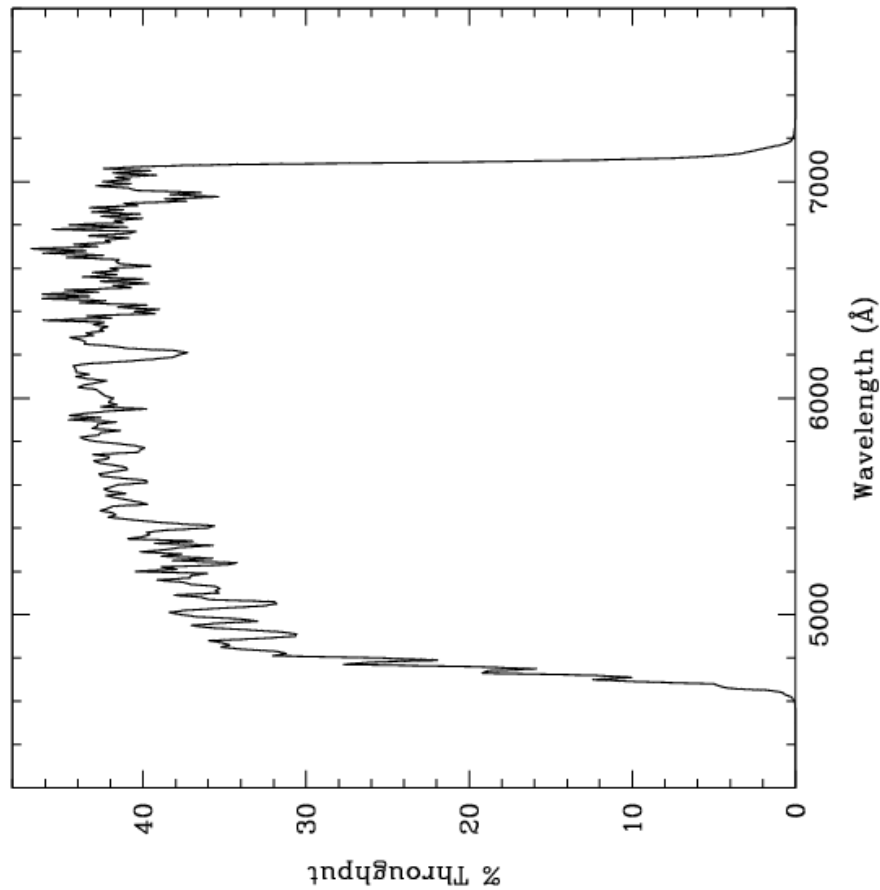


Figure 10.17: Point source S/N vs. $V + AB_V$ for the WFC/F606W filter. Top curves are for low sky; bottom curves are for average sky.

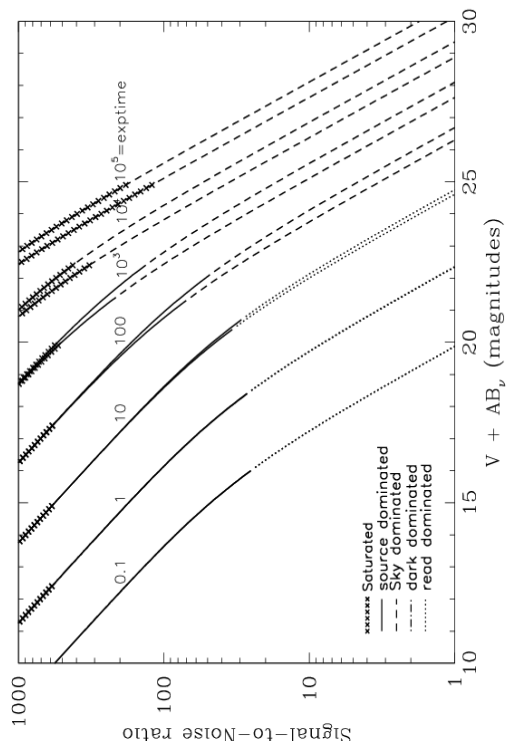
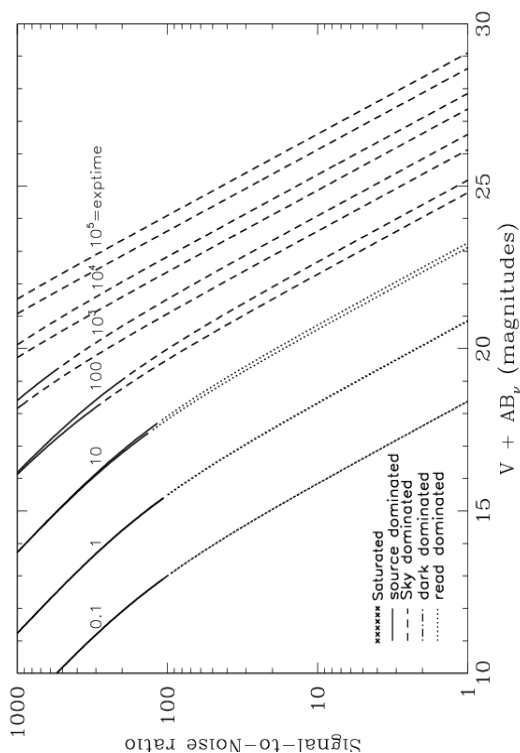


Figure 10.18: Extended source S/N vs. $V + AB_V$ for the WFC/F606W. Top curves are for low sky and bottom curves are for average sky for a 1 arcsec^2 area.



WFC/F625W

Description

Sloan Digital Sky Survey r filter.

Figure 10.19: Integrated system throughput for WFC/F625W.

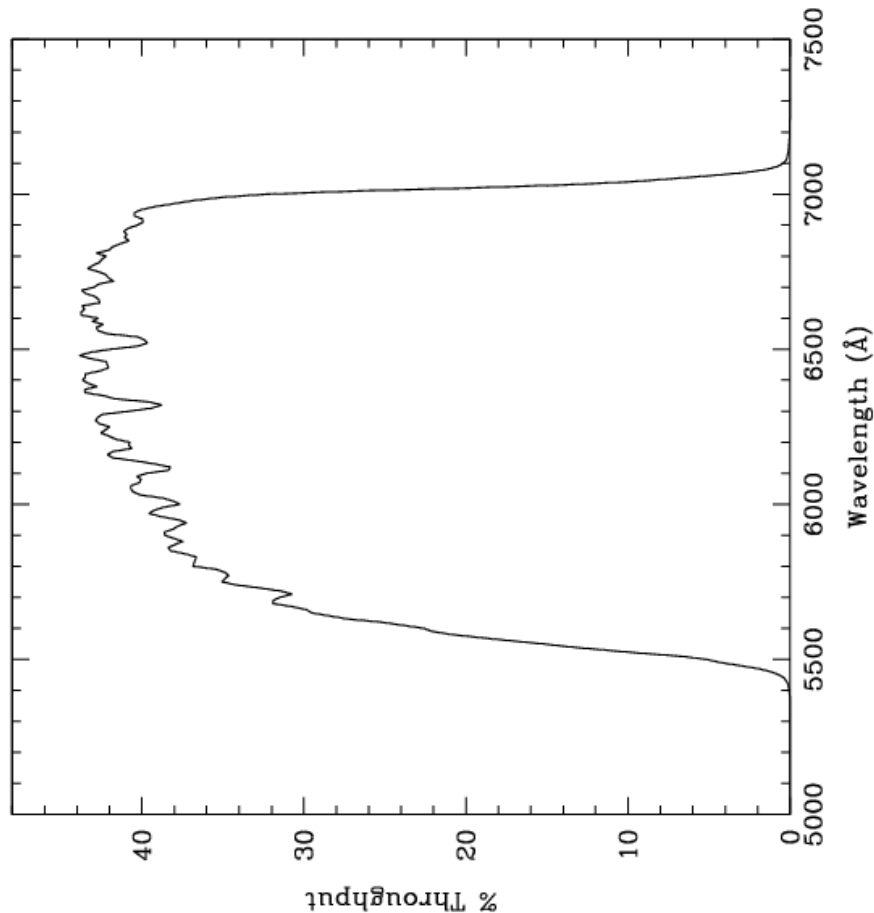


Figure 10.20: Point source S/N vs. $V+AB_V$ for the WFC/F625W filter. Top curves are for low sky; bottom curves are for average sky.

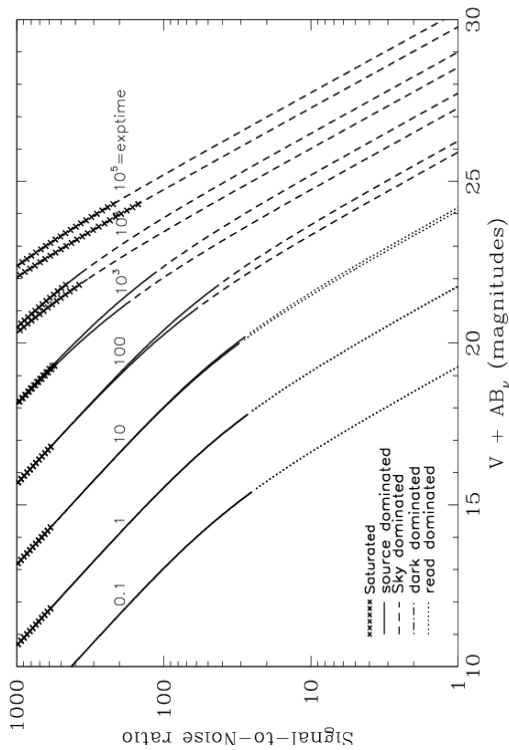
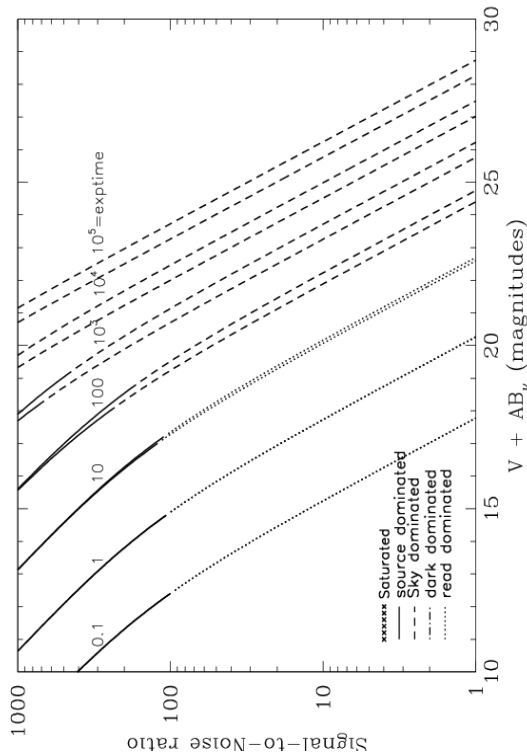


Figure 10.21: Extended source S/N vs. $V+AB_V$ for the WFC/F625W filter. Top curves are for low sky and bottom curves are for average sky for a 1 arcsec^2 area.



WFC/F658N

Description

H α filter.

Figure 10.22: Integrated system throughput for WFC/F658N.

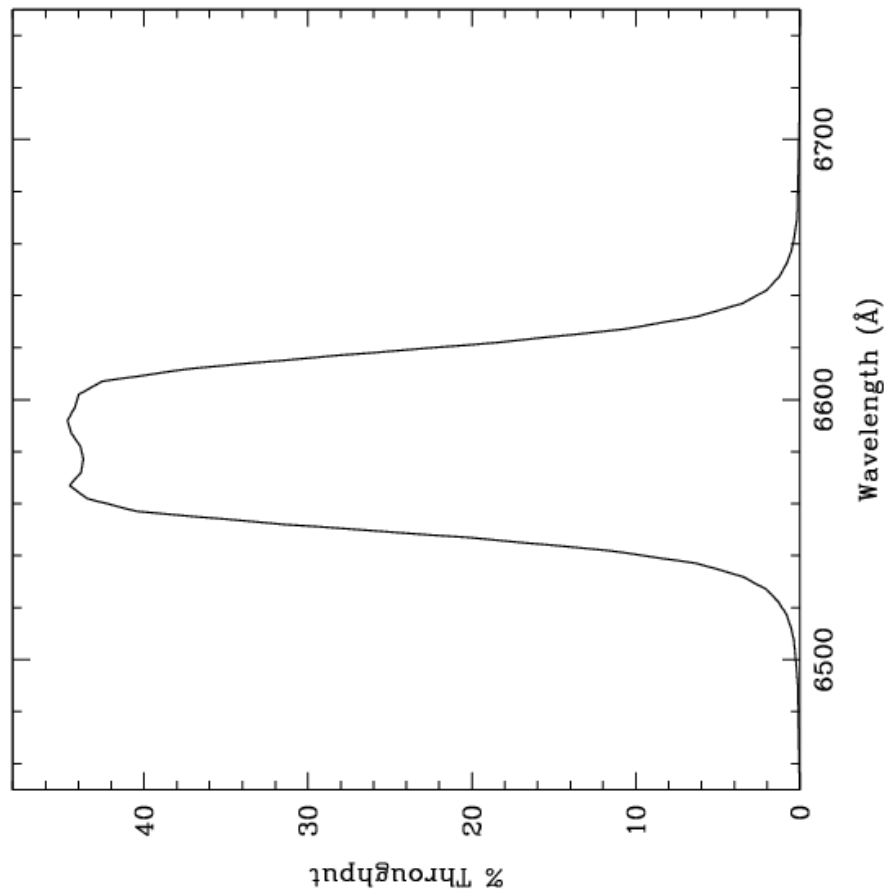


Figure 10.23: Point source S/N vs. $V+AB_V$ for the WFC/F658N filter. Top curves are for low sky; bottom curves are for average sky.

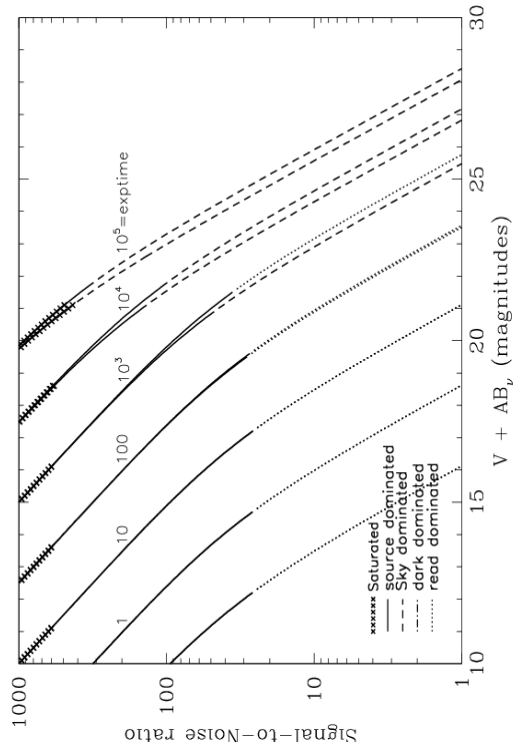
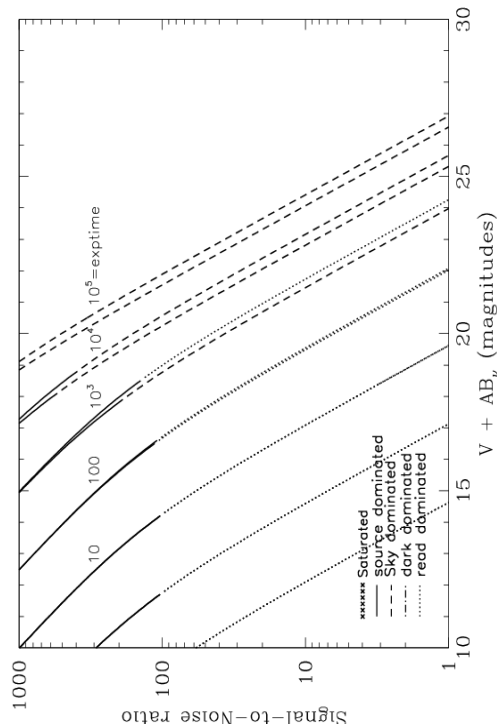


Figure 10.24: Extended source S/N vs. $V+AB_V$ for the WFC/F658N filter. Top curves are for low sky and bottom curves are for average sky for 1 arcsec² area.



WFC/F660N

Description

NII filter.

Figure 10.25: Integrated system throughput for WFC/F660N.

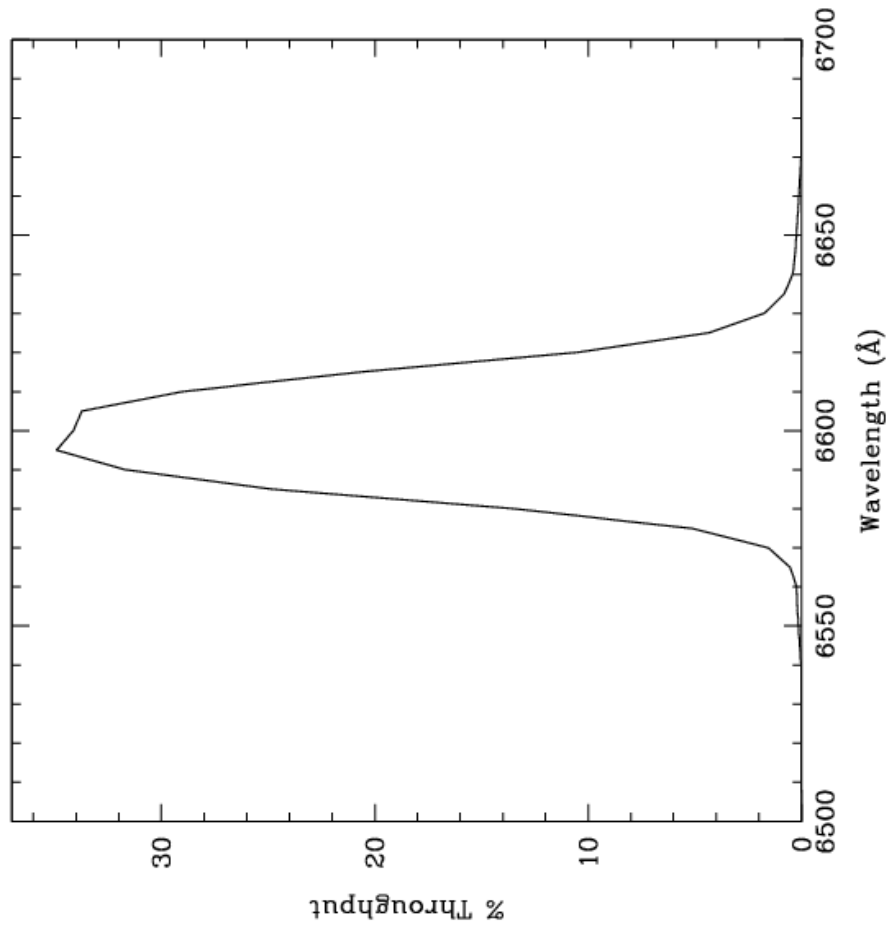


Figure 10.26: Point source S/N vs. $V+AB_V$ for the WFC/F660N filter. Top curves are for low sky; bottom curves are for average sky.

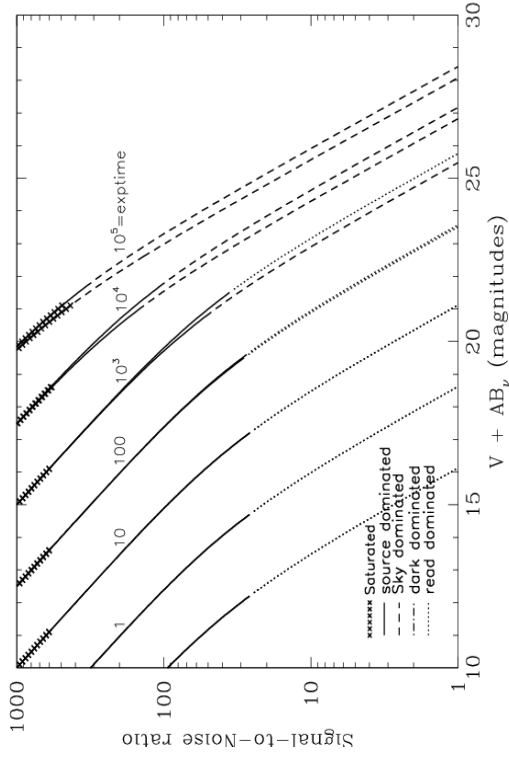
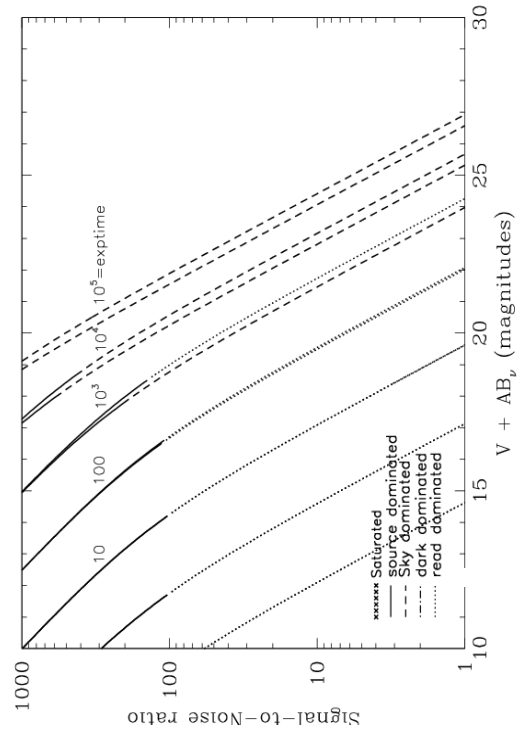


Figure 10.27: Extended source S/N vs. $V+AB_V$ for the WFC/F660N filter. Top curves are for low sky and bottom curves are for average sky for a 1 arcsec^2 area.



WFC/F775W

Description

Sloan Digital Sky Survey i filter

Figure 10.28: Integrated system throughput for WFC/F775W.

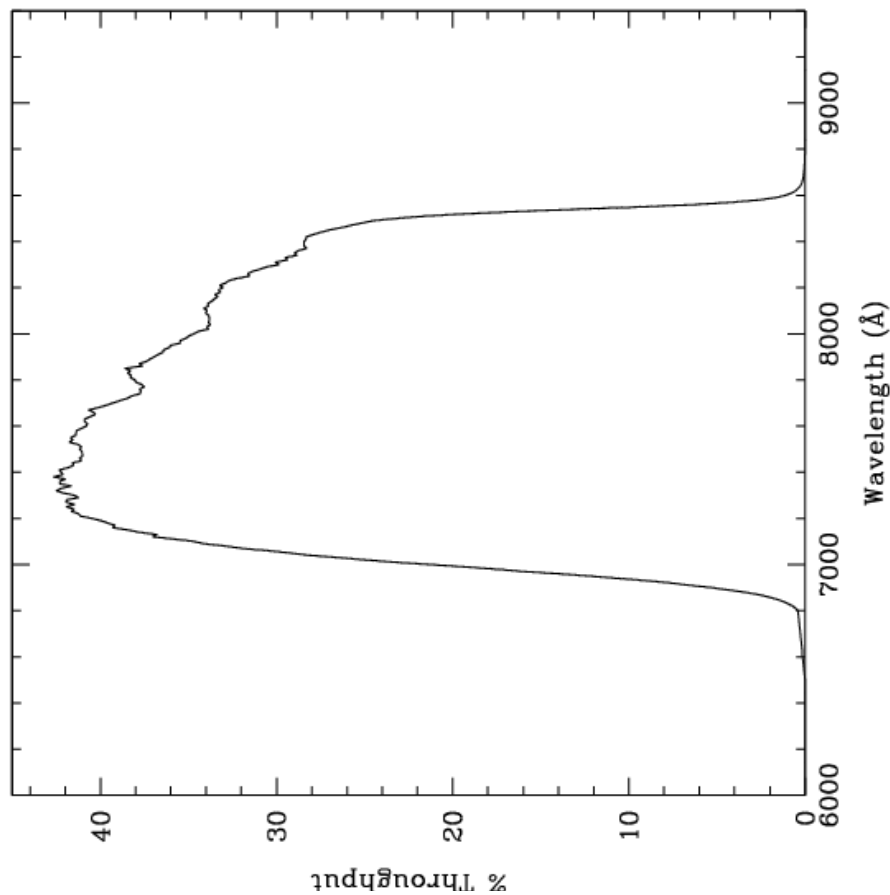


Figure 10.29: Point source S/N vs. $V+AB_V$ for the WFC/F775W filter. Top curves are for low sky; bottom curves are for average sky.

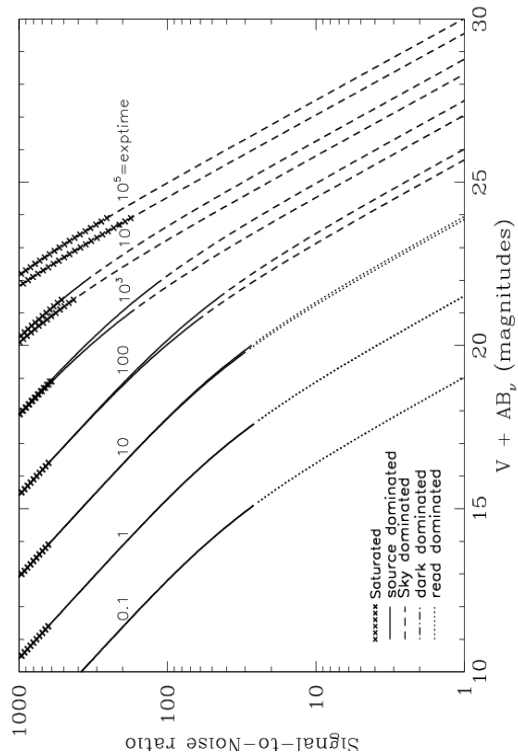
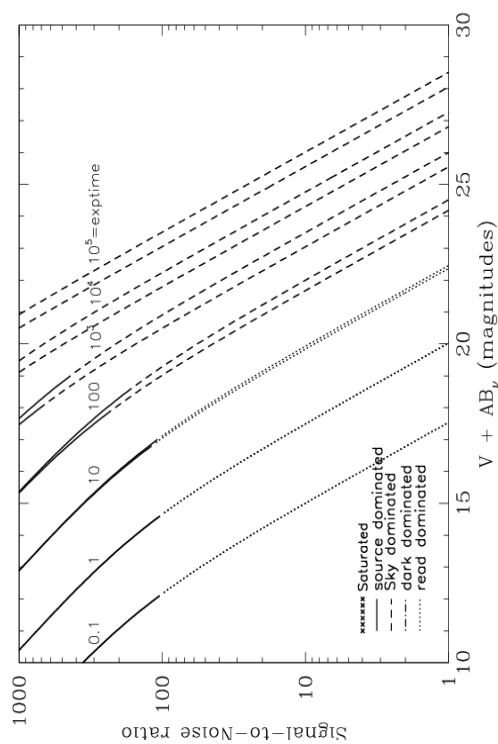


Figure 10.30: Extended source S/N vs. $V+AB_V$ for the WFC/F775W filter. Top curves are for low sky and bottom curves are for average sky for a 1 arcsec² area.



WFC/F814W

Description

Broad I filter.

Figure 10.31: Integrated system throughput for WFC/F814W.

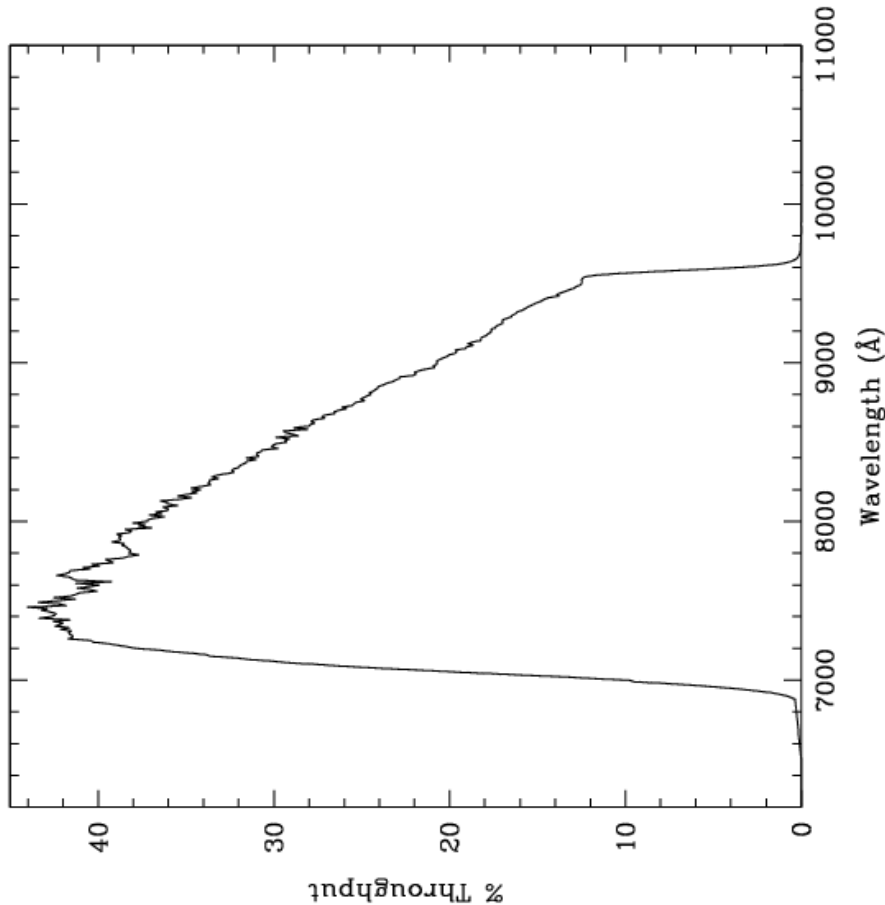


Figure 10.32: Point source S/N vs. $V+AB_V$ for the WFC/F814W filter. Top curves are for low sky; bottom curves are for average sky.

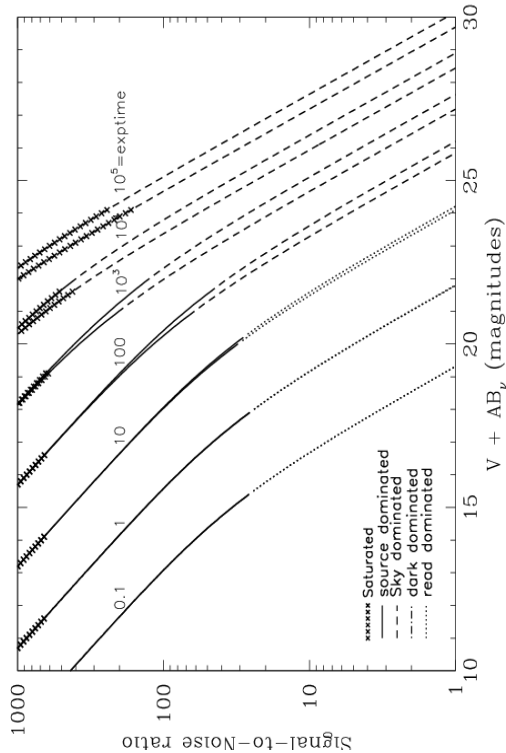
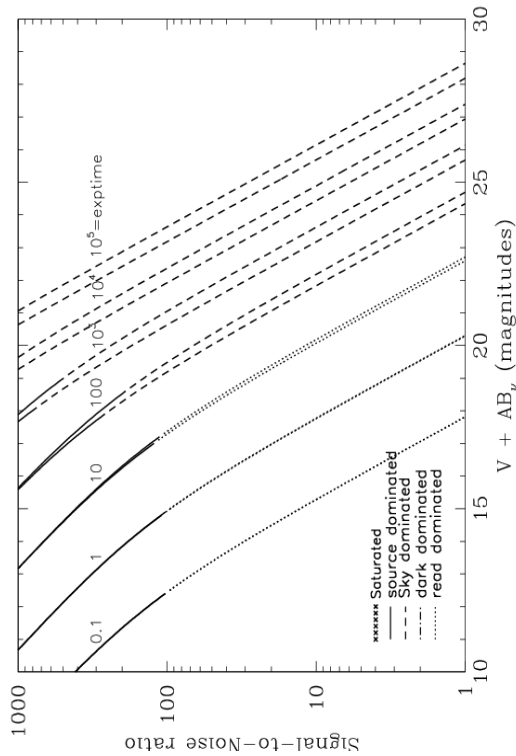


Figure 10.33: Extended source S/N vs. $V+AB_V$ for the WFC/F814W filter. Top curves are for low sky and bottom curves are for average sky for a 1 arcsec^2 area.



WFC/F850LP

Description

Sloan Digital Sky Survey z filter.

Figure 10.34: Integrated system throughput for WFC/F850LP.

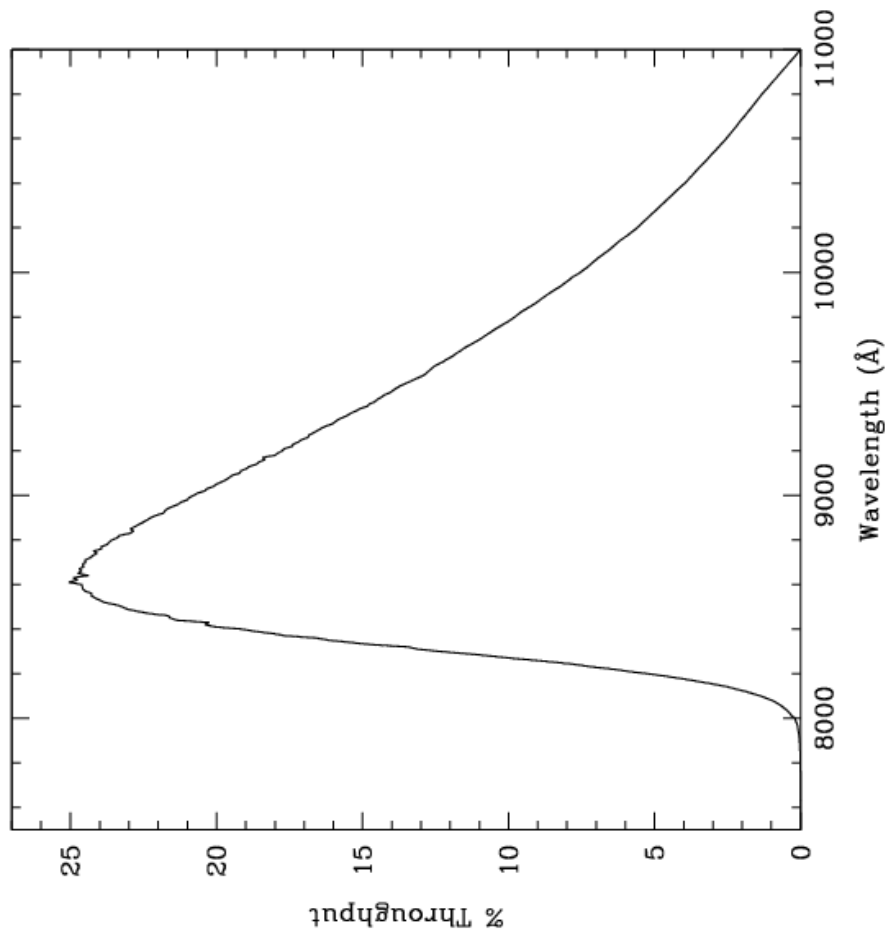


Figure 10.35: Point source S/N vs. $V+AB_V$ for the WFC/F850LP filter. Top curves are for low sky; bottom curves are for average sky.

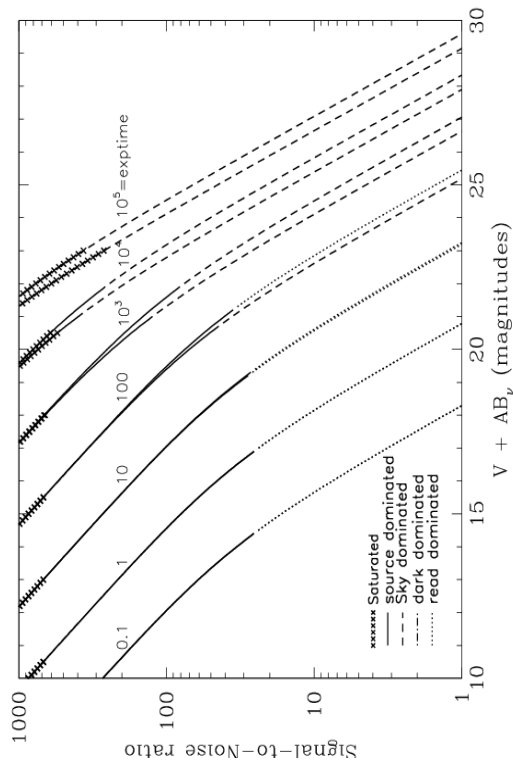
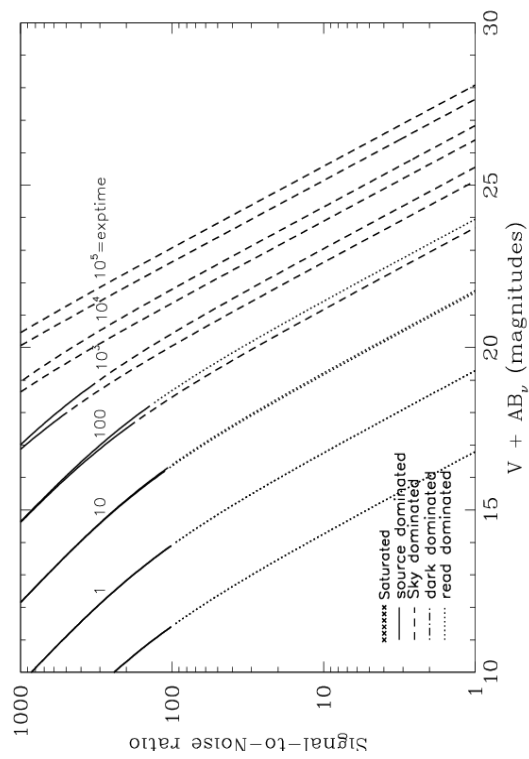


Figure 10.36: Extended source S/N vs. $V+AB_V$ for the WFC/F850LP filter. Top curves are for low sky and bottom curves are for average sky for a 1 arcsec^2 area.



WFC/G800L

Description

Grism.

Figure 10.37: Integrated system throughput for WFC/G800L.

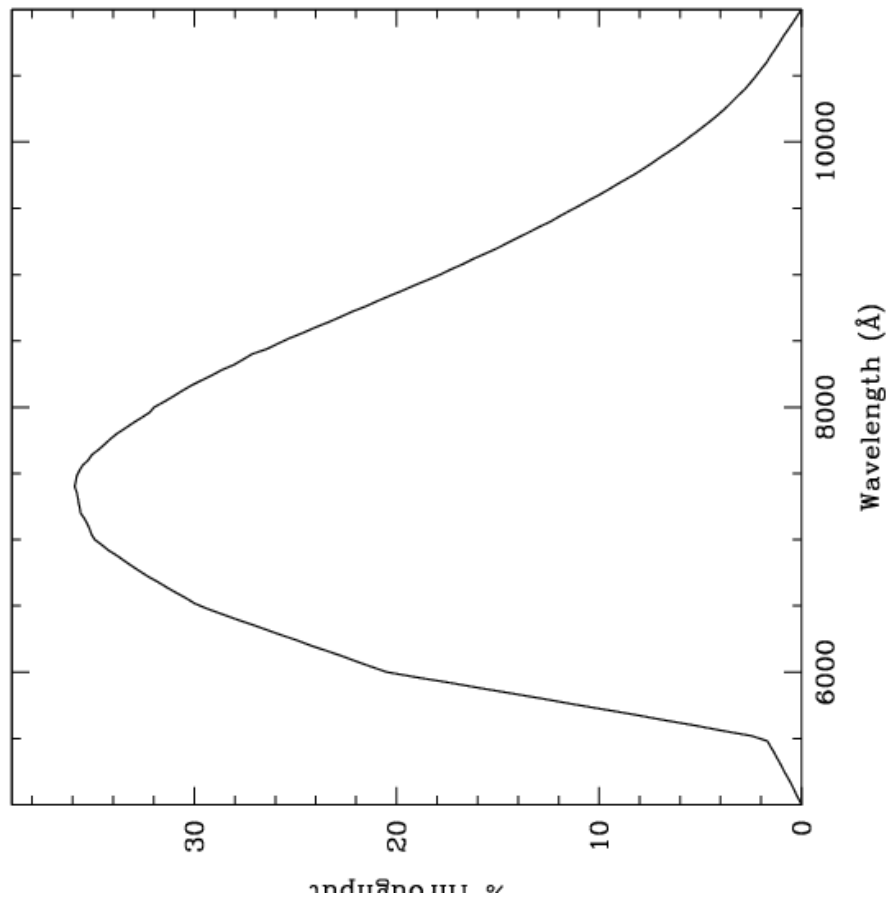


Figure 10.38: Point source S/N vs. $V+AB_V$ for the WFC/G800L filter. Top curves are for low sky; bottom curves are for average sky.

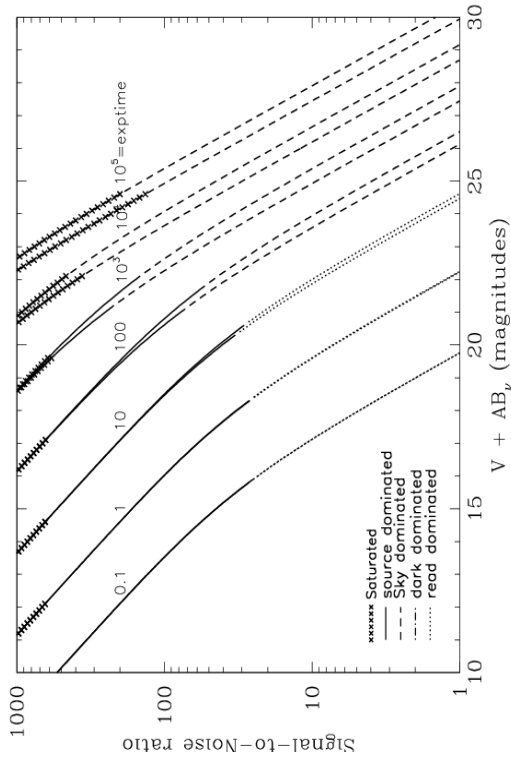
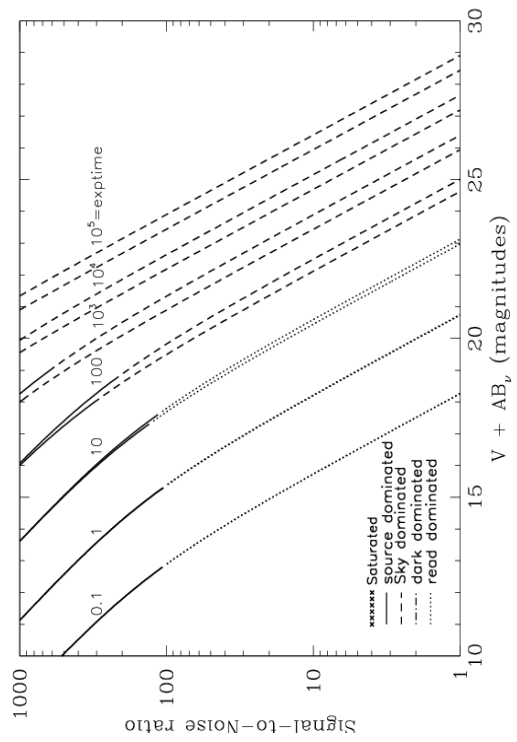


Figure 10.39: Extended source S/N vs. $V+AB_V$ for the WFC/G800L filter. Top curves are for low sky and bottom curves are for average sky for a 1 arcsec^2 area.



WFC/CLEAR

Description

Clear filter.

Figure 10.40: Integrated system throughput for WFC/Clear.

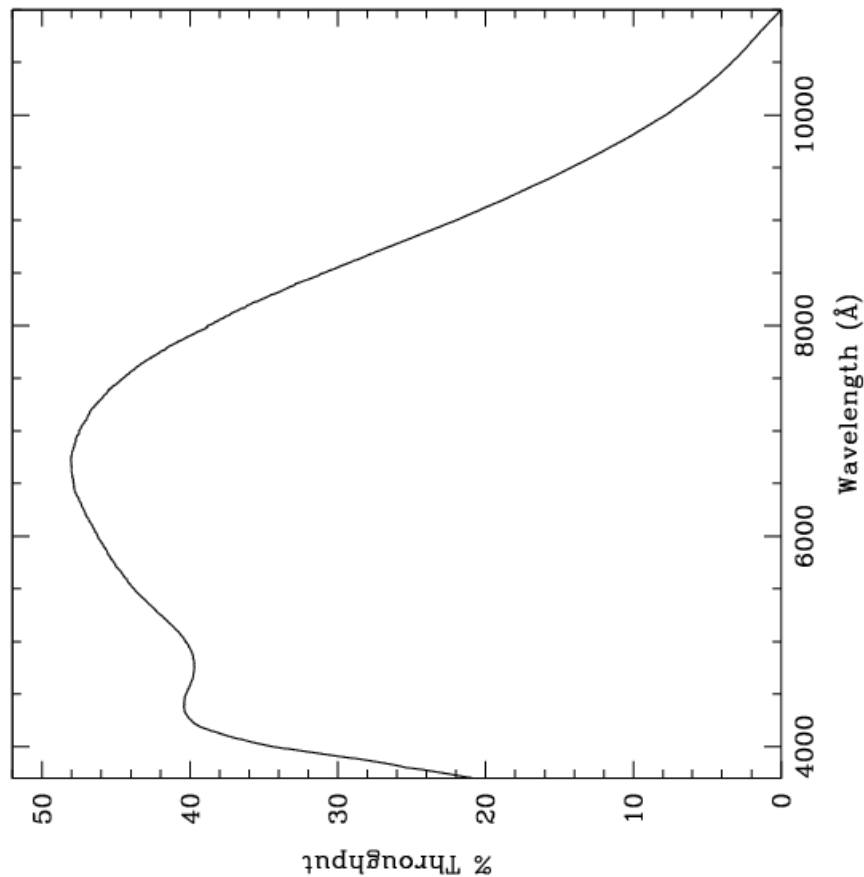


Figure 10.41: Point source S/N vs. $V+AB_V$ for the WFC/Clear filter. Top curves are for low sky; bottom curves are for average sky.

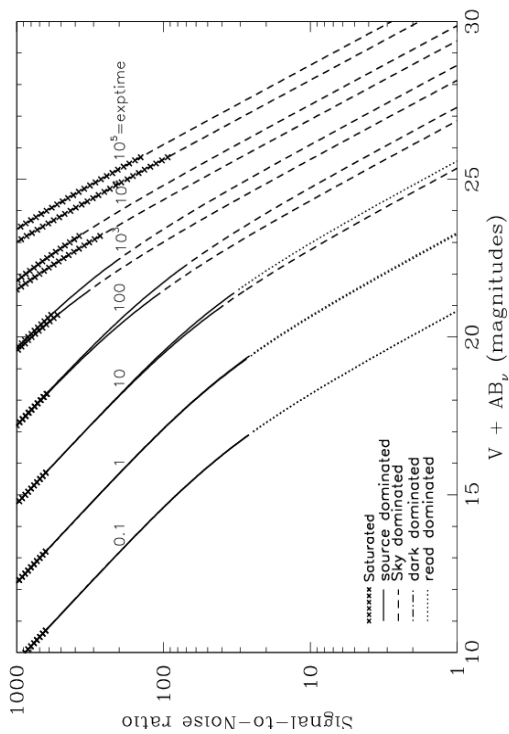
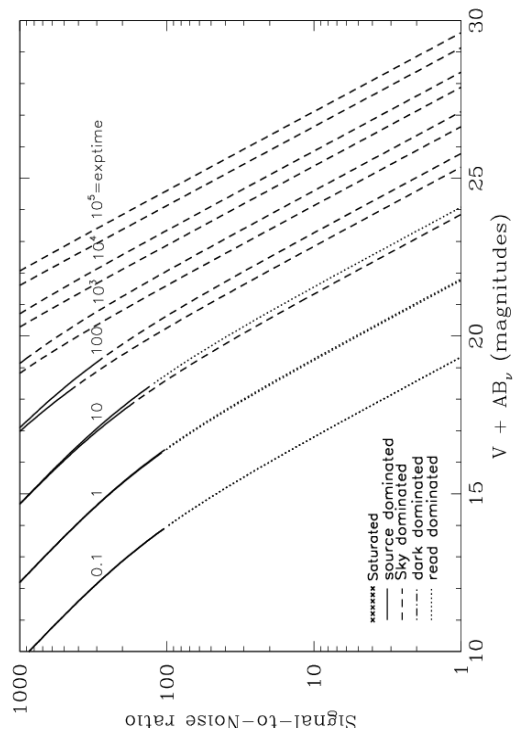


Figure 10.42: Extended source S/N vs. $V+AB_V$ for the WFC/Clear filter. Top curves are for low sky and bottom curves are for average sky for a 1 arcsec² area.



HRC/F220W

Description

Near-UV filter.

Figure 10.43: Integrated system throughput for HRC/F220W.

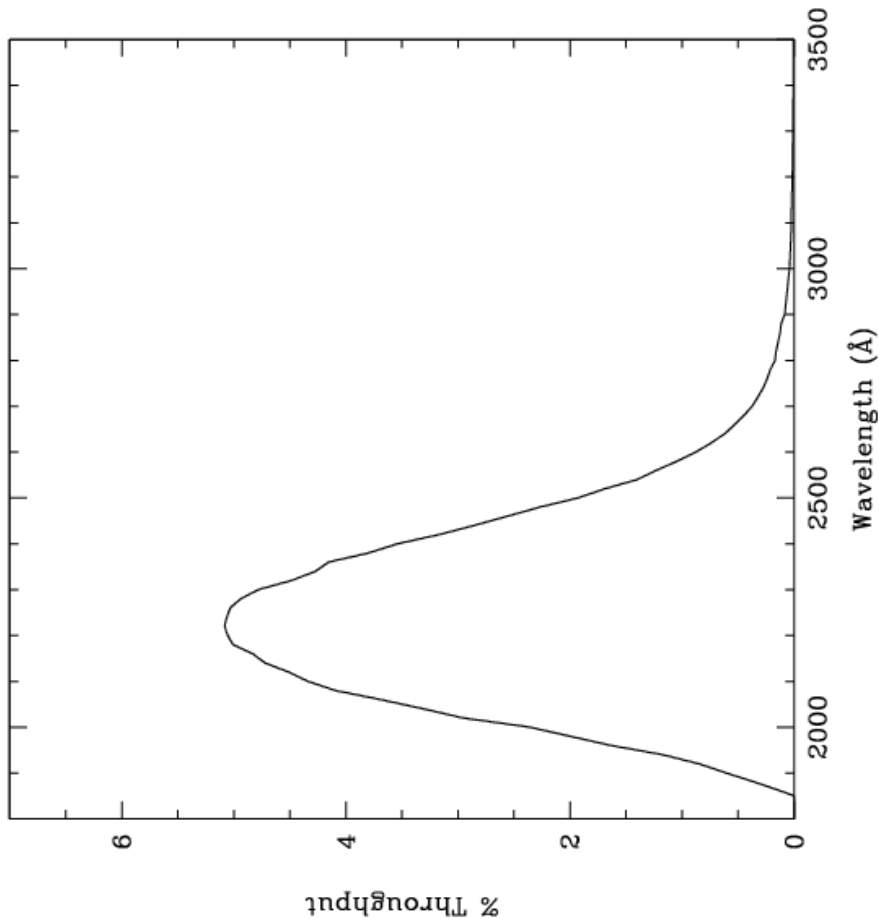


Figure 10.44: Point source S/N vs. $V+AB_V$ for the HRC/F220W filter. Top curves are for low sky; bottom curves are for average sky.

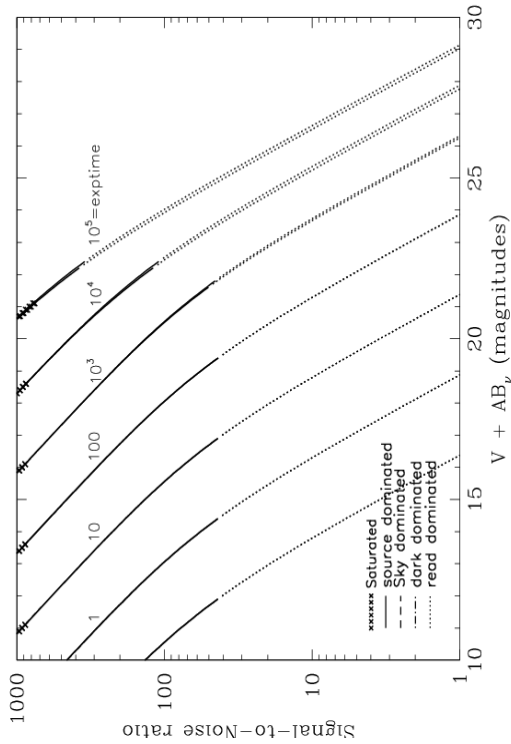
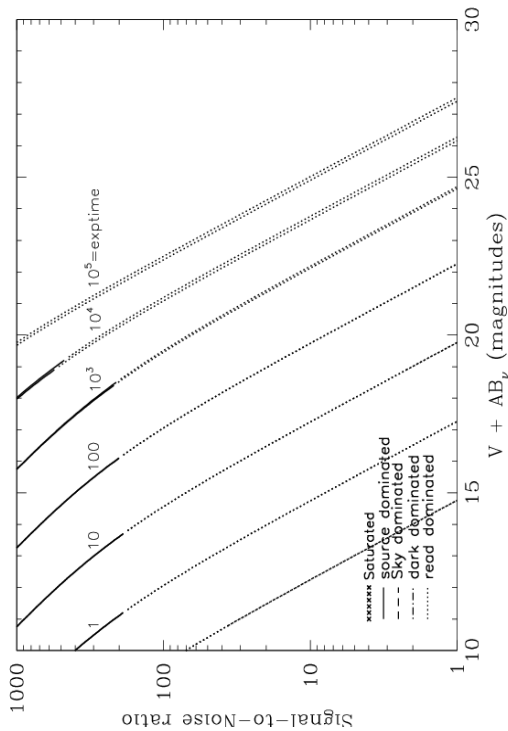


Figure 10.45: Extended source S/N vs. $V+AB_V$ for the HRC/F220W filter. Top curves are for low sky and bottom curves are for average sky for a 1 arcsec² area.



HRC/F250W

Description

Near-UV filter.

Figure 10.46: Integrated system throughput for HRC/F250W.

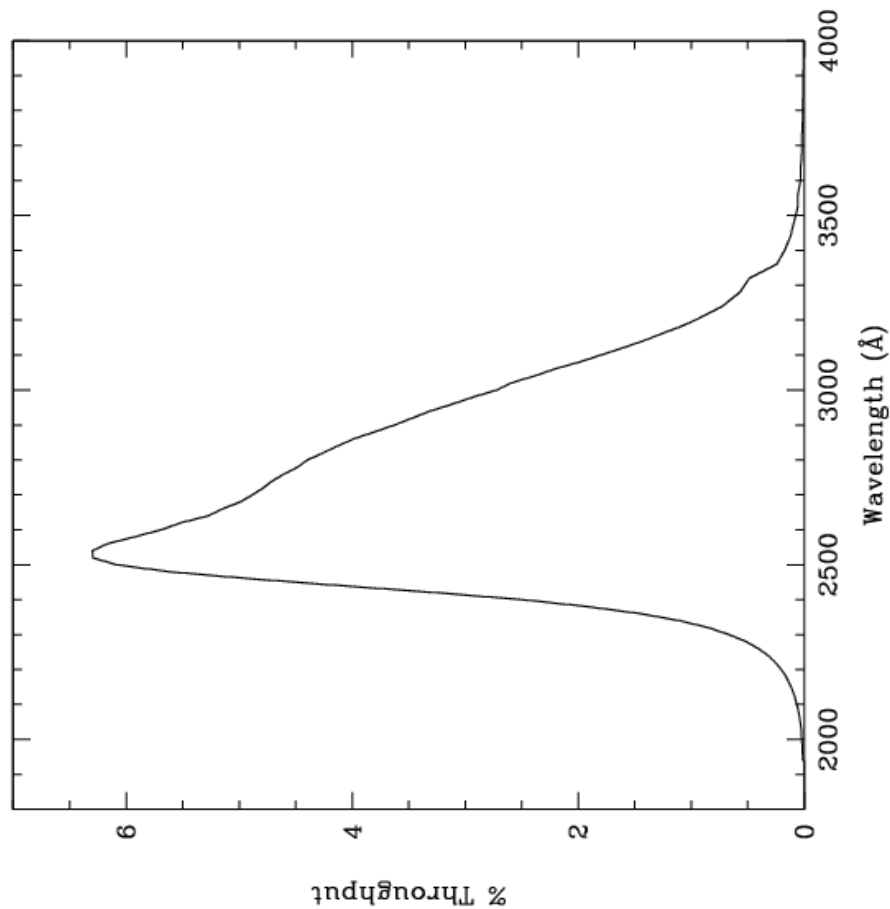


Figure 10.47: Point Source S/N vs. $V+AB_V$ for the HRC/F250W filter. Top curves are for low sky; bottom curves are for average sky.

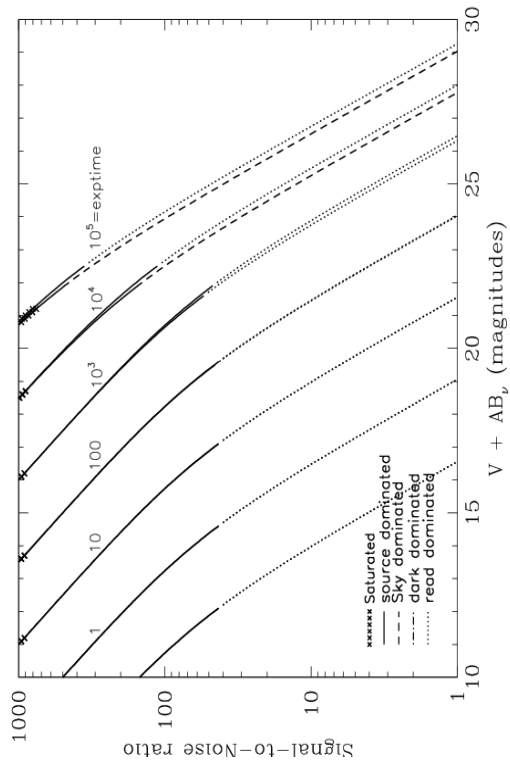
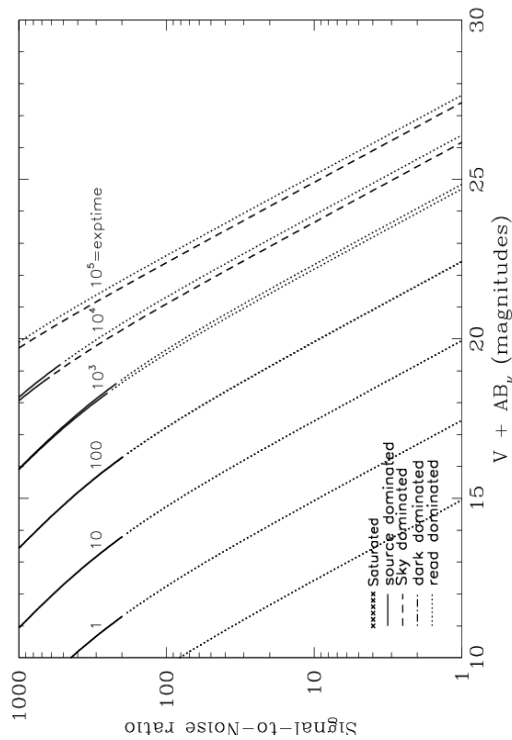


Figure 10.48: Extended Source S/N vs. $V+AB_V$ for the HRC/F250W filter. Top curves are for low sky and bottom curves are for average sky for a 1 arcsec^2 area.



HRC/F330W

Description

HRC u filter.

Figure 10.49: Integrated system throughput for HRC/F330W.

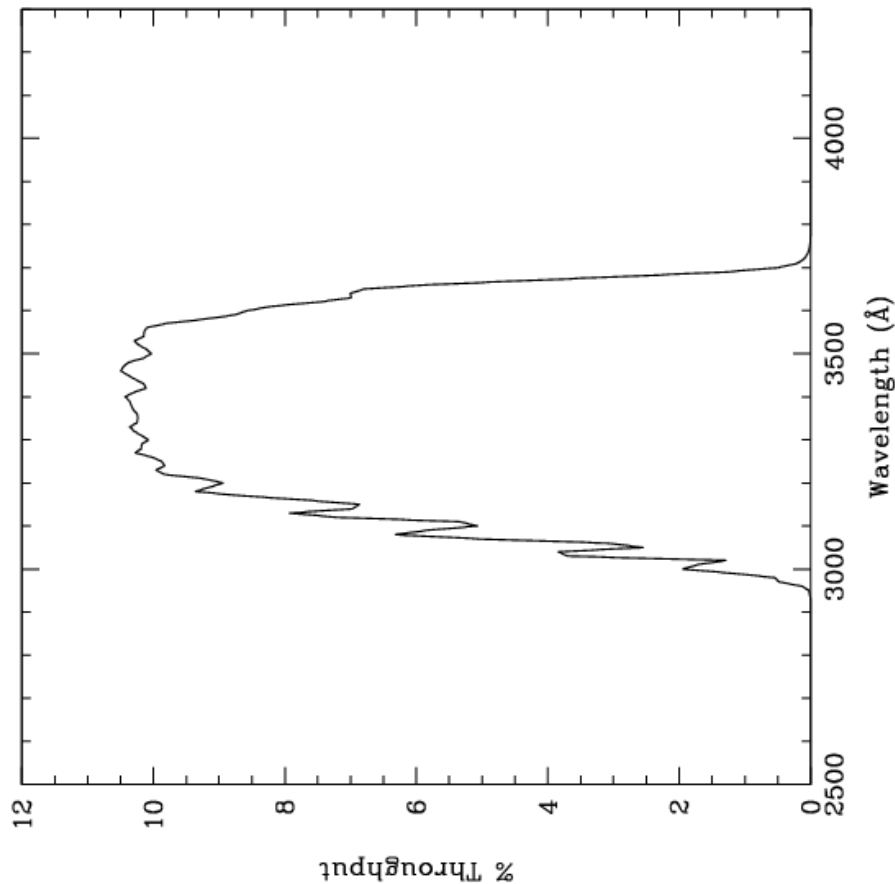


Figure 10.50: Point source S/N vs. $V+AB_V$ for the HRC/F330W filter. Top curves are for low sky; bottom curves are for average sky.

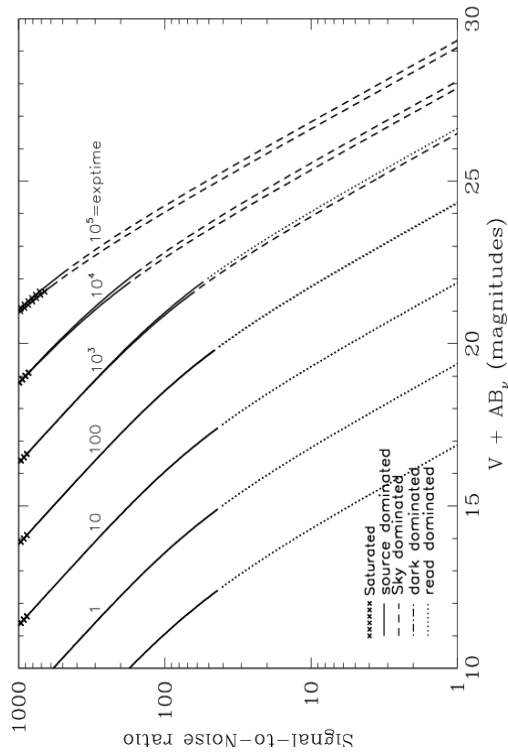
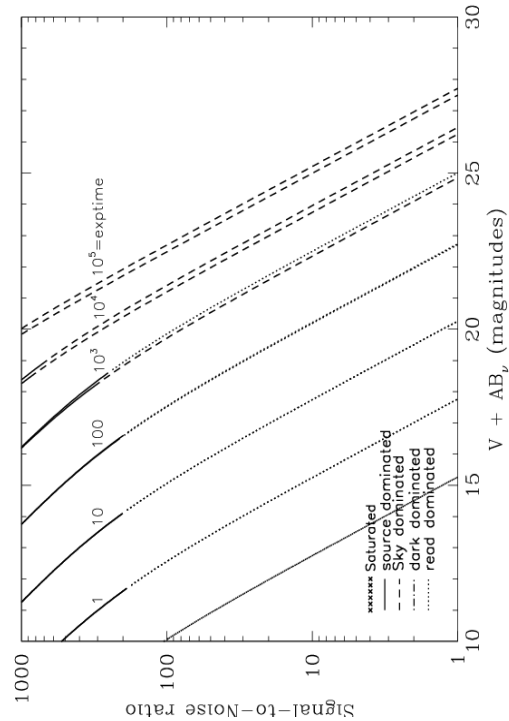


Figure 10.51: Extended source S/N vs. $V+AB_V$ for the HRC/F330W filter. Top curves are for low sky and bottom curves are for average sky for a 1 arcsec² area.



HRC/F344N

Description

NeV filter.

Figure 10.52: Integrated system throughput for HRC/F344N.

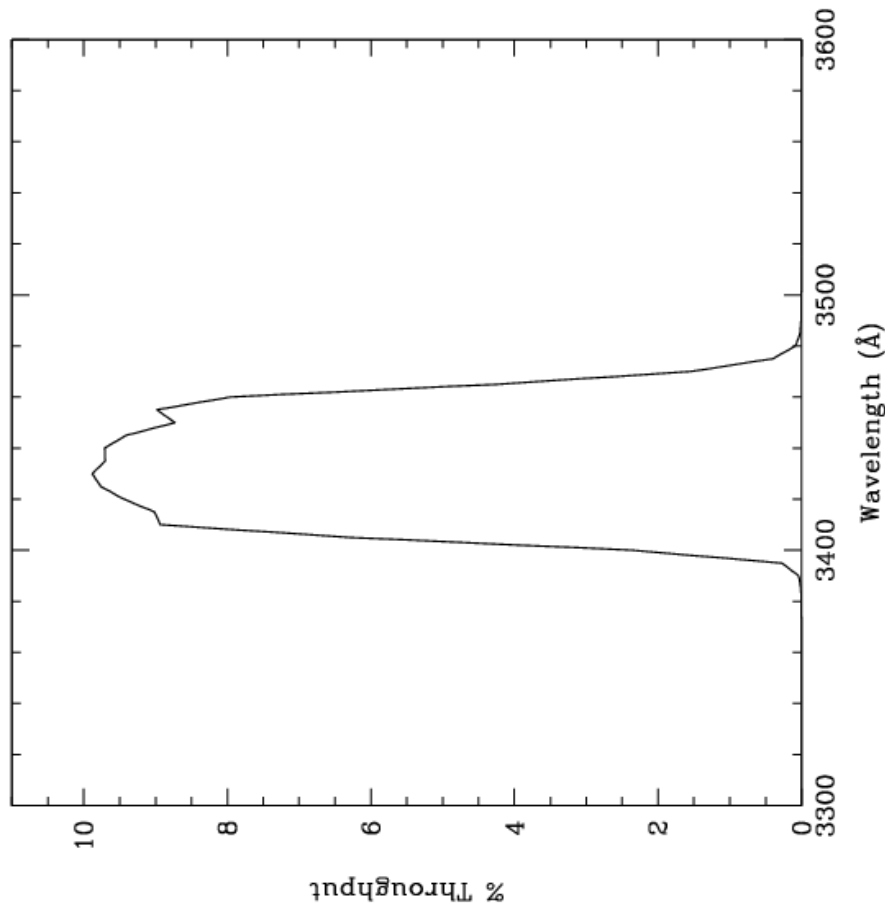


Figure 10.53: Point source S/N vs. $V + AB_V$ for the HRC/F344N filter. Top curves are for low sky; bottom curves are for average sky.

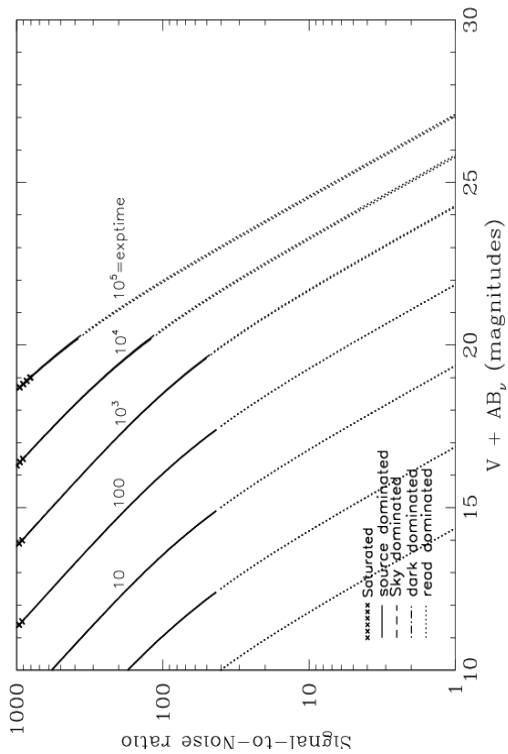
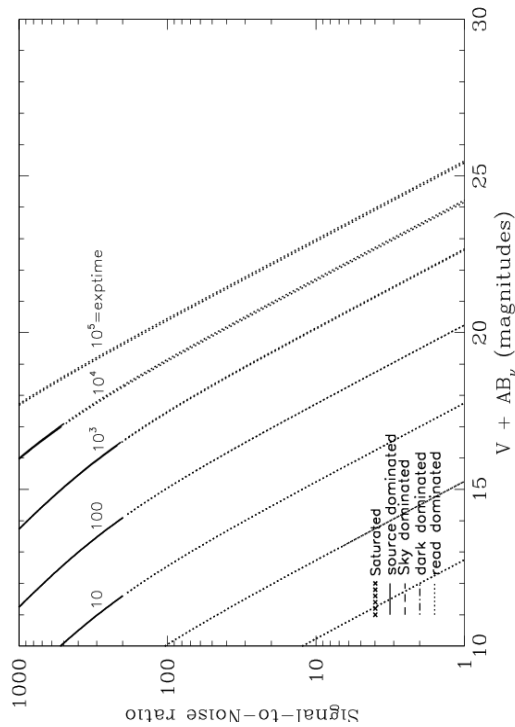


Figure 10.54: Extended source S/N vs. $V + AB_V$ for the HRC/F344N filter. Top curves are for low sky and bottom curves are for average sky for a 1 arcsec^2 area.



HRC/F435W

Description

Johnson B filter.

Figure 10.55: Integrated system throughput for HRC/F435W.

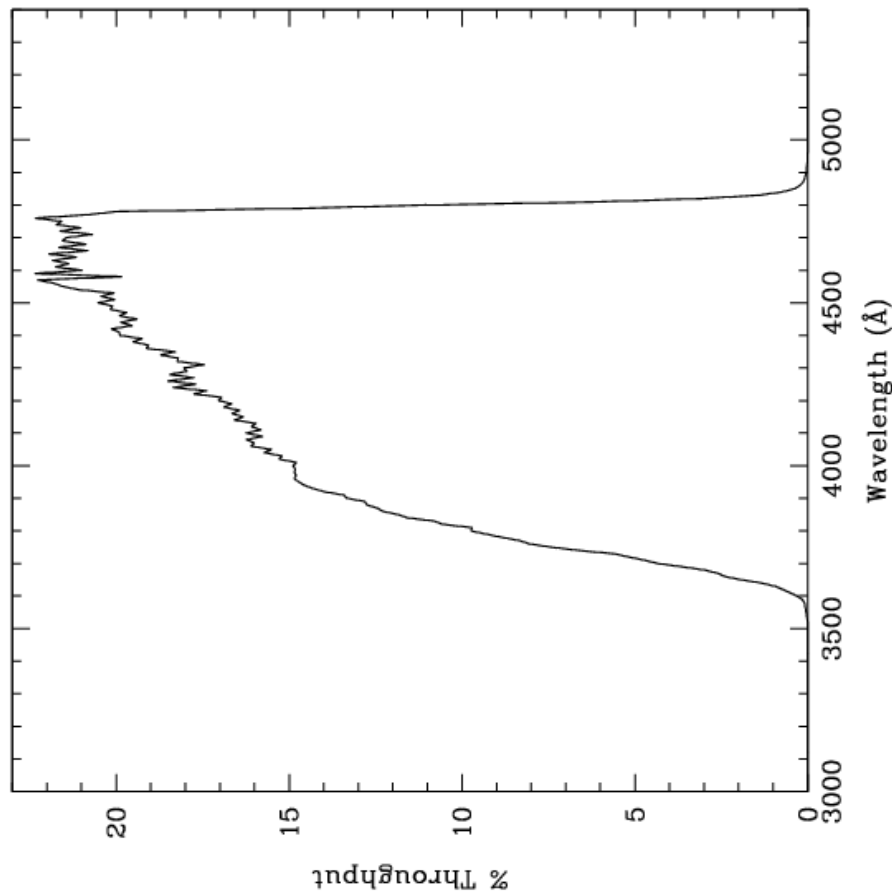


Figure 10.56: Point source S/N vs. $V+AB_V$ for the HRC/F435W filter. Top curves are for low sky; bottom curves are for average sky.

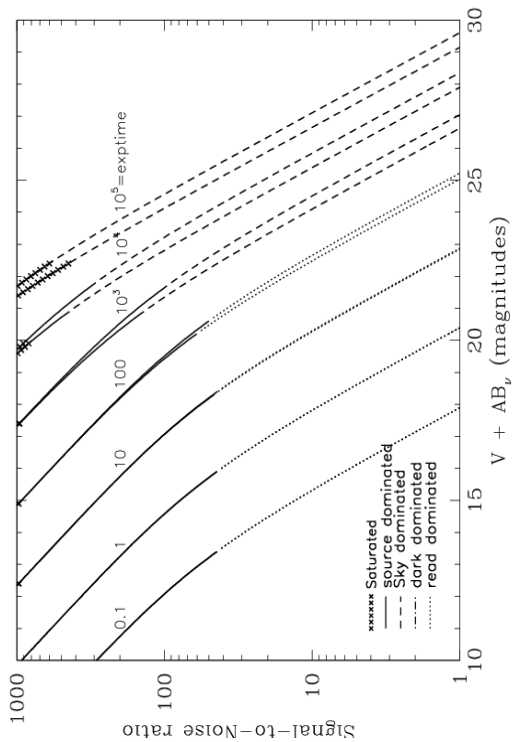
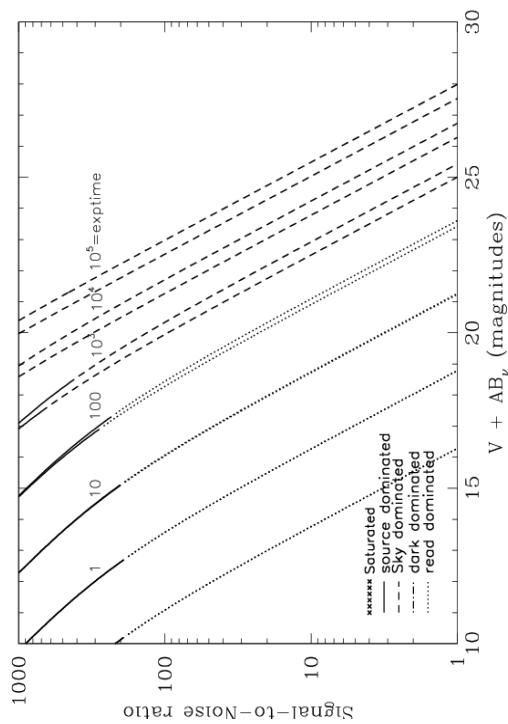


Figure 10.57: Extended source S/N vs. $V+AB_V$ for the HRC/F435W filter. Top curves are for low sky and bottom curves are for average sky for a 1 arcsec^2 area.



HRC/F475W

Description

Sloan Digital Sky Survey g filter.

Figure 10.58: Integrated system throughput for HRC/F475W.

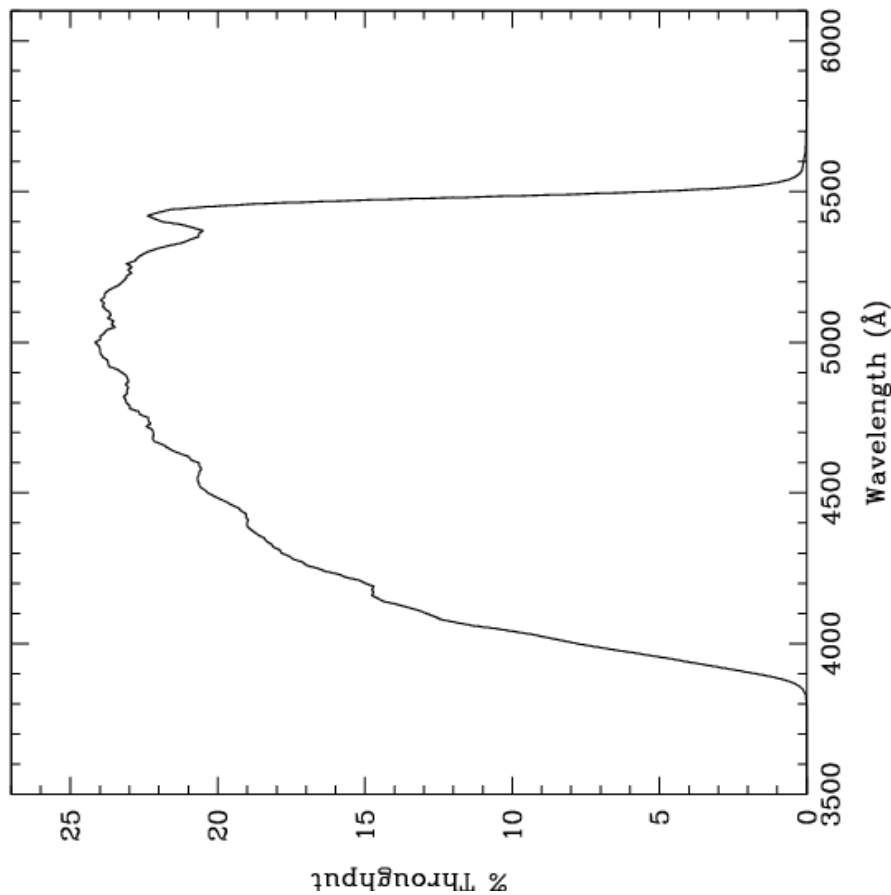


Figure 10.59: Point source S/N vs. $V+AB_V$ for the HRC/F475W filter. Top curves are for low sky; bottom curves are for average sky.

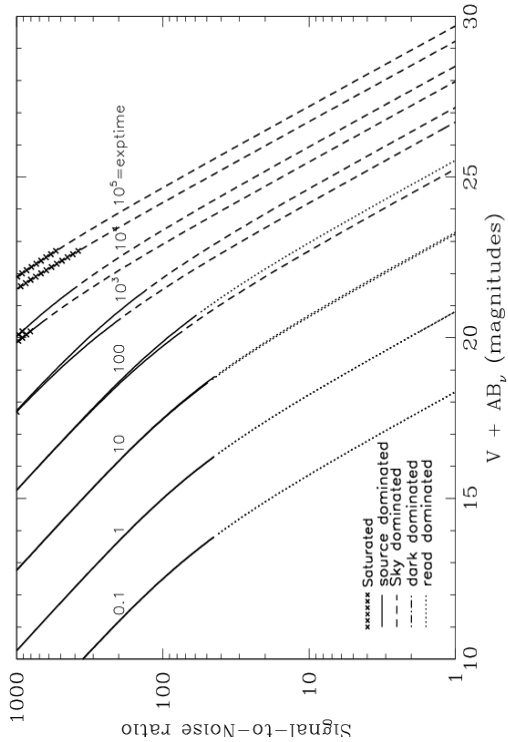
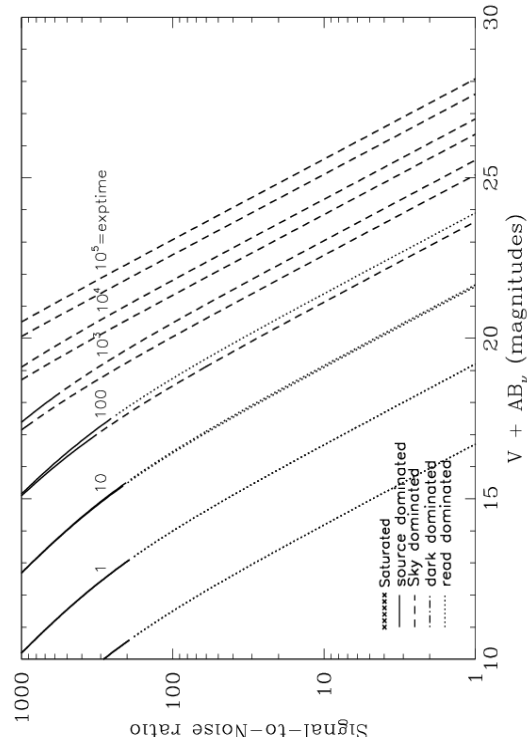


Figure 10.60: Extended source S/N vs. $V+AB_V$ for the HRC/F475W filter. Top curves are for low sky and bottom curves are for average sky for a 1 arcsec^2 area.



HRC/F502N

Description

OIII filter.

Figure 10.61: Integrated system throughput for HRC/F502N.

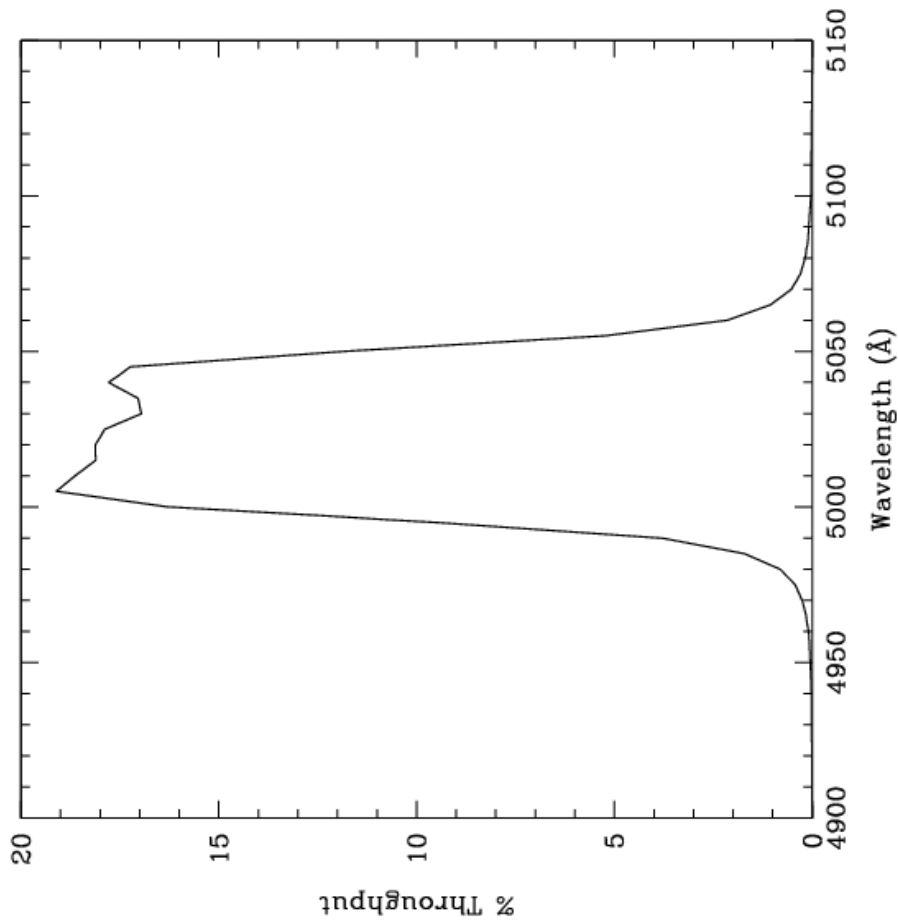


Figure 10.62: Point source S/N vs. $V + AB_V$ for the HRC/F502N filter. Top curves are for low sky; bottom curves are for average sky.

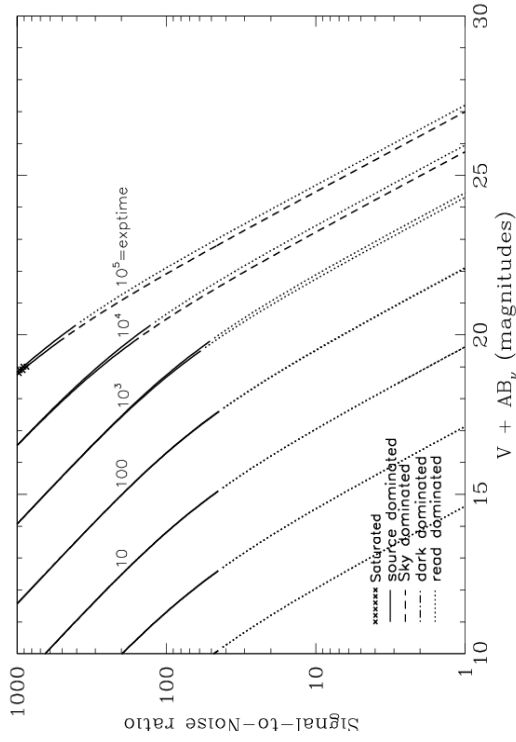
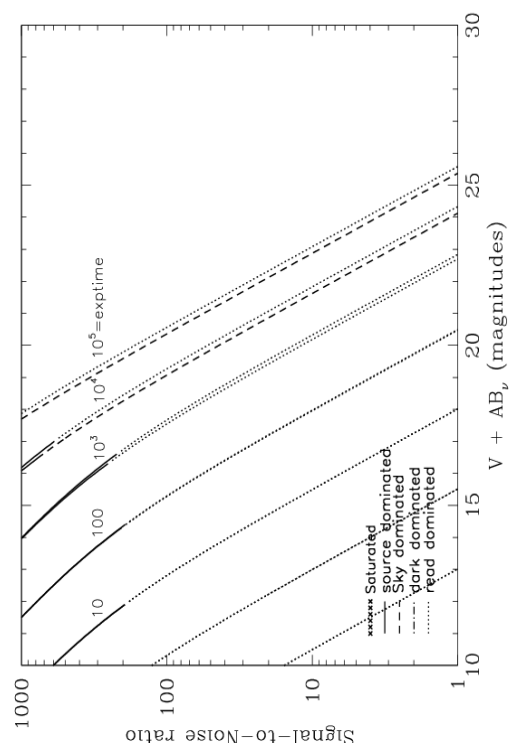


Figure 10.63: Extended source S/N vs. $V + AB_V$ for the HRC/F502N filter. Top curves are for low sky and bottom curves are for average sky for a 1 arcsec^2 area.



HRC/F550M

Description

Narrow V filter.

Figure 10.64: Integrated system throughput for HRC/F550M.

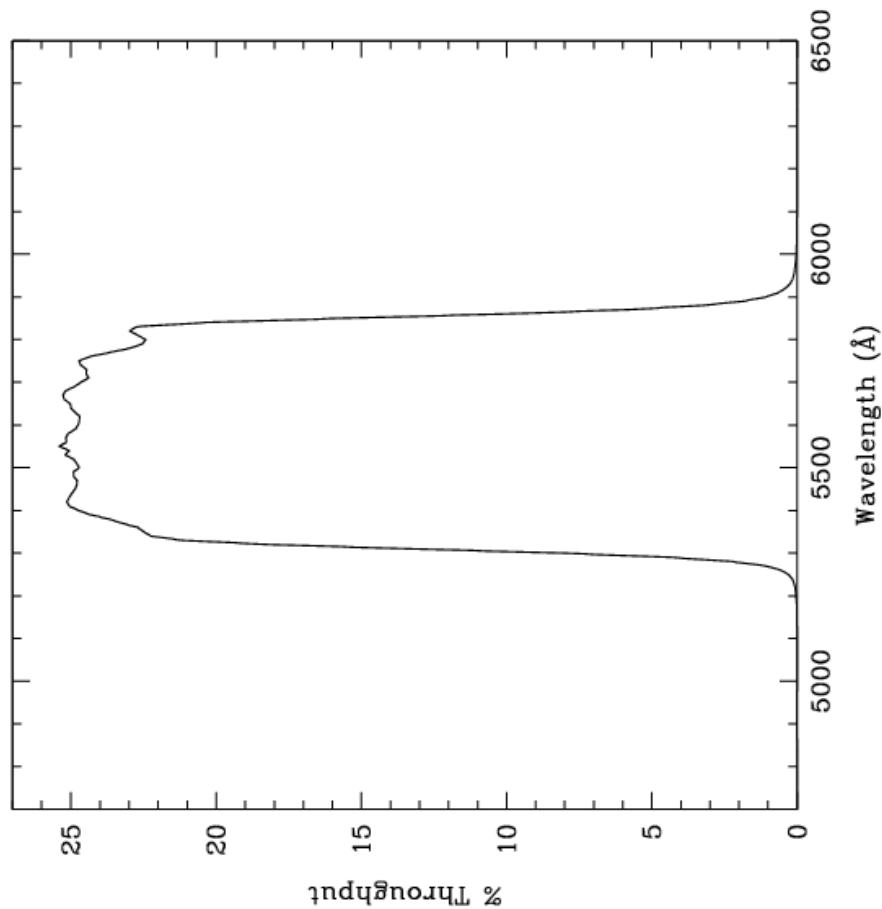


Figure 10.65: Point source S/N vs. $V+AB_V$ for the HRC/F550M filter. Top curves are for low sky; bottom curves are for average sky.

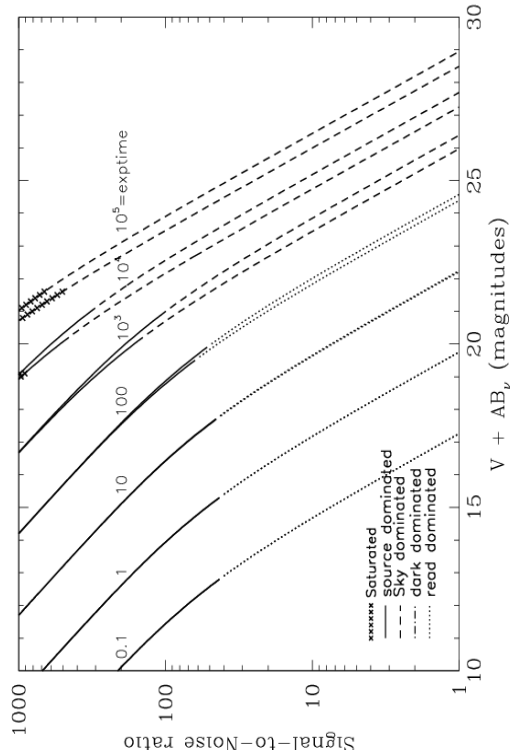
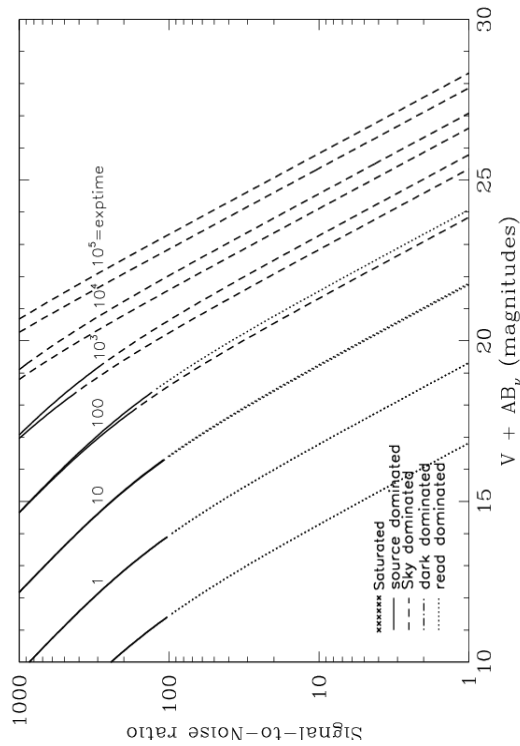


Figure 10.66: Extended source S/N vs. $V+AB_V$ for the HRC/F550M filter. Top curves are for low sky and bottom curves are for average sky for a 1 arcsec^2 area.



HRC/F555W

Description

Johnson V filter.

Figure 10.67: Integrated system throughput for HRC/F555W.

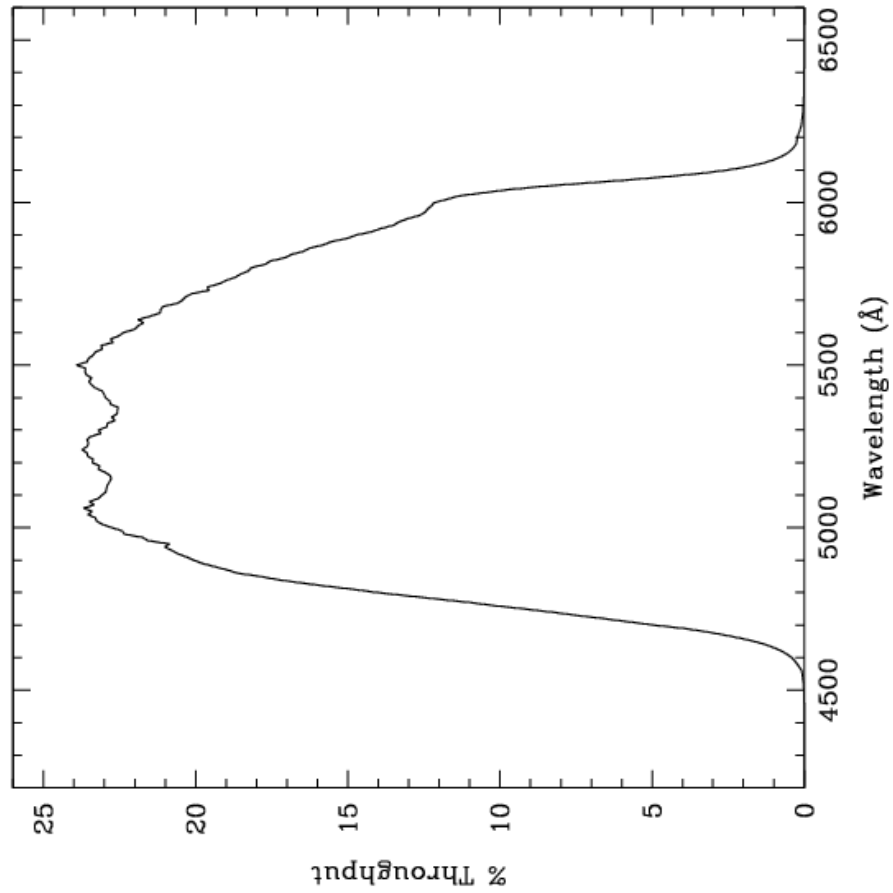


Figure 10.68: Point source S/N vs. $V+AB_V$ for the HRC/F555W filter. Top curves are for low sky; bottom curves are for average sky.

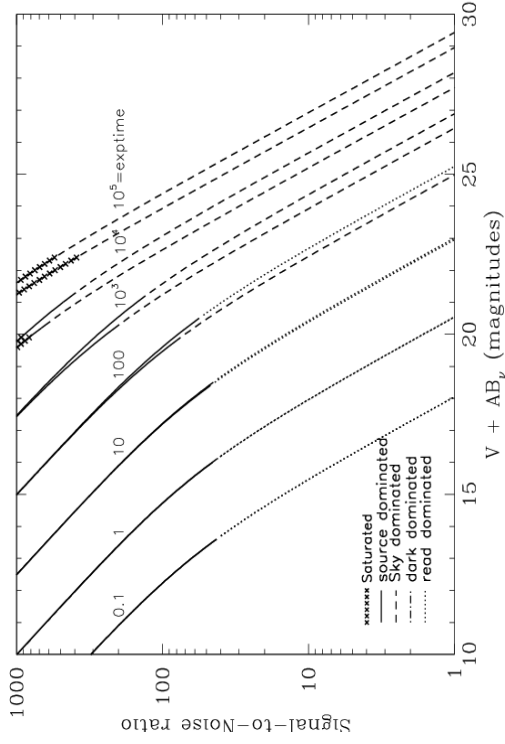
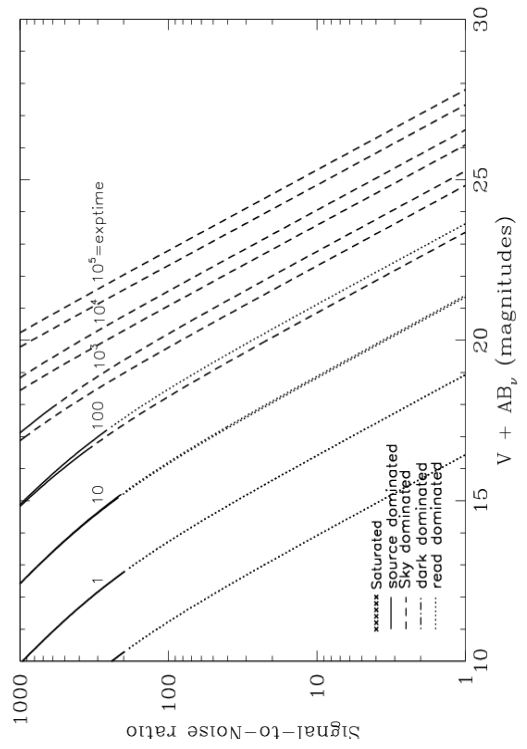


Figure 10.69: Extended source S/N vs. $V+AB_V$ for the HRC/F555W filter. Top curves are for low sky and bottom curves are for average sky for a 1 arcsec² area.



HRC/F606W

Description

Broad V filter.

Figure 10.70: Integrated system throughput for HRC/F606W.

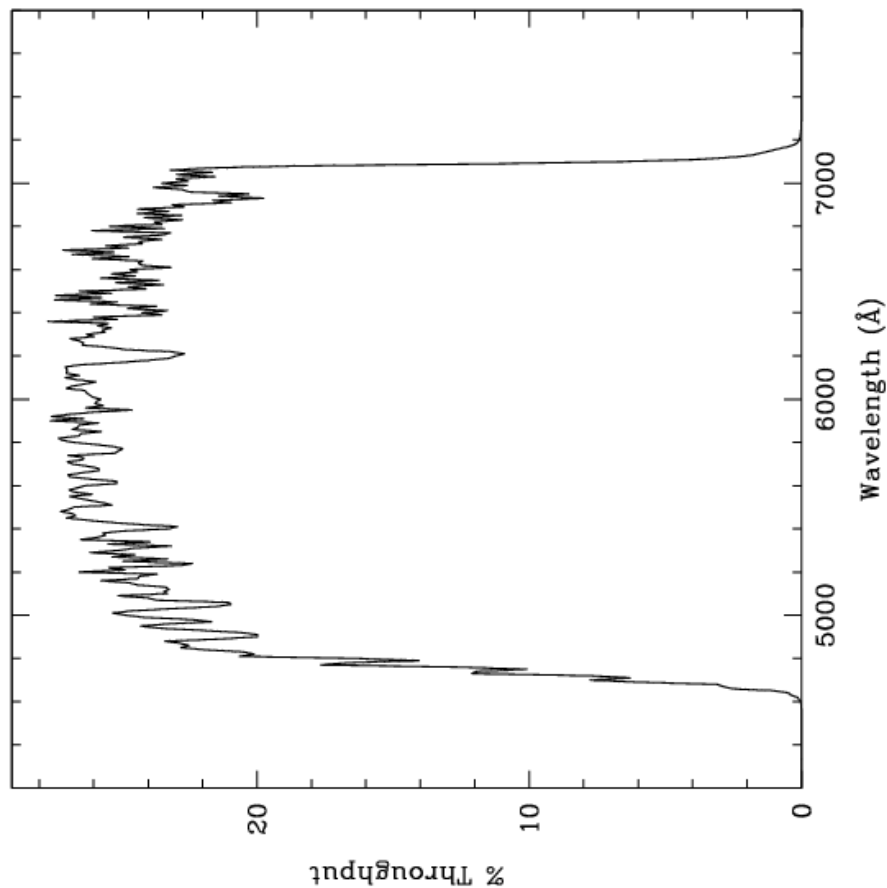


Figure 10.71: Point source S/N vs. $V+AB_V$ for the HRC/F606W filter. Top curves are for low sky; bottom curves are for average sky.

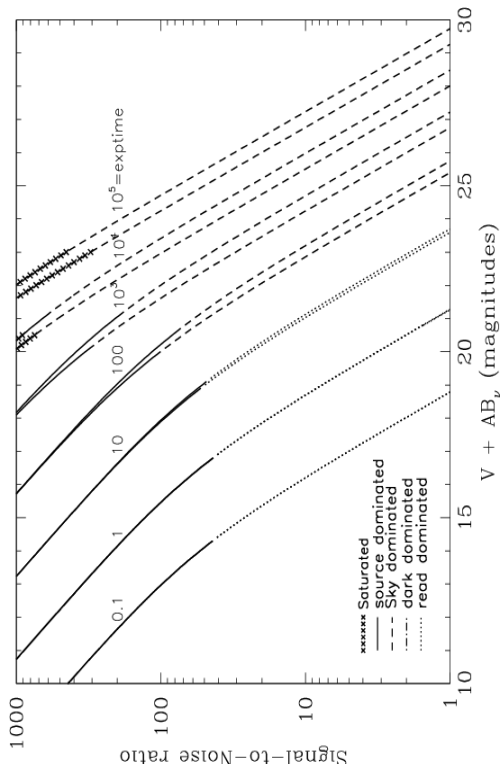
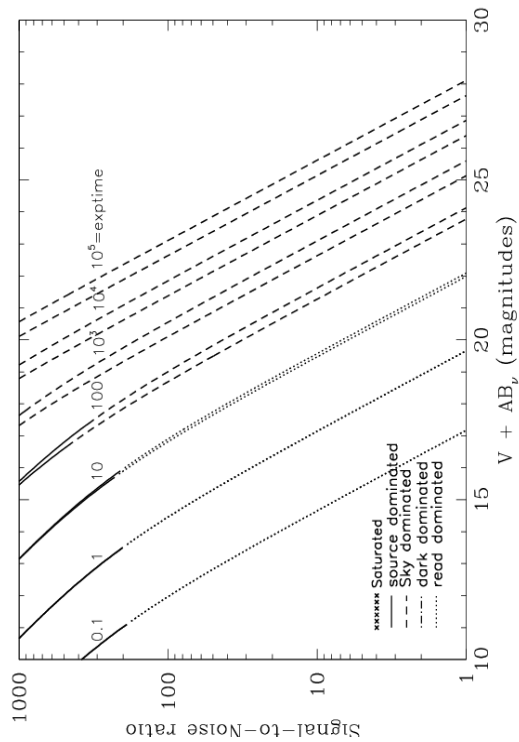


Figure 10.72: Extended source S/N vs. $V+AB_V$ for the HRC/F606W filter. Top curves are for low sky and bottom curves are for average sky for a 1 arcsec² area.



HRC/F625W

Description

Sloan Digital Sky Survey r filter.

Figure 10.73: Integrated system throughput for HRC/F625W.

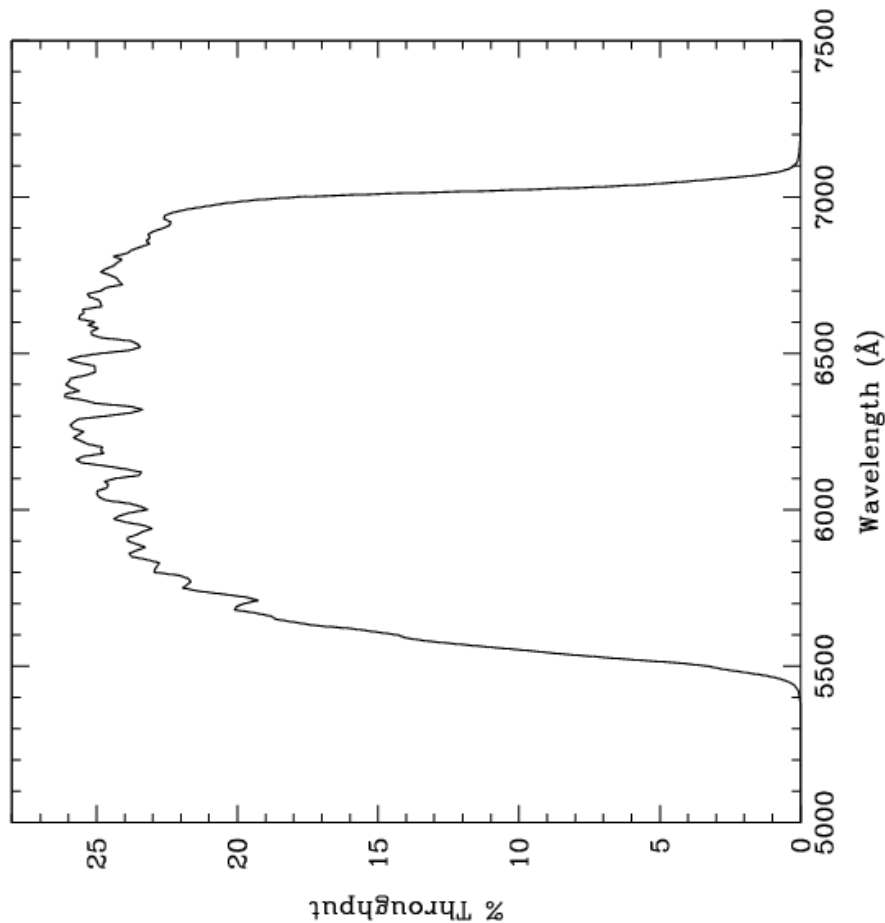


Figure 10.74: Point source S/N vs. $V+AB_V$ for the HRC/F625W filter. Top curves are for low sky; bottom curves are for average sky.

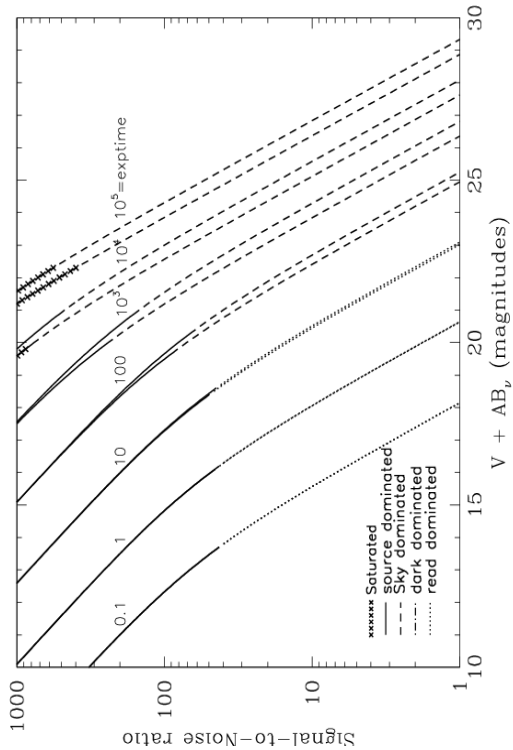
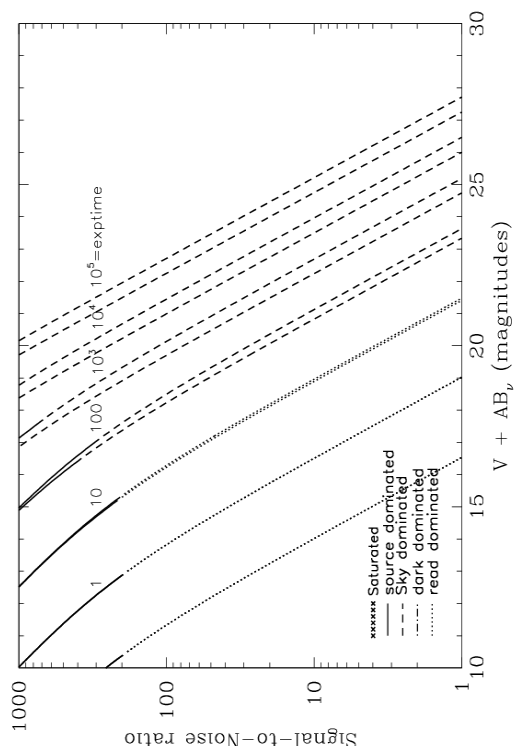


Figure 10.75: Extended source S/N vs. $V+AB_V$ for the HRC/F625W filter. Top curves are for low sky and bottom curves are for average sky for a 1 arcsec² area.



HRC/F658N

Description

H α filter.

Figure 10.76: Integrated system throughput for HRC/F658N.

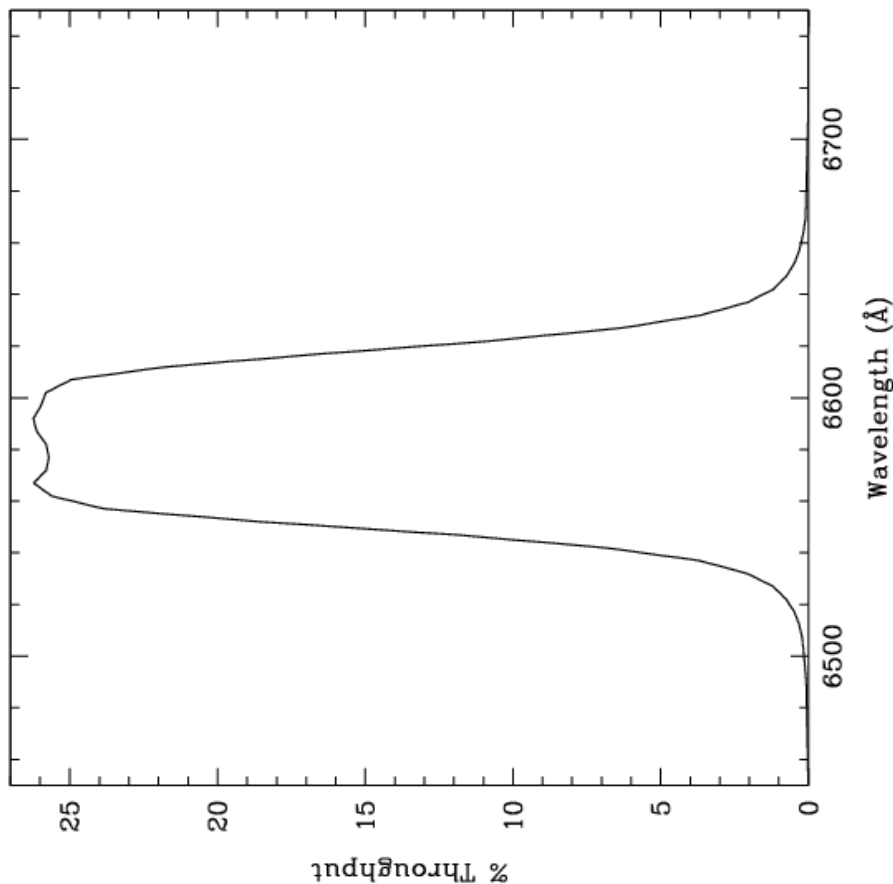


Figure 10.77: Point source S/N vs. $V+AB_V$ for the HRC/F658N filter. Top curves are for low sky; bottom curves are for average sky.

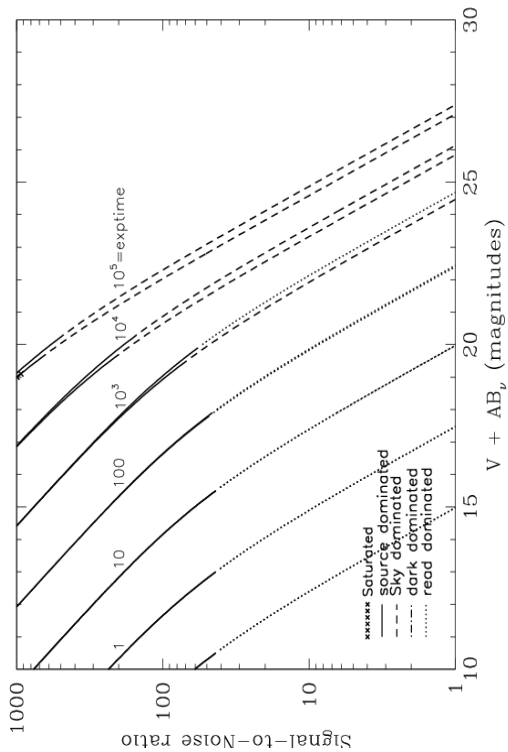
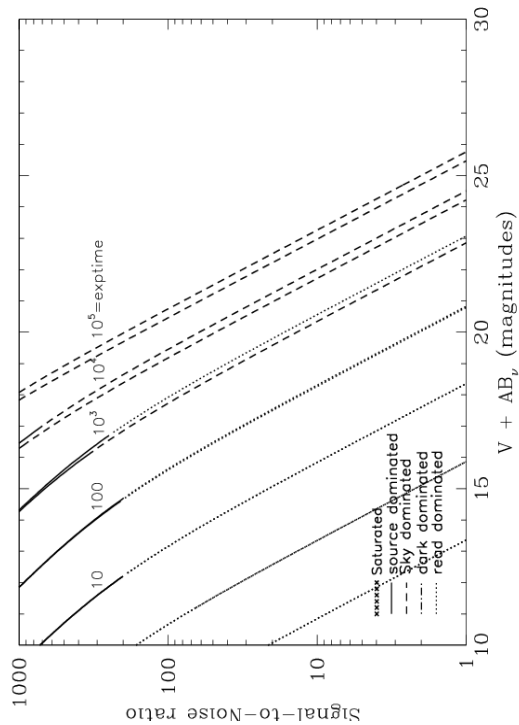


Figure 10.78: Extended source S/N vs. $V+AB_V$ for the HRC/F658N filter. Top curves are for low sky and bottom curves are for average sky for a 1 arcsec^2 area.



HRC/F660N

Description

NII filter.

Figure 10.79: Integrated system throughput for HRC/F660N.

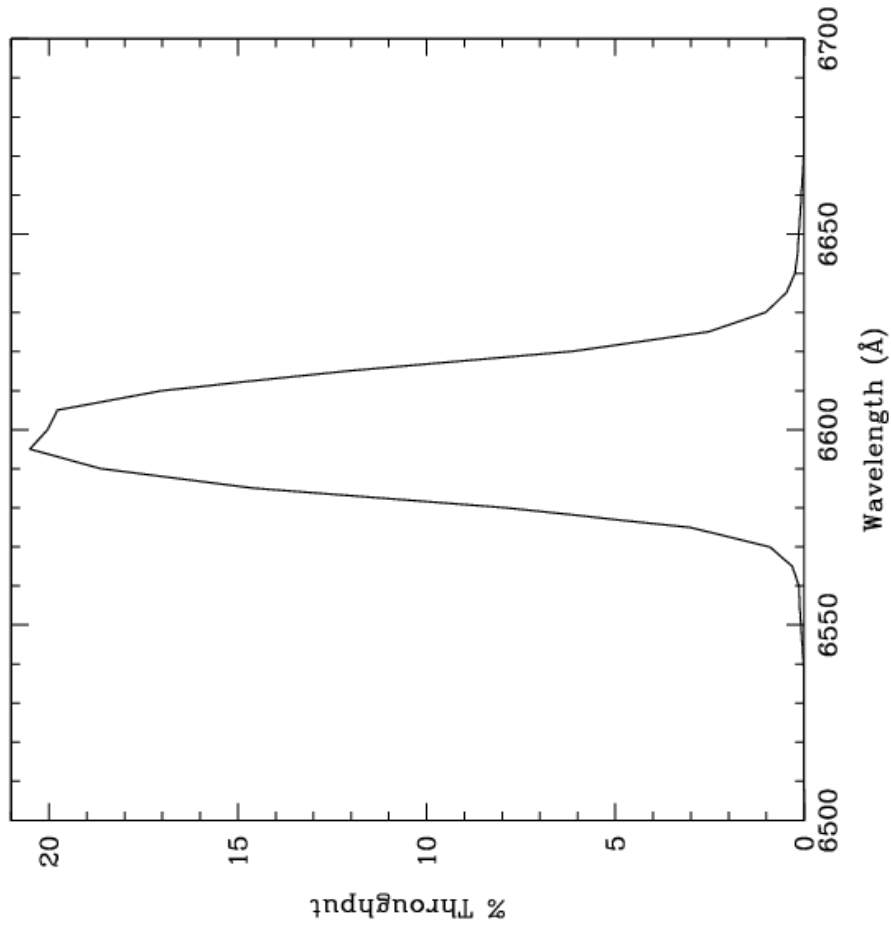


Figure 10.80: Point source S/N vs. $V + AB_V$ for the HRC/F660N filter. Top curves are for low sky; bottom curves are for average sky.

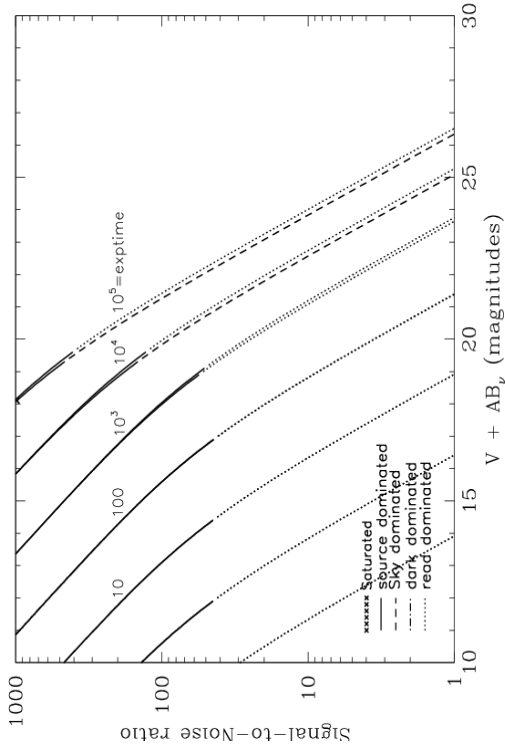
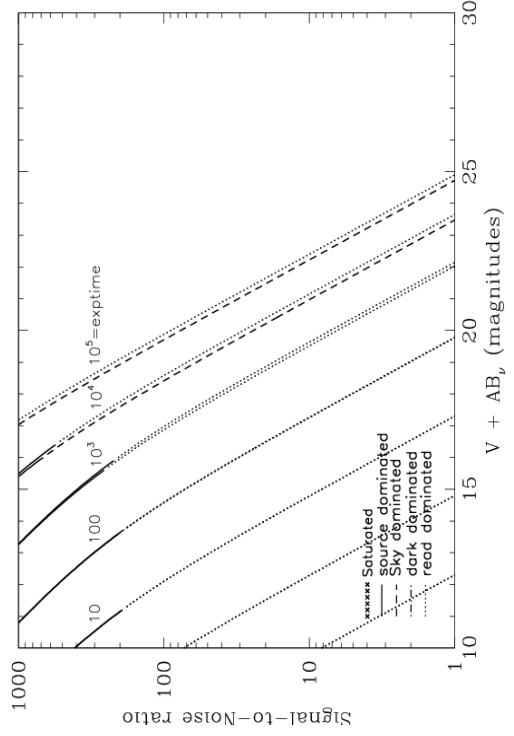


Figure 10.81: Extended source S/N vs. $V + AB_V$ for the HRC/F660N filter. Top curves are for low sky and bottom curves are for average sky for a 1 arcsec² area.



HRC/F775W

Description

Sloan Digital Sky Survey i filter.

Figure 10.82: Integrated system throughput for HRC/F775W.

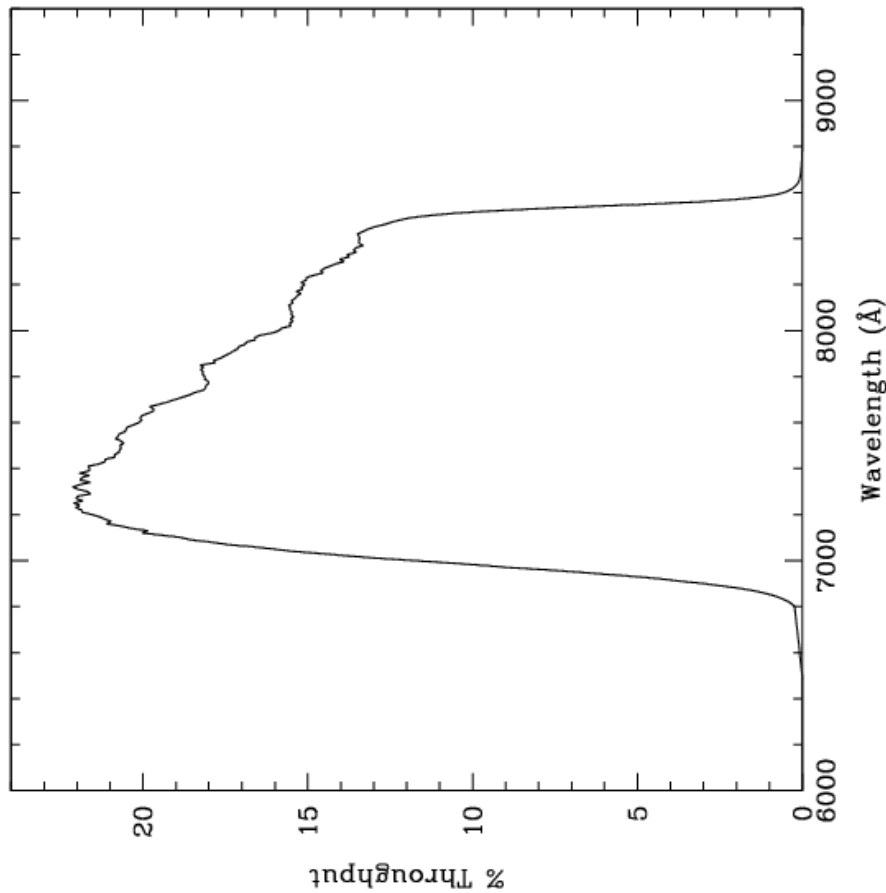


Figure 10.83: Point source S/N vs. $V+AB_V$ for the HRC/F775W filter. Top curves are for low sky; bottom curves are for average sky.

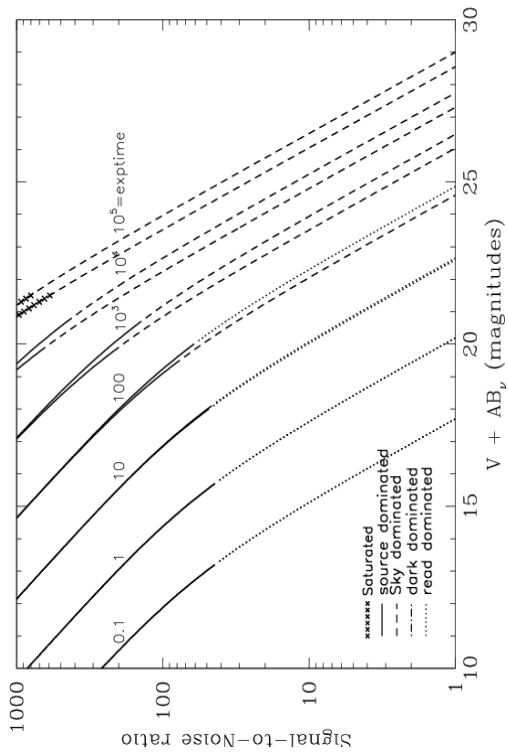
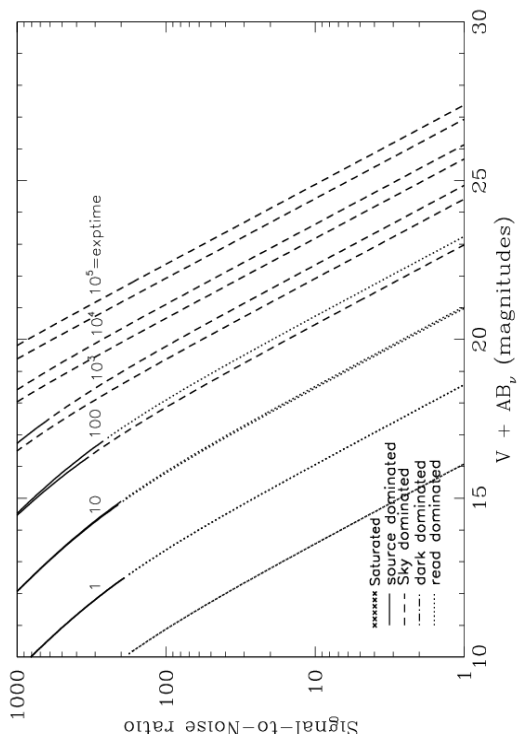


Figure 10.84: Extended source S/N vs. $V+AB_V$ for the HRC/F775W filter. Top curves are for low sky and bottom curves are for average sky for a 1 arcsec^2 area.



HRC/F814W

Description

Broad I filter.

Figure 10.85: Integrated system throughput for HRC/F814W.

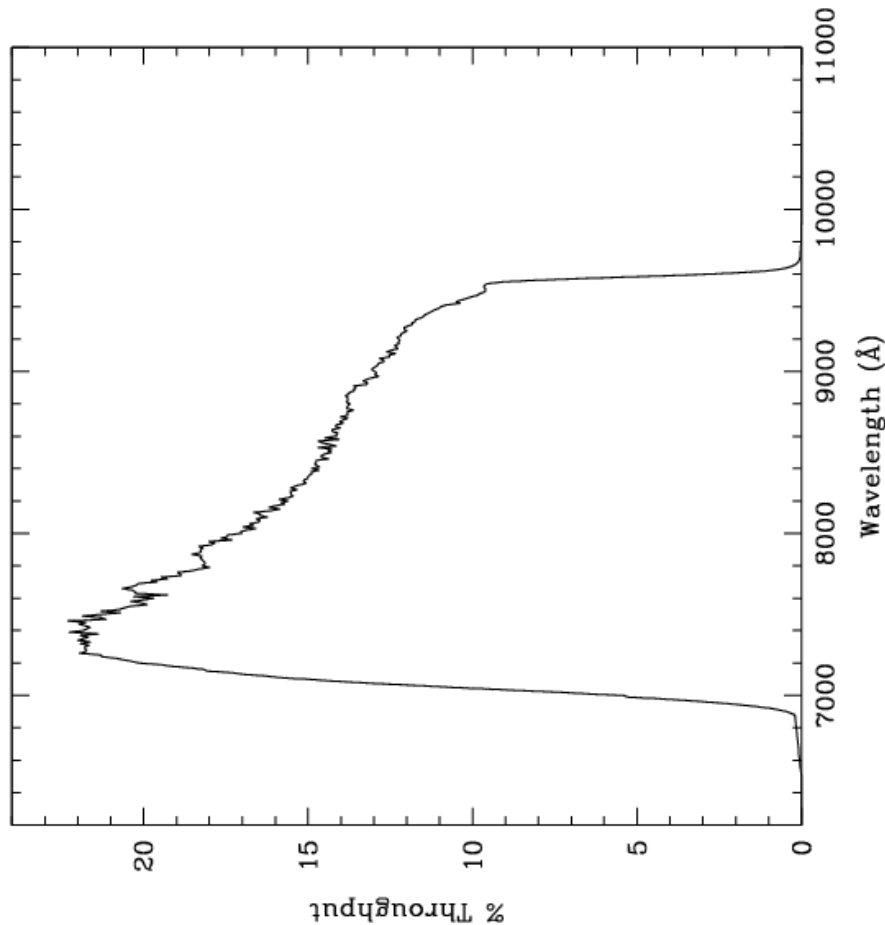


Figure 10.86: Point source S/N vs. $V+AB_V$ for the HRC/F814W filter. Top curves are for low sky; bottom curves are for average sky.

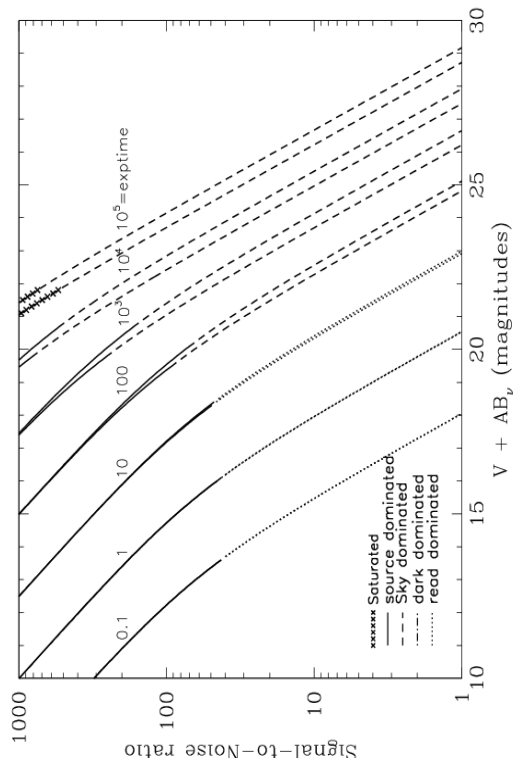
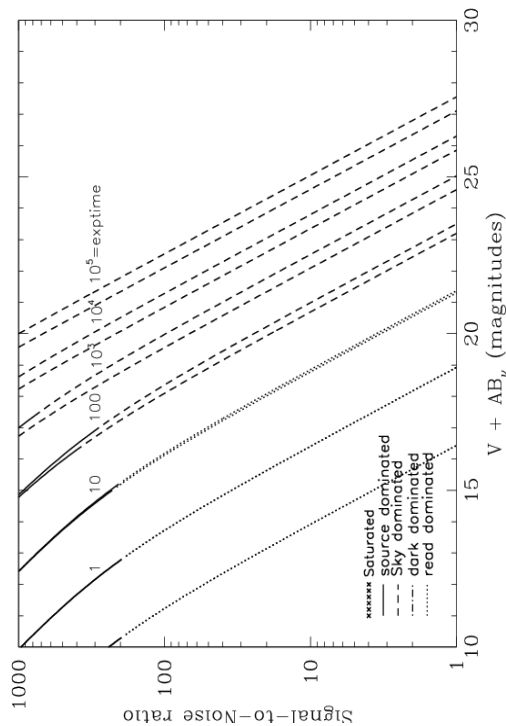


Figure 10.87: Extended source S/N vs. $V+AB_V$ for the HRC/F814W filter. Top curves are for low sky and bottom curves are for average sky for a 1 arcsec² area.



HRC/F850LP

Description

Sloan Digital Sky Survey z filter.

Figure 10.88: Integrated system throughput for HRC/F850LP.

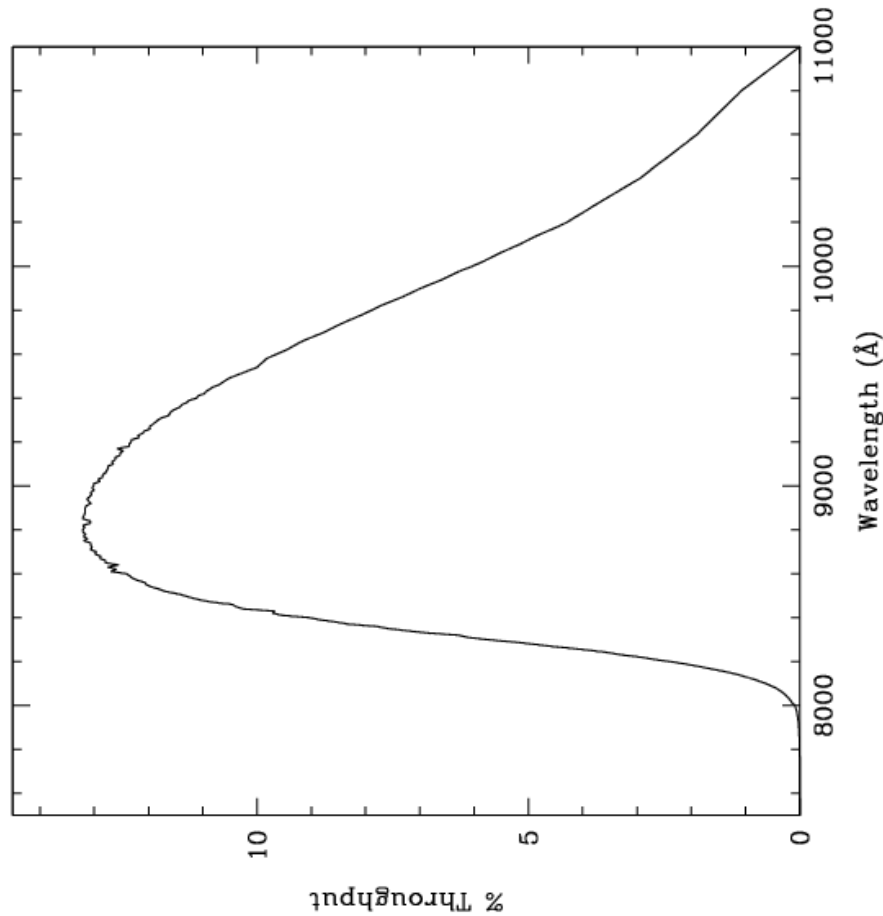


Figure 10.89: Point source S/N vs. $V+AB_V$ for the HRC/F850LP filter. Top curves are for low sky; bottom curves are for average sky.

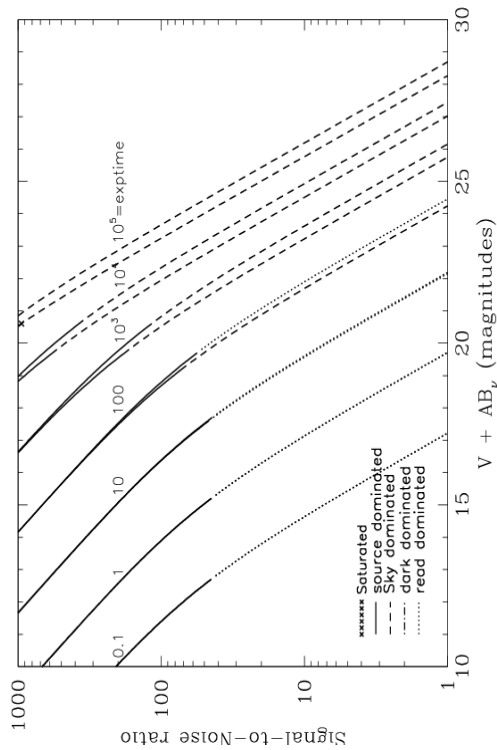
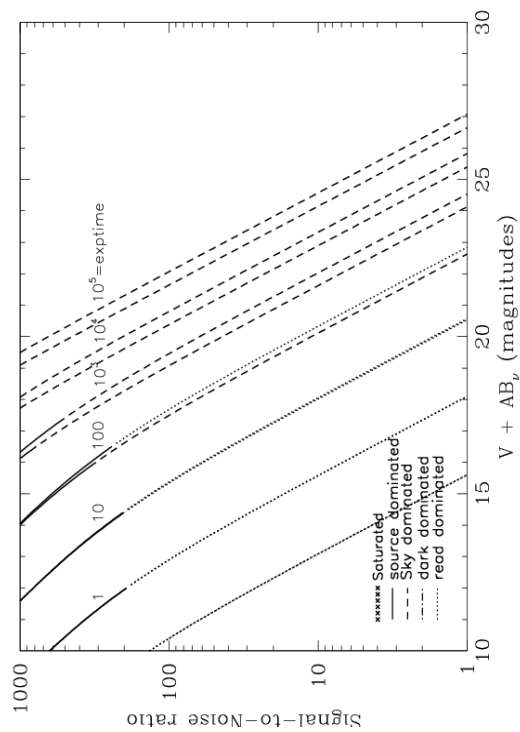


Figure 10.90: Extended source S/N vs. $V+AB_V$ for the HRC/F850LP filter. Top curves are for low sky and bottom curves are for average sky for a 1 arcsec^2 area.



HRC/F892N

Description

Methane filter.

Figure 10.91: Integrated system throughput for HRC/F892N.

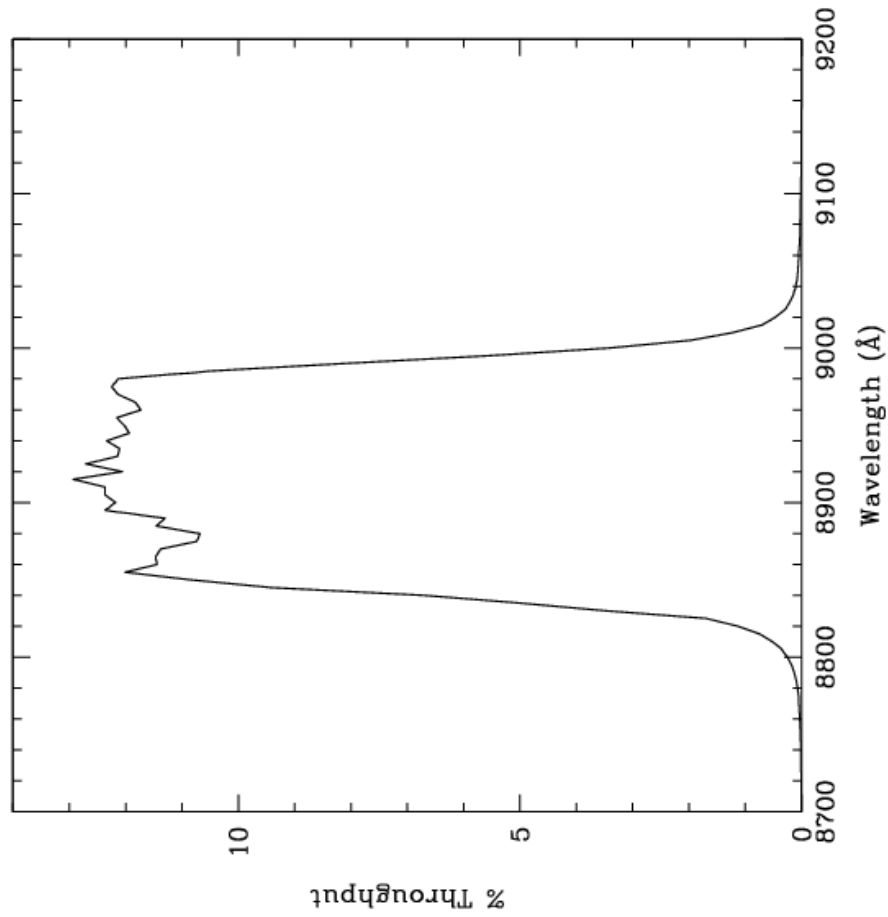


Figure 10.92: Point source S/N vs. $V + AB_V$ for the HRC/F892N filter. Top curves are for low sky; bottom curves are for average sky.

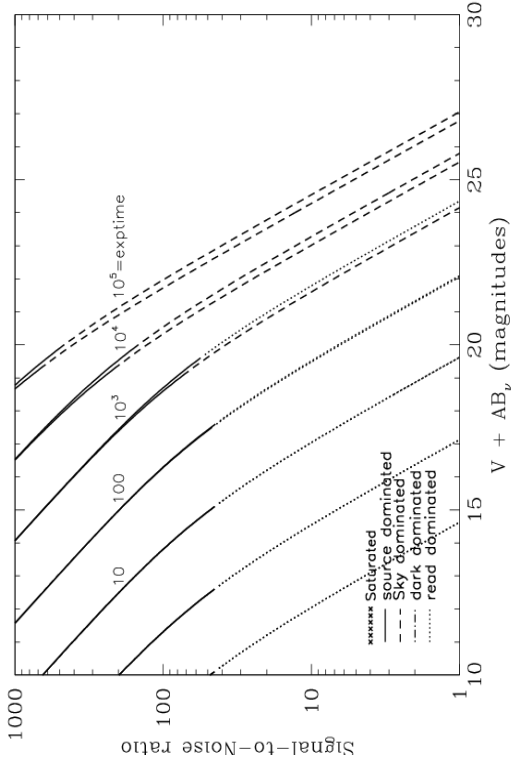
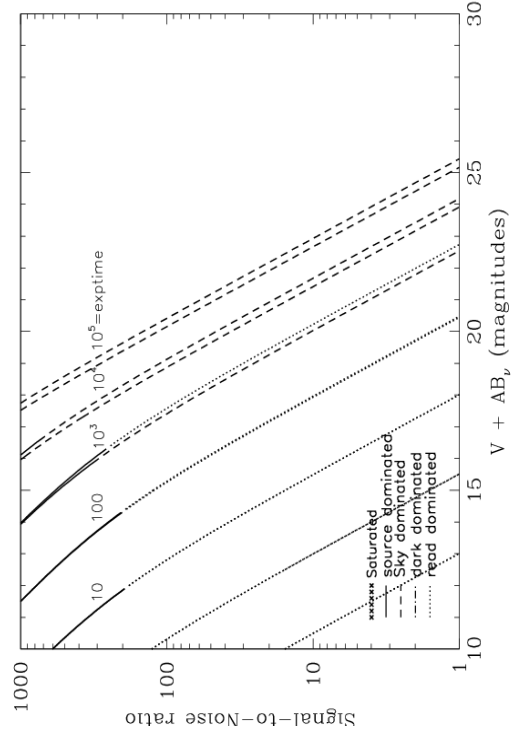


Figure 10.93: Extended source S/N vs. $V + AB_V$ for the HRC/F892N filter. Top curves are for low sky and bottom curves are for average sky for a 1 arcsec² area.



HRC/G800L

Description

Grism.

Figure 10.94: Integrated system throughput for HRC/G800L.

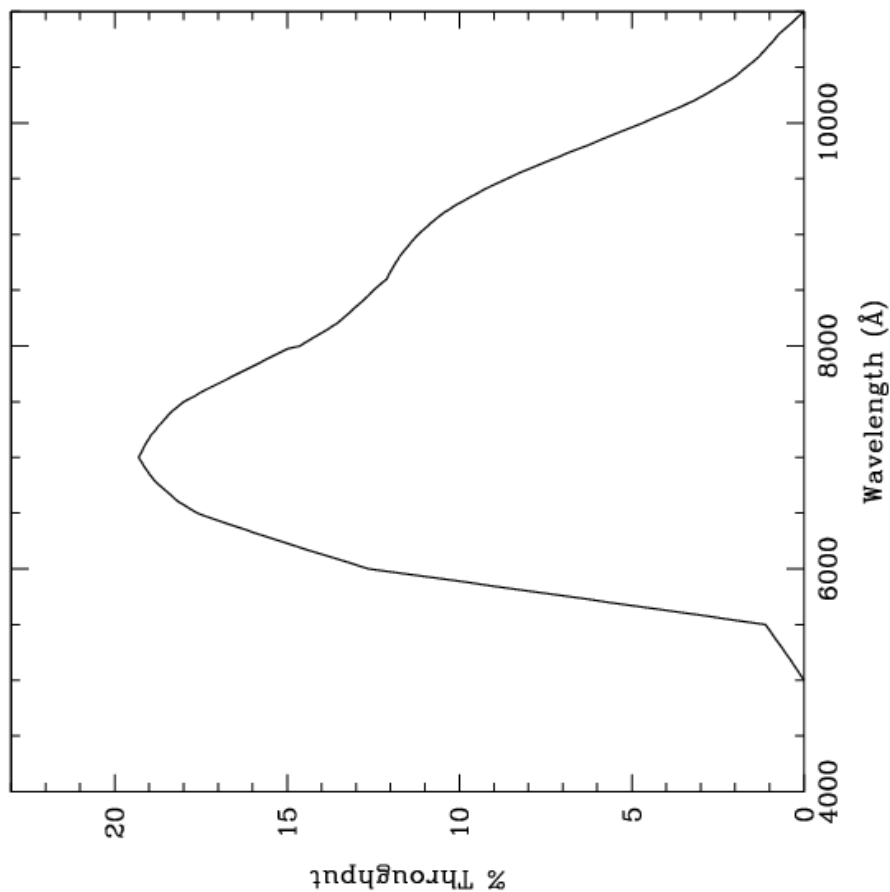


Figure 10.95: Point source S/N vs. $V + AB_V$ for the HRC/G800L filter. Top curves are for low sky; bottom curves are for average sky.

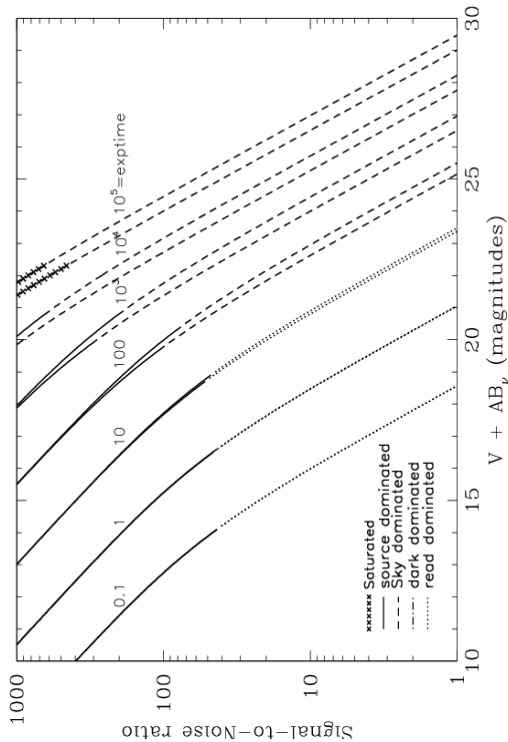
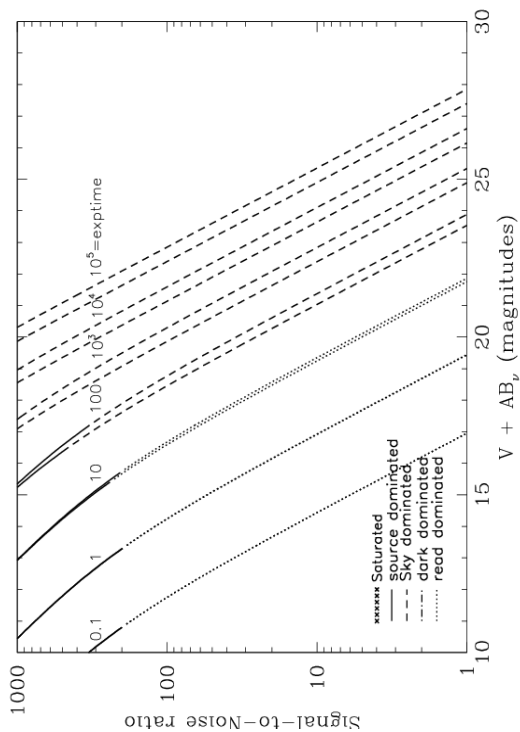


Figure 10.96: Extended source S/N vs. $V + AB_V$ for the HRC/G800L filter. Top curves are for low sky and bottom curves are for average sky for a 1 arcsec^2 area.



HRC/PR200L

Description

HRC Prism.

Figure 10.97: Integrated system throughput for HRC/PR200L.

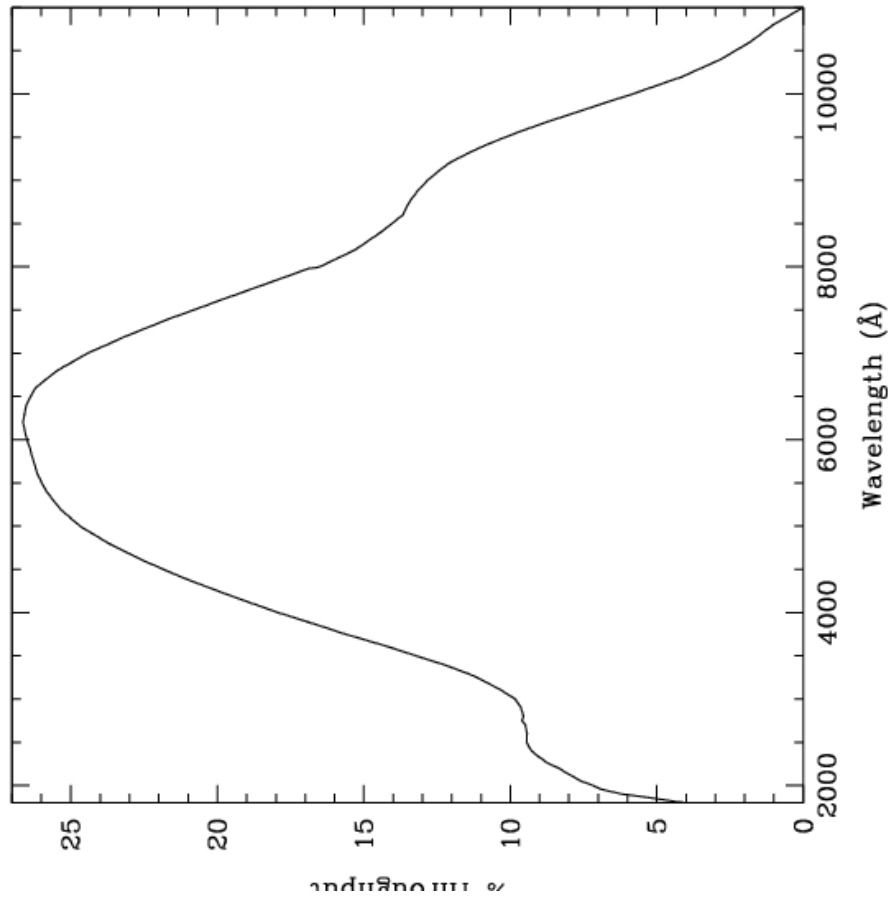


Figure 10.98: Point source S/N vs. $V+AB_V$ for the HRC/PR200L filter. Top curves are for low sky; bottom curves are for average sky.

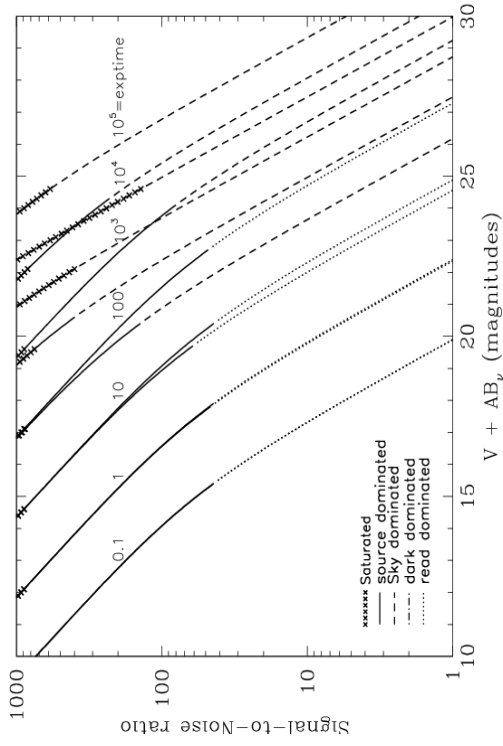
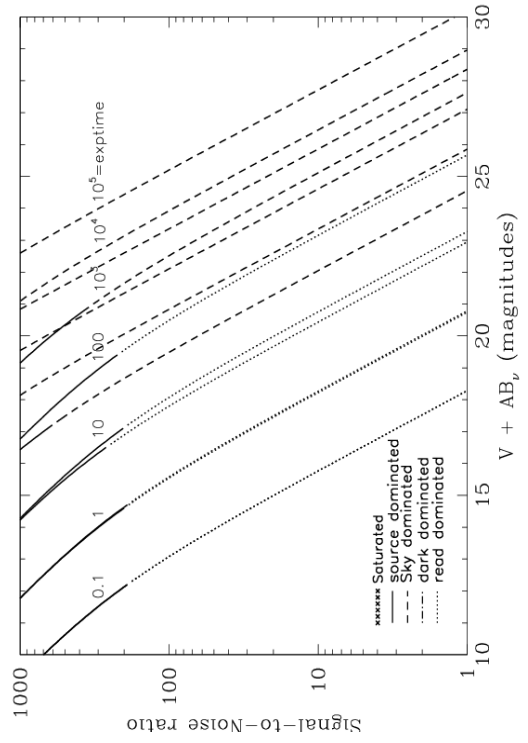


Figure 10.99: Extended source S/N vs. $V+AB_V$ for the HRC/PR200L filter. Top curves are for low sky and bottom curves are for average sky for a 1 arcsec^2 area.



HRC/CLEAR

Description
HRC Clear Filter.

Figure 10.100: Integrated system throughput for HRC/Clear

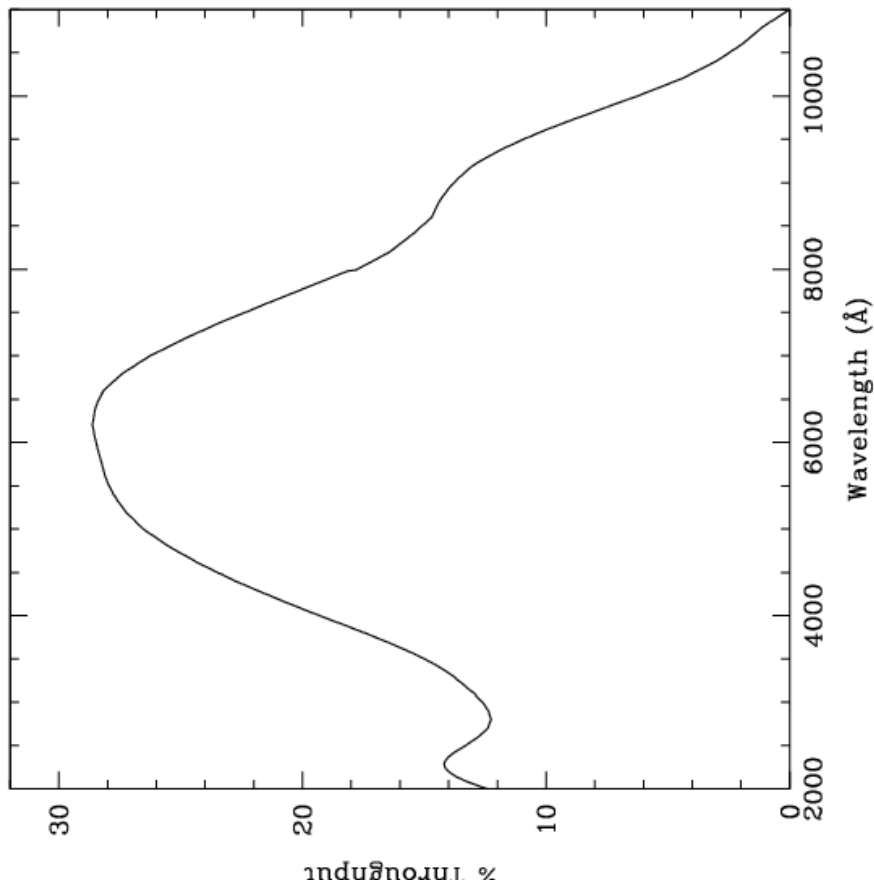


Figure 10.101: Point source S/N vs. $V+AB_V$ for the HRC/Clear filter. Top curves are for low sky; bottom curves are for average sky.

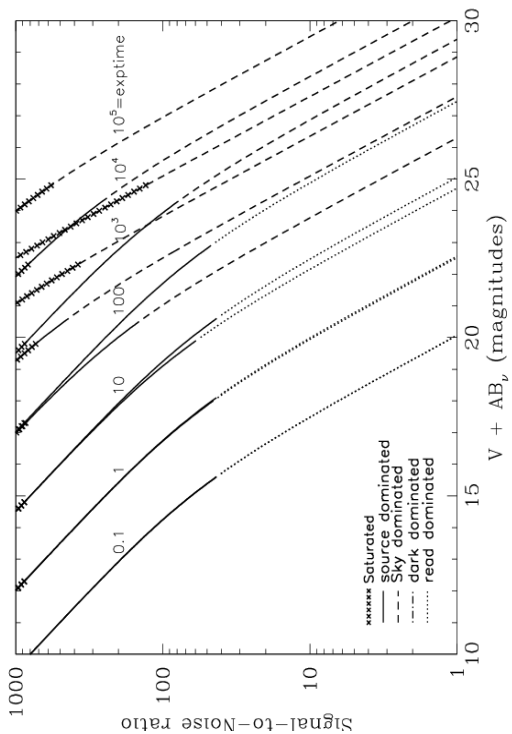
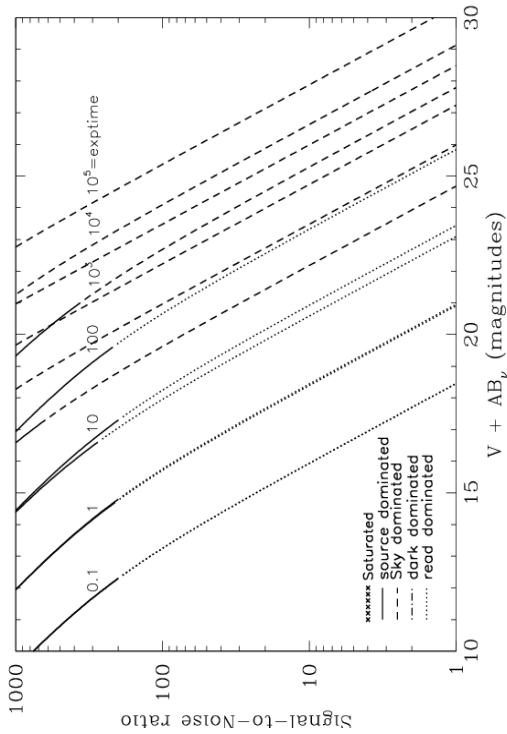


Figure 10.102: Extended source S/N vs. $V+AB_V$ for the HRC/Clear filter. Top curves are for low sky and bottom curves are for average sky for a 1 arcsec^2 area.



SBC/F115LP

Description

MgF₂ filter.

Figure 10.103: Integrated system throughput for SBC/F115LP.

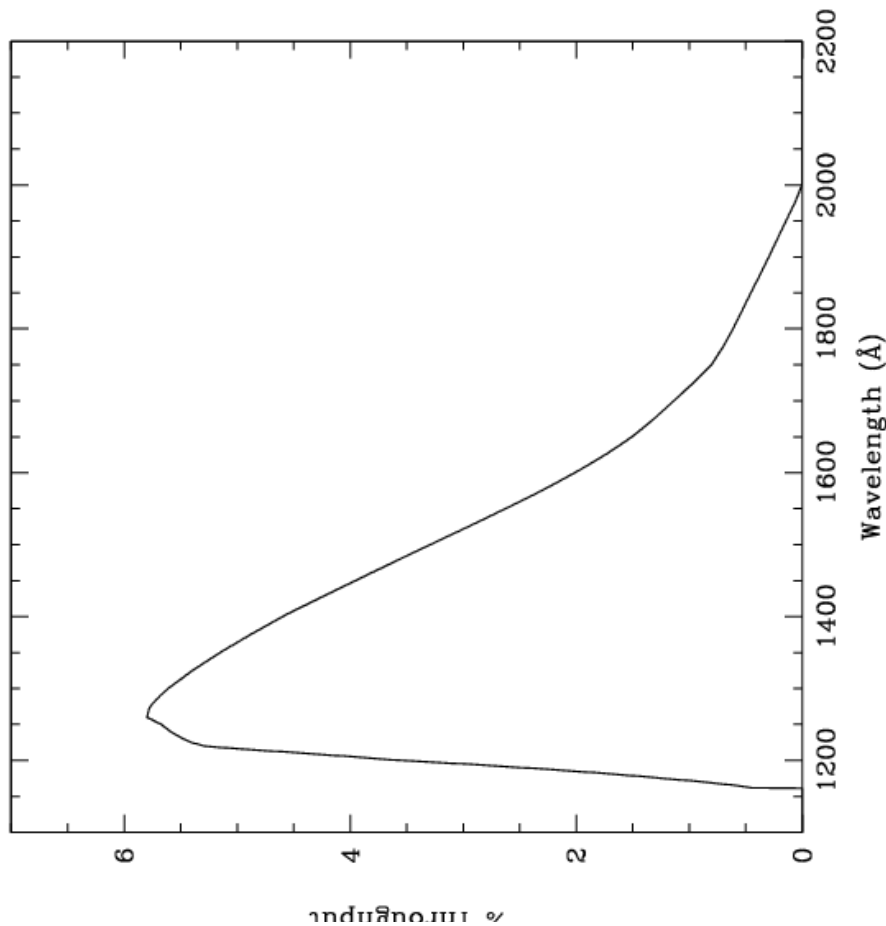


Figure 10.104: Point source S/N vs. $V+AB_V$ for the SBC/F115LP filter. Top curves are for low sky; bottom curves are for average sky.

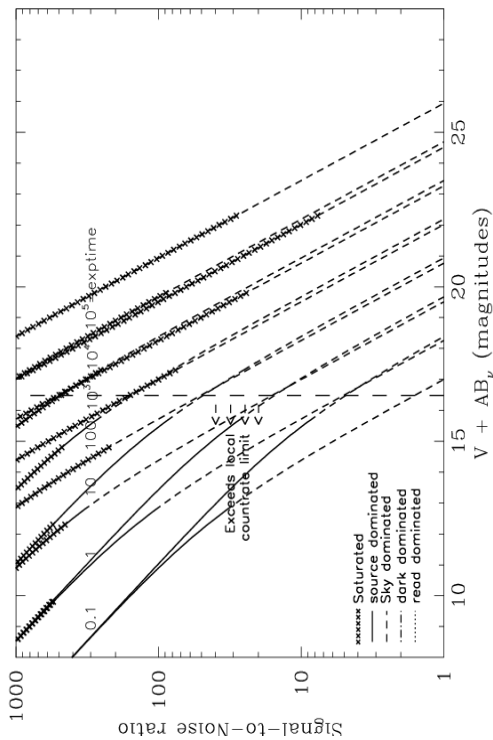
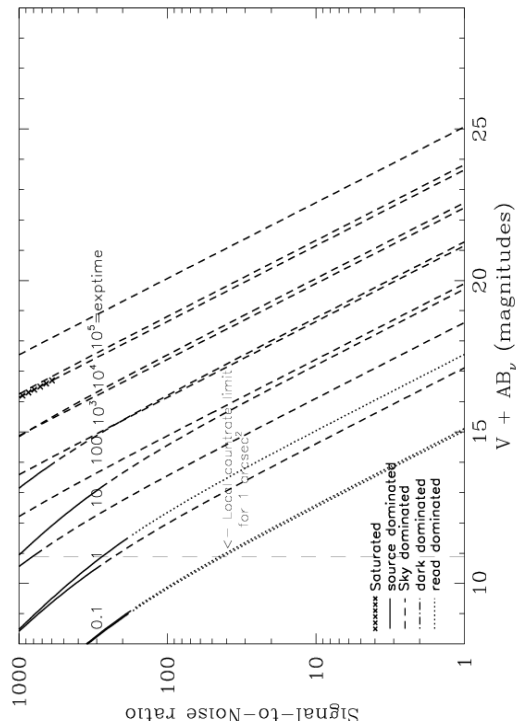


Figure 10.105: Extended source S/N vs. $V+AB_V$ for the SBC/F115LP filter. Top curves are for low sky and bottom curves are for average sky for a 1 arcsec² area.



SBC/F122M

Description

Lyman α filter.

Figure 10.106: Integrated system throughput for SBC/F122M.

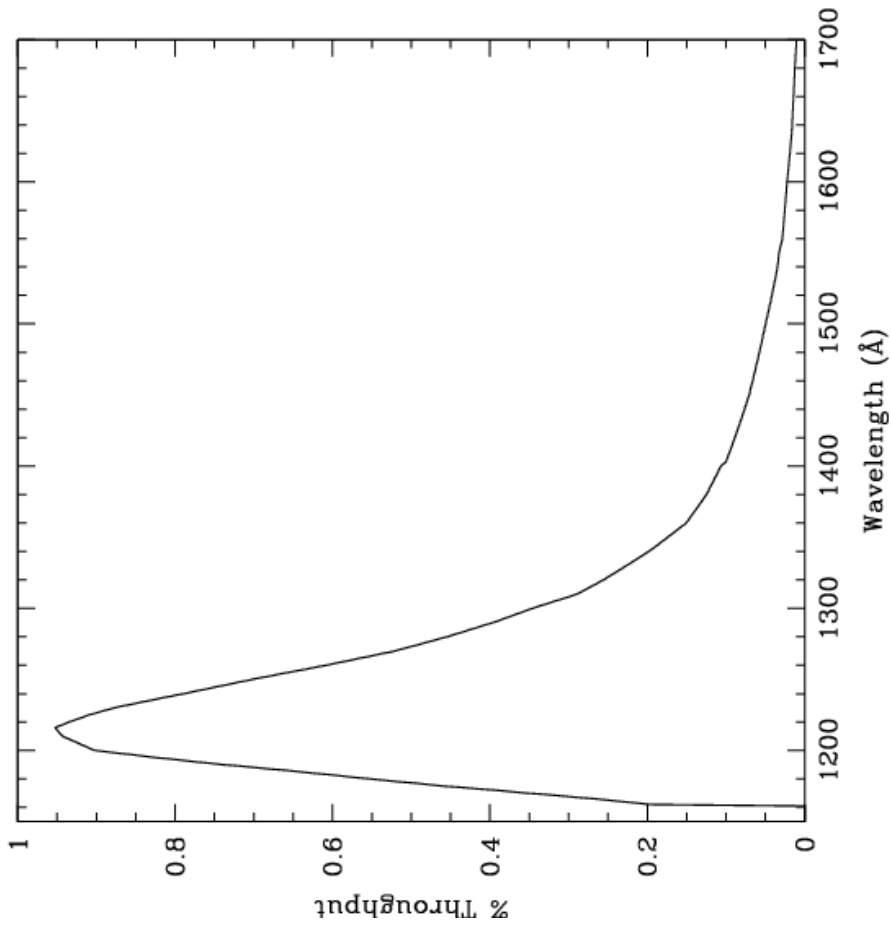


Figure 10.107: Point source S/N vs. $V+AB_V$ for the SBC/F122M filter. Top curves are for low sky; bottom curves are for average sky.

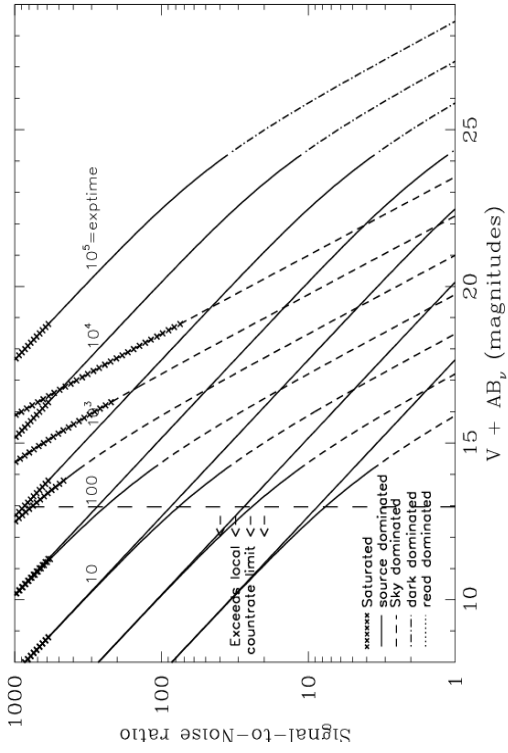
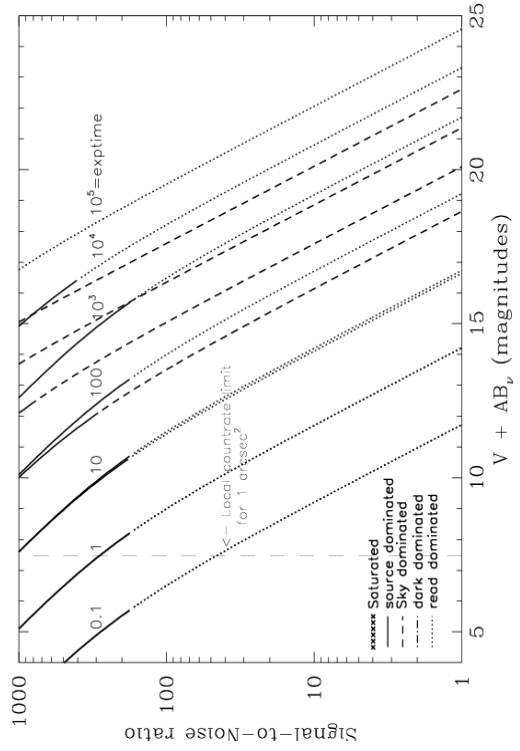


Figure 10.108: Extended source S/N vs. $V+AB_V$ for the SBC/F122M filter. Top curves are for low sky and bottom curves are for average sky for a 1 arcsec² area.



SBC/F125LP

Description

CaF₂ filter.

Figure 10.109: Integrated system throughput for SBC/F125LP.

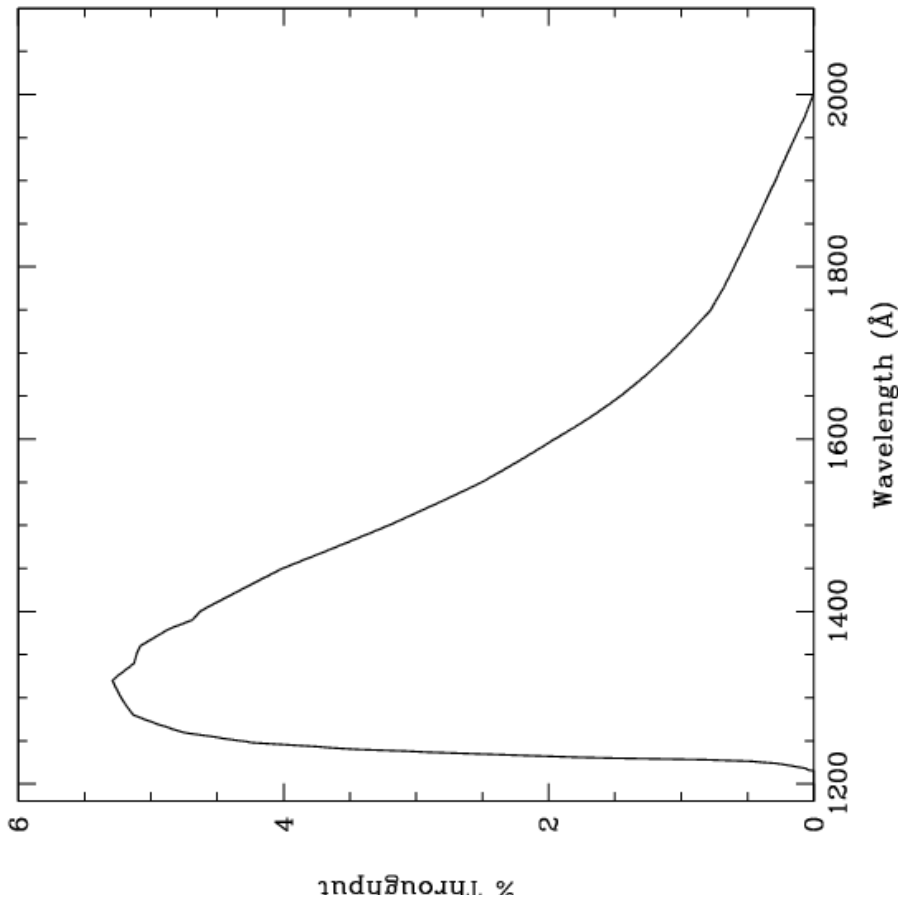


Figure 10.110: Point source S/N vs. $V+AB_V$ for the SBC/F125LP filter. Top curves are for low sky; bottom curves are for average sky.

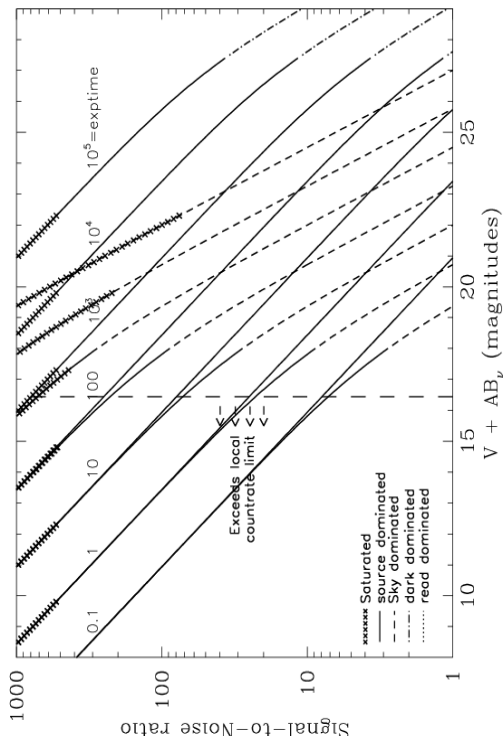
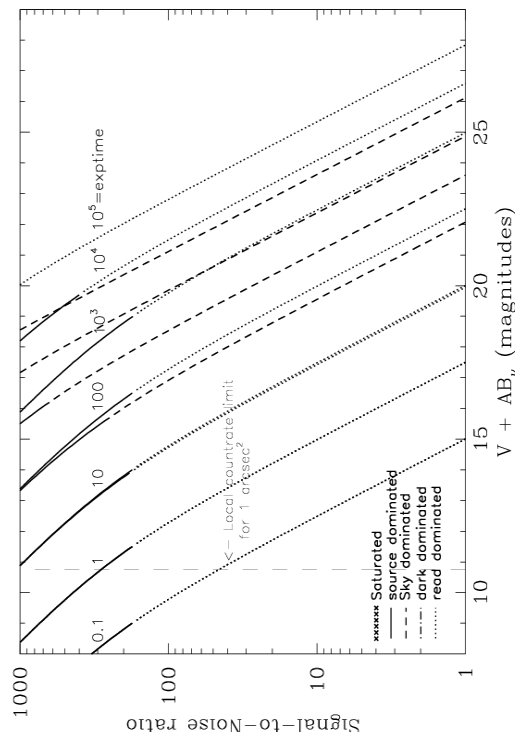


Figure 10.111: Extended source S/N vs. $V+AB_V$ for the SBC/F125LP filter. Top curves are for low sky and bottom curves are for average sky for a 1 arcsec² area.



SBC/F140LP

Description
BaF₂ filter.

Figure 10.112: Integrated system throughput for SBC/F140LP.

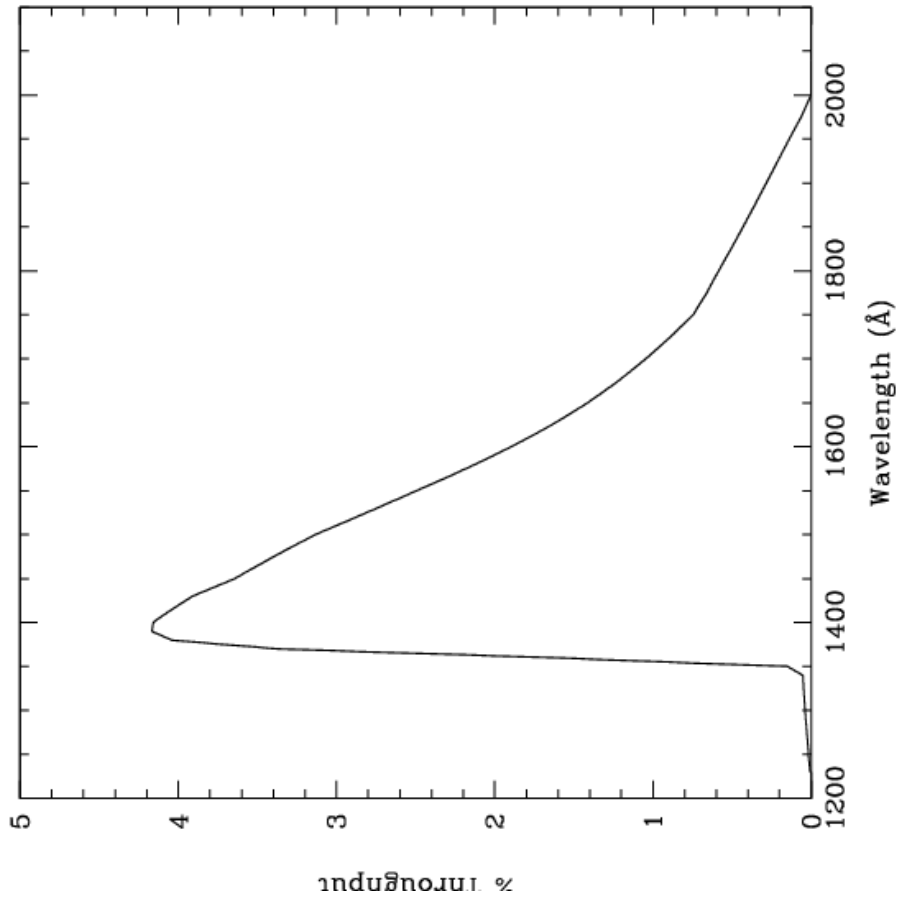


Figure 10.113: Point source S/N vs. $V+AB_V$ for the SBC/F140LP filter. Top curves are for low sky; bottom curves are for average sky.

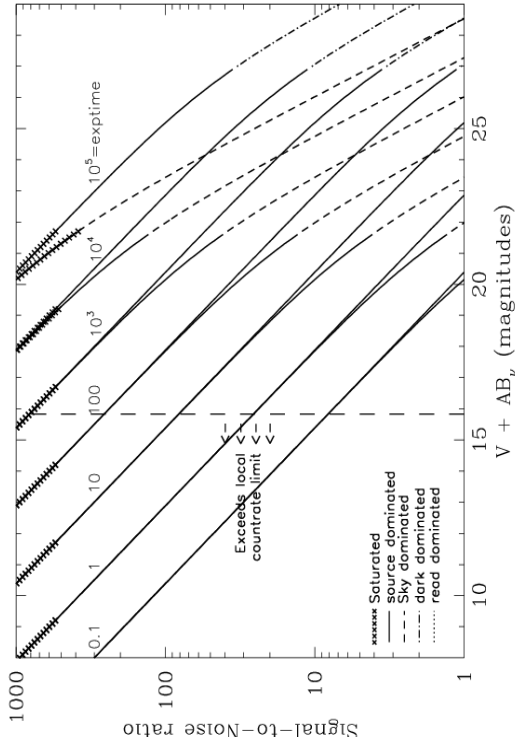
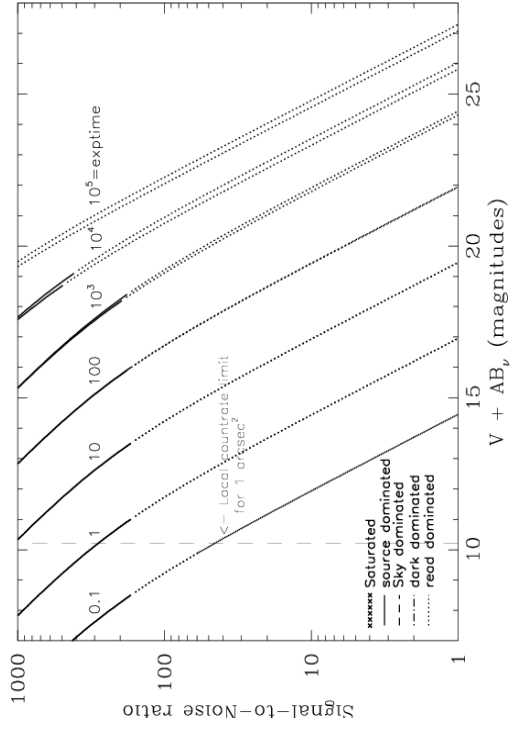


Figure 10.114: Extended source S/N vs. $V+AB_V$ for the SBC/F140LP filter. Top curves are for low sky and bottom curves are for average sky for a 1 arcsec² area.



SBC/F150LP

Description

Crystal Quartz filter.

Figure 10.115: Integrated system throughput for SBC/F165LP.

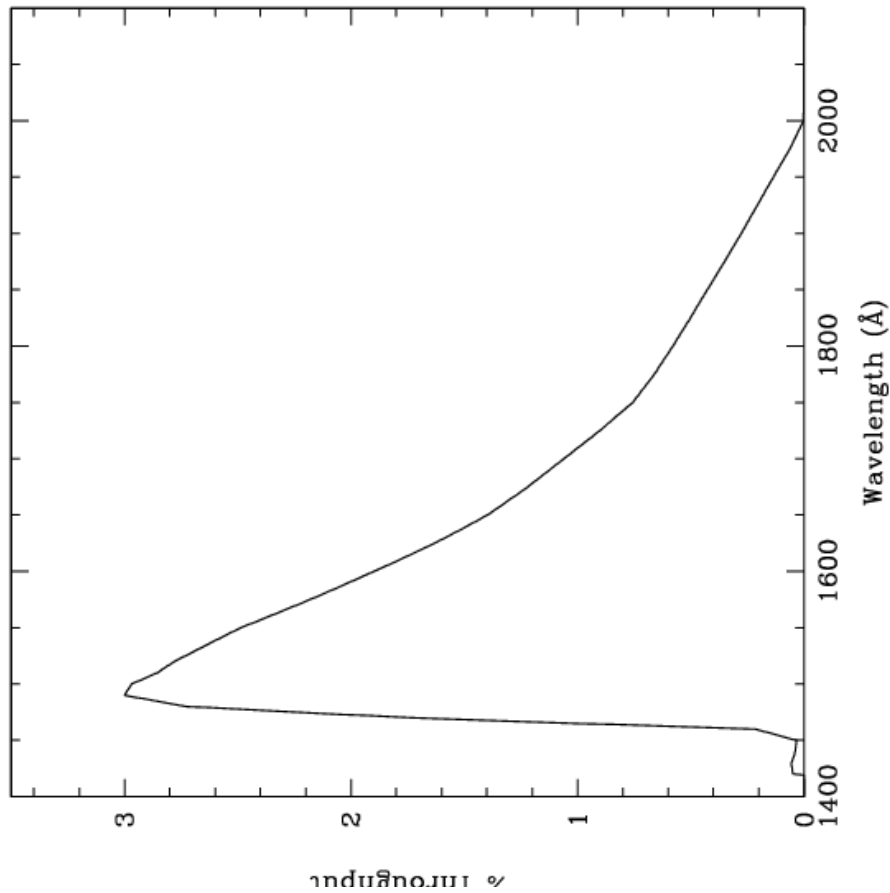


Figure 10.116: Point source S/N vs. $V+AB_V$ for the SBC/F150LP filter. Top curves are for low sky; bottom curves are for average sky.

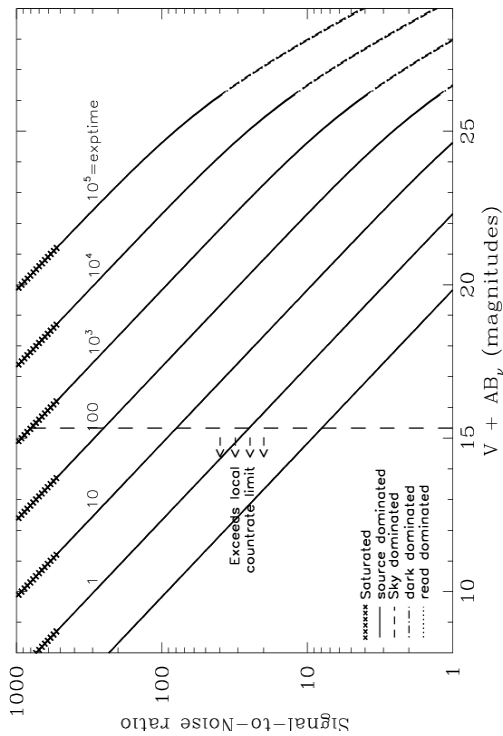
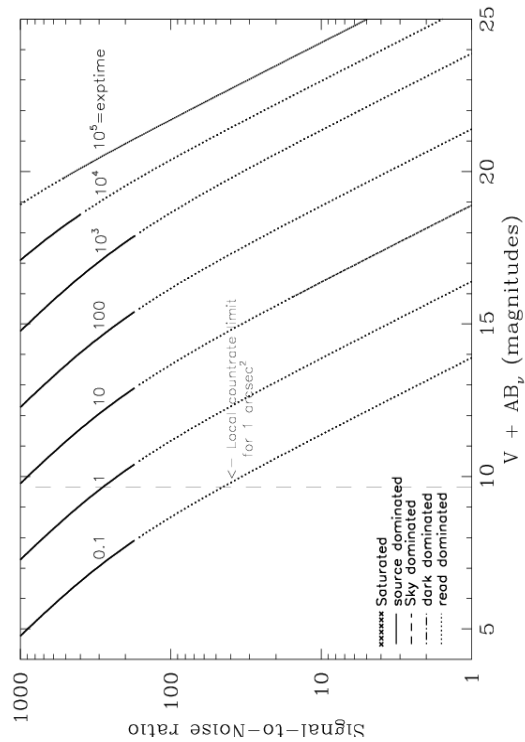


Figure 10.117: Extended source S/N vs. $V+AB_V$ for the SBC/F150LP filter. Top curves are for low sky and bottom curves are for average sky for a 1 arcsec^2 area.



SBC/F165LP

Description

Dynasil filter.

Figure 10.118: Integrated system throughput for SBC/F165LP.

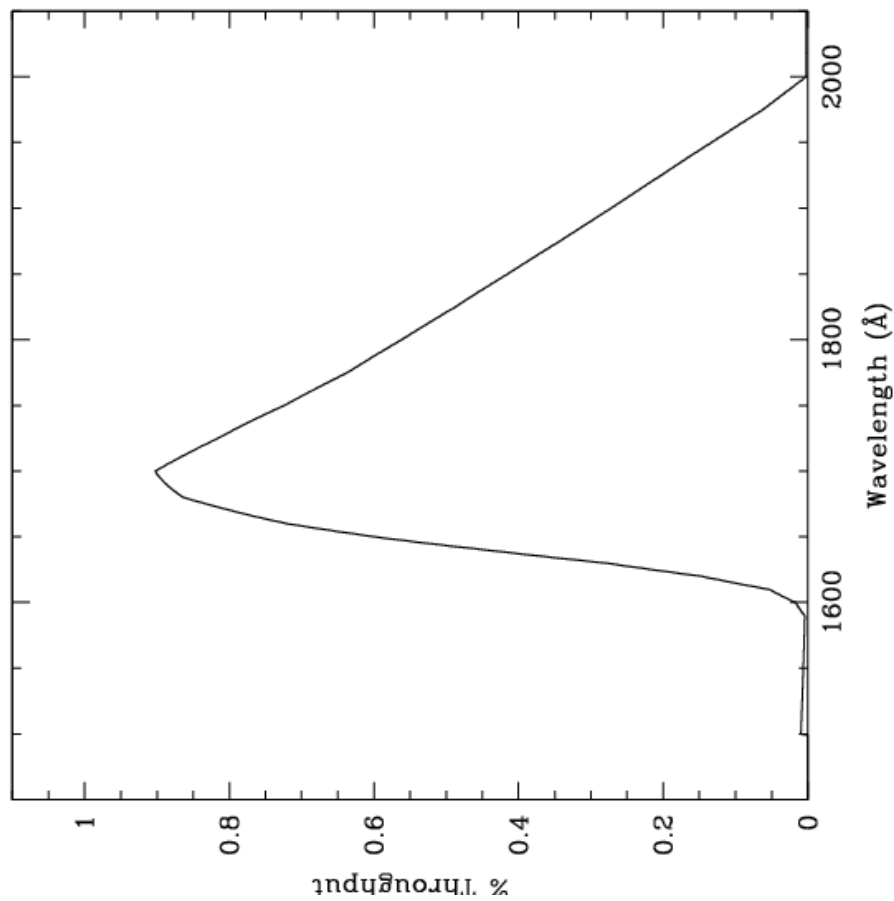


Figure 10.119: Point source S/N vs. $V+AB_V$ for the SBC/F165LP filter. Top curves are for low sky; bottom curves are for average sky.

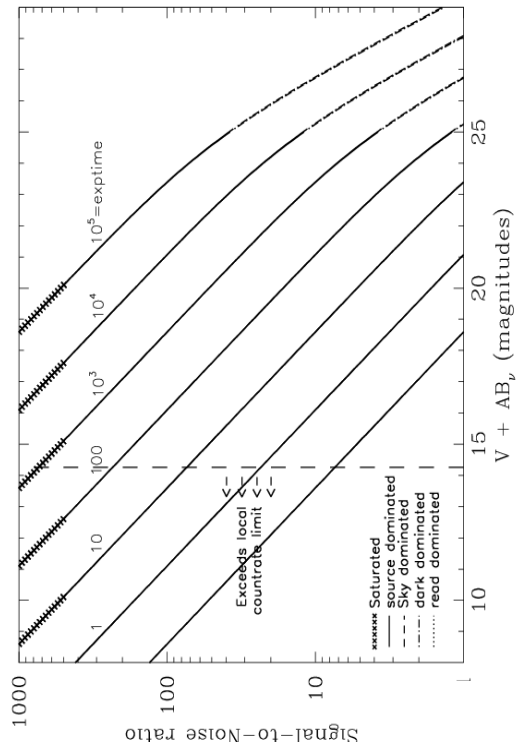
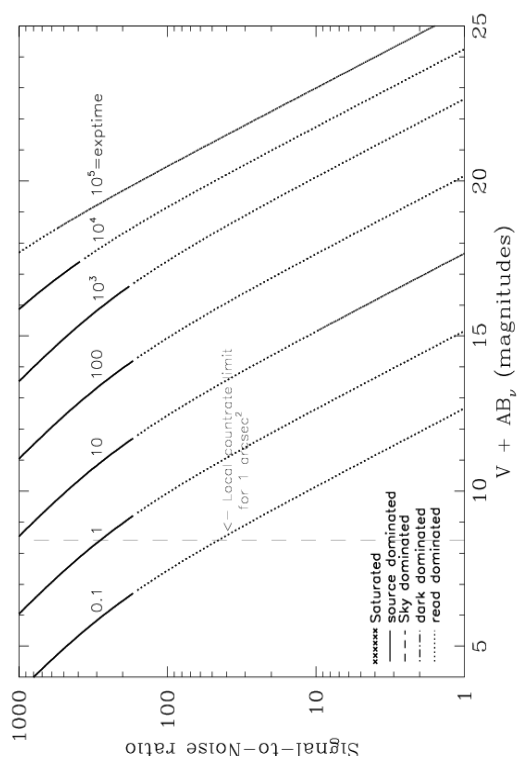


Figure 10.120: Extended source S/N vs. $V+AB_V$ for the SBC/F165LP filter. Top curves are for low sky and bottom curves are for average sky for a 1 arcsec^2 area.



SBC/PR110L

Description

LiF₂ Prism.

Figure 10.121: Integrated system throughput for SBC/PR110LP.

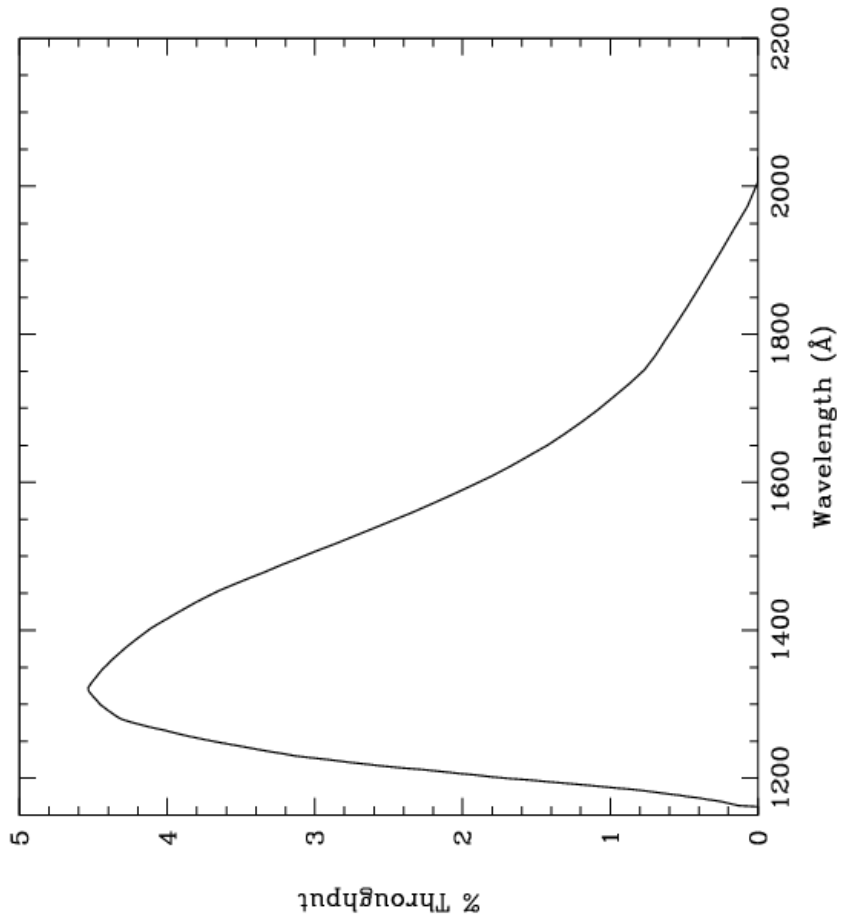


Figure 10.122: Point source S/N vs. $V+AB_V$ for the SBC/PR110LP filter. Top curves are for low sky; bottom curves are for average sky.

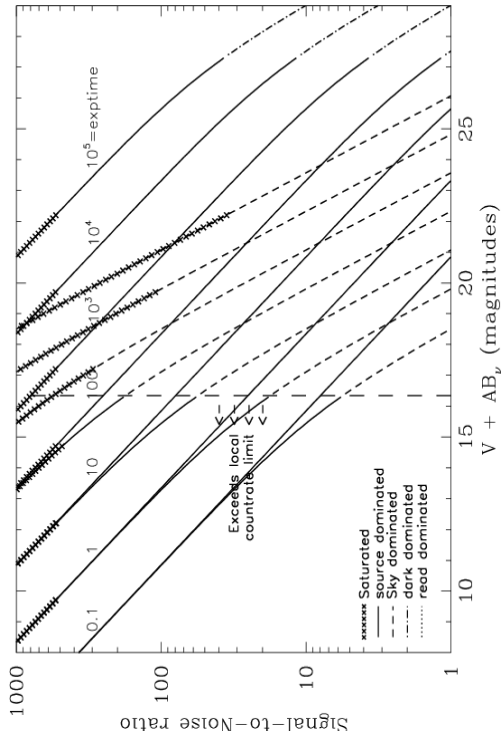
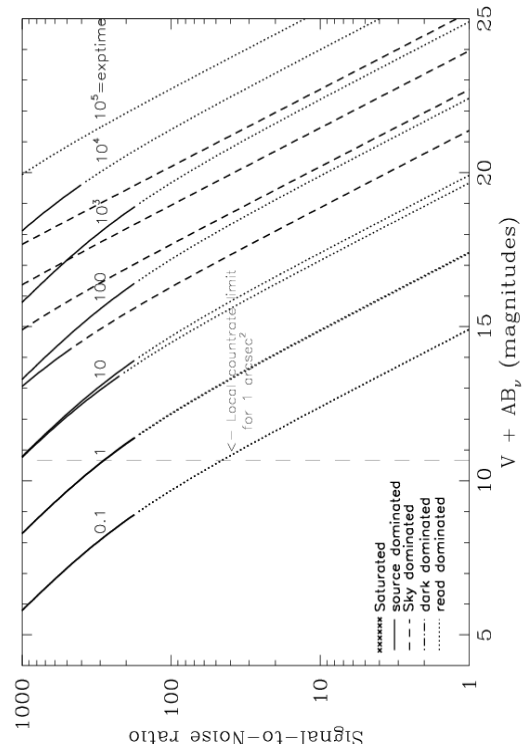


Figure 10.123: Extended source S/N vs. $V+AB_V$ for the SBC/PR110LP filter. Top curves are for low sky and bottom curves are for average sky for a 1 arcsec² area.



SBC/PR130L

Description

CaF₂ Prism.

Figure 10.124: Integrated system throughput for SBC/PR130LP.

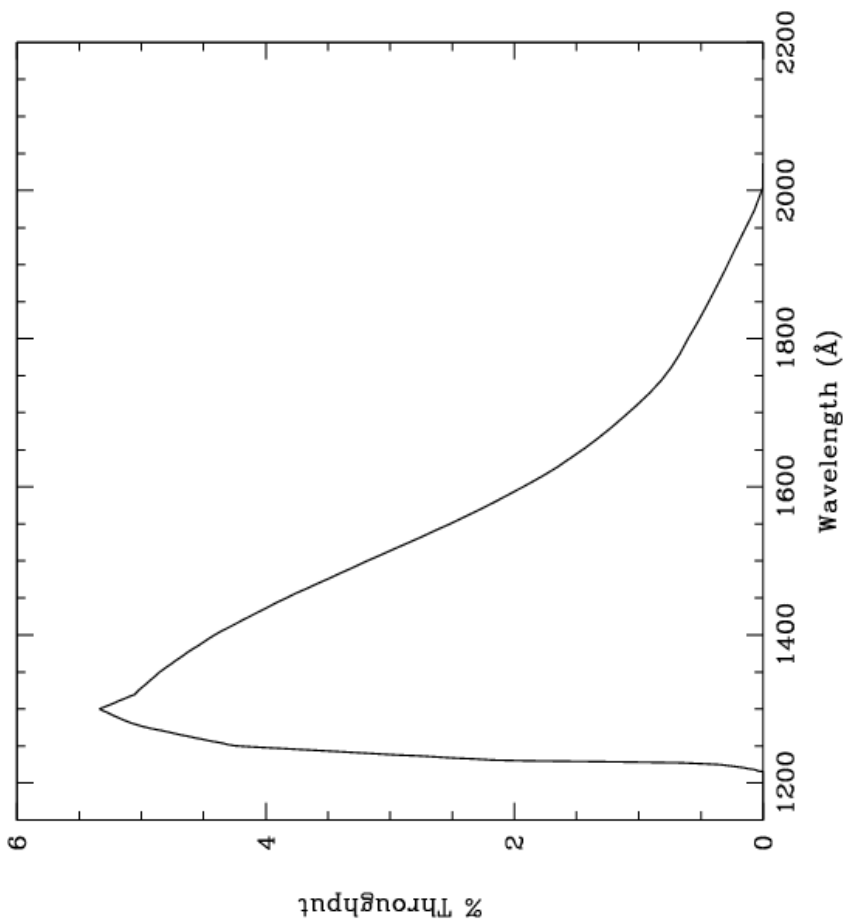


Figure 10.125: Point source S/N vs. $V+AB_V$ for the SBC/PR130LP filter. Top curves are for low sky; bottom curves are for average sky.

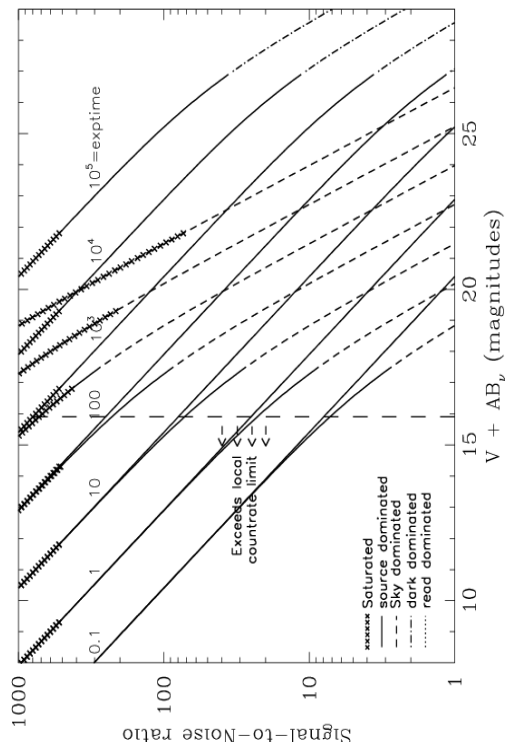


Figure 10.126: Extended source S/N vs. $V+AB_V$ for the SBC/PR130LP filter. Top curves are for low sky and bottom curves are for average sky for a 1 arcsec² area.

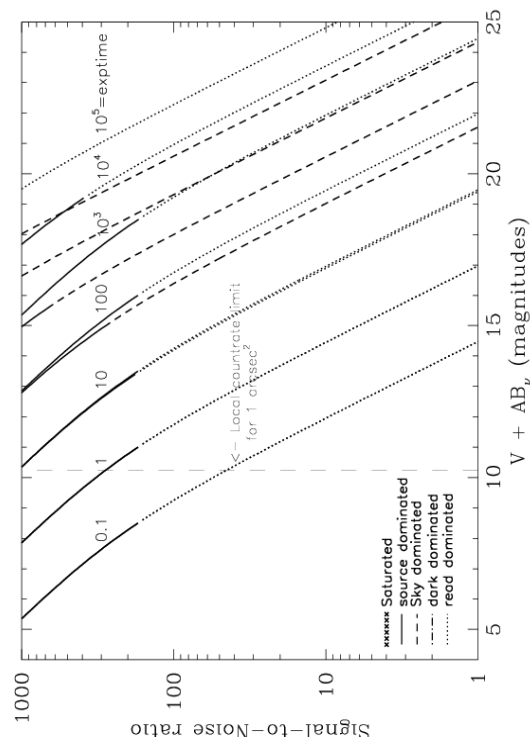


Table 10.1: Color corrections AB_V to go from Johnson V magnitude to AB magnitude for the WFC.

| Spectrum | F435W | F475W | F502N | F550M | F555W | F606W | F625W | F658N | F660N | F775W | F814W | F850LP | F892N | G800L | CLEAR |
|---|-------|-------|-------|-------|-------|-------|-------|-------|-------|-------|-------|--------|-------|-------|-------|
| AvgSky | 0.62 | 0.33 | 0.21 | -0.04 | 0.05 | -0.10 | -0.22 | -0.24 | -0.27 | -0.40 | -0.42 | -0.47 | -0.47 | -0.35 | -0.05 |
| LowSky | 0.52 | 0.26 | 0.14 | -0.03 | 0.03 | -0.07 | -0.15 | -0.18 | -0.20 | -0.26 | -0.27 | -0.30 | -0.31 | -0.23 | 0.00 |
| O5 V | -0.44 | -0.28 | -0.15 | 0.05 | -0.04 | 0.12 | 0.27 | 0.38 | 0.39 | 0.67 | 0.75 | 1.00 | 0.98 | 0.55 | 0.04 |
| B0 V | -0.43 | -0.28 | -0.17 | 0.06 | -0.04 | 0.12 | 0.29 | 0.40 | 0.39 | 0.64 | 0.71 | 0.94 | 0.92 | 0.54 | 0.04 |
| A0 V | -0.07 | -0.08 | -0.07 | 0.02 | 0.00 | 0.08 | 0.15 | 0.33 | 0.29 | 0.35 | 0.39 | 0.48 | 0.48 | 0.29 | 0.14 |
| A5 V | 0.04 | -0.01 | -0.03 | 0.00 | 0.00 | 0.06 | 0.10 | 0.22 | 0.16 | 0.23 | 0.25 | 0.31 | 0.30 | 0.19 | 0.13 |
| F2 V | 0.26 | 0.12 | 0.05 | -0.01 | 0.02 | 0.00 | -0.03 | 0.00 | -0.03 | -0.05 | -0.05 | -0.04 | -0.05 | -0.04 | 0.06 |
| G2 V | 0.54 | 0.28 | 0.14 | -0.03 | 0.04 | -0.07 | -0.16 | -0.16 | -0.17 | -0.30 | -0.31 | -0.34 | -0.34 | -0.26 | 0.00 |
| K0 V | 0.77 | 0.40 | 0.19 | -0.06 | 0.05 | -0.12 | -0.25 | -0.31 | -0.31 | -0.42 | -0.44 | -0.47 | -0.49 | -0.37 | -0.04 |
| M0 V | 1.41 | 0.80 | 0.67 | -0.14 | 0.11 | -0.33 | -0.59 | -0.84 | -0.84 | -1.21 | -1.31 | -1.55 | -1.52 | -1.09 | -0.53 |
| M6 V | 1.72 | 0.89 | 0.71 | -0.18 | 0.12 | -0.40 | -0.66 | -1.17 | -1.15 | -2.11 | -2.34 | -2.80 | -2.74 | -1.96 | -1.27 |
| O7 I | -0.40 | -0.25 | -0.13 | 0.04 | -0.03 | 0.11 | 0.25 | 0.35 | 0.35 | 0.63 | 0.70 | 0.94 | 0.92 | 0.52 | 0.05 |
| B0 I | -0.34 | -0.21 | -0.11 | 0.03 | -0.03 | 0.10 | 0.22 | 0.31 | 0.31 | 0.52 | 0.58 | 0.77 | 0.75 | 0.43 | 0.05 |
| F0 III | 0.19 | 0.07 | 0.00 | 0.00 | 0.01 | 0.01 | 0.01 | 0.06 | 0.03 | 0.06 | 0.06 | 0.07 | 0.05 | 0.04 | 0.10 |
| G0 III | 0.63 | 0.32 | 0.15 | -0.03 | 0.04 | -0.09 | -0.19 | -0.24 | -0.25 | -0.36 | -0.38 | -0.43 | -0.45 | -0.31 | -0.02 |
| K2 III | 1.13 | 0.57 | 0.33 | -0.07 | 0.07 | -0.19 | -0.37 | -0.48 | -0.48 | -0.68 | -0.72 | -0.83 | -0.89 | -0.60 | -0.17 |
| M0 III | 1.56 | 0.80 | 0.56 | -0.12 | 0.11 | -0.33 | -0.58 | -0.74 | -0.75 | -1.24 | -1.35 | -1.59 | -1.62 | -1.12 | -0.55 |
| M6 III | 1.65 | 0.92 | 1.19 | -0.12 | 0.18 | -0.64 | -0.95 | -1.20 | -1.15 | -2.91 | -3.24 | -3.89 | -3.74 | -2.83 | -2.10 |
| Elliptical | 0.95 | 0.51 | 0.34 | -0.07 | 0.07 | -0.19 | -0.36 | -0.48 | -0.48 | -0.81 | -0.92 | -1.07 | -1.18 | -0.72 | -0.27 |
| Sa | 0.80 | 0.45 | 0.30 | -0.06 | 0.07 | -0.18 | -0.36 | -0.54 | -0.51 | -0.75 | -0.84 | -0.94 | -1.05 | -0.66 | -0.24 |
| Sb | 0.81 | 0.44 | 0.27 | -0.06 | 0.06 | -0.18 | -0.34 | -0.50 | -0.48 | -0.75 | -0.85 | -0.97 | -1.09 | -0.66 | -0.24 |
| Sc | 0.08 | 0.00 | -0.71 | 0.07 | -0.03 | -0.17 | -0.26 | -1.76 | -0.84 | 0.40 | 0.77 | 1.67 | 1.26 | 0.20 | 0.08 |
| Starburst E(B-V) 0.51-0.60 | 0.41 | 0.24 | -0.02 | 0.00 | 0.04 | -0.22 | -0.39 | -1.38 | -0.87 | -0.59 | -0.67 | -0.75 | -0.80 | -0.56 | -0.23 |
| Starburst E(B-V)<0.1 | 0.23 | 0.05 | -0.96 | 0.09 | -0.03 | -0.10 | -0.14 | -1.16 | -0.35 | -0.15 | -0.19 | -0.18 | -0.23 | -0.16 | -0.03 |
| Sun | 0.58 | 0.30 | 0.17 | -0.03 | 0.04 | -0.07 | -0.17 | -0.17 | -0.20 | -0.26 | -0.27 | -0.27 | -0.28 | -0.23 | 0.01 |
| Vega | -0.12 | -0.11 | -0.07 | 0.02 | 0.00 | 0.08 | 0.16 | 0.35 | 0.32 | 0.39 | 0.43 | 0.56 | 0.49 | 0.32 | 0.14 |

Table 10.2: Color corrections AB_v to go from Johnson V magnitude to AB magnitude for the HRC.

| Spectrum | F220W | F250W | F330W | F344N | F435W | F475W | F502N | F550M | F555W | F606W | F625W | F658N | F660N | F775W | F814W | F850LP | F892N | G800L | PR200L | Clear |
|----------------------------------|-------|-------|-------|-------|-------|-------|-------|-------|-------|-------|-------|-------|-------|-------|-------|--------|-------|-------|--------|-------|
| AvgSky | 3.56 | 2.58 | 2.01 | 1.89 | 0.63 | 0.32 | 0.21 | -0.04 | 0.05 | -0.09 | -0.22 | -0.24 | -0.27 | -0.39 | -0.42 | -0.47 | -0.47 | -0.35 | 0.21 | 0.29 |
| LowSky | 5.31 | 3.37 | 1.84 | 1.72 | 0.65 | 0.33 | 0.22 | -0.04 | 0.05 | -0.11 | -0.24 | -0.27 | -0.30 | -0.45 | -0.48 | -0.55 | -0.30 | -0.39 | 0.18 | 0.26 |
| O5 V | -1.53 | -1.24 | -0.86 | -0.81 | -0.44 | -0.26 | -0.15 | 0.04 | -0.04 | 0.11 | 0.27 | 0.38 | 0.39 | 0.66 | 0.76 | 1.02 | 0.98 | 0.55 | -0.45 | -0.57 |
| B0 V | -1.16 | -0.98 | -0.72 | -0.69 | -0.44 | -0.27 | -0.17 | 0.06 | -0.04 | 0.11 | 0.28 | 0.40 | 0.39 | 0.63 | 0.72 | 0.96 | 0.92 | 0.54 | -0.31 | -0.41 |
| A0 V | 1.75 | 1.54 | 1.19 | 1.16 | -0.06 | -0.08 | -0.07 | 0.02 | 0.00 | 0.07 | 0.15 | 0.33 | 0.29 | 0.35 | 0.39 | 0.48 | 0.48 | 0.29 | 0.33 | 0.39 |
| A5 V | 2.60 | 2.15 | 1.41 | 1.35 | 0.05 | -0.01 | -0.03 | 0.00 | 0.00 | 0.05 | 0.10 | 0.22 | 0.16 | 0.23 | 0.25 | 0.31 | 0.29 | 0.19 | 0.36 | 0.43 |
| F2 V | 3.49 | 2.52 | 1.45 | 1.35 | 0.27 | 0.11 | 0.05 | -0.01 | 0.02 | 0.00 | -0.03 | 0.00 | -0.03 | -0.05 | -0.05 | -0.04 | -0.05 | -0.04 | 0.31 | 0.38 |
| G2 V | 5.66 | 3.29 | 1.63 | 1.63 | 0.55 | 0.26 | 0.14 | -0.03 | 0.04 | -0.06 | -0.15 | -0.16 | -0.17 | -0.30 | -0.31 | -0.34 | -0.34 | -0.26 | 0.25 | 0.33 |
| K0 V | 6.82 | 4.47 | 2.39 | 2.26 | 0.78 | 0.38 | 0.19 | -0.06 | 0.05 | -0.11 | -0.24 | -0.31 | -0.31 | -0.42 | -0.44 | -0.47 | -0.49 | -0.37 | 0.23 | 0.31 |
| M0 V | 7.73 | 5.93 | 3.90 | 3.76 | 1.40 | 0.76 | 0.67 | -0.14 | 0.12 | -0.31 | -0.58 | -0.84 | -0.84 | -1.20 | -1.32 | -1.57 | -1.52 | -1.09 | -0.24 | -0.15 |
| M6 V | 7.30 | 6.31 | 4.31 | 4.23 | 1.71 | 0.84 | 0.71 | -0.18 | 0.13 | -0.37 | -0.65 | -1.17 | -1.15 | -2.09 | -2.37 | -2.83 | -2.75 | -1.98 | -0.99 | -0.90 |
| O7 I | -0.33 | -0.55 | -0.60 | -0.56 | -0.40 | -0.24 | -0.13 | 0.04 | -0.03 | 0.10 | 0.25 | 0.35 | 0.35 | 0.62 | 0.71 | 0.96 | 0.92 | 0.51 | -0.11 | -0.14 |
| B0 I | -0.72 | -0.69 | -0.55 | -0.54 | -0.34 | -0.20 | -0.11 | 0.03 | -0.03 | 0.09 | 0.22 | 0.31 | 0.31 | 0.51 | 0.59 | 0.78 | 0.75 | 0.43 | -0.15 | -0.21 |
| F0 III | 3.69 | 2.75 | 1.58 | 1.47 | 0.20 | 0.06 | 0.00 | 0.00 | 0.01 | 0.01 | 0.01 | 0.06 | 0.03 | 0.06 | 0.06 | 0.07 | 0.05 | 0.04 | 0.34 | 0.42 |
| G0 III | 6.58 | 4.21 | 2.24 | 2.13 | 0.63 | 0.31 | 0.15 | -0.03 | 0.04 | -0.08 | -0.19 | -0.24 | -0.25 | -0.36 | -0.38 | -0.43 | -0.45 | -0.31 | 0.24 | 0.32 |
| K2 III | 8.43 | 6.56 | 3.78 | 3.56 | 1.13 | 0.54 | 0.33 | -0.07 | 0.07 | -0.17 | -0.36 | -0.48 | -0.48 | -0.67 | -0.73 | -0.84 | -0.89 | -0.60 | 0.11 | 0.19 |
| M0 III | 7.71 | 7.02 | 5.14 | 5.01 | 1.55 | 0.76 | 0.56 | -0.11 | 0.12 | -0.31 | -0.57 | -0.74 | -0.75 | -1.23 | -1.36 | -1.61 | -1.62 | -1.12 | -0.25 | -0.17 |
| M6 III | 6.27 | 6.17 | 4.45 | 4.28 | 1.67 | 0.89 | 1.19 | -0.12 | 0.18 | -0.60 | -0.93 | -1.20 | -1.15 | -2.88 | -3.29 | -3.93 | -3.74 | -2.87 | -1.83 | -1.75 |
| Elliptical | 5.20 | 4.63 | 2.82 | 2.63 | 0.95 | 0.48 | 0.34 | -0.07 | 0.07 | -0.17 | -0.36 | -0.48 | -0.48 | -0.80 | -0.93 | -1.08 | -1.18 | -0.72 | 0.01 | 0.09 |
| Sa | 4.35 | 3.53 | 2.38 | 2.34 | 0.80 | 0.43 | 0.30 | -0.06 | 0.07 | -0.17 | -0.35 | -0.54 | -0.51 | -0.75 | -0.85 | -0.94 | -1.05 | -0.66 | 0.03 | 0.11 |
| Sb | 3.73 | 3.10 | 2.11 | 2.16 | 0.81 | 0.42 | 0.27 | -0.06 | 0.07 | -0.17 | -0.34 | -0.50 | -0.48 | -0.74 | -0.86 | -0.98 | -1.09 | -0.66 | 0.02 | 0.10 |
| Sc | 2.09 | 1.15 | 0.15 | -0.07 | 0.07 | -0.01 | -0.70 | 0.07 | -0.03 | -0.17 | -0.25 | -1.76 | -0.85 | 0.34 | 0.77 | 12.85 | 9.95 | 0.19 | 0.22 | 0.285 |
| Starburst E(B-V) 0.51-0.60 | 1.82 | 1.63 | 1.13 | 1.14 | 0.41 | 0.23 | -0.02 | 0.00 | 0.04 | -0.21 | -0.38 | -1.38 | -0.87 | -0.59 | -0.68 | -0.76 | -0.80 | -0.57 | 0.00 | 0.05 |
| Starburst E(B-V)<0.1 | 0.98 | 0.95 | 0.81 | 0.80 | 0.22 | 0.04 | -0.96 | 0.09 | -0.03 | -0.10 | -0.14 | -1.16 | -0.35 | -0.15 | -0.20 | -0.18 | -0.23 | -0.16 | 0.11 | 0.16 |
| Sun | 5.67 | 3.55 | 1.83 | 1.72 | 0.58 | 0.28 | 0.17 | -0.03 | 0.04 | -0.06 | -0.16 | -0.17 | -0.20 | -0.26 | -0.27 | -0.27 | -0.28 | -0.23 | 0.27 | 0.36 |
| Vega | 1.65 | 1.48 | 1.18 | 1.14 | -0.10 | -0.10 | -0.07 | 0.02 | 0.00 | 0.08 | 0.16 | 0.35 | 0.32 | 0.38 | 0.44 | 0.56 | 0.49 | 0.32 | 0.33 | 0.39 |

Table 10.3: Color corrections AB_V to go from Johnson V magnitude to AB magnitude for the SBC.

| Spectrum | F115LP | F122M | F125LP | F140LP | F150LP | F165LP | PR110L | PR130L |
|---------------------------------------|--------|-------|--------|--------|--------|--------|--------|--------|
| AvgSky | 12.00 | 14.41 | 11.83 | 11.23 | 10.60 | 9.25 | 11.81 | 11.81 |
| LowSky | -1.78 | -2.95 | 2.73 | 6.80 | 10.34 | 9.00 | -1.27 | 2.69 |
| O5 V | -2.07 | -2.18 | -2.04 | -1.96 | -1.91 | -1.82 | -2.05 | -2.04 |
| B0 V | -1.64 | -1.53 | -1.69 | -1.67 | -1.63 | -1.54 | -1.66 | -1.69 |
| A0 V | 2.65 | 3.88 | 2.47 | 2.09 | 1.91 | 1.82 | 2.51 | 2.46 |
| A5 V | 5.41 | 7.44 | 5.24 | 4.65 | 4.05 | 3.14 | 5.23 | 5.22 |
| F2 V | 7.91 | 10.17 | 7.74 | 7.14 | 6.51 | 5.18 | 7.72 | 7.71 |
| G2 V | 13.82 | 16.35 | 13.65 | 13.05 | 12.42 | 11.07 | 13.63 | 13.63 |
| K0 V | 10.07 | 10.43 | 10.00 | 9.79 | 9.61 | 9.31 | 10.01 | 9.99 |
| M0 V | 11.58 | 11.94 | 11.50 | 11.29 | 11.11 | 10.81 | 11.51 | 11.49 |
| M6 V | 12.06 | 12.42 | 11.98 | 11.77 | 11.59 | 11.29 | 11.99 | 11.97 |
| O7 I | -0.57 | -0.42 | -0.61 | -0.68 | -0.70 | -0.71 | -0.59 | -0.61 |
| B0 I | -0.80 | -0.61 | -0.87 | -0.83 | -0.78 | -0.75 | -0.82 | -0.86 |
| F0 III | 7.81 | 10.09 | 7.63 | 7.04 | 6.41 | 5.07 | 7.62 | 7.61 |
| G0 III | 9.80 | 10.16 | 9.72 | 9.52 | 9.34 | 9.03 | 9.74 | 9.72 |
| K2 III | 13.32 | 13.68 | 13.24 | 13.04 | 12.86 | 12.55 | 13.26 | 13.24 |
| M0 III | 11.07 | 11.42 | 10.99 | 10.78 | 10.60 | 10.30 | 11.00 | 10.98 |
| M6 III | 10.37 | 10.73 | 10.29 | 10.09 | 9.91 | 9.61 | 10.31 | 10.29 |
| Elliptical | 6.24 | 6.71 | 6.11 | 6.08 | 5.98 | 5.90 | 6.18 | 6.10 |
| Sa | 5.66 | 6.23 | 5.52 | 5.42 | 5.27 | 5.06 | 5.59 | 5.52 |
| Sb | 4.63 | 5.18 | 4.49 | 4.38 | 4.27 | 4.24 | 4.56 | 4.49 |
| Sc | 2.87 | 3.52 | 2.71 | 2.60 | 2.45 | 2.32 | 2.78 | 2.71 |
| Starburst E(B-V) 0.51-0.60 | 2.68 | 3.31 | 2.52 | 2.44 | 2.35 | 2.13 | 2.60 | 2.52 |
| Starburst E(B-V)<0.1 | 1.33 | 1.88 | 1.18 | 1.13 | 1.09 | 1.06 | 1.25 | 1.18 |
| Sun | 12.00 | 11.78 | 12.29 | 11.79 | 11.21 | 10.02 | 12.02 | 12.28 |
| Vega | 2.74 | 3.95 | 2.56 | 2.20 | 2.04 | 1.91 | 2.61 | 2.56 |

10.3 Distortion in the ACS

The ACS detectors exhibit more distortion than previous HST instruments. The principal reason for this is that the optics have been designed with a minimum number of components, consistent with correcting for the spherical aberration induced by the OTA, without introducing coma. The result is a high throughput, but focal surfaces far from normal to the principal rays. The WFC detector is tilted at 22 deg giving an elongation of 8% while the HRC and SBC have a 25° tilt leading to an elongation of 12%. In each case, the scales in arcseconds per pixel are smaller along the radial direction of the OTA (Optical Telescope Assembly) field of view than along the tangential direction.

The orientations of the ACS detector edges are approximately in line with the V2 and V3 coordinate axes of the telescope. Consequently, the eigenaxes of the scale transformation are along the diagonals for WFC, and the apertures and pixels appear non-rectangular in the sky projection. For the HRC and SBC the situation is even more irregular because the aperture diagonals do not lie along a radius of the HST field of view. Figure 7.8 shows the ACS apertures in the telescope's V2V3 reference frame. For a telescope roll angle of zero this would correspond to an on-sky view with the V3 axis aligned with North and the V2 with East.

There is not only a strong geometric distortion of ACS detectors but a significant variation of the scale across each detector. For the WFC the scale is changing in amount of 10% from corner to corner. For the HRC and SBC this variation is only about 1% as they cover much smaller fields of view. The area on the sky covered by a WFC pixel varies by about 18% from corner to corner, corrections for which must be made in photometry of extended objects. This variation of scale creates a problematic effect in combining ACS images by the fact that an integral pixel shift near the center of the detector will translate into a non-integral displacement for pixels near the edges. This will imply some computational complexity in accurate alignment in order to combine images and will depend on the accuracy of the geometric distortion model.

Accurate geometric distortion corrections for the WFC and HRC detectors by Anderson & King (Anderson & King, 2002,2004,2006) were derived from observations of the globular cluster 47 Tuc, with multiple pointings and orientations, and through the F475W filter. The geometric distortion models for each of the WFC chips and the HRC detector are expressed in a 4th order polynomial and filter dependent look-up tables. The solution for both cameras is accurate to 0.01 pixels. The coefficients of the 4th order polynomial the filter dependent look-up tables as well as correction images are installed in the ACS on-the-fly re-calibration (OTFR) pipeline and could be used independently in IRAF task CALACS.

Additionally, an area of the open cluster NGC188, for which accurate astrometry is available, was used to establish the exact location and orientation of the aperture in telescope coordinates. At the same time, the scale factors were confirmed.

For the SBC, the geometric distortion was derived using the observation of globular cluster NGC6681 taken through F125LP. The alignment was established by observing the same globular cluster with the HRC and SBC consecutively to establish the relative locations. The SBC position was derived from the HRC position.

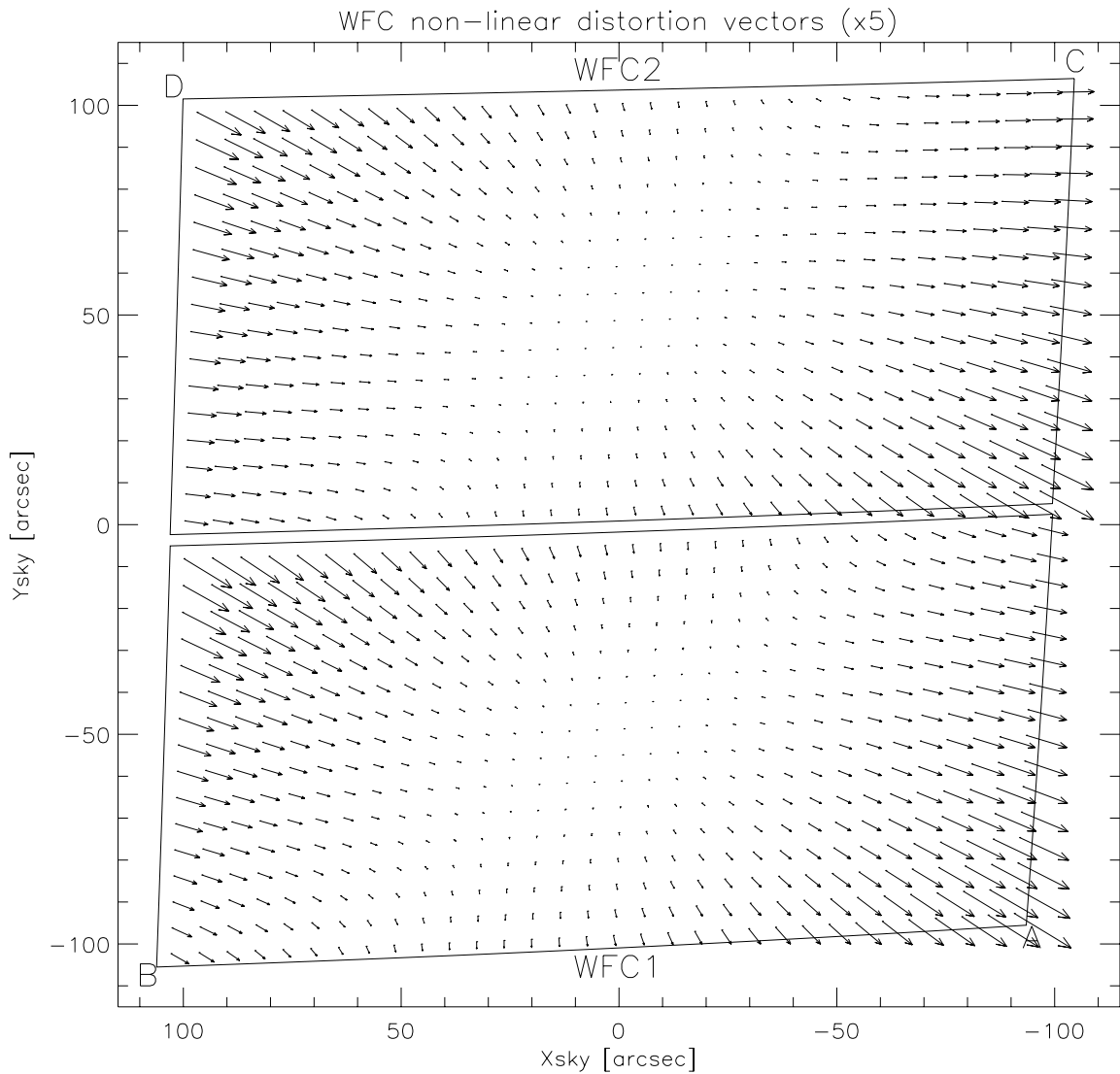
10.3.1 WFC

The rhombus shape of the WFC is evident in Figure 7.8. The angle between the X and Y axes is 84.9° for WFC1 and 86.1° for WFC2. The geometric distortion map for WFC1 and WFC2 is illustrated in Figure 10.127, a vector diagram shows the contribution of the non-linear part of a quadratic fit only. The size of the residuals are scaled by a factor of 5 relative to the sky coordinates and could reach the residuals at about 4.1 arcseconds or 82 ACS/WFC pixels. At the center of chip WFC1 the scale in the X direction is 0.0493 arcseconds per pixel, and 0.0486 arcseconds per pixel in the Y direction. In the case of WFC2, the scale is 0.0498 arcseconds per pixel, and 0.0503 arcseconds per pixel in X and Y direction respectively. Between the corner of WFC nearest to the V1 axis and the diagonally opposite corner, the scale increases by 10%. Because of that WFC1 forms a slightly distorted rectangle 201 by 100 arcseconds in size, while WFC2 is 203 by 103 arcseconds. There is a 2.5 arcsecond gap between the two chips.

As it has been shown by Anderson (2007), the linear terms of the ACS/WFC geometric distortion are changing over time and distortion-corrected positions could be off by up to 0.3 pixels from the beginning of ACS observation.

Geometric distortion affects not only the astrometry but the photometry as well, since it induces an apparent variation in surface brightness across the field of view. In order to preserve the photometric accuracy, an additional correction to the photometry is required, by multiplying the ACS/WFC flat-fielded images by the pixel area map. The effective area of each pixel is shown in Figure 10.128 as a contour plot. The range of area is from 0.89 to 1.08 time to the central value.

Figure 10.127: The geometric distortion map for the ACS/WFC, which shows only the non-linear component to the solution. Note that this figure is rotated 180° with respect to the pipeline calibration products, where WFC2 is the lower half of the detector.



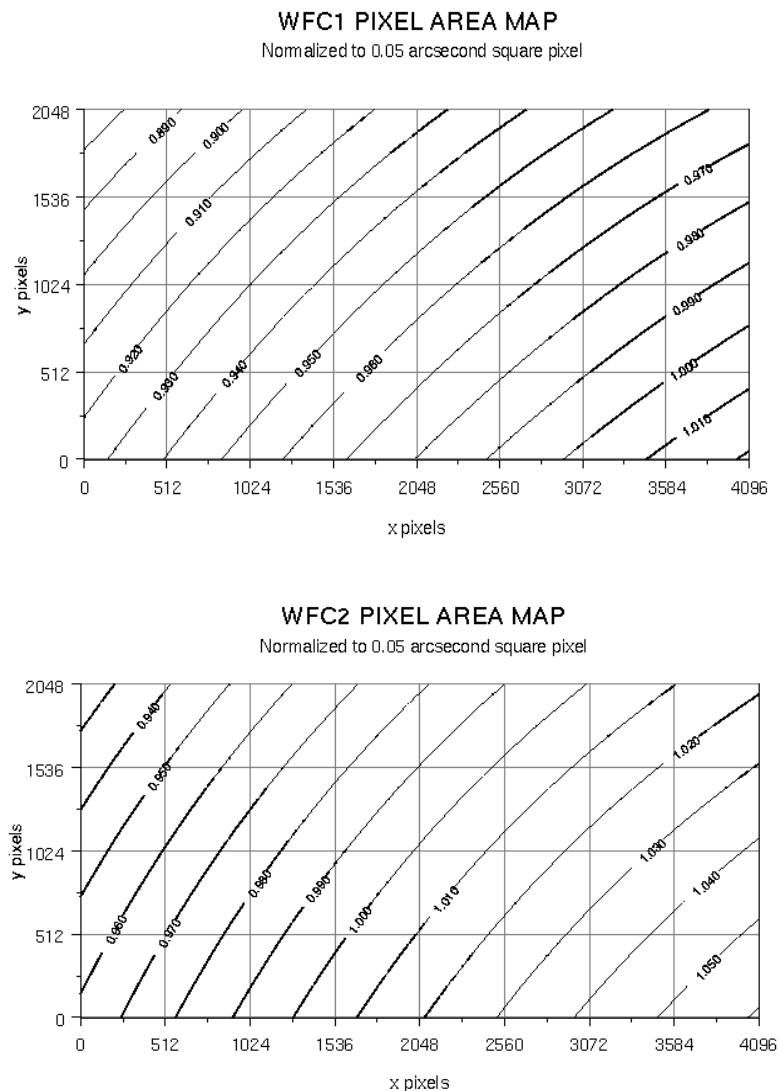
10.3.2 HRC

The High Resolution Channel has its edges aligned approximately along the V2 and V3 axes. In this case, the center of the aperture lies on a line passing through the V2V3 origin and making an angle of 22° with the V3 axis. The diagonal of the aperture does not correspond to a radius of the HST field of view. So the distortion has no particular symmetry with respect to the detector axes. The focal plane of HRC is also 25° away from the plane normal to the light path, and because of this the scales along the axes differ by 14%. The full field of view of the HRC is less than 30

arcseconds, therefore the scale variation over the field is much less than for the WFC and it is about 1%. At the center, the X and Y scales are 0.0284 and 0.0248 arcseconds/pixel respectively. The average scales across the middle of the detector are 0.02842 and 0.02485 arcseconds/pixel making the X and Y widths 29.1 and 25.4 arcseconds. The slightly non-square projected aperture shape is evident in Figure 7.8. The angle between the X and Y axes on the sky is $84^{\circ}.2$. The geometric distortion map for HRC is given in Figure 10.129, where the residuals from the non-linearity are scaled by a factor of 10 relative to the sky coordinates and could reach the residuals at about 0.14 arcseconds, or 4.9 ACS/HRC pixels.

The same as for the WFC, geometric distortion affects not only the astrometry but the photometry as well, and a correction for the pixel area is required to restore the proper total counts of the target. The effective area of each pixel is shown in Figure 10.130 as a contour plot. The maximum deviation from the central value is about 3%.

Figure 10.128: The map of the effective pixel areas of the ACS/WFC chips.



10.3.3 SBC

The Solar Blind Channel contains the MAMA detector. It is centered close to the HRC position in the V2V3 plane and has a slightly larger field of view, about 35 by 31 arcseconds. The scales and distortions have now been measured directly. The maximum distortion displacement is about 2 pixels or 0.06 arcseconds. Figure 10.131 shows the distortion map for the SBC detector.

The HRC and SBC both have much smaller areas than the WFC. In the X direction the scale is 0.0338 arcseconds/pixel while in the Y direction it is 0.0301 arcseconds/pixel. Like the HRC, the SBC exhibits a 13% difference between X and Y scales with a variation across the aperture of a little over 2%. The same as for the other cameras, due to geometric distortion, the photometry is also affected by a variation in pixel size across the SBC. The effective area for each pixel is shown in Figure 10.131 as a contour plot. The maximum deviation from the central value is just over 2%. (Gilliland et.al. 2007)

Figure 10.131: The map of the effective pixel areas of the SBC. The areas are normalized to 0.025 arcsecond square pixels.

Figure 10.129: The geometric distortion map for the HRC.

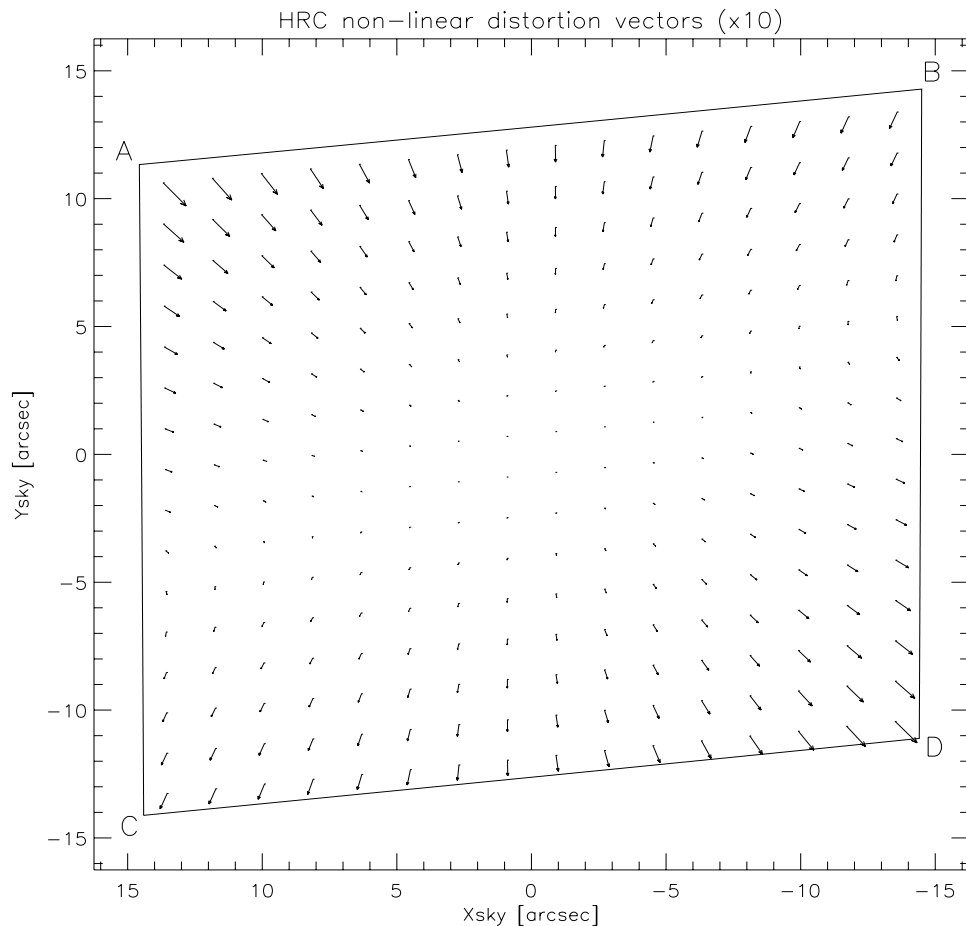


Figure 10.130: The map of the effective pixel areas of the HRC.

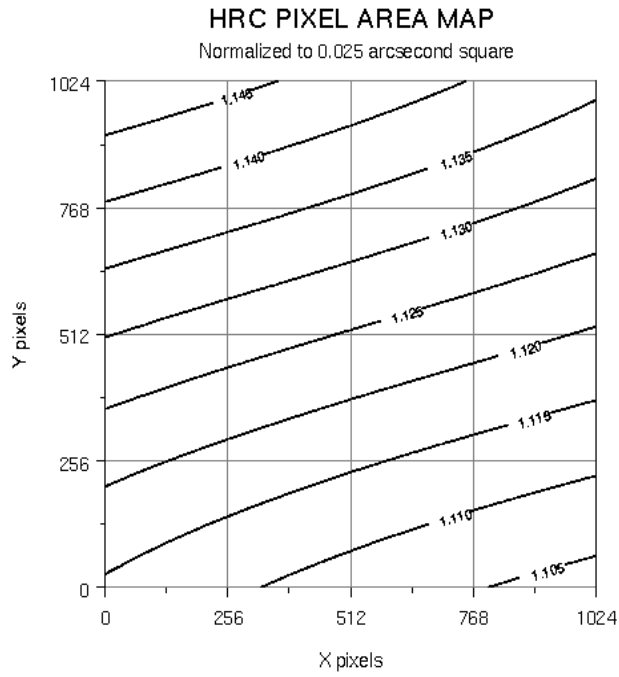


Figure 10.131: The geometric distortion map for the ACS/SBC

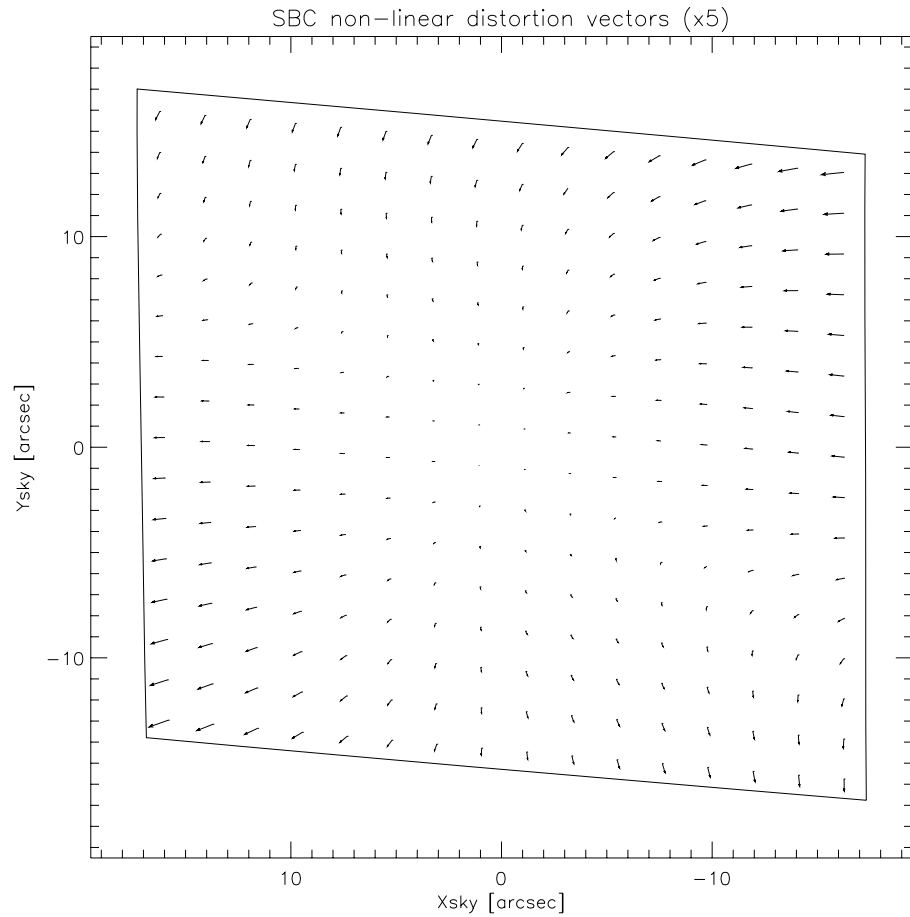
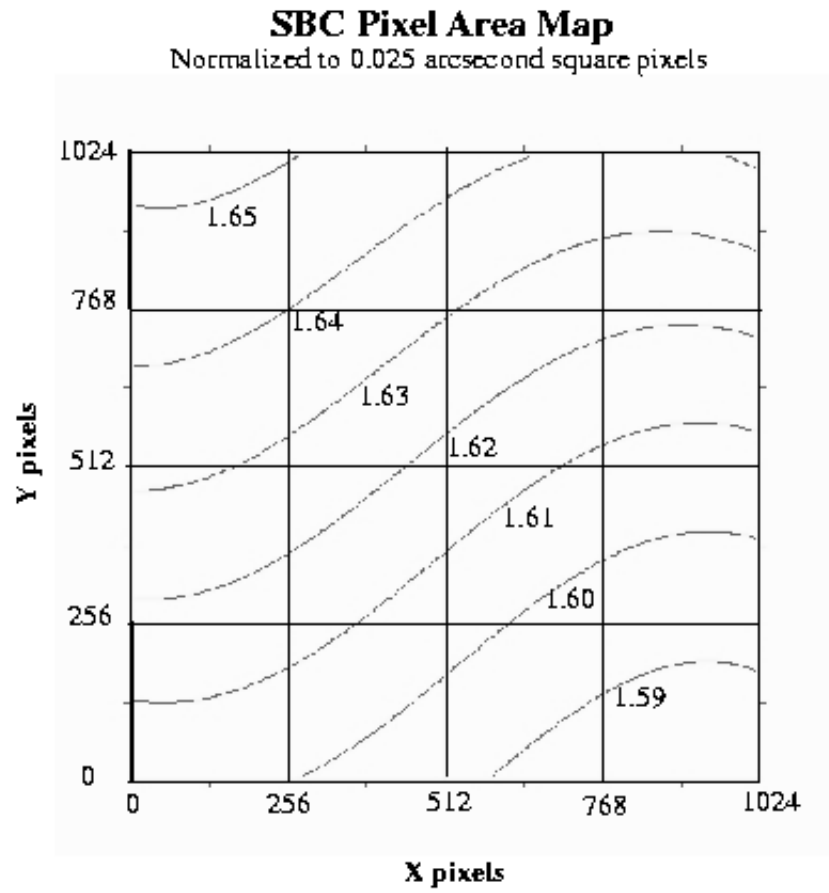


Figure 10.132: The map of the effective pixel areas of the ACS/SBC



Glossary

The following terms and acronyms are used in this Handbook.

ADC: Analog to digital

ABMAG: $-2.5 \log (F_{\nu}) - 48.60$ where F_{ν} is the flux from the source in $\text{erg cm}^{-2} \text{sec}^{-1} \text{Hz}^{-1}$

AB_ν: Correction to ABMAG to account for the fact that the source spectrum is not constant in F_{ν} ($\text{ABMAG}=\text{V}+\text{AB}_{\nu}$)

ACS: Advanced Camera for Surveys

APT: Astronomer's Proposal Tool

aXe: Spectroscopic Data Extraction Software

BOP: Bright Object Protection

calacs: ACS calibration pipeline software

CCD: Charge Coupled Device. Solid-state, light detecting device

CMD: Color Magnitude Diagram

CP: Call for Proposals

CR: Cosmic ray

CR-SPLIT: Division of a CCD exposure into shorter exposures to be used for cosmic ray rejection

CTE: Charge transfer efficiency

CVZ: Continuous viewing zone

DN: Data number

ETC: Exposure Time Calculator. ETCs are Web-based tools which can be accessed through the ACS Web pages.

ERO: Early release observations

FGS: Fine Guidance Sensors

FOS: Faint Object Spectrograph

FOV: Field of view

FTP: File Transfer Protocol. Basic tool used to retrieve files from a remote system. Ask your system manager for information about using FTP.

FUV: Far ultraviolet (~ 912 to 2000 \AA)

- FWHM***: Full width at half maximum
- GALEX***: Galaxy Evolution Explorer
- GHR***: Goddard High-Resolution Spectrograph
- GO***: General Observer
- GSC***: Guide Star Catalog
- GSCII***: Guide Star Catalog II
- GTO***: Guaranteed Time Observer
- Help Desk***: Facility for getting help on HST related topics via email.
help@stsci.edu.
- HRC***: High Resolution Channel
- HST***: Hubble Space Telescope
- IDT***: Investigation Definition Team
- IR***: Infrared
- IRAF***: Image Reduction and Analysis System. The environment in which STSDAS operates.
- ISR***: Instrument Science Report
- IUE***: International Ultraviolet Explorer Satellite
- K***: Degree Kelvin
- L-flats***: Low Frequency Variations Flats
- LMC***: Large Magellanic Cloud
- MAMA***: Multi-Anode Microchannel Array
- MCP***: Microchannel Plate
- MPP***: Multi Pinned Phased, a CCD mode that reduces dark current rate
- NICMOS***: Near-Infrared Camera and Multi-Object Spectrograph
- NUV***: Near ultraviolet (~2000 to 4000 Å)
- OTA***: Optical Telescope Assembly
- PASP***: Publications of the Astronomical Society of the Pacific
- PC***: Program Coordinator
- Phase I proposal***: A proposal for observing time on HST
- Phase II program***: An approved HST program; includes precise detail of how program is to be executed
- PI***: Principal investigator
- P-flats***: pixel-to-pixel high-frequency flats
- PRF***: Pixel Response Function
- PSF***: Point-spread function.
- PyRAF***: version of IRAF implemented in the Python language

QE: Quantum Efficiency

QEH: Quantum Efficiency Hysteresis

Quadrant: Section of detector that is read-out by an amplifier. For WFC, there are 4 amplifiers, two for each detector, so each amplifier reads one 2048 x 2048 pixel quadrant.

RA: Right Ascension

RAS: HST simulator used in ground tests to accurately simulate the full field OTA illumination, and is used to calibrate HST instruments. Also known as RAS/HOMS, the Refractive Aberrated Simulator/Hubble Opto-Mechanical Simulator.

reference file: data file containing ACS parameters or calibration information which is used by the calibration pipeline

rms: Root mean square

RQE: Responsive Quantum Efficiency

SAA: South Atlantic anomaly

SBC: Solar-Blind Channel

SDSS: Sloan Digital Sky Survey

SITe: Scientific Image Technologies; company that designed the ACS CCDs

SLIM: Slitless Spectroscopy Simulator

SMOV: Servicing Mission Observatory Verification

S/N: signal-to-noise ratio

SNAPSHOT: Short exposures taken during unused blocks of telescope time.

ST-ECF: Space Telescope European Coordinating Facility

STAN: Space Telescope Analysis Newsletter

STIS: Space Telescope Imaging Spectrograph

STScI: Space Telescope Science Institute

STSDAS: Space Telescope Science Data Analysis System. The complete suite of IRAF data analysis and calibration routines used to process HST data.

synphot: STSDAS synthetic photometry (IRAF) software package

TAC: Telescope Allocation Committee

TECs: Thermal Electric Coolers

Tiny Tim: PSF simulation software developed by John Krist & Richard Hook

URL: Uniform resource locator. Address for WWW.

UV: Ultraviolet

WFC: Wide-Field Channel

WFPC2: Wide Field Planetary Camera-2. Replacement for WF/PC installed during first servicing mission of December 1993.

WWW: World Wide Web. Hypertext-oriented method for finding and retrieving information over the Internet.

Index

A

AB(nu) 180, 199, 243
Aberrated Beam Coronagraph 86
Aberration Correction 11
ABMAG 177, 199
ACCUM mode
 HRC 135
 SBC 136
 WFC 132
ACQ mode
 effective neutral density filters 137
 HRC 136
Apertures
 available-but-unsupported 121, 142
 coronagraph/acqs 89, 150
 HRC 135, 148, 150
 polarizers 146
 ramps 143, 148
 SBC 151
 small filters 146
 subarrays 134, 146
 WFC 133, 142, 146
A-to-D Converter
 HRC 27, 135
 WFC 27, 132
Auto-Parallels 158, 161

B

Bandpass 56, 201
Blooming 27
BOP
 screening 130
 solar system objects 130

Bright Object Protection 53
 global limit 52, 128
 limiting V magnitudes 125
 local limit 52, 128
 policy 132
 global limit table 128
 parallels 131
 Phase I 126
 Phase II 126
 safety 53
Buffer
 compression 133
 HRC 136
 internal memory 14
 overheads 133
 SBC 136
 SBC 16 bit 49
 WFC 133

C

CALACS 73
Calibration
 accuracies 16
 lamps 13
 non-science exposures/GO obtained 122
 polarizers 79
CCDs
 HRC. See HRC
 WFC. See WFC
Charge Transfer Efficiency 41
 background considerations 42
 parallel measurement/table 41
 predicted/expected losses 43, 124
 science applications 43

- serial measurement/table 41
- utilizing POS TARGS 43
- Coordinated Parallels 157
- Coronagraphy
 - coronagraph design 86
 - exposure time calculation 101
 - Lyot stop 86
 - occulting finger 88
 - occulting masks 86
 - PSF 99
 - target acquisition 136
- Cosmic Rays
 - CR-splitting 37
 - HRC 39
 - WFC 39
- Count Rate Limits
 - SBC 46, 53
- CR-SPLIT 138, 158, 168
- CTE 41

D

- Dark Current
 - SBC 46
- Dark Frames
 - HRC/WFC 30
- Data Number (DN) 24, 132, 135
- Data Storage
 - buffer dumps 14, 133
 - buffer size 14
 - data transfer rate/overheads 14
 - data volume 122
- Detectors
 - HRC. See HRC
 - SBC. See SBC
 - WFC. see WFC
- Dithering
 - cosmic rays 37
 - goals 137
- Drizzle/Multidrizzle 139
- Dynamic Range 141

E

- Earthshine 187, 195
- Encircled Energy

- models 72
- Exposure Time Calculations 175
 - bright object limits 125
 - ETC 175
 - examples 191
 - sky backgrounds 195
 - useful quantities tables 177
- Exposures
 - minimum/maximum exposure time 10, 136
 - overheads 168
 - target-acquisition 122
- Extinction 190

F

- Field of View (FOV)
 - HRC 148
 - ramps 144
 - SBC 151
 - WFC 142
- Filter Wheel
 - SBC 13
 - WFC/HRC 13
- Filters 17, 176
 - HRC/F220W 214, 215
 - HRC/F250W 216
 - HRC/F330W 217
 - HRC/F344N 218
 - HRC/F435W 219
 - HRC/F475W 220
 - HRC/F502N 221
 - HRC/F550M 222
 - HRC/F555W 223
 - HRC/F606W 224
 - HRC/F625W 225
 - HRC/F658N 226
 - HRC/F660N 227
 - HRC/F775W 228
 - HRC/F814W 229
 - HRC/F850LP 230
 - HRC/F892N 231
 - HRC/G800L 232
 - HRC/PR200L 233
 - Johnson-Cousins 64
 - narrow-band 65
 - Ramp Filters

HRC 66
 WFC 65
 SBC Summary Table 58
 SBC/F115LP 235
 SBC/F122M 236
 SBC/F125LP 237
 SBC/F140LP 238
 SBC/F150LP 239
 SBC/F165LP 240
 SBC/PR110LP 241
 SBC/PR130LP 242
 Sloan Digital Sky Survey 65
 WFC/F435W 201
 WFC/F475W 202
 WFC/F502N 203
 WFC/F550M 204
 WFC/F555W 205
 WFC/F606W 206
 WFC/F625W 207
 WFC/F658N 208
 WFC/F660N 209
 WFC/F775W 210
 WFC/F814W 211
 WFC/F850LP 212
 WFC/G800L 213
 WFC/HRC Summary Table 57
 Flat Field
 HRC 25
 WFC 25
 Fringing 23
 Full Well 27

G

Gain
 ACCUM default 61
 ACQ default 61
 HRC 24, 135
 WFC 24
 Geocoronal emission 189
 Geometric Distortion
 PSF 72
 temporal changes 138
 WFC 64

H

Hot Pixels
 anneal cycles 35
 creation rate table 34
 data quality array 37
 dither pattern 37
 permanent growth table 37
 shot noise 37
 spontaneous healing 38
 warm pixels definition 33
 HRC
 ACCUM 135
 ACQ 136
 apertures 135, 148
 A-to-D converter 135
 buffer 136
 characteristics 66
 coating 22
 cosmic rays 39
 dark count 15
 detector architecture 10
 field of view 15
 flat field 25
 fringing 23
 full well 27
 full width half maximum (FWHM) 66
 gain 135, 141
 multiple electron events 44, 67
 operating temperature 15
 Performance Characteristics Table 15
 physical overscan 23
 pixel size 15
 plate scale 15, 156
 point spread function 71
 QE hysteresis 23
 quantum efficiency 15
 ramp filters 135, 145
 read noise 15, 29
 readout 23
 red leaks 67
 saturation 27
 subarrays 136
 virtual overscan 23

http 2

[//www.stsci.edu/hst/acs](http://www.stsci.edu/hst/acs) 2

I

Imaging

- anomalies 124
- BOP 125
- HRC detector 66
- limiting magnitude 62
- saturation 64
- SBC detector 68
- signal-to-noise 63
- throughput 62
- WFC detector 64

Imaging caveats 60

- filters see filters 60

Integrated System Throughput 62

L

Lamps

- deuterium 13
- tungsten 13

Light Paths 12

Limiting Magnitudes 62

Linearity

- CCDs 141
- SBC 52

LOW-SKY 189, 192

Lyot Stop 86

M

MAMA. See SBC

Memory. See Buffer

Multidrizzle/Drizzle 139

O

Optical Path

- HRC/SBC 12
- WFC 12

Optics

- coronagraph 11
- corrective optics 11
- fold mirror 11
- HRC/SBC 11
- spherical aberration 11
- WFC 11

Orbit-Time Determination 166

Orientation

- computing 152
- ORIENTAT 153
- PA_APER 153

Overheads

- buffer dumps 133, 168
- buffer size 168
- examples 170
- guide star ACQ/reACQ 166
- HRC/SBC toggle 169
- observatory level 166
- readout 167
- science exposure level 167
- spectroscopy 168
- subarrays 169
- table 167
- target acquisition 167
- WFC parallel buffer dumps 169

P

Parallel Observations

- APT 156
- auto-parallels 158
- coordinated parallels 157
- pointing 156
- pure parallels 161
- SBC in parallel 131

Patterns 137

Phase I

- bright object limits 126
- preparation 3, 117

Photometry

- encircled energy 72, 177
- zero point 177

Pivot Wavelength 177

Plate Scale 137, 156

Polarimetry

- Calibration 79
- filters 82, 84
- FOV 83
- throughput 80

Post-flash 13, 124

PSF

- coronagraphy 99

- encircled energy 72
 - geometric distortion 72
 - HRC 71
 - HRC halo 66
 - models 71
 - pixel response function 70
 - residual aberrations 76
 - undersampling 64, 66
 - WFC 71
 - Pure Parallel Program 162
- Q**
- Quantum Efficiency Hysteresis 23
- R**
- Ramp Filters
 - aperture location 135
 - apertures 143
 - Readout Time 10, 167
 - Red Leaks
 - HRC 67
 - SBC 68
- S**
- Saturation
 - CCDs 27
 - SBC 49
 - SBC
 - ACCUM mode 44, 136
 - apertures 151
 - BOP 131
 - buffer 136
 - characteristics 46, 68
 - flat field 51
 - global count rate 52
 - limiting count rates 54
 - local count rate 52
 - MAMA detector
 - non-linearity 52
 - optical path 12
 - physical description 10
 - plate scale 15
 - policy 11, 131
 - PSF 48
 - red leaks 68
 - repeller wire 45
 - signal to noise limitation 50
 - spectral response 46
 - Scheduling
 - SBC considerations 48
 - Sensitivity
 - HRC/G800L 108
 - HRC/PR 200L 109
 - WFC/G800L 106, 107
 - Shutter 28
 - Signal-to-Noise 182
 - sky background 195
 - Solar System Objects 130
 - South Atlantic Anomaly 48
 - Spectral Response. See Imaging throughput 62
 - Spectroscopy
 - HRC 107
 - SBC 110
 - WFC 105
 - STIS 48
 - Subarrays
 - amplifier 134
 - coronagraph 136
 - data volume 134
 - HRC 136
 - overscan 134
 - Synphot 176
- T**
- Target ACQ
 - accuracy 13
 - aperture 13
 - coronagraph 13
 - ramp filters 13
 - Tiny TIM 71
 - Transmission Curves
 - broad-band filters 58
 - medium-band filters 59
 - narrow-band filters 59
 - SBC filters 59
 - SDSS filters 58
- W**
- WFC
 - ACCUM 132
 - apertures 133, 142

- characteristics 64
- cosmic rays 39
- dark count 15
- detector architecture 10
- field of view 15
- flat field 25
- fringing 23
- full well 27
- full width half maximum (FWHM) 64
- gain 132, 140
- non-repeatability 28
- operating temperature 15
- Performance Characteristics Table 15
- pixel size 15
- plate scale 15, 156
- point spread function 71
- QE hysteresis 23
- quantum efficiency 15
- ramp filters 135, 143
- read noise 15
- readout 23
- saturation 27
- virtual overscan 23

Z

- Zodiacal Light 195